Research Article
Cholestasis and Autoimmune Diseases

JOURNAL
OF HEPATOLOGY

Plectin controls biliary tree architecture and stability in cholestasis

Graphical abstract

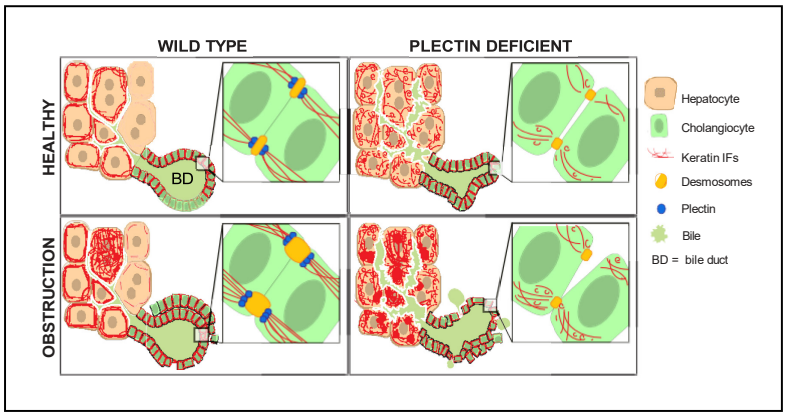

Highlights

- A novel liver-specific plectin knockout mouse model was generated.
- Plectin deficiency leads to aberrant organization and instability of epithelial keratin filaments.
- Plectin is responsible for a proper canalicular network formation and biliary tree architecture.
- Plectin preserves bile duct integrity under cholestatic stress.

Authors

Marketa Jirouskova, Katerina Nepomucka, Gizem Oyman-Eyrilmez, ..., Radislav Sedlacek, Gerhard Wiche, Martin Gregor

Correspondence

martin.gregor@img.cas.cz
(M. Gregor)

Lay summary

Plectin is a cytolinker protein capable of interconnecting all three cytoskeletal filament systems and linking them to plasma membrane-bound junctional complexes. In liver, the plectin-controlled cytoskeleton mechanically stabilizes epithelial cells and provides them with the capacity to adapt to increased bile pressure under cholestasis.

http://dx.doi.org/10.1016/j.jhep.2017.12.011
 J. Hepatol. 2018, 68, 1006–1017

Research Article
Cholestasis and Autoimmune Diseases

JOURNAL OF HEPATOLOGY

Plectin controls biliary tree architecture and stability in cholestasis

Marketa Jirouskova[1,¥], Katerina Nepomucka[1,2,¥], Gizem Oyman-Eyrilmez[1], Alzbeta Kalendova[1], Helena Havelkova[1], Lenka Sarnova[1], Karel Chalupsky[3], Bjoern Schuster[3], Oldrich Benada[4], Petra Miksatkova[5], Martin Kuchar[5], Ondrej Fabian[6], Radislav Sedlacek[3,7], Gerhard Wiche[8], Martin Gregor[1,⇑]

[1]*Laboratory of Integrative Biology, Institute of Molecular Genetics of the Czech Academy of Sciences, Prague, Czech Republic;* [2]*Department of Physiology, Faculty of Science, Charles University, Prague, Czech Republic;* [3]*Czech Centre for Phenogenomics, Institute of Molecular Genetics of the Czech Academy of Sciences, Prague, Czech Republic;* [4]*Laboratory of Molecular Structure Characterization, Institute of Microbiology of the Czech Academy of Sciences, Prague, Czech Republic;* [5]*Forensic Laboratory of Biologically Active Substances, Department of Chemistry of Natural Compounds, University of Chemistry and Technology Prague, Prague, Czech Republic;* [6]*Department of Pathology and Molecular Medicine, Charles University, Prague, and University Hospital Motol, Prague, Czech Republic;* [7]*Laboratory of Transgenic Models of Diseases, Institute of Molecular Genetics of the Czech Academy of Sciences, Prague, Czech Republic;* [8]*Department of Biochemistry and Cell Biology, Max F. Perutz Laboratories, University of Vienna, Austria*

..Background & Aims: Plectin, a highly versatile cytolinker protein, controls intermediate filament cytoarchitecture and cellular stress response. In the present study, we investigate the role of plectin in the liver under basal conditions and in experimental cholestasis.

Methods: We generated liver-specific plectin knockout (*Ple*^{Dalb}) mice and analyzed them using two cholestatic liver injury models: bile duct ligation (BDL) and 3,5-diethoxycarbonyl-1,4-dihydrocollidine (DDC) feeding. Primary hepatocytes and a cholangiocyte cell line were used to address the impact of plectin on keratin filament organization and stability *in vitro*.

Results: Plectin deficiency in hepatocytes and biliary epithelial cells led to aberrant keratin filament network organization, biliary tree malformations, and collapse of bile ducts and ductules. Further, plectin ablation significantly aggravated biliary damage upon cholestatic challenge. Coincidently, we observed a significant expansion of A6-positive progenitor cells in *Ple*^{Dalb} livers. After BDL, plectin-deficient bile ducts were prominently dilated with more frequent ruptures corresponding to an increased number of bile infarcts. In addition, more abundant keratin aggregates indicated less stable keratin filaments in *Ple*^{Dalb} hepatocytes. A transmission electron microscopy analysis revealed a compromised tight junction formation in plectin-deficient biliary epithelial cells. In addition, protein profiling showed increased expression of the adherens junction protein E-Cadherin, and inefficient upregulation of the desmosomal protein desmoplakin in response to BDL. *In vitro* analyses revealed a higher susceptibility of plectin-deficient keratin networks to stress-induced collapse, paralleled by elevated activation of p38 MAP kinase.

Conclusion: Our study shows that by maintaining proper keratin network cytoarchitecture and biliary epithelial stability, plectin plays a critical role in protecting the liver from stress elicited by cholestasis.

Lay summary: Plectin is a cytolinker protein capable of interconnecting all three cytoskeletal filament systems and linking them to plasma membrane-bound junctional complexes. In liver, the plectin-controlled cytoskeleton mechanically stabilizes epithelial cells and provides them with the capacity to adapt to increased bile pressure under cholestasis.

Introduction

The biliary tree is a complex three-dimensional (3D) tubular network that drains the bile produced by hepatocytes to the small intestine. The bile is secreted into the bile canaliculi and flows through interconnected small and large bile ducts (BDs), which are lined with cuboidal biliary epithelial cells (BECs). Disorders affecting the function of BECs underlie diverse cholangiopathies (*e.g.* primary sclerosing cholangitis and primary biliary cirrhosis), often characterized by cholestatic condition.[1] Biliary obstructions elicit a toxic response, and increased biliary pressure leads to epithelial ruptures and leakage of bile into the parenchyma. In response to a subsequent hepatocellular injury, BECs and hepatic progenitor cells (termed the oval cells in rodents) start to proliferate in a "ductular reaction". Their expansion gives rise to an increased number of biliary ductules. Thus, by forming a significantly denser duct meshwork around the portal vein, the biliary system adapts to effectively drain the accumulated biliary fluid.

A prominent group of genes that becomes upregulated in response to a cholestatic insult encodes keratins.[2–4] In the liver, both hepatocytes and BECs express keratins (K) 8 and 18, whereas only BECs additionally contain K7, K19 and K23.[4,5] Mutations in keratin genes resulting in unstable and abnormally organized keratin filaments (KFs) predispose their carriers to various liver diseases, including cholangiopathies.[6,7] Mouse models that either lack or mimic mutant human K8 or K18 show

Keywords: Cytolinker; Keratin filaments; Bile duct ligation; DDC diet; Cell-cell junctions.
Received 30 June 2017; received in revised form 27 November 2017; accepted 12 December 2017; available online 20 December 2017

⇑ Corresponding author. Address: Laboratory of Integrative Biology, Institute of Molecular Genetics of the Czech Academy of Sciences, Víden˘ská 1083, Prague 4, CZ-14220, Czech Republic. Tel.: +420 241 063 461; fax: +420 224 310 955.
E-mail address: martin.gregor@img.cas.cz (M. Gregor).
¥ These authors contributed equally to this work.

increased fragility of hepatocytes, increased necrosis and hemorrhage with subsequent lethality (as reviewed in[8]). Although little is known about biliary keratins, an attenuated ductular reaction and aggravated cholestatic injury upon targeted inactivation of K19[9] suggest their critical role in biliary epithelium.

Proper organization of intermediate filament (IF) networks is maintained by cytoskeletal linker proteins (cytolinkers) of the plakin protein family. Plectin, a prototypical ubiquitously expressed cytolinker, crosslinks IFs and anchors them at junctional complexes, including hemidesmosomes (HDs) and desmosomes (Ds) of epithelial cells.[10] In addition, plectin binds to actomyosin and microtubule network systems, thus affecting not only mechanical but also dynamic properties of the cytoskeleton. Multiple studies have shown that the deletion of plectin leads to aberrant KF organization[11,12] manifesting as more bundled and less flexible filaments.[11] Without plectin, KF networks are less stable and more prone to collapse under both mechanical and non-mechanical stress conditions.[11] The absence of a plectin-mediated IF anchorage has been found to alter the structure and functionality of junctional complexes.[12–15] For instance, homeostasis and stability of HDs in keratinocytes is strictly dependent on plectin-mediated KF recruitment,[15] and a reduction in the number of HDs and their dysfunction are directly linked to skin fragility.[12,15] Similarly, a tissue-specific plectin deletion in mouse endothelium has adverse effects on the formation of adherens and tight junctions (AJs and TJs) with consequences for endothelial barrier function.[13]

The overall objective of this study was to determine how plectin controls KF networks in the liver and how it contributes to their hepatoprotective roles. Our results demonstrate an absolute plectin requirement for maintaining proper biliary tree architecture and epithelial stability in cholestatic injury.

Materials and methods

Animal experiments

Liver-specific deletion of the plectin (*Plec*) gene was achieved by breeding $Ple^{fl/fl}$ mice[16] ($Ple^{fl/fl}$) with *Alb-Cre* transgenic mice (MGI 2176228; The Jackson Laboratory, Bar Harbor, ME) to generate $Ple^{fl/fl}$/*Alb-Cre* mice (Ple^{Dalb}). All animal studies were performed in accordance with European Directive 86/609/EEC and they were approved by the Czech Central Commission for Animal Welfare. All experiments were performed using age-matched littermate male mice. To induce cholestatic liver injury, mice were either subjected to BDL or fed a diet supplemented with 0.1% DDC.

Electron microscopy

In situ whole liver perfusion was performed at 1.5 ml/min (20 min) with glutaraldehyde (1.5%) in phosphate-buffered saline (PBS; pH 7.2). Liver pieces were immersed in a fixative solution (1% glutaraldehyde and 4% paraformaldehyde in PBS) for 48 h and further processed for transmission and scanning electron microscopy.

Isolation and cultivation of primary hepatocytes

Primary hepatocytes were isolated from $Ple^{fl/fl}$ and Ple^{Dalb} mice by a collagenase perfusion as previously described.[17] To study the canalicular formation and morphology *in vitro*, hepatocytes were grown in a collagen sandwich culture.[18]

CRISPR-mediated targeting of plectin in mouse cholangiocytes

Immortalized mouse cholangiocytes (MSC; a gift of Y. Ueno, Tohoku University, Japan) were maintained in Dulbecco's modified Eagle medium (DMEM) as described previously.[19] A plectin knockout (KO) MSC cell line was generated by targeting genomic sequences of intron 25 and 31 of plectin using CRISPR/Cas9 system.[20]

Statistical analysis

Data from animal experiments are reported as arithmetic means ± standard error of means (SEM) of 3–7 animals in each group. *In vitro* data, presented as means ± SEM, were obtained from three independent experiments. Normally distributed data were analyzed by Student's *t* test using GraphPad Prism 5 (GraphPad Software, Inc., La Jolla, CA) with a p value <0.05 considered as statistically significant.

For further details regarding the materials used, please refer to the CTAT table and supplementary information.

Results

Plectin colocalizes with KFs and junctional complex proteins in mouse liver epithelial cells

Early on plectin was shown to be abundantly expressed in the liver and to prominently associate with canaliculi.[21] To study the localization of plectin in more detail, we subjected mouse liver paraffin sections to immunofluorescence microscopy. In both hepatocytes and BECs, plectin clearly delineated cell boundaries, where it partially colocalized with pan-keratin (pan-K) positive IFs (Fig. 1A). Plectin also showed extensive colocalization with the tight junction (TJ) protein zonula occludens-1 (ZO-1, Fig. 1B) and the AJ protein E-Cadherin (Fig. S1) at the surface of BECs and bile canaliculi. As plectin was reported to protect KF cytoarchitecture from various types of stress,[11] we analyzed whether plectin expression was upregulated in two liver injury mouse models. We observed substantially increased expression of plectin at both mRNA and protein levels in livers subjected to BDL or in DDC-fed animals (Fig. 1C, D). In line with previous findings[3,22] the upregulation was paralleled by an increase in K18 and K19 expression (Fig. 1C, D). Together, these results suggest a potential involvement of plectin in response to a cholestatic liver disease.

Liver-specific plectin deficiency leads to aberrant organization of epithelial KFs

To explore the role of plectin in liver epithelium, we generated liver-specific plectin knockout (Ple^{Dalb}) mice (see Materials and Methods). A successful ablation of plectin in liver epithelium was confirmed by immunofluorescence microscopy and plectin expression analysis (Fig. S2). Under physiological conditions, Ple^{Dalb} mice display no signs of gross pathology, as we observed normal serum liver enzyme levels (Fig. S3) and detected no obvious histological abnormalities (Fig. S4). Moreover, no significant changes were found in either the biliary bile acid composition, expression of bile acid transporters and receptors or bile flow rates (Fig. 2A–D).

As plectin acts as a major organizer of keratin cytoarchitecture,[11] we compared the appearance of KFs in $Ple^{fl/fl}$ and Ple^{Dalb} liver sections by immunofluorescence microscopy. In $Ple^{fl/fl}$ hepatocytes, K8 and K18 displayed a mostly perimembraneous staining pattern, whereas in Ple^{Dalb} cells, KFs were evenly

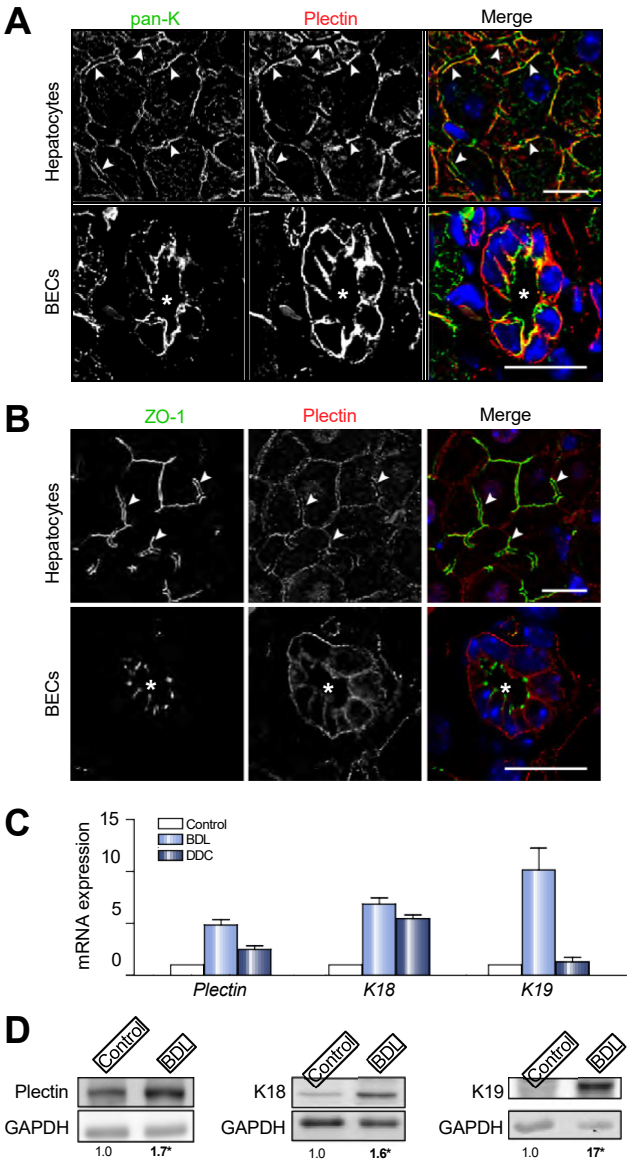

Fig. 1. Plectin expression in mouse liver epithelial cells. (A, B) Paraffin mouse liver sections were immunolabelled using antibodies to plectin, pan-keratin (pan-K; A) or ZO-1 (B). Nuclei were stained with DAPI (blue). Detailed images of hepatocytes and BECs are shown. The arrowheads indicate bile canaliculi; the asterisks, biliary lumen. Scale bars, 10 1m. (C) The relative mRNA levels of plectin, *K18* and *K19* in livers of mice challenged with BDL, the DDC diet, and untreated controls. n = 4. (D) Immunoblots of liver lysates prepared from mice challenged with BDL or unchallenged controls using antibodies to plectin, K18 and K19. GAPDH, loading control. Numbers below lines indicate relative band intensities normalized to average control values. n = 3–4; **p* <0.05, control *vs.* BDL calculated using Student's *t* test. BDL, bile duct ligation; BECs, biliary epithelial cells; DDC, 3,5-diethoxycarbonyl-1,4-dihydrocollidine; GAPDH, glyceraldehyde 3-phosphate dehydrogenase; K18/19, keratin 18/19; pan-K, pan-keratin; ZO-1, zonula occludens-1.

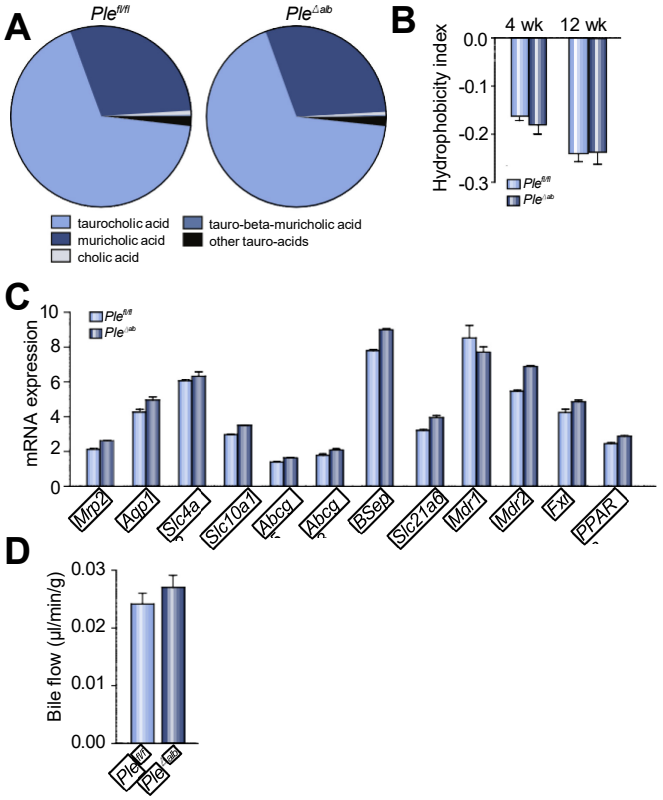

Fig. 2. Comparable bile composition, expression of bile acids transporters and receptors, and bile flow rate in *Ple*$^{fl/fl}$ and *Ple*^{Dalb} mice. (A) The bile acid composition was analyzed using liquid chromatography-tandem mass spectrometry. n = 5. (B) Bile hydrophobicity index was calculated from the biliary bile acid composition at the age indicated. n = 5. (C) The relative mRNA levels of bile acid transporters and receptors. n = 7–9. (D) The bile flow was measured in 12-week-old *Ple*$^{fl/fl}$ and *Ple*^{Dalb} mice. n = 5–6. Results from *Ple*$^{fl/fl}$ and *Ple*^{Dalb} mice were compared using Student's *t* test. *Ple*^{Dalb}, liver-specific *Plec* knockout; *Ple*$^{fl/fl}$, *Plec*$^{flox/flox}$.

distributed throughout the cytoplasm (Fig. 3A, B; see also 3D reconstruction in Fig. S5A and Videos S1 and S2). In contrast to hepatocytes, the general appearance of the K18 and K19 staining patterns did not significantly differ between *Ple*^{Dalb} and *Ple*$^{fl/fl}$ BECs (Fig. 3C, D). However, quantitative fluorescence microscopy revealed that the absence of plectin resulted in a decrease of K18 fluorescence intensity at the apical membrane, accompanied by an increase of K19 fluorescence intensity at the basal membrane, leading to a partial loss of typically polarized keratin cytoarchitecture (Fig. 3C, D; box plot graphs). This was further clearly discernible from 3D reconstruction analysis of pan-K-immunolabelled BECs (Fig. S5B). Similar trends were observed for their type II pairing partners K8 and K7 (Fig. S6A, B). The changes observed in KF localization were not a consequence of altered keratin expression levels, as no differences were found by immunoblotting liver lysates (Fig. 3E, S6C). Thus, plectin deficiency results in cytosolic localization of KFs in hepatocytes and in the redistribution of apicobasal localization of KFs in *Ple*^{Dalb} BECs, affecting KF cytoarchitecture in these cells.

Ple^{Dalb} mice show malformations of interlobular BDs and ductules accompanied by ductular reaction

The plectin-mediated IF network anchorage is known to impart mechanical stability on cells required to maintain proper tissue architecture.[15,16] To determine the ductular luminal shape, we performed a morphometric analysis of K19-immunolabelled intralobular BDs and luminized ductules in 4- and 12-week-old mice. Strikingly, both BDs and ductules in *Ple*^{Dalb} mice showed a reduction in the cross-sectional luminal area, while no differences in the luminal perimeter were detected (Fig. 4A). When the luminal shape was quantified by calculating

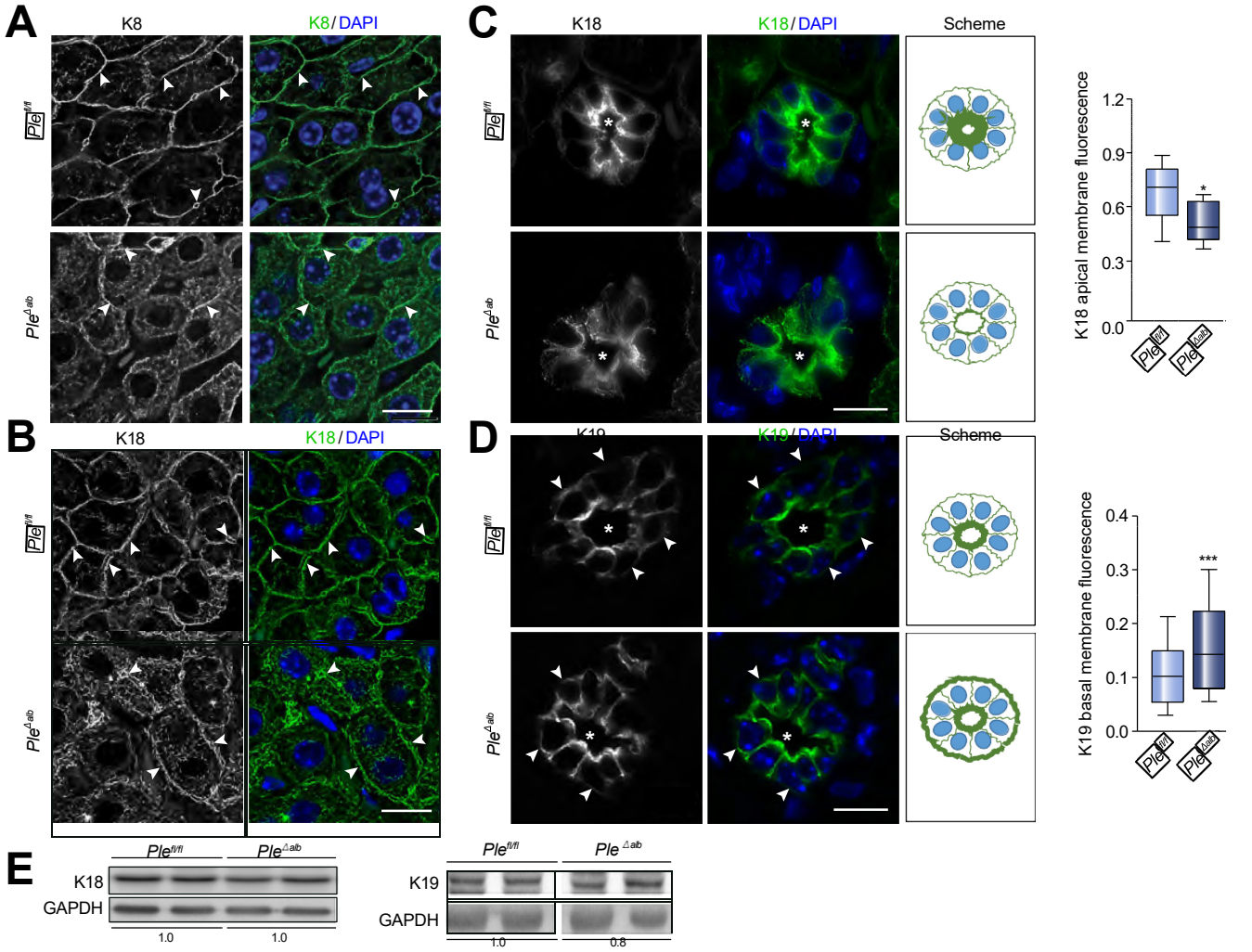

Fig. 3. Plectin organizes KFs in both hepatocytes and BECs. (A–D) Immunolabelling of K8 (A) and K18 (B) in hepatocytes and K18 (C) and K19 (D) in BECs. Nuclei were stained with DAPI (blue). Drawn schemes depict reduced apical membrane K18 (C) and increased basal membrane K19 (D) staining in *Ple*^{Dalb} BECs. The arrowheads, bile canaliculi (A, B) or basal membrane of BECs (C, D); the asterisks, biliary lumen. Scale bars, 10 1m. The box plot graphs show the quantification of the apical membrane (C) and the basal membrane (D) fluorescence intensities in individual BECs normalized to total fluorescence intensity per cell. >250 BECs were analyzed in three mice per genotype. The box represents the 25–75th percentiles, and the median is indicated. *p <0.05, ***p <0.001 calculated using Student's t test. (E) Liver lysates were subjected to immunoblotting using antibodies to K18 and K19. GAPDH, loading control. Numbers below lines indicate relative band intensities normalized to average control values. BECs, biliary epithelial cells; GAPDH, glyceraldehyde 3-phosphate dehydrogenase; K8/18/19, keratin 8/18/19; *Ple*^{Dalb}, liver-specific *Plec* knockout; *Ple*$^{fl/fl}$, *Plec*$^{flox/flox}$.

the circularity and the axial ratio (see Materials and Methods), both parameters indicated significantly irregular and rather elongated ductular lumens in *Ple*^{Dalb} livers compared to more rounded lumens in *Ple*$^{fl/fl}$ livers (Fig. 4A). This phenotype was not aggravated with aging as seen from morphometric analysis of luminized structures of 20- and 40-week-old mice (Fig. S7). Ductular dysmorphology was paralleled by a prominent increase in the number of ductules and K19-positive (K19^{+}) cells per portal field in *Ple*^{Dalb} livers (Fig. 4B), while the numbers of interlobular BDs and individual K19^{+} cells remained unchanged compared to *Ple*$^{fl/fl}$ livers (Fig. 4B, S8A). A further analysis showed a comparable content of A6-positive (A6^{+}) progenitors/oval cells in *Ple*$^{fl/fl}$ and *Ple*^{Dalb} livers (Fig. S8B). These findings suggest that under physiological conditions, aberrant KF cytoarchitecture in plectin-deficient BECs leads to collapse of ductular lumens and to a mild ductular reaction.

Plectin is responsible for a proper canalicular network formation in the liver

Given the ductular dysmorphology in *Ple*^{Dalb} livers we next assessed whether plectin deficiency also affects the canalicular formation. In sharp contrast to regularly shaped bile canaliculi in *Ple*$^{fl/fl}$ livers (Fig. 4C, S8C), scanning electron microscopy of *Ple*^{Dalb} livers showed distorted, wider, and more meandering bile canaliculi with frequent blind end loops (Fig. 4C and S8C). A quantitative analysis of canalicular morphology revealed a significantly wider range of canalicular widths in *Ple*^{Dalb} compared to *Ple*$^{fl/fl}$ livers (Fig. 4C). An analysis of 3D reconstructions of ZO-1-immunolabelled sections confirmed partially dilated, more meandering and prominently misshaped bile canaliculi in *Ple*^{Dalb} livers (Fig. 4D). Further, an increased number of branching points indicated denser canalicular networks. Immunofluorescence microscopy of F-actin-labelled collagen

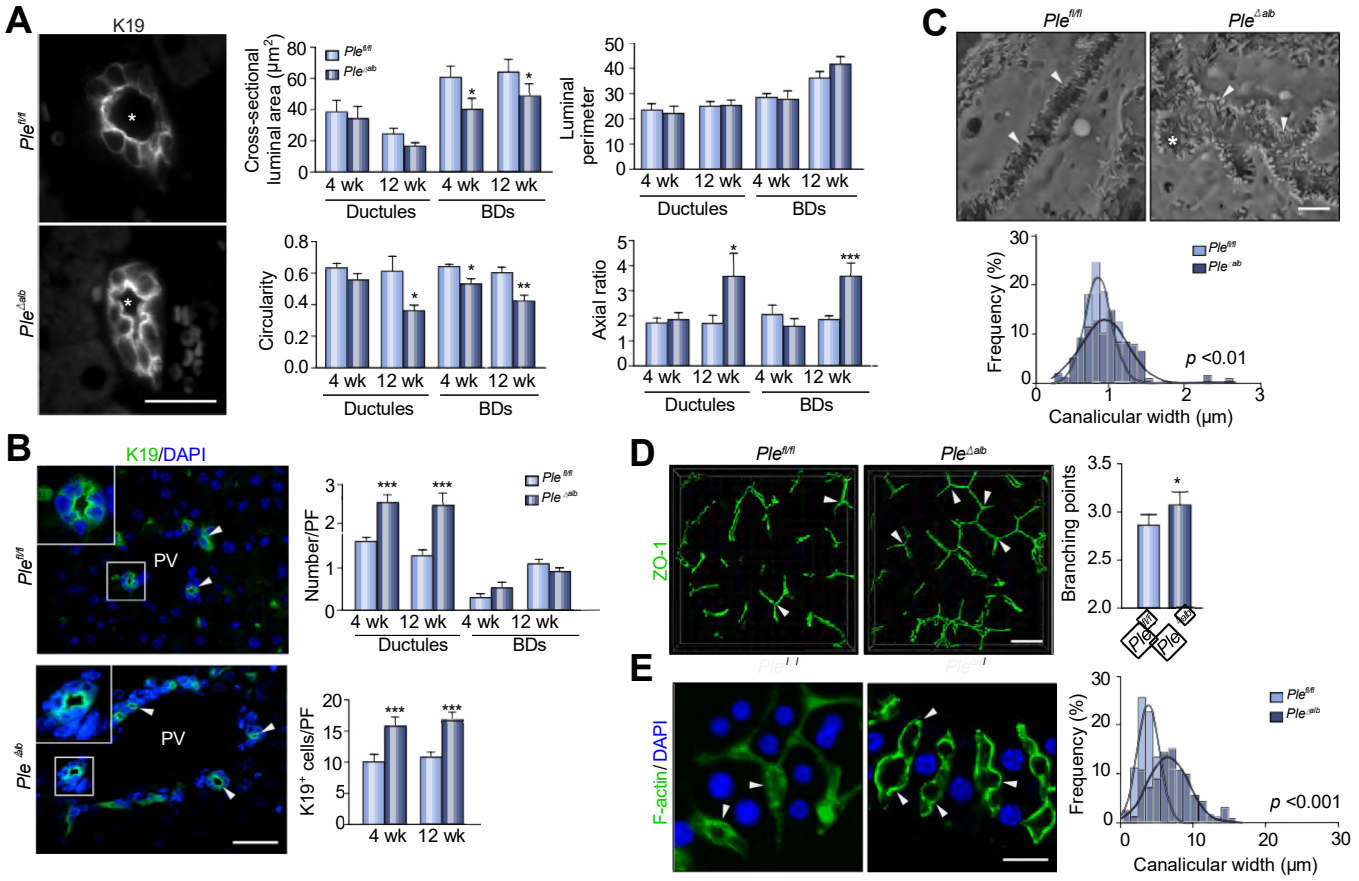

Fig. 4. Biliary tree malformations and a ductular reaction in *Ple*^{Dalb} mice. (A) Morphometric evaluation of interlobular ductules and BDs in *Ple*$^{fl/fl}$ and *Ple*^{Dalb} liver sections from 4- and 12-week-old mice stained with antibodies to K19. The asterisks, biliary lumen. Scale bar, 10 µm. The cross-sectional luminal area, the luminal perimeter, the circularity and the axial ratio (the ratio between the largest and the smallest orthogonal luminal diameter) were determined for >10 ductules and >10 BDs in three mice per genotype. (B) Representative immunofluorescence images of portal fields from liver sections immunolabelled with antibodies to K19. Nuclei were stained with DAPI. The arrowheads, ductular structures. Scale bar, 50 µm. Boxed areas show ~x2 images. The bar graphs show the number of ductules and BDs and the number of K19⁺ cells in >10 PF in three mice per genotype. (C) Representative SEM micrographs of bile canaliculi. The arrowheads, bile canaliculi; the asterisk, blind loop in *Ple*^{Dalb} canaliculi only. Scale bar, 1 µm. Histogram of morphometric analyses of canalicular widths from six images in two mice per genotype. (D) 3D reconstruction of deconvolved images of ZO-1 immunolabelled bile canaliculi (the arrowheads, branching points). Scale bar, 10 µm. The bar graph shows the number of branching points per optical field. n = 6. (E) 3D cultures of primary hepatocytes isolated from *Ple*$^{fl/fl}$ and *Ple*^{Dalb} mice labelled with phalloidin to visualize F-actin. Nuclei were stained with DAPI. The arrowheads, misshaped canaliculi. Scale bar, 1 µm. The histogram shows the canalicular width distribution. n = 68–80, three independent experiments. *p <0.05, **p <0.01, ***p <0.001 calculated using Student's t test. BDs, bile ducts; K19, keratin 19; PF, portal field; *Ple*^{Dalb}, liver-specific *Plec* knockout; *Ple*$^{fl/fl}$, *Plec*$^{flox/flox}$; PV, portal vein; ZO-1, zonula occludens-1.

sandwich cultures of *Ple*$^{fl/fl}$ and *Ple*^{Dalb} primary hepatocytes[18] revealed highly irregular and significantly wider *Ple*^{Dalb} canaliculi with grossly dilated segments (Fig. 4E), which closely resembled abnormalities seen in a canalicular *Ple*^{Dalb} network *in vivo*.

Plectin deficiency aggravates BDL-induced liver injury

To assess whether the prominent upregulation of plectin expression upon cholestatic challenge (Fig. 1D) was indicative of its protective role during injury, we subjected *Ple*$^{fl/fl}$ and *Ple*^{Dalb} mice to BDL for 5 and 14 days. We observed similar levels of alanine aminotransferase (ALT), aspartate aminotransferase, alkaline phosphatase (ALP), and total serum bile acid (tBA), but higher total bilirubin levels in *Ple*^{Dalb} compared to *Ple*$^{fl/fl}$ mice (Fig. 5A, B, S9A). A histological analysis of liver sections after 14 days of BDL showed significantly increased numbers of bile infarcts and larger areas of necrotic tissue in *Ple*^{Dalb} compared to *Ple*$^{fl/fl}$ livers (Fig. 5C). *Ple*^{Dalb} livers also showed more extensive fibrosis, as revealed by a morphometric analysis of Sirius red-stained liver sections and immunoblot analyses for collagen I and α-smooth muscle actin (Fig. 5D, S9B). Ductular reaction, assessed by a histological evaluation of K19⁺ areas on liver sections and an immunoblot analysis of liver lysates, was similar in *Ple*$^{fl/fl}$ and *Ple*^{Dalb} mice after both 5 and 14 days of BDL (Fig. S9C). Nonetheless, Ki-67 staining revealed significantly higher BEC proliferation in *Ple*^{Dalb} mice after 14 days of injury (Fig. 5E). Coincidently, A6 antigen staining showed approximately twofold increase in the progenitor cell area in *Ple*^{Dalb} mice after both 5 and 14 days of BDL (Fig. 5F). Together these data show higher susceptibility of *Ple*^{Dalb} mice to BDL-induced injury accompanied by more severe portal fibrosis with considerable BEC and oval cell proliferation.

Plectin is required in recovery from DDC-induced injury

As BDL-induced cholestasis affects primarily large BD epithelial cells,[23] next we studied the role of plectin in a second model of cholestasis that affects primarily small BDs.[24] In line with the

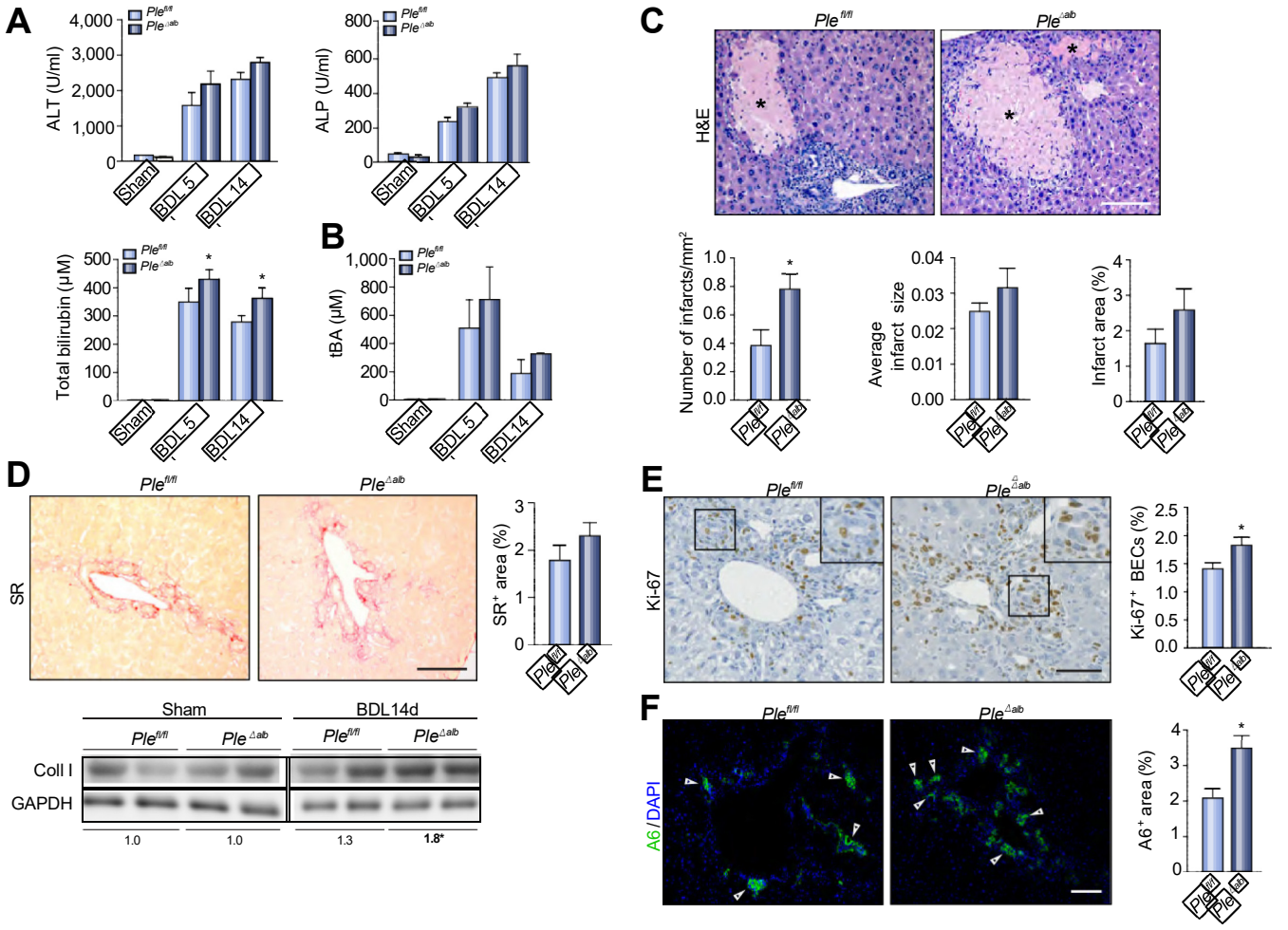

Fig. 5. Plectin liver-specific deficiency aggravates the BDL-induced injury. (A, B) Serum levels of ALT, ALP, total bilirubin (A) and total serum bile acid (tBA, B) determined from sham-operated controls (sham) and BDL mice 5 and 14 days after surgery. n = 6–7. (C) Representative images of H&E stained liver sections and corresponding morphometric analysis of bile infarcts (the asterisks) in livers from *Ple*$^{fl/fl}$ and *Ple*^{Dalb} mice subjected to BDL for 14 days. n = 6. (D) Representative images of SR stained liver sections from BDL-treated mice. Scale bar, 200 1m. The bar graph shows the percentage of the SR^{+} area per liver section. n = 8. Immunoblots of liver lysates from BDL-challenged or sham-operated mice probed with antibodies to collagen I. GAPDH, loading control. The numbers below lines indicate relative band intensities normalized to average control values. n = 3–4. (E) Representative images of liver sections from BDL-challenged mice immunolabelled for Ki-67. Scale bar, 150 1m. Boxed areas show ~x2 images. The bar graph shows the percentage of Ki-67^{+} BECs. n = 3–4. (F) Immunolabelling of A6^{+} progenitor cells with nuclei stained with DAPI. The arrowheads, A6^{+} cells. Scale bar, 200 1m. The bar graph shows the percentage of the A6^{+} area per liver section. n = 3; *p <0.05 calculated using Student's t test. ALT, alanine aminotransferase; ALP, alkaline phosphatase; BDL, bile duct ligation; BECs, biliary epithelial cells; Col I, collagen I; GAPDH, glyceraldehyde 3-phosphate dehydrogenase; H&E, hematoxylin and eosin; *Ple*^{Dalb}, liver-specific *Plec* knockout; *Ple*$^{fl/fl}$, *Plec*$^{flox/flox}$; SR, Sirius red; tBA, total bile acids.

results from the BDL model, 14 days of DDC-feeding resulted in slightly higher ALP and bilirubin levels in *Ple*^{Dalb} compared to the levels in *Ple*$^{fl/fl}$ mice, pointing to more extensive biliary epithelial damage. On the other hand, a significantly attenuated elevation of ALT and tBA levels in *Ple*^{Dalb} mice suggested unexpectedly lower hepatocellular injury (Fig. 6A, B). This coincided with less extensive fibrosis in *Ple*^{Dalb} mice assessed from Sirius red-stained liver sections (Fig. 6C). The extent of the ductular reaction and the proliferative response to DDC-induced injury was comparable in both genotypes, as no differences were found in K19^{+} area, K19 expression levels, and Ki-67 staining (Fig. S10A–C). In sharp contrast, we observed a more than threefold increase in the A6^{+} progenitor cell area in *Ple*^{Dalb} mice (Fig. 6D). These findings indicate that in this model the genetic loss of plectin increases the susceptibility of BECs to DDC intoxication and leads to a substantially elevated activation of oval cells, but has a protective effect on hepatic parenchyma.

To study whether plectin deficiency affects the ability of the liver to regenerate after cholestatic injury, mice fed for 14 days with DDC were allowed three days of standard chow to recover. After the recovery period, ALT, ALP, and bilirubin levels decreased in both *Ple*$^{fl/fl}$ and *Ple*^{Dalb} mice; however, the recovery levels were significantly higher in *Ple*^{Dalb} than in *Ple*$^{fl/fl}$ mice (Fig. 6A). Moreover, while serum tBA levels in *Ple*$^{fl/fl}$ mice were five-times lower after recovery, in *Ple*^{Dalb} mice they stayed as high as during the injury period (Fig. 6B). Consistently, we also observed persisting fibrosis in these animals (Fig. 6C). Similar to the injury period, both *Ple*$^{fl/fl}$ and *Ple*^{Dalb} mice showed a comparable ductular reaction and a proliferative response (Fig. S10A–C) with no significant differences in the number of A6^{+} cells (Fig. 6D). Collectively, these results show that although DDC exposure leads to lower hepatocellular damage in *Ple*^{Dalb} mice, its resolution is slower, strongly suggesting that plectin provides the liver with the capability to recover from DDC-induced injury more efficiently.

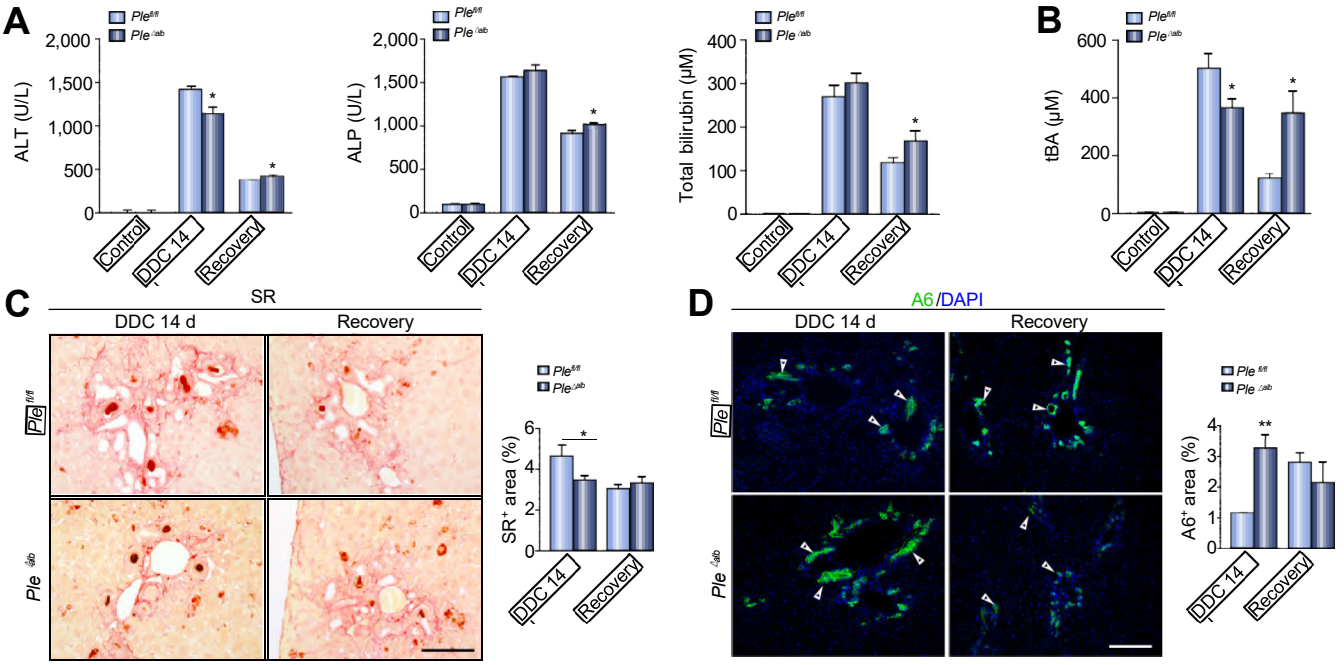

Fig. 6. *Ple*^{Dalb} mice show impaired recovery from DDC-induced injury. (A, B) Serum levels of ALT, ALP, total bilirubin (A) and total bile acids (tBA; B) determined in samples from untreated controls and mice fed with the DDC diet for 14 days (DDC 14 d) or allowed to recover from the injury for three days (recovery). n = 3–7. (C) Representative images of SR stained liver sections from DDC-treated and recovering mice. Scale bar, 250 1m. The bar graph shows the percentage of the SR$^+$ area per liver section. n = 6. (D) Immunolabelling of A6 in BECs with nuclei stained with DAPI. The arrowheads, A6$^+$ cells. Scale bar, 200 1m. The bar graph shows the percentage of the A6$^+$ area per liver section. n = 3–4; *p <0.05, **p <0.01 calculated using Student's t test. ALP, alkaline phosphatase; ALT, alanine aminotransferase; AST, aspartate transaminase; BECs, biliary epithelial cells; DDC, 3,5-diethoxycarbonyl-1,4-dihydrocollidine; *Ple*^{Dalb}, liver-specific *Plec* knockout; *Ple*$^{fl/fl}$, *Plec*$^{flox/flox}$; SR, Sirius red; tBA, total bile acids.

Plectin preserves BD integrity under BDL-induced cholestatic stress

Aberrant KF cytoarchitecture of *Ple*^{Dalb} BECs associated with collapse of ductular structures and a worse outcome of BDL injury led us to assess the BD appearance in livers upon BDL challenge. A morphometric analysis of liver sections immunolabelled for pan-K and E-Cadherin revealed that intralobular BDs of *Ple*$^{fl/fl}$ mice after 14 days of BDL were mostly round with their lumens formed by tightly packed BECs with the nuclear long axis perpendicular to the ductal wall (Fig. 7A, S11A). In contrast, *Ple*^{Dalb} BDs showed significantly larger luminal areas (Fig. 7A) surrounded by loosely packed BECs that were often misaligned and had lost their polarized orientation (Fig. 7A, S11B). More dilated and round stress-loaded BDs in *Ple*^{Dalb} BDL-injured livers were in stark contrast to untreated BDs, where plectin deficiency led to luminal collapse (Fig. 4A). Together, these observations likely reflected reduced stability of *Ple*^{Dalb} ducts resulting in a prominent dilatation upon BDL-induced bile pressure. Moreover, *Ple*^{Dalb} BDs displayed more ruptures (Fig. 7A) corresponding to aggravated BDL-induced liver injury (Fig. 5). This further confirmed the fragility of plectin-deficient biliary epithelium. We did not observe any comparable changes in the cross-sectional luminal area and in BD morphology in DDC-treated animals (Fig. S11B).

As the cohesion of BECs is maintained by junctional complexes, we compared morphology of TJs, AJs, and Ds formed by unchallenged *Ple*$^{fl/fl}$ and *Ple*^{Dalb} BECs using transmission electron microscopy (TEM). Quantitative analyses showed a significantly reduced length of TJs in *Ple*^{Dalb} liver, but no apparent differences in the appearance of AJs and Ds (Fig. 7B). A further analysis revealed that the expression levels of the desmosomal proteins desmoglein and desmoplakin as well as their localizations were comparable between unchallenged *Ple*$^{fl/fl}$ and *Ple*^{Dalb} livers (Fig. 7E, F and not shown). However, *Ple*^{Dalb} liver lysates showed an ~50% increase in E-Cadherin protein levels (Fig. 7D), which was not accompanied by any obvious changes in AJ morphology (Fig. S12A). Although these results suggest a distortion of biliary cell-cell junctions and a possible impairment of the biliary barrier, we observed no penetration of fluorescein isothiocyanate-dextran (4 and 40 kDa) from blood to bile (Fig. S12B, C). Given our findings in BDL-treated *Ple*^{Dalb} mice, we further quantified the expression levels of junctional proteins by immunoblotting (Fig. 7C–F). In line with previous findings,[2] BDL caused a general upregulation of these proteins. No significant differences were observed for ZO-1, E-Cadherin and desmoglein expressions between *Ple*^{Dalb} and *Ple*$^{fl/fl}$ mice (Fig. 7C–E). In contrast, BDL induced an upregulation of desmoplakin to a significantly lesser extent in *Ple*^{Dalb} than in *Ple*$^{fl/fl}$ mice (Fig. 7F). These results clearly show that plectin deficiency leads to a considerable distortion of biliary cell-cell contacts and compromises the ability of BDs to cope with BDL insult.

Plectin stabilizes KFs under stress and affects the p38 MAP kinase signaling pathway in liver epithelial cells

Previous studies have linked the resilience to cholestatic injury with KF network stability.[3,25] Given the changes in KF organization in *Ple*^{Dalb} livers, we assessed their reorganization in response to stress conditions in liver epithelial cells. Immunofluorescence microscopy for K8 on liver sections after 5 and 14 days of BDL, revealed, as previously reported,[3,25] an increase in the density of the KF network (not shown). Additionally, we found single hepatocytes containing K8$^+$ aggregates,

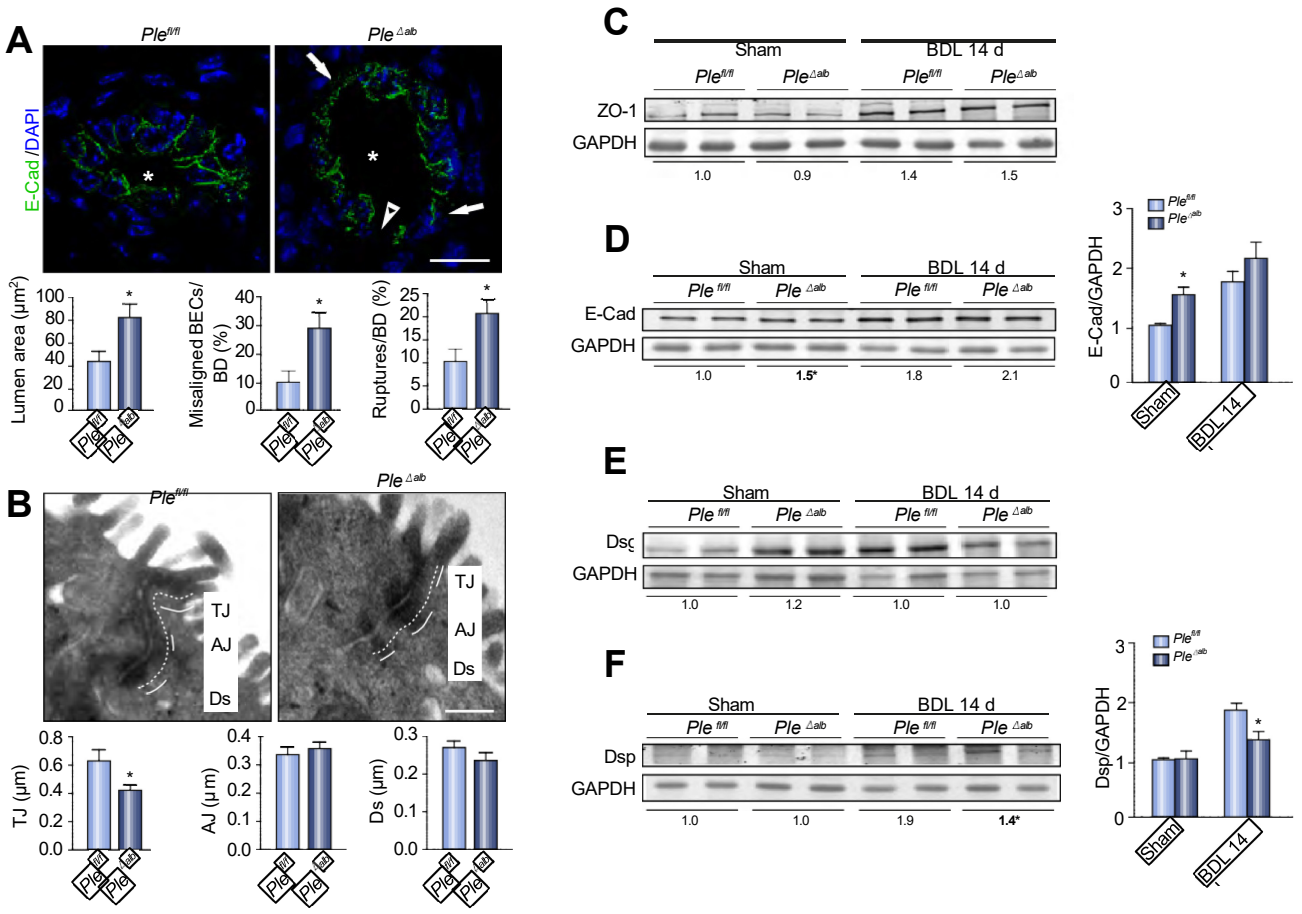

Fig. 7. Plectin stabilizes BD integrity in cholestasis. (A) Representative immunofluorescence images of ductular structures immunolabelled with antibodies to E-Cad (green). Nuclei were stained with DAPI (blue). The arrows, BEC with misaligned nucleus; the arrowhead, BD rupture; the asterisks, biliary lumen. Scale bar, 10 1m. The bar graphs show statistical evaluation of morphometric analysis of ductular structures. The cross-sectional luminal area, the number of misaligned cells (cells losing their polarized orientation with the nuclear long axis perpendicular to the ductal wall) and the number of ruptures were determined for >10 ductular structures in two mice per genotype. (B) Representative TEM micrographs of ductular junctional complexes. Drawn bars (white) indicate TJ, AJ and Ds. Scale bar, 1.5 1m. Bar graphs show a statistical evaluation of junctional complex length measurement from 2-3 BDs from two mice per genotype. (C-F) Immunoblots of liver lysates prepared from BDL-challenged mice or sham-operated controls using antibodies to (C) ZO-1, (D) E-Cad, (E) Dsg, and (F) Dsp. GAPDH, loading control. The numbers below lines and the bar graphs show relative band intensities normalized to average sham *Ple*$^{fl/fl}$ values. n = 3–4; *p <0.05 calculated using Student's t test. AJ, adherens junctions; BD, bile ducts; BDL, BD ligation; BECs, biliary epithelial cells; Ds, desmosomes; Dsg, desmoglein; Dsp, desmoplakin; E-Cad, E-Cadherin; GAPDH, glyceraldehyde 3-phosphate dehydrogenase; *Ple*^{Dalb}, liver-specific *Plec* knockout; *Ple*$^{fl/fl}$, *Plec*$^{flox/flox}$; TJ, tight junctions; ZO-1, zonula occludens-1.

which were 1.5-times more abundant in *Ple*^{Dalb} than in *Ple*$^{fl/fl}$ livers (Fig. 8A). To confirm the role of plectin in a stress-induced KF reorganization *in vitro*, we treated primary hepatocytes and the mouse cholangiocyte cell line (MSC[19]) with the phosphatase inhibitor okadaic acid (OA). Untreated *Ple*^{Dalb} hepatocytes and plectin-deficient MSCs (KO MSCs; see Materials and Methods) showed less delicate keratin IF networks when compared to their wild-type (WT) counterparts (Fig. 8B). After exposure to OA, KFs in KO cells formed thicker bundles and their collapse was evident from either cytoplasmic areas devoid of keratin staining (hepatocytes) or the formation of keratin granules (MSCs) (Fig. 8B). Consistent with a higher frequency of K8^{+} aggregates observed in BDL-treated *Ple*^{Dalb} livers, KF networks were found significantly more often collapsed in OA-treated plectin-deficient than in wild-type cells (Fig. 8B). Together, these data suggest that plectin stabilizes KFs under stress conditions both *in vitro* and *in vivo*.

The reorganization of KFs is known to be mediated via MAP kinase p38,[26] a stress-response kinase also implicated in the cholestatic liver disease.[27] As our previous data suggested a plectin-dependent regulation of the p38 signaling pathway,[11] we examined whether the changes in KF appearance upon BDL or OA treatment were paralleled by p38 activation. Using anti-phospho-p38 antibodies, we found significantly lower p38 activities in *Ple*^{Dalb} compared to *Ple*$^{fl/fl}$ liver lysates from sham-operated mice (Fig. 8C). Surprisingly, this downregulation was not confirmed *in vitro*; the basal phosphorylation of p38 kinase did not differ between plectin-deficient and wild-type hepatocytes or MSCs (Fig. 8D, E). As expected, BDL resulted in p38 activation, which was substantially elevated in *Ple*^{Dalb} livers despite its comparatively low levels under basal conditions (Fig. 8C). Consistent with these results, p38 phosphorylation was found to be higher both in OA-treated plectin-deficient hepatocytes and in MSCs compared to their wild-type counterparts (Fig. 8D, E). Hence, the enhanced stress-induced activation of p38 kinase correlated well with the increased fragility of the IF networks observed in plectin-deficient liver epithelial cells.

Discussion

In this study, we show that plectin plays an essential role in the proper organization of KF networks in both hepatocytes as well

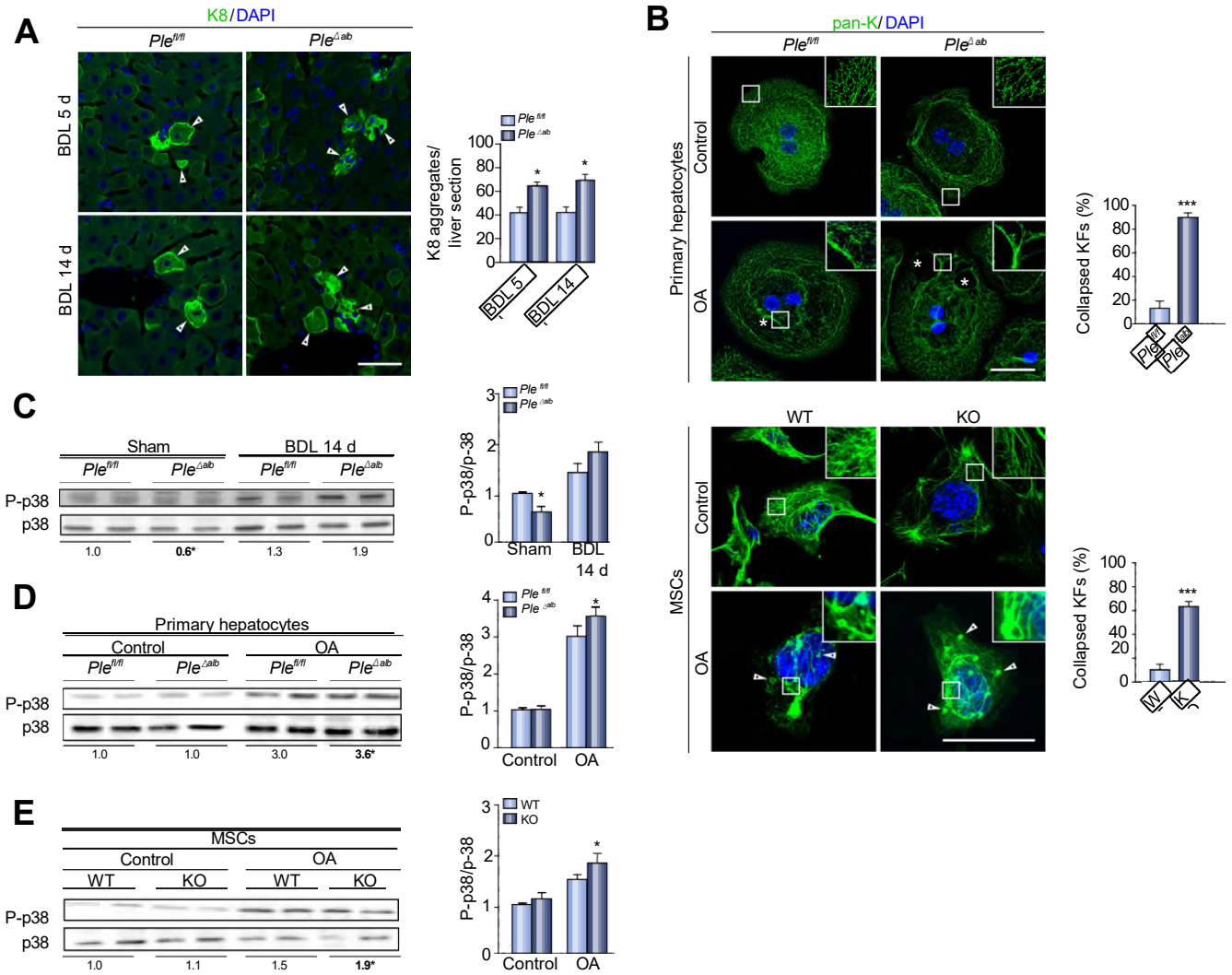

Fig. 8. Plectin deficiency leads to increased KF network collapse and aberrant stress signaling in liver epithelial cells. (A) Liver sections from *Ple*$^{fl/fl}$ and *Ple*^{Dalb} mice challenged with BDL for 5 and 14 days were immunolabelled using antibodies to K8. Nuclei were stained with DAPI. The arrowheads, K8 aggregates. Scale bar, 25 1m. The bar graph shows the number of hepatocytes with K8 aggregates per liver section. n = 3. (B) Primary hepatocytes and immortalized MSCs were untreated (control), or incubated with OA and immunolabelled for pan-keratin (pan-K). Nuclei were stained with DAPI. The asterisks, areas devoid of keratin staining; the arrowheads, keratin granules. Scale bars, 10 1m. Boxed areas show ~x3 images. The bar graphs show the percentage of cells with collapsed KFs. n = 600, three independent experiments. (C-E) Immunoblots of lysates prepared from mouse liver (C), primary hepatocytes (D) and MSCs (E) shown in A and B using anti-p38, and anti-phospho-p38 (P-p38) antibodies. The numbers below lines and the bar graphs indicate relative band intensities normalized to average control values. n = 3–4; **p* <0.05, ****p* <0.001 calculated using Student's *t* test. BDL, bile duct ligation; K8, keratin 8; KF, keratin filaments; KO, knockout; MSCs, mouse cholangiocytes; OA, okadaic acid; P-p38, phospho-p38; pan-K, pan-keratin; *Ple*^{Dalb}, liver-specific *Plec* knockout; *Ple*$^{fl/fl}$, *Plec*$^{flox/flox}$; WT, wild-type.

as in BECs. In the absence of plectin, hepatocytic keratins K8 and K18 no longer showed their typical distribution along the plasma membrane, but loose individual filaments were found scattered throughout the whole cytoplasmic space. In BECs, where plectin deficiency showed a less dramatic effect, an apicobasal redistribution of the keratin network was observed. Besides these changes in the KF organization, plectin deficiency also led to the dysregulation of cell-cell contacts in biliary epithelium. Plectin-deficient BECs formed shorter TJs, and higher expression levels of the AJ marker protein E-Cadherin were found in *Ple*^{Dalb} livers. Despite a partial loss of cytoarchitecture polarity and aberrant cell-cell junctions in BECs, *Ple*^{Dalb} mice showed no defects in bile formation or composition. In line with similar findings in mice lacking K8/K18[28] or K19,[9] these results suggest that under physiological conditions localization of membrane transporter and receptor proteins is unaffected and biliary epithelium is intact in *Ple*^{Dalb} mice.

Our extensive scanning electron microscopy analysis revealed a denser network of distorted, wider and more meandering bile canaliculi formed by adjacent plectin-deficient compared to wild-type hepatocytes in *Ple*$^{fl/fl}$ livers. As no similar observations have been reported in mice deficient for individual keratins,[9,28] it is unlikely that bile canalicular abnormalities seen in *Ple*^{Dalb} mice and 3D cultures of primary plectin-deficient hepatocytes can be attributed to an altered KF networks *per se*. However, prior studies have shown that plectin-controlled IF cytoarchitecture is required for actomyosin-generated cytoskeletal tension.[13,29] It is noteworthy that two key tension transducers/sensors, a-catenin[30] and b-catenin,[31] have been independently implicated in a bile

canalicular formation *in vivo*. Furthermore, Li *et al.*[32] have shown that mechanical intercellular tension guides canalicular elongation and accounts for different luminal morphologies. Hence, we propose that an aberrant bile canalicular formation in *Ple*^{Dalb} mice may reflect modified mechanical properties of plectin-deficient hepatocytes as a consequence of reduced cellular mechanical tension. Experiments to test this hypothesis, both *in vivo* and *in vitro*, are currently ongoing.

We found that plectin deficiency leads to the destabilization of BDs and their collapse. In line with the generally accepted view that plectin provides tissues (*e.g.* skin, muscle) with mechanical stability,[10,15,33] BD dysmorphology is thus likely a consequence of the shear stress exerted on less stable (plectin-deficient) BECs. Interestingly, this dysmorphology of the plectin-deficient biliary tree is paralleled by a mild ductular reaction. Although this could be due to a local bile stasis in irregularly shaped canaliculi or ductules, we have not found any significant upregulations in ALP or bilirubin levels that would indicate cholestatic conditions in *Ple*^{Dalb} mice under basal conditions.

Experimental models of cholestasis caused aggravated liver injury in *Ple*^{Dalb} mice. After BDL, mechanically unstable plectin-deficient BDs significantly dilated in response to increased bile pressure, which ultimately led to more frequent BD ruptures and an increased number of bile infarcts corresponding to more severe liver injury. Similarly to BDL, the extent of biliary damage in the DDC model was higher in *Ple*^{Dalb} than *Ple*$^{fl/fl}$ mice; however, parenchyma damage was only modest in *Ple*^{Dalb} mice. This likely reflects the fact that DDC affects primarily small ducts,[24] which are less prone to hepatobiliary injury.[34] Furthermore, reduced liver injury in *Ple*^{Dalb} mice is consistent with the observation that DDC induced upregulation of plectin expression to a much lesser extent than BDL. This suggests that plectin is not required for the reorganization of KF cytoarchitecture[25] under DDC-induced cholestasis. However, slower recovery from DDC-induced liver injury indicates that plectin has the capacity to repair periportal damage associated with DDC exposure.

Interestingly, *Ple*^{Dalb} mice had also higher serum levels of liver injury markers in cholic acid (CA)-induced cholestasis model[35] (not shown). Although plectin-deficient hepatocytes show unaltered transporter systems under physiological conditions, observation from the CA-based experiment implies that they might have limited capacity to overcome bile acid overload. To elucidate underlying plectin-related mechanisms and to find their contribution to the BDL- and DDC-induced phenotypes is a goal for our ongoing studies.

Although both BDL and DDC cholestatic models yielded aggravated liver injury in *Ple*^{Dalb} mice, the extent of the injury was surprisingly mild, given the reduced mechanical stability of plectin-deficient BDs. This unexpected observation could be attributed to a ductular reaction occurring in response to plectin ablation under basal conditions. A resulting denser meshwork with an increased number of ductules could more effectively drain bile under experimental cholestasis, thus constituting a "pre-adaptation" of the *Ple*^{Dalb} bile tree, which partially mitigates cholestatic insult.

We observed a significant expansion of A6^{+} progenitor cells in *Ple*^{Dalb} livers in both models of cholestasis. Surprisingly, this was not accompanied by a corresponding increase in K19^{+} cells, likely indicating a lack of oval cell differentiation in these models. As K19 KO mice on a DDC diet display an attenuated ductular reaction and hampered oval cell proliferation,[9] the role of plectin in oval cell induction and expansion appears to be KF-independent. Further studies are required to find out i) whether plectin directly regulates progenitor proliferation and differentiation, ii) whether the overactivation of oval cells attenuates liver damage, and iii) what is the impact of plectin deficiency in long-term DDC-induced liver injury.

Strong upregulation of plectin in models of cholestatic challenge and increased liver damage of *Ple*^{Dalb} mice suggest that the role of plectin is hepatoprotective. Interestingly, an upregulation in response to cholestatic challenge has been described for keratins (K8/K18,[36]K19,[9]K23[4]) and other plakins such as epiplakin[25] and periplakin,[2] *i.e.* proteins that are required for the maintenance of mechanical stability of cells and tissues. Besides proteins directly linked to cytoarchitecture and cell mechanics, liver epithelial cells also conjointly upregulate constituents of cell-cell junctions,[2,37] structures that are essential for intercellular cohesion. This implies an intriguing possibility that overexpression of these proteins constitutes a complex adaptive response to cholestasis, which provides biliary epithelium with resilience against increased bile pressure. Here we show that apart from perturbing the KF organization of hepatocytes and BECs, plectin deficiency leads to distortion of TJs, accompanied by the upregulation of the AJ protein E-Cadherin. Moreover, *Ple*^{Dalb} mice fail to induce upregulation of desmoplakin, a proposed direct binding partner of plectin,[38] which mediates the anchorage of keratin IFs to desmosomes. Although these changes do not directly hamper the biliary barrier of *Ple*^{Dalb} mice, they provide strong evidence that plectin maintains the stability of biliary epithelium and facilitates adaptive reorganization of cytoarchitecture and cell-cell cohesion.

Prior studies have demonstrated that KF networks exert non-mechanical functions, providing epithelial cells with protection against deformation-unrelated stress. Previously, we have shown that plectin-deficient keratinocytes increase the p38 MAP kinase activity in response to OA-induced stress, and we proposed a feedback loop between plectin-organized KFs and p38 activation leading to overactivation of p38 under stress condition.[11] In addition, plectin scaffolds and regulates the activity of AMPK,[14] a key sensor of metabolic stress which stabilizes tight junctions, preserves cell polarity, and thereby maintains epithelial barrier functions.[39] Showing higher stress-induced upregulation of p38 activity in both plectin-deficient liver (cholestasis) and primary hepatocytes (OA treatment), our results clearly indicate the role of plectin in the p38-mediated stress response in liver epithelia. Plectin's control of cytoskeletal integrity and its interplay with signaling pathways thus emerges as a critical determinant of the biliary barrier. Further studies are needed to delineate precise underlying mechanisms and their roles in the development and progression of human liver diseases.

Financial support

This work was supported by the Grant Agency of the Czech Republic (GA15-23858S); Institutional Research Project of the Czech Academy of Sciences (RVO 68378050); COST Action CA15214-EuroCellNet, Strategy AV21 – QUALITAS; the Grant Agency of Charles University (896916); MEYS CR projects (LQ1604 NPU II, LO1509 NPU, LM2015062, LO1419, LM2015040, OP RDI CZ.1.05/2.1.00/19.0395 and OP RDE CZ.02.1.01/0.0/0.0/16_013/0001775); Operational Program

Prague–Competitiveness projects (CZ.2.16/3.1.00/24023 and CZ.2.16/3.1.00/21547); and the Austrian Science Research Fund (FWF grant I1413-1309).

Conflict of interest

The authors declare no conflicts of interest that pertain to this work.

Please refer to the accompanying ICMJE disclosure forms for further details.

Authors' contributions

Study concept and design: M.G., M.J. Acquisition of data: K.N., M.J., G.O.-E., H.H., L.S., K.C., O.B, P.M., O.F. Analysis and interpretation of data: M.J., M.G., K.N., K.C., P.M., O.F. Drafting of the manuscript: M.G., M.J., K.N., A.K. Critical revision of the manuscript for important intellectual content: all authors. Obtained funding: M.G., R.S., G.W. Technical or material support: B.S., M.K., G.W., R.S.

Acknowledgement

We would like to thank Y. Ueno (Tohoku University, Japan) and H. Francis (Texas A&M HSC/COM, Digestive Disease Research Center, Temple, USA) for generously providing the MSC cell line, and V. M. Factor (National Cancer Institute, Bethesda, MD, USA) for A6 antibodies. H. Denk (Institute of Pathology, Medical University of Graz, Graz, Austria), M. Jirsa, E. Honsova, E. Sticova (all Institute for Clinical and Experimental Medicine, Prague, Czech Republic) and M. Efenberkova (Institute of Molecular Genetics of the Czech Academy of Sciences, Prague, Czech Republic) for their expertise and H. Denk and M. Jirsa for their critical reading of the manuscript.

Supplementary data

Supplementary data associated with this article can be found, in the online version, at https://doi.org/10.1016/j.jhep.2017.12.011.

References

Author names in bold designate shared co-first authorship

[1] Lazaridis KN, Strazzabosco M, Larusso NF. The cholangiopathies: disorders of biliary epithelia. Gastroenterology 2004;127:1565–1577.
[2] Ito S, Satoh J, Matsubara T, Shah YM, Ahn SH, Anderson CR, et al. Cholestasis induces reversible accumulation of periplakin in mouse liver. BMC Gastroenterol 2013;13:116.
[3] Fickert P, Trauner M, Fuchsbichler A, Stumptner C, Zatloukal K, Denk H. Cytokeratins as targets for bile acid-induced toxicity. Am J Pathol 2002;160:491–499.
[4] Guldiken N, Kobazi Ensari G, Lahiri P, Couchy G, Preisinger C, Liedtke C, et al. Keratin 23 is a stress-inducible marker of mouse and human ductular reaction in liver disease. J Hepatol 2016;65:552–559.
[5] Omary MB, Ku NO, Toivola DM. Keratins: guardians of the liver. Hepatology 2002;35:251–257.
[6] Ku NO, Strnad P, Bantel H, Omary MB. Keratins: Biomarkers and modulators of apoptotic and necrotic cell death in the liver. Hepatology 2016;64:966–976.
[7] Zhong B, Strnad P, Selmi C, Invernizzi P, Tao GZ, Caleffi A, et al. Keratin variants are overrepresented in primary biliary cirrhosis and associate with disease severity. Hepatology 2009;50:546–554.
[8] Omary MB, Ku NO, Strnad P, Hanada S. Toward unraveling the complexity of simple epithelial keratins in human disease. J Clin Invest 2009;119:1794–1805.
[9] Chen Y, Guldiken N, Spurny M, Mohammed HH, Haybaeck J, Pollheimer MJ, et al. Loss of keratin 19 favours the development of cholestatic liver disease through decreased ductular reaction. J Pathol 2015;237:343–354.
[10] Castanon MJ, Walko G, Winter L, Wiche G. Plectin-intermediate filament partnership in skin, skeletal muscle, and peripheral nerve. Histochem Cell Biol 2013;140:33–53.
[11] Osmanagic-Myers S, Gregor M, Walko G, Burgstaller G, Reipert S, Wiche G. Plectin-controlled keratin cytoarchitecture affects MAP kinases involved in cellular stress response and migration. J Cell Biol 2006;174:557–568.
[12] Moch M, Windoffer R, Schwarz N, Pohl R, Omenzetter A, Schnakenberg U, et al. Effects of plectin depletion on keratin network dynamics and organization. PLoS One 2016;11:e0149106.
[13] Osmanagic-Myers S, Rus S, Wolfram M, Brunner D, Goldmann WH, Bonakdar N, et al. Plectin reinforces vascular integrity by mediating crosstalk between the vimentin and the actin networks. J Cell Sci 2015;128:4138–4150.
[14] Gregor M, Zeöld A, Oehler S, Marobela KA, Fuchs P, Weigel G, et al. Plectin scaffolds recruit energy-controlling AMP-activated protein kinase (AMPK) in differentiated myofibres. J Cell Sci 2006;119:1864–1875.
[15] Walko G, Vukasinovic N, Gross K, Fischer I, Sibitz S, Fuchs P, et al. Targeted proteolysis of plectin isoform 1a accounts for hemidesmosome dysfunction in mice mimicking the dominant skin blistering disease EBS-Ogna. PLoS Genet 2011;7:e1002396.
[16] Ackerl R, Walko G, Fuchs P, Fischer I, Schmuth M, Wiche G. Conditional targeting of plectin in prenatal and adult mouse stratified epithelia causes keratinocyte fragility and lesional epidermal barrier defects. J Cell Sci 2007;120:2435–2443.
[17] Jirouskova M, Zbodakova O, Gregor M, Chalupsky K, Sarnova L, Hajduch M, et al. Hepatoprotective effect of MMP-19 deficiency in a mouse model of chronic liver fibrosis. PLoS One 2012;7:e46271.
[18] Swift B, Pfeifer ND, Brouwer KL. Sandwich-cultured hepatocytes: an in vitro model to evaluate hepatobiliary transporter-based drug interactions and hepatotoxicity. Drug Metab Rev 2010;42:446–471.
[19] Mano Y, Ishii M, Kisara N, Kobayashi Y, Ueno Y, Kobayashi K, et al. Duct formation by immortalized mouse cholangiocytes: an in vitro model for cholangiopathies. Lab Invest 1998;78:1467–1468.
[20] Cong L, Ran FA, Cox D, Lin S, Barretto R, Habib N, et al. Multiplex genome engineering using CRISPR/Cas systems. Science 2013;339:819–823.
[21] Wiche G, Krepler R, Artlieb U, Pytela R, Denk H. Occurrence and immunolocalization of plectin in tissues. J Cell Biol 1983;97:887–901.
[22] Stumptner C, Fuchsbichler A, Lehner M, Zatloukal K, Denk H. Sequence of events in the assembly of Mallory body components in mouse liver: clues to the pathogenesis and significance of Mallory body formation. J Hepatol 2001;34:665–675.
[23] Alpini G, Glaser SS, Ueno Y, Pham L, Podila PV, Caligiuri A, et al. Heterogeneity of the proliferative capacity of rat cholangiocytes after bile duct ligation. Am J Physiol 1998;274:G767–775.
[24] Fickert P, Stoger U, Fuchsbichler A, Moustafa T, Marschall HU, Weiglein AH, et al. A new xenobiotic-induced mouse model of sclerosing cholangitis and biliary fibrosis. Am J Pathol 2007;171:525–536.
[25] Szabo S, Wogenstein KL, Osterreicher CH, Guldiken N, Chen Y, Doler C, et al. Epiplakin attenuates experimental mouse liver injury by chaperoning keratin reorganization. J Hepatol 2015;62:1357–1366.
[26] Woll S, Windoffer R, Leube RE. P38 MAPK-dependent shaping of the keratin cytoskeleton in cultured cells. J Cell Biol 2007;177:795–807.
[27] Tormos AM, Arduini A, Talens-Visconti R, del Barco Barrantes I, Nebreda AR, Sastre J. Liver-specific p38alpha deficiency causes reduced cell growth and cytokinesis failure during chronic biliary cirrhosis in mice. Hepatology 2013;57:1950–1961.
[28] Fickert P, Fuchsbichler A, Wagner M, Silbert D, Zatloukal K, Denk H, et al. The role of the hepatocyte cytokeratin network in bile formation and resistance to bile acid challenge and cholestasis in mice. Hepatology 2009;50:893–899.
[29] Gregor M, Osmanagic-Myers S, Burgstaller G, Wolfram M, Fischer I, Walko G, et al. Mechanosensing through focal adhesion-anchored intermediate filaments. FASEB J 2014;28:715–729.
[30] Herr KJ, Tsang YH, Ong JW, Li Q, Yap LL, Yu W, et al. Loss of alpha-catenin elicits a cholestatic response and impairs liver regeneration. Sci Rep 2014;4:6835.
[31] Yeh TH, Krauland L, Singh V, Zou B, Devaraj P, Stolz DB, et al. Liver-specific beta-catenin knockout mice have bile canalicular abnormalities, bile secretory defect, and intrahepatic cholestasis. Hepatology 2010;52:1410–1419.

[32] Li Q, Zhang Y, Pluchon P, Robens J, Herr K, Mercade M, et al. Extracellular matrix scaffolding guides lumen elongation by inducing anisotropic intercellular mechanical tension. Nat Cell Biol 2016;18:311–318.
[33] Konieczny P, Fuchs P, Reipert S, Kunz WS, Zeold A, Fischer I, et al. Myofiber integrity depends on desmin network targeting to Z-disks and costameres via distinct plectin isoforms. J Cell Biol 2008;181:667–681.
[34] Glaser SS, Gaudio E, Rao A, Pierce LM, Onori P, Franchitto A, et al. Morphological and functional heterogeneity of the mouse intrahepatic biliary epithelium. Lab Invest 2009;89:456–469.
[35] Fickert P, Zollner G, Fuchsbichler A, Stumptner C, Pojer C, Zenz R, et al. Effects of ursodeoxycholic and cholic acid feeding on hepatocellular transporter expression in mouse liver. Gastroenterology 2001;121:170–183.
[36] Fickert P, Zollner G, Fuchsbichler A, Stumptner C, Weiglein AH, Lammert F, et al. Ursodeoxycholic acid aggravates bile infarcts in bile duct-ligated and Mdr2 knockout mice via disruption of cholangioles. Gastroenterology 2002;123:1238–1251.
[37] Maly IP, Landmann L. Bile duct ligation in the rat causes upregulation of ZO-2 and decreased colocalization of claudins with ZO-1 and occludin. Histochem Cell Biol 2008;129:289–299.
[38] Eger A, Stockinger A, Wiche G, Foisner R. Polarisation-dependent association of plectin with desmoplakin and the lateral submembrane skeleton in MDCK cells. J Cell Sci 1997;110:1307–1316.
[39] Porat-Shliom N, Tietgens AJ, Van Itallie CM, Vitale-Cross L, Jarnik M, Harding OJ, et al. Liver kinase B1 regulates hepatocellular tight junction distribution and function in vivo. Hepatology 2016;64:1317–1329.

Video Article

Isolation and 3D Collagen Sandwich Culture of Primary Mouse Hepatocytes to Study the Role of Cytoskeleton in Bile Canalicular Formation In Vitro

Katerina Korelova[1], Marketa Jirouskova[1], Lenka Sarnova[1], Martin Gregor[1]

[1]Laboratory of Integrative Biology, Institute of Molecular Genetics of the Czech Academy of Sciences

Correspondence to: Martin Gregor at martin.gregor@img.cas.cz

URL: https://www.jove.com/video/60507
DOI: doi:10.3791/60507

Keywords: Biology, Issue 154, primary hepatocyte isolation, 3D collagen sandwich culture, bile canaliculus, cytoskeleton, immunolabelling, hepatocellular injury

Date Published: 12/20/2019

Citation: Korelova, K., Jirouskova, M., Sarnova, L., Gregor, M. Isolation and 3D Collagen Sandwich Culture of Primary Mouse Hepatocytes to Study the Role of Cytoskeleton in Bile Canalicular Formation In Vitro. *J. Vis. Exp.* (154), e60507, doi:10.3791/60507 (2019).

Abstract

Hepatocytes are the central cells of the liver responsible for its metabolic function. As such, they form a uniquely polarized epithelium, in which two or more hepatocytes contribute apical membranes to form a bile canalicular network through which bile is secreted. Hepatocyte polarization is essential for correct canalicular formation and depends on interactions between the hepatocyte cytoskeleton, cell-cell contacts, and the extracellular matrix. In vitro studies of hepatocyte cytoskeleton involvement in canaliculi formation and its response to pathological situations are handicapped by the lack of cell culture, which would closely resemble the canaliculi network structure in vivo. Described here is a protocol for the isolation of mouse hepatocytes from the adult mouse liver using a modified collagenase perfusion technique. Also described is the production of culture in a 3D collagen sandwich setting, which is used for immunolabeling of cytoskeletal components to study bile canalicular formation and its response to treatments in vitro. It is shown that hepatocyte 3D collagen sandwich cultures respond to treatments with toxins (ethanol) or actin cytoskeleton altering drugs (e.g., blebbistatin) and serve as a valuable tool for in vitro studies of bile canaliculi formation and function.

Video Link

The video component of this article can be found at https://www.jove.com/video/60507/

Introduction

Hepatocytes, the central cellular structures of the liver that are responsible for its metabolic functions, are uniquely polarized epithelial cells. Their polarization, appearing in mammals shortly after birth, results in formation of the biliary canalicular network and is essential for proper bile secretion. Apical membranes of hepatocytes collectively form bile canaliculi, whereas basal membranes remain in contact with the endothelium of sinusoids. The loss of hepatocyte polarization leads to redistribution of bile transporters and results in pathological processes connected with bile retention in the liver (i.e., cholestasis).

The establishment and maintenance of hepatocyte polarization and the development of bile canaliculi entail complex mechanisms. The underlying processes depend on collective interplay among the hepatocyte cytoskeleton, cell-cell contacts, and interactions with the extracellular matrix[1]. The hepatocyte cytoskeleton consists of all three filament networks, the actin cytoskeleton, microtubules, and intermediate filaments, which provide structural support for canalicular formation. The differential role of cytoskeletal components in the regeneration and maintenance of bile canalicular networks has been previously illustrated in vitro in 3D collagen-sandwich hepatocyte cultures[2].

Actin microfilaments and microtubules are important during the initial stages of hepatocyte membrane polarization at the sites of canaliculus generation[2]. The actin cytoskeleton establishes the structure and function of bile canaliculi, forming membrane-associated microfilaments and the circumferential ring, thus supporting the canalicular architecture and inserting the actin cytoskeleton into tight and adherens junctions[3]. The ring of keratin intermediate filaments outside the actin cytoskeleton further stabilizes the canalicular structure[3].

The importance of proteins in hepatocyte junctional complexes in the organization of bile canaliculi architecture has been well-documented in several knock-out mouse models, which show distorted canaliculi in mice lacking both tight and/or adherens junctional proteins[4,5,6]. The deletion of the adherens junction protein α-catenin has been shown to lead to disorganization of the hepatocyte actin cytoskeleton, dilatation of bile canalicular lumens, leaky tight junctions, and effectively to a cholestatic phenotype[4]. Moreover, in vitro studies have shown the importance of adherens junction components E-cadherin and β-catenin in remodeling of the hepatocellular apical lumen and protein trafficking[7].

Strikingly, ablation of the cytoskeleton crosslinking protein plectin, which is the major keratin organizer, has revealed phenotypes comparable to those linked to the actin cytoskeleton[8]. This suggests a critical role of keratin intermediate filaments in supporting of the canalicular structure. In vitro studies utilizing 3D hepatocyte collagen sandwiches have also shown the importance of the AMP-activated protein kinase and its upstream activator LKB1 in bile canalicular network formation[9]. These findings were then further confirmed by subsequent in vivo studies[10,11]. Thus, it has become clear that in vitro studies are necessary to further the understanding of signaling processes involved in the establishment of hepatocyte polarization, proper canalicular network formation, and bile secretion.

A major challenge in studying processes connected with bile canalicular formation and its response to pathological situations in vitro is using a cell culture conditions that closely resemble the situation in vivo[12]. Freshly isolated primary hepatocytes are not polarized; thus, they lose their function, morphology, and functional bile canaliculi in 2D culture conditions (e.g., changes in gene regulation, polarization, and de-differentiation[13,14,15]). Despite this fact, freshly isolated hepatocytes most closely reflect the nature of the liver in vivo, unlike liver-derived cell lines[16]. Even though they have been used in the past, immortalized cell lines do not exert the epithelial-like characteristic morphology of hepatocytes, and the bile canalicular lumens formed by these cells resemble liver canaliculi poorly[7]. Recently, 3D cultures of primary hepatocytes, from both mice and rats, have become a useful tool to investigate processes involved in bile canalicular network formation in vitro[9]. Primary hepatocytes cultured between two layers of collagen (referred to as a 3D collagen sandwich culture) can repolarize in several days. Because of high technical demands required when culturing mouse hepatocytes in 3D collagen sandwiches, here we present a complex protocol to isolate, to cultivate, and to immunolabel mouse hepatocytes embedded in 3D collagen sandwiches in order to characterize the involvement of cytoskeletal components during bile canalicular formation.

Protocol

All animal experiments were performed in accordance with European Directive 2010/63/EU and they were approved by the Czech Central Commission for Animal Welfare.

1. Materials

1. House animals under specific pathogen-free conditions according to the guidelines of the Federation for Laboratory Animal Science Associations with free access to regular chow and drinking water. House animals under a 12 h/12 h dark/light cycle. For hepatocyte isolation and culture, use 8–12 week-old animals.
2. Stock solutions A and B
    1. Prepare stock solution A and stock solution B according to **Table 1** and **Table 2**, respectively, in advance. Dissolve all components in 1 L of distilled H_2O (dH_2O).
    2. Adjust the pH of solutions to 7.2 and filter the solutions through a 0.2 µm filter. Both solutions can be stored at 4 °C for up to 6 months.
3. Stock solution C
    1. Prepare solution C on the day of primary hepatocyte isolation.
    2. Add all components according to **Table 3,** fill to a 50 mL total volume with dH_2O, and dissolve. Adjust the pH to 7.3.
    3. Aliquot 50 mL of the solution in 50 mL tubes. Use one tube per animal. Place all required aliquots in a pre-warmed water bath (37 °C).
4. Stock solution D
    1. Prepare solution D on the day of primary hepatocyte isolation.
    2. Add all components according to **Table 4**, fill to a 30 mL total volume with dH_2O, and dissolve. Adjust the pH to 7.3.
    3. Aliquot 30 mL of the solution in 50 mL tubes. Add collagenase I (5 mg/30 mL) into solution D. Use one aliquot per animal. Place all aliquots in a pre-warmed water bath (37 °C).
5. Stock solution E
    1. Prepare solution E on the day of primary hepatocyte isolation.
    2. Add all components according to **Table 5,** fill to a 50 mL total volume with dH_2O, and dissolve. Adjust the pH to 7.3.
    3. Aliquot 50 mL of the solution in 50 mL tubes. Add albumin V (0.65 g/50 mL) into solution E. Use one aliquot per animal. Place all aliquots in a pre-warmed water bath (37 °C).

2. Preparation of collagen sandwiches

1. One day before primary hepatocyte isolation, prepare the first layer of the collagen I sandwich.
   NOTE: Work on ice and use pre-chilled solutions, tips, plates, and tubes to minimize unwanted gelation of collagen I.
2. Neutralize the required amount of collagen I (from rat tail) according to the manufacturer's protocol. A volume of 100 µL of neutralized collagen (1.5 mg/mL) per experimental sample (3.5 cm dish) is required. To prepare 1 mL of neutralized collagen (1.5 mg/mL), add 100 µL of 10x DMEM, 1.5 µL of 1M NaOH, and 48.5 µL of dH_2O into 500 µL of collagen (stock concentration = 3 mg/mL). Check the pH of neutralized collagen with litmus paper (the pH should be ~7.5).
3. Disperse 100 µL of neutralized collagen solution evenly using a pre-chilled 200 µL tip over the surface of a 3.5 cm dish set on ice.
4. Incubate overnight under standard culture conditions (incubator with 5% CO_2 at 37 °C). On the day of primary hepatocyte isolation, add 1 mL of pre-warmed (37 °C) PBS to the first collagen layer. Allow the collagen to rehydrate for 2-3 h at 37 °C.

3. Equipment set up

1. Prepare all equipment as listed in **Table of Materials** and set up as shown in **Figure 1**.

4. Surgical procedure

1. Anesthetize the mouse by intramuscular injection of tiletamine (60 mg/kg of body weight), zolazepam (60 mg/kg), and xylazine (4.5 mg/kg). After several minutes, confirm proper anesthetization by the toe pinch. If animal does not respond to the pinch, proceed to 4.2.

2. Place the anesthetized mouse on a dissection mat and tape the lower and upper extremities to fix the mouse in a supine position. Swab the abdomen with 70% ethanol and open the abdomen with a V-shape incision from the pubic area to front legs. Fold the skin over the chest to uncover the abdominal cavity. Place the dissecting mat under a dissecting microscope.
3. Bend an insulin syringe needle (30 G) to a 45° angle. Expose the inferior vena cava (IVC) by moving the intestines and colon in the caudal direction.
4. Fill 2.5 mL of pre-warmed (37 °C) solution C into a 2 mL syringe with a cannula. Ensure that there are no air bubbles in the cannula or syringe.
5. Before cannulation of the IVC, reposition the liver lobes by pressing them up to the diaphragm with a wet (PBS) cotton swab. Place a silk suture around the IVC just below the liver (**Figure 2A,B**).
6. Inject 10 µL of heparin (5000 U/mL) into the portal vein using an insulin syringe with a 30 G needle bent at a 45° angle (**Figure 2C**).
7. To cannulate the liver, make a small incision with microsurgical scissors to the IVC directly next to the liver (below the suture; **Figure 2D**) that is large enough to insert the cannula. Secure the cannula in the position using sutures and two surgical knots (**Figure 2E**).
8. Cut the portal vein (**Figure 2F**) to allow the perfusion buffers to flow out from the liver to prevent expansion of the liver.
9. Manually perfuse the liver with 1.5 mL of pre-warmed solution C by slowly pressing the syringe connected to the cannula (this should take ~15 s). The removal of blood from the liver by discoloration of the liver can now be observed.
10. Pre-fill a peristaltic pump with pre-warmed (37 °C) solution C. Check the perfusion apparatus and ensure that there are no air bubbles in the system.
11. Cautiously disconnect the cannula from the syringe and connect it to the tubing of the peristaltic pump running at flow rate of 2.5 mL/min. Work quickly but carefully and ensure that the cannula remains in position and that no bubbles enter the tubing or cannula.
12. Perfuse the liver with solution C for 2 min (5 mL of solution C). Change to solution D and continue the perfusion for an additional 10 min (25 mL of solution D).
13. Once the liver has been perfused, remove it from the abdominal cavity. The liver will now be very fragile and pale in color (**Figure 3**).

5. Isolation of primary hepatocytes

1. Remove the liver from the mouse. The cannula will still be tied to the liver, so use the forceps to lift the cannula with the liver, and carefully cut off all fascia connections. Transfer the liver to a 50 mL tube containing 20 mL of pre-warmed solution E.
2. Hold the cannula with the liver using forceps and disassociate the tissue by rubbing the liver around the wall of the tube to transfer the isolated hepatocytes into buffer. Keep the isolated cells on ice.
   NOTE: Isolated primary hepatocytes are viable for several hours while kept on ice. Users can repeat steps 4.1 through 5.2 isolating primary hepatocytes from another donor mouse, if necessary, or proceed to the next step.
3. Place a 70 µm nylon cell strainer on top of a 50 mL tube and filter the isolated cells.
4. Centrifuge the tube at 50 x *g* and 4 °C for 5 min. Aspirate the supernatant. To remove dead cells and increase the percentage of viable cells, resuspend the pellet in 20 mL of 40% percol in DMEM.
5. Centrifuge the tube at 50 x *g* and 4 °C for 5 min. Aspirate the supernatant containing dead cells and resuspend the pellet in 20 mL of solution E.
6. Centrifuge tubes at 50 x *g* and 4 °C for 5 min. Aspirate the supernatant and resuspend the pellet in 10 mL of solution E.
7. Check the primary hepatocyte yield and viability using trypan blue staining. Count the cell number using a Neubauer cell counting chamber and adjust the cell concentration to 3.75 x 10^5 viable cells/mL. Keep the cells on ice.

6. Cultivation of primary hepatocytes in 3D collagen sandwiches

1. Prepare hepatocyte culture medium (HCM). Add 15 µL of glucagon (1 mg/mL), 15 µL of hydrocortisone (50 mg/mL), and 40 µL of insulin (10 mg/mL) to 50 mL of complete medium (DMEM, high glucose, 10% FBS, 1% penicillin-streptomycin).
2. Evenly disperse 2 mL (5 x 10^5 cells/mL) of viable primary hepatocytes in a pre-coated 3.5 cm dish. Incubate the cells with 5% CO_2 at 37 °C for 3 h. Important: Evenly distribute the cells by tilting the dish in all directions just before putting the dish into incubator.
3. Prepare neutralized collagen I (100 µL/3.5 cm dish; i.e., a sufficient volume for all dishes as described above [step 2.1]). Keep on ice till use.
4. After 3 h, carefully remove the medium and unattached cells and add 100 µL of neutralized collagen I to each 3.5 cm dish to form the top layer of collagen sandwich on cells. Incubate the collagen sandwich under standard cell-culture conditions (5% CO_2 at 37 °C) for 1 h. After a 1 h incubation, carefully add 2 mL of HCM.
5. After 24 h of culture, change the HCM medium for a fresh one.
6. Culture for 3–8 days, depending on the formation of bile canaliculi. Check the culture every day under a microscope (**Figure 4**). Change the HCM every second day.

7. Immunolabeling of primary hepatocytes in 3D collagen sandwiches

1. Remove the media from the hepatocyte sandwiches, then wash carefully with pre-warmed PBS. Fix the sandwich cultures with 1 mL of 4% paraformaldehyde in PBS for 30 min at room temperature (RT).
2. After fixation, wash the sandwiches 3x for 10 min in 2 mL of PBS + 0.1% Tween 20 (PBS-T).
3. Permeabilize cells with 1 mL of 0.1 M glycine, 0.2% Triton X-100 in PBS at RT for 1 h. Wash 3x for 10 min in PBS-T.
4. Gently disturb the top layer of collagen using a 10 µL loading tip connected to a vacuum aspiration to ensure sufficient antibody penetration.
5. Block with 1 mL of 5% BSA in PBS-T (i.e., blocking solution) for 2 h. Incubate with primary antibodies diluted in blocking solution overnight at 37 °C. Wash 3x for 15 min in PBS-T.
6. After washing, incubate with secondary antibody at 37 °C for 5 h. Wash 3x for 15 min in PBS-T followed by 1x wash with distilled H_2O.
7. Mount with anti-fade mounting media (see **Table of Materials**) for microscopy.

Representative Results

Mouse primary hepatocytes were isolated and seeded in 3D collagen sandwiches. Bile canaliculi between two adjacent cells started to form within several hours after seeding. Cells formed clusters and self-organized in an approximately regular network of bile canaliculi within 1 day (**Figure 4**). Within 3–6 days, clusters of 5–10 cells were usually observed, with fully polarized hepatocytes forming a canalicular network (**Figure 4**).

Treatment of primary mouse hepatocytes in 3D collagen sandwiches with either toxin (ethanol) or cytoskeleton-altering drugs (e.g., blebbistatin, okadaic acid) resulted in changes in the hepatocyte cytoskeleton, canaliculi width, shape, and number of bile canaliculi illustrated by immunolabeling with an antibody to keratin 8 (the most abundant keratin in hepatocytes), phalloidin (visualizing F-actin), and antibody to tight junction protein zonula occludens-1 (ZO-1; **Figure 5**).

Ethanol treatment had only a mild effect on organization of keratin 8; however, it increased the tortuosity (as seen from F-actin staining) and distribution of bile canalicular widths (**Figure 5**). The signal intensity of ZO-1 staining was decreased in ethanol-treated bile canaliculi compared to untreated controls, suggesting a loss of tight junctions after ethanol treatment. The inhibition of actomyosin contractility with blebbistatin significantly affected the shape and number of bile canaliculi. The regular canalicular network was reorganized, compared to untreated hepatocytes, into disorderly shaped bile canaliculi with an increased incidence of thick rounded bile canaliculi instead of thin long ones (as seen in the histogram of canalicular widths).

Additionally, treatment with okadaic acid (OA) inhibiting phosphatases strongly affected the physical properties of keratins, as previously shown[8,17]. OA changes the solubility of keratin filaments; thus, the treatment resulted in profound reorganization of the keratin meshwork, which collapsed into large perinuclear aggregates. Both F-actin and tight junction protein ZO-1 were not localized into any particular structures, suggesting almost complete disappearance of organized bile canaliculi and a complete loss of hepatocyte polarity. The remaining bile canaliculi were significantly narrowed compared to untreated controls, as seen in the canalicular width histogram (**Figure 5**).

To correlate microscopic observations of changes in the hepatocyte cytoskeleton with the hepatocellular biochemical response to treatment, the protocol also measured levels of alanine aminotransferase (ALT) and aspartate transaminase (AST) (two liver enzymes that are commonly used as hepatocellular injury markers) in supernatant from the 3D collagen sandwiches (**Figure 6**)[18]. Ethanol treatment significantly elevated the levels of both ALT and AST, suggesting severe hepatocellular injury. Blebbistatin treatment did not lead to any considerable changes in both ALT and AST levels compared to okadaic acid treatment, which triggered mild biochemical changes with increased levels of ALT, but no change in levels of AST. Thus, biochemical markers of hepatocellular injury measured in vitro from hepatocyte supernatant correlate with the cytoskeletal changes observed by immunostaining.

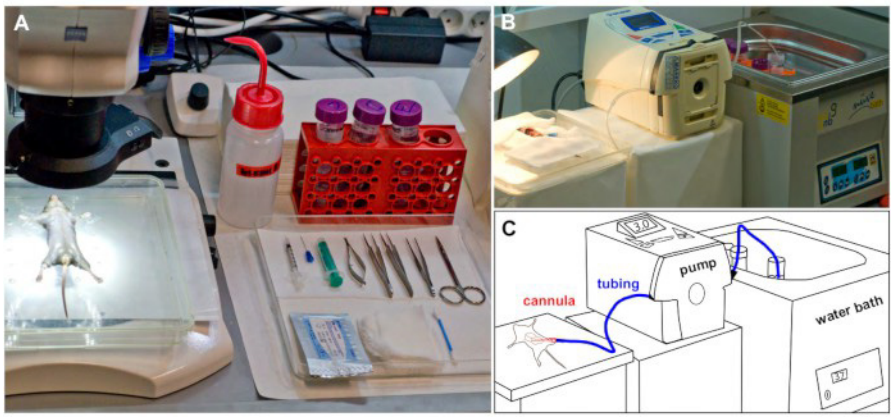

Figure 1: Experimental set up. (**A**) Mouse fixed in a supine position, is placed under a dissecting microscope before the surgery. All surgical instruments required are placed on a tray. (**B**) The perfusion suite during mouse liver perfusion showing silicone tubing connecting the reservoir with warm buffer and the perfused mouse. (**C**) Schematic representation of B. Please click here to view a larger version of this figure.

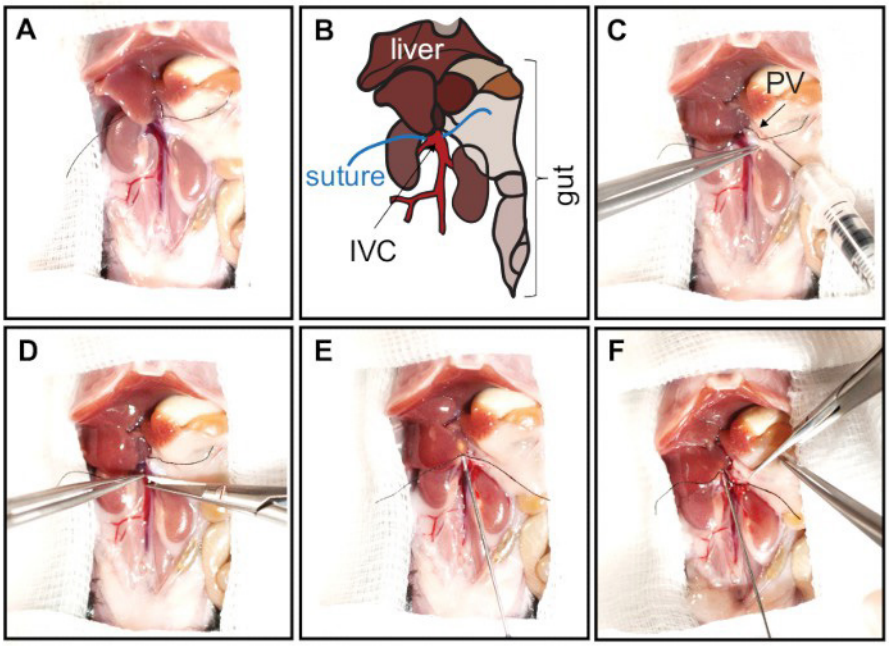

Figure 2: Opening of the abdominal cavity and cannulation of the IVC. The abdomen is opened with a V-shape incision from the pubic area to front legs. The skin is folded over the chest to expose and enlarge the abdominal cavity. To expose the IVC, the intestines and colon are carefully moved caudally. (**A, B**) Prior to cannulation of the IVC, liver lobes should be repositioned by pressing them upwards to the diaphragm with a PBS-wetted cotton swab. The IVC is then carefully separated from surrounding tissues, and a silk suture is placed around the IVC in close proximity of the liver. Panel B represents schematics of the abdominal cavity shown in panel A. The liver lobes, gut, inferior vena cava (IVC, red), and sutures are indicated. (**C**) Heparin is injected into the portal vein (PV, arrow) with an insulin syringe (30 G needle bent at 45° angle). (**D**) To cannulate the liver, the IVC is incised directly next to the liver (below the suture). (**E**) The cannula is inserted and secured with sutures by tying two surgical knots. (**F**) The portal vein is fully cut to allow free buffer outflow, preventing liver expansion. Please click here to view a larger version of this figure.

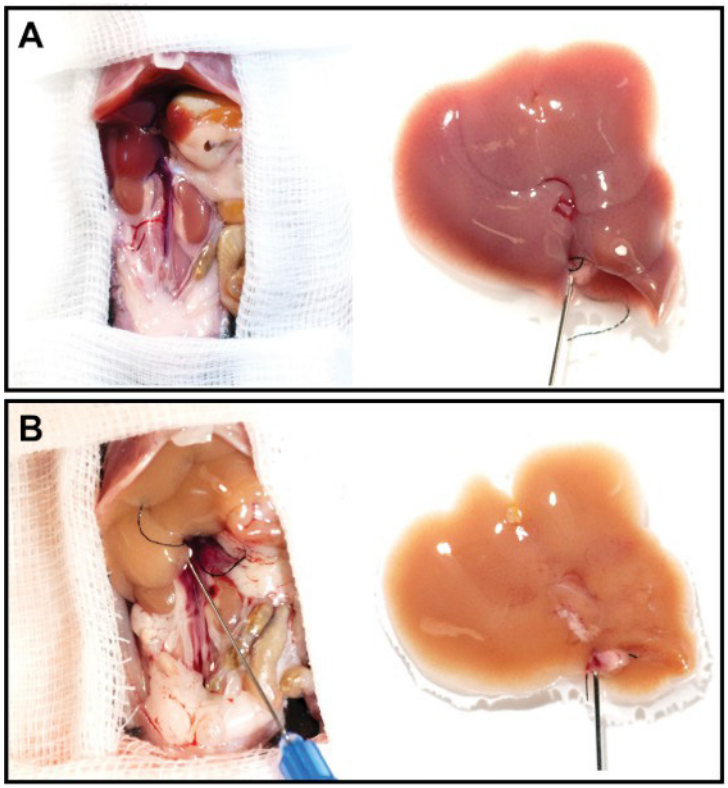

Figure 3: Representative liver images before and after perfusion. (**A, B**) The cannulated liver was resected and perfused for 12 min at a flow rate of 2.5 mL/min. Note the significantly discolored liver after perfusion (B) compared to the freshly resected liver (A). Please click here to view a larger version of this figure.

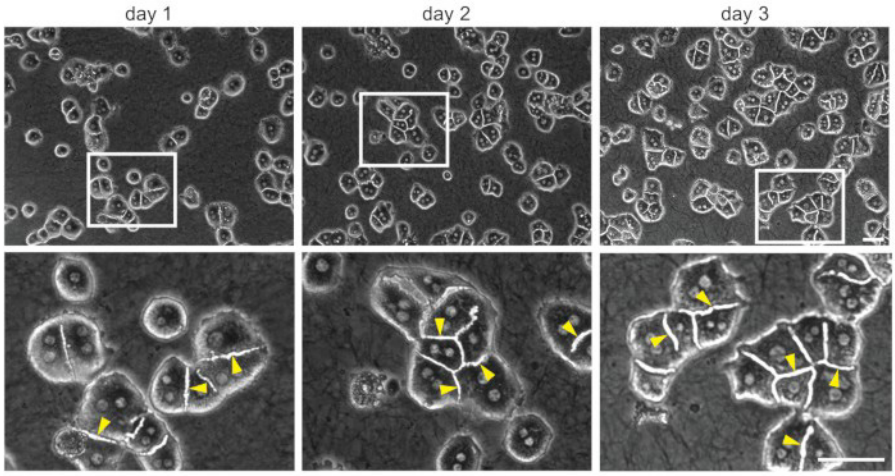

Figure 4: 3D collagen sandwich culture of primary mouse hepatocytes. Representative bright-field images of mouse primary hepatocytes cultured for 1, 2, and 3 days in 3D conditions. It should be noted that larger clusters of highly organized cells are formed after 3 days in culture. Boxed areas show ~3x magnified images. Arrowheads indicate the bile canaliculi. Scale bar = 100 µm. Please click here to view a larger version of this figure.

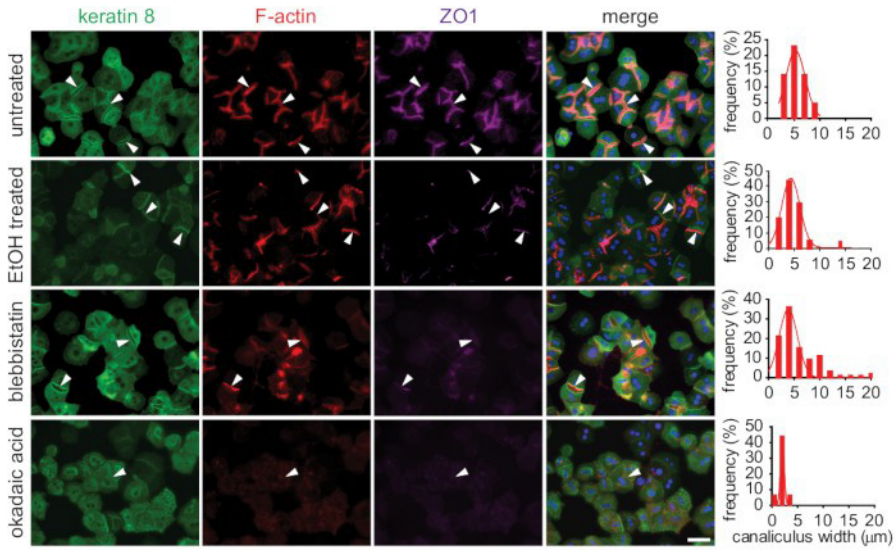

Figure 5: Evaluation of the morphological response to toxic stress by immunofluorescent microscopy. Primary mouse hepatocytes cultured in 3D collagen sandwiches were treated with toxins (ethanol, blebbistatin, or okadaic acid) on day 3 of culture. Fixed cells were stained to visualize cytoskeletal components: keratin 8 (green), F-actin (red), and zonula occludens-1 (ZO-1, magenta) by immunofluorescence. The toxic treatment led to disorganization of visualized cytoskeletal components, and it reduced the number and increased the tortuosity of bile canaliculi. Canalicular widths were measured in both untreated and treated hepatocytes and are depicted as histograms of widths distribution. Arrowheads indicate the bile canaliculi. Scale bar = 100 μm. Please click here to view a larger version of this figure.

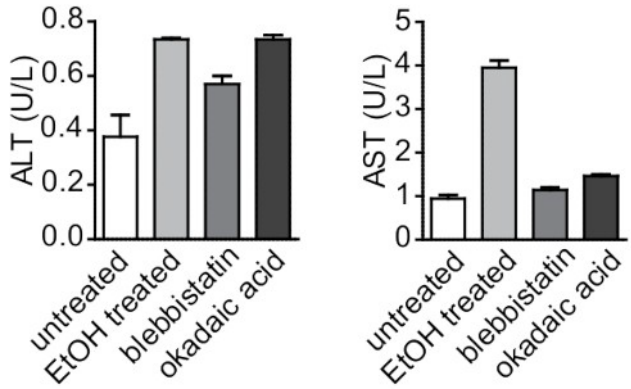

Figure 6: Biochemical analysis of the response of 3D hepatocyte collagen sandwiches to toxic injury in vitro. ALT and AST, well-established markers of hepatocellular injury, were measured in supernatant from 3D hepatocyte collagen sandwiches treated with toxins (ethanol, blebbistatin, and okadaic acid). ALT and AST were elevated in treated cells compared to untreated ones. Data are reported as arithmetic means ± SEM. Please click here to view a larger version of this figure.

Stock Solution A (10x)	
Reagent	Final concentration (g/liter)
NaCl	80
KCl	4
$MgSO_4 \cdot 7H_2O$	1.97
$Na_2HPO_4 \cdot 2H_2O$	0.598
KH_2PO_4	0.6

Table 1: Stock solution A recipe.

Stock Solution B (10x)	
Reagent	Final concentration (g/liter)
NaCl	69
KCl	3.6
KH_2PO_4	1.30
$MgSO_4 \cdot 7H_2O$	2.94
$CaCl_2$	2.772

Table 2: Stock solution B recipe.

Solution C	
Reagent	
Stock Solution A (10x)	5 mL
$NaHCO_3$	0.1094 g
EGTA	0.0095 g
dH_2O	to 50 mL

Table 3: Stock solution C recipe.

Solution D	
Reagent	
Stock solution A (10x)	3 mL
$NaHCO_3$	0.065 g
$CaCl_2$	0.0125 g
dH_2O	to 30 mL

Table 4: Stock solution D recipe.

Solution E	
Reagent	
Stock solution B (10x)	5 mL
$NaHCO_3$	0.1 g
glucose	0.045 g
dH_2O	to 50 mL

Table 5: Stock solution E recipe.

Discussion

The use of mouse primary hepatocyte cultures is important for in vitro studies to better understand the signaling processes involved in the establishment of hepatocyte polarization, proper canalicular structure formation, and bile secretion. The challenges in isolation and long-term culture of mouse primary hepatocytes in 2D culture have driven the invention of several technical approaches with increased isolation effectivity and longevity of isolated cells, each with several advantages and disadvantages. It is now widely accepted that 2D cultures of primary hepatocytes mimic only limited number of attributes of liver biology for a short period of time. Thus, 3D cultivation in a collagen sandwich arrangement is widely replacing the 2D conditions, particularly when focused on function of the cytoskeleton in liver biology (e.g., toxic drug effects or spatial organization of bile transport).

Since the 1980s, several protocols for isolation of mouse hepatocytes with various modifications have been described. The two-step collagenase perfusion approach has become widely used in many laboratories. The addition of gradient centrifugation into the isolation protocol allows the removal of dead cells[19,20] and significantly increases the number of viable cells (here, routinely to ~93%). Even though this step extends the handling time of the cells and results in reduced cell numbers[21], this step is viewed as necessary in the 3D collagen sandwich culture for proper bile canalicular network formation. Additionally, it is more important to proceed quickly and accurately during perfusion steps, which shortens the time the cells are handled.

Other important factors that increase the viability of the cells and their ability to form canalicular networks in 3D is the usage of freshly prepared solutions and avoidance of bubbles during perfusion. Therefore, solutions should be prepared on the day of mouse hepatocyte isolation, and the

peristaltic pump and tubing should be checked when changing solutions. If the protocol is closely followed, the isolation of primary hepatocytes should be successful with a high yield of viable cells.

Another critical factor in long-term 3D hepatocyte culture is the initial source of primary hepatocytes that are used. It is important to use animals that are 8–12 weeks old, which serve as optimal donors of hepatocytes. The use of hepatocytes from older animals was not as successful in long-term culture, as these hepatocytes changed their morphology more often, depolarized, and ceased to form canalicular networks. Also, plating hepatocytes on properly neutralized collagen gel formed from relatively highly concentrated solution is a vital step. In most protocols, concentrations of about 1 mg/mL are used. After many optimizations, a concentration of 1.5 mg/mL is optimal for long-term hepatocyte cultivation and provides highly organized hepatocytes with formed bile canaliculi.

This easy-to-follow protocol allows long-term cultivation of primary mouse hepatocytes. Representative results demonstrate a broad spectrum of use for 3D cultured primary mouse hepatocytes when studying the role of cytoskeletal components in bile canaliculi formation.

Disclosures

The authors have nothing to disclose.

Acknowledgments

This work was supported by the Grant Agency of the Czech Republic (18-02699S); the Grant Agency of the Ministry of Health of the Czech Republic (17-31538A); the Institutional Research Project of the Czech Academy of Sciences (RVO 68378050) and MEYS CR projects (LQ1604 NPU II, LTC17063, LM2015040, OP RDI CZ.1.05/2.1.00/19.0395, and OP RDE CZ.02.1.01/0.0/0.0/16_013/0001775); Charles University (personal stipend to K.K.), and an Operational Program Prague–Competitiveness project (CZ.2.16/3.1.00/21547). We acknowledge the Light Microscopy Core Facility, IMG CAS, Prague, Czech Republic (supported MEYS CR projects LM2015062 and LO1419) for support with the microscopy imaging presented.

References

1. Gissen, P., Arias, I. M. Structural and functional hepatocyte polarity and liver disease. *Journal of Hepatology.* **63** (4), 1023-1037 (2015).
2. LeCluyse, E. L., Fix, J. A., Audus, K. L., Hochman, J. H. Regeneration and maintenance of bile canalicular networks in collagen-sandwiched hepatocytes. *Toxicology In Vitro.* **14** (2), 117-132 (2000).
3. Tsukada, N., Ackerley, C. A., Phillips, M. J. The structure and organization of the bile canalicular cytoskeleton with special reference to actin and actin-binding proteins. *Hepatology.* **21** (4), 1106-1113 (1995).
4. Herr, K. J. *et al.* Loss of alpha-catenin elicits a cholestatic response and impairs liver regeneration. *Scientific Reports.* **4**, 6835 (2014).
5. Yeh, T. H. *et al.* Liver-specific beta-catenin knockout mice have bile canalicular abnormalities, bile secretory defect, and intrahepatic cholestasis. *Hepatology.* **52** (4), 1410-1419 (2010).
6. Pradhan-Sundd, T. *et al.* Dual catenin loss in murine liver causes tight junctional deregulation and progressive intrahepatic cholestasis. *Hepatology.* **67** (6), 2320-2337 (2018).
7. Theard, D., Steiner, M., Kalicharan, D., Hoekstra, D., van Ijzendoorn, S. C. Cell polarity development and protein trafficking in hepatocytes lacking E-cadherin/beta-catenin-based adherens junctions. *Molecular Biology of the Cell.* **18** (6), 2313-2321 (2007).
8. Jirouskova, M. *et al.* Plectin controls biliary tree architecture and stability in cholestasis. *Journal of Hepatology.* **68** (5), 1006-1017 (2018).
9. Fu, D., Wakabayashi, Y., Ido, Y., Lippincott-Schwartz, J., Arias, I. M. Regulation of bile canalicular network formation and maintenance by AMP-activated protein kinase and LKB1. *Journal of Cell Science.* **123** (Pt 19), 3294-3302 (2010).
10. Woods, A. *et al.* LKB1 is required for hepatic bile acid transport and canalicular membrane integrity in mice. *Biochemical Journal.* **434** (1), 49-60 (2011).
11. Porat-Shliom, N. *et al.* Liver kinase B1 regulates hepatocellular tight junction distribution and function in vivo. *Hepatology.* **64** (4), 1317-1329 (2016).
12. Sarnova, L., Gregor, M. Biliary system architecture: experimental models and visualization techniques. *Physiological Research.* **66** (3), 383-390 (2017).
13. Talamini, M. A., Kappus, B., Hubbard, A. Repolarization of hepatocytes in culture. *Hepatology.* **25** (1), 167-172 (1997).
14. Bhandari, R. N. *et al.* Liver tissue engineering: a role for co-culture systems in modifying hepatocyte function and viability. *Tissue Engineering.* **7** (3), 345-357 (2001).
15. Godoy, P. *et al.* Recent advances in 2D and 3D in vitro systems using primary hepatocytes, alternative hepatocyte sources and non-parenchymal liver cells and their use in investigating mechanisms of hepatotoxicity, cell signaling and ADME. *Archives of Toxicology.* **87** (8), 1315-1530 (2013).
16. Wilkening, S., Stahl, F., Bader, A. Comparison of primary human hepatocytes and hepatoma cell line Hepg2 with regard to their biotransformation properties. *Drug Metabolism and Disposition.* **31** (8), 1035-1042 (2003).
17. Strnad, P., Windoffer, R., Leube, R. E. In vivo detection of cytokeratin filament network breakdown in cells treated with the phosphatase inhibitor okadaic acid. *Cell and Tissue Research.* **306** (2), 277-293 (2001).
18. Chalupsky, K. *et al.* ADAM10/17-Dependent Release of Soluble c-Met Correlates with Hepatocellular Damage. *Folia Biologica.* **59** (2), 76-86 (2013).
19. Li, W. C., Ralphs, K. L., Tosh, D. Isolation and culture of adult mouse hepatocytes. *Methods in Molecular Biology.* **633**, 185-196 (2010).
20. Horner, R. *et al.* Impact of Percoll purification on isolation of primary human hepatocytes. *Scientific Reports.* **9** (1), 6542 (2019).
21. Severgnini, M. *et al.* A rapid two-step method for isolation of functional primary mouse hepatocytes: cell characterization and asialoglycoprotein receptor based assay development. *Cytotechnology.* **64** (2), 187-195 (2012).

membrane, together with the auxin directional-transport system, indicates that auxin molecules function differently at different subcellular locations within a plant cell. Thus, the development of new tools and reagents to visualize the distribution of auxin molecules *in vivo* is a matter of urgency: one of the strategies probably relies on interdisciplinary studies with chemists and/or physicists.

Do you feel a push towards more applied science? How does that affect your own work? In China, the majority of grant funding in plant biology tends to support research in applied sciences, such as crop development and improvement. There is little space for basic research using the model plant *Arabidopsis*. Most, if not all, young scientists have turned to work on crop science due to funding restrictions. However, research using the model systems that provide the basic understanding of general principles in biology is critical and necessary for the long term. Also, benefiting from new advances in technology including plant transformation and genome editing, I believe further development of additional model plants beyond *Arabidopsis*, such as rice, is equally important, so that a good portion of scientists can still carry out hypothesis-driven research rather than species-based research. In my research group, our major interest is to understand the mechanism of differential auxin responses in plant development by using *Arabidopsis* as a model system, but we have also started to work on rice and quinoa. Interestingly, rice as a typical monocot plant species has a lower auxin sensitivity and shows strikingly different auxin responses than those in both *Arabidopsis* and quinoa as dicots. Thus, by working on both monocot and dicot models, my goal is to elucidate the molecular mechanisms for how auxin triggers plant-cell signalling at the species level, and also lead a research team that balances both basic research and applied science.

Haixia Institute of Science and Technology, Fujian Agriculture and Forestry University, Fuzhou, 350007, China.
E-mail: tdxu@sibs.ac.cn

Quick guide

Plectin

Magdalena Prechova, Katerina Korelova, and Martin Gregor*

What is plectin? Plectin is a giant cytoskeletal crosslinker (also known as a cytolinker) protein of more than 4,500 amino acids. It belongs to the plakin family of giant proteins, including desmoplakin, envoplakin and periplakin. Plectin was first described in 1980 as a polypeptide component that co-purified with the intermediate filament protein vimentin from glia-derived cells. The term ‘plectin’ comes from the Latin word ‘plecto’, which means to plait, weave or braid.

What does plectin look like? Electron microscopy of plectin molecules reveals a dumbbell-like shape. The ~200-nm-long central α-helical domain forms the handle of the dumbbell, and two terminal globular domains form the weights of the dumbbell.

The giant plectin molecule has several functional domains (Figure 1A). The amino-terminal domain contains the canonical actin-binding domain (ABD) and the plakin domain. The ABD is made up of two calponin homology domains (CH1 and CH2), and the plakin domain has nine spectrin repeats with a Src homology 3 (SH3) domain located within the fifth repeat. The central fibrous rod domain mediates dimerization through coiled-coil interactions, and the lateral association of rod domains leads to the formation of plectin oligomers.

The carboxy-terminal domain is formed by six plectin repeat domains (PRDs; roughly 300 amino acids each), separated by variable linker regions, and a short carboxy-terminal tail. Each PRD has a highly conserved central core. The linker region between the fifth and sixth PRD harbors binding sites for intermediate filaments (IFs), thus constituting the IF-binding domain.

Plectin is very versatile in its interactions with binding partners because different ABD-preceding sequences (encoded by alternatively spliced first exons) provide transcript diversity. Plectin has at least 14 known isoforms, of which four are prominently expressed in epithelia (plectins 1, 1a, 1c, and 1f). Isoform-specific sequences define ABD specificity and facilitate the targeting of plectin molecules to particular subcellular structures, such as the nucleus, microtubules, and focal adhesions.

What are plectin’s known associates? Because of their numerous functional domains, all plectin isoforms interact with a wide variety of proteins. Although plectin is a plakin family protein and is thus able to interact with actin filaments and microtubules, plectin is primarily an IF-binding protein. Plectin has been shown to bind directly to several IF proteins, including epithelial keratins (both types I and II), neurofilaments, vimentin, desmin, glial fibrillary acid protein, and lamin B. In addition, plectin associates with cell adhesion constituents, such as integrin β4 and bullous pemphigoid antigens (BPAG1/2) at hemidesmosomes, periplakin at desmosomes, and zonula occludens 1 (ZO-1) at tight junctions, or with the nucleus-associated protein nesprin-3. Additionally, plectin provides a scaffolding platform for various signalling molecules such as serine/threonine protein kinases (for example, Fer, AMP-activated protein kinase, protein kinase A, and MAPK-interacting kinase 2) or non-receptor tyrosine kinases (for example, Src and Pyk2). In addition, plectin has been shown to regulate protein kinase C activity by sequestering its receptor protein RACK1.

What is the role of plectin in cytoarchitecture? In its capacity as an IF crosslinker, plectin plays an important role in shaping and compartmentalizing IF networks within the cytoplasm. In epithelial cells (Figure 1B, left), plectin supports the formation of the submembranous circumferential keratin rim. This rim is associated with other keratin IFs that are arranged into desmosome-anchored radial filaments, which (in a plectin-dependent manner) link the nuclear and peripheral compartments of the cell. Plectin also anchors the keratin network to hemidesmosomes,

which are the cell junctions mediating the adhesion of epithelial cells to the subjacent extracellular matrix (called the basement membrane).

In mesenchymal fibroblasts (Figure 1B, right), plectin-crosslinked vimentin IFs form a compact, cage-like core structure that encases and positions the nucleus, while being stably connected to another type of cell adhesion — focal adhesions. The formation of a robust (matrix-anchored) IF core structure is a prerequisite for the proper shape and polarization of cells, determining the directionality and speed of migration.

Plectin-facilitated assembly of cytoskeletal components under both compression and tension balances internal tension and stabilizes cellular structures, thus maintaining cellular integrity (Figure 1B). For instance, a plectin-controlled circumferential keratin network in epithelial cells is required for an even spatial distribution of actomyosin-generated forces between the plasma membrane, desmosomes, and cytoplasmic keratin IFs. In a similar fashion, plectin secures the mechanical crosstalk between actomyosin and vimentin IFs at focal adhesions in fibroblasts.

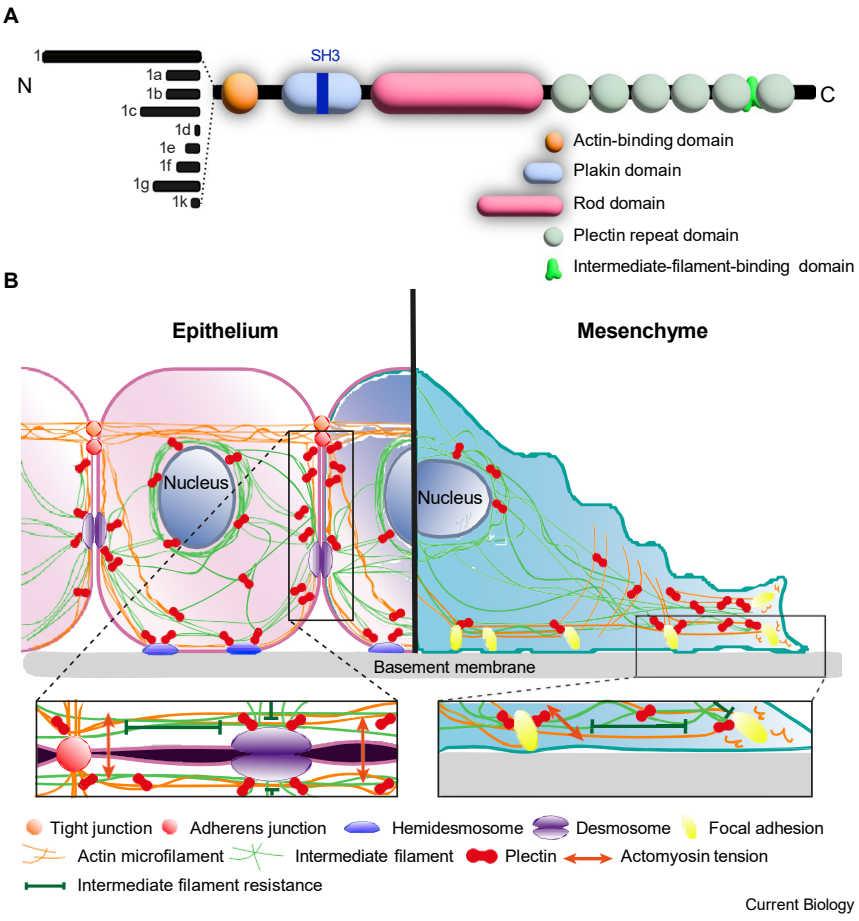

Figure 1. Structure, subcellular localization, and function of plectin.
(A) The isoform-specific amino-terminal sequence (plectin isoforms 1, 1a, 1b, etc.; black) is spliced into the actin-binding domain (orange) and a plakin domain (blue) consisting of nine spectrin repeats and the SH3 domain. Only canonical isoforms are shown. The central coiled-coil rod domain (pink) facilitates dimerization. The six carboxy-terminal plectin repeat domains harbor the intermediate-filament-binding domain (green). (B) Schematic overview of plectin localization and plectin-mediated crosslinking/anchoring in epithelial (left) and mesenchymal (right) cells. Plectin crosslinks intermediate filaments (epithelial keratin and mesenchymal vimentin) with actin filaments. Plectin anchors the resulting cytoskeletal network to cell–cell adhesions (desmosomes and adherent junctions) and cell–ECM adhesions (hemidesmosomes and focal adhesions). Cells are in a state of isometric tension, with actomyosin-generated forces being balanced by the resistive capacity of the intermediate filament network. C, carboxyl terminus; N, amino terminus; SH3, Src homology 3 domain.

How does plectin affect the mechanical stability of tissues?

By linking various cytoskeletal components, plectin imparts tensional homeostasis and mechanical stability to maintain tissue architecture. Plectin dysfunction mechanically uncouples the individual cytoskeletal network components, leading to aberrant cytoskeletal configuration. This is typically associated with the redistribution of internal tension, which drives the lateral bundling of cytoplasmic IFs. This redistribution in turn promotes actomyosin assembly and increases cell contractility. The resulting cytoarchitecture is highly susceptible to mechanical stress and contributes to the higher fragility of load-bearing tissues.

In epithelial sheets, intercellular junctions lose mechanical support without plectin. The resulting collapsed keratin IFs — together with actin filaments — transfer the increased and unevenly distributed cytoskeletal tension to desmosomes and adherens junctions, respectively. Furthermore, uncoupling of keratin IFs from extracellular matrix-anchored hemidesmosomes leads to weakened cell adhesion. Together, this results in the profound destabilization of tissue organization and the failure of coordinated cytoskeletal stress adaptation. On a cellular level, this manifests as epithelial fragility and results in the disruption of epithelial barrier function.

Can you live without plectin?

The improper function of plectin at the cellular level gives rise to a heterogeneous group of plectinopathies. Genetic studies identified over 116 mutations in the *PLEC* gene associated with these plectinopathies. These multisystem disorders include an autosomal dominant form of epidermolysis bullosa simplex (EBS), limb-girdle muscular dystrophy, aplasia cutis congenita, and an autosomal recessive form of EBS, which may associate with muscular dystrophy, pyloric atresia, and/or congenital myasthenic syndrome. Several mutations were also linked to cardiomyopathy and

malignant arrhythmias. Progressive familial intrahepatic cholestasis has also been noted. In genetic mouse models, loss of plectin leads to skin fragility, extensive intestinal lesions, instability of the biliary epithelium, and progressive muscle wasting.

What remains to be studied about plectin? Plectin is upregulated in various tumor types, where its expression often increases during carcinogenesis. Therefore, plectin has been proposed to serve as a robust cancer biomarker. Given the critical role plectin plays in tissue mechanics, which is a key aspect of cancer onset and progression, it is surprising that only a few studies aiming at deciphering the role of plectin in cancer have been published so far. Other interesting lines of future plectin research include examining the specific functions of plectin isoforms and whether plectin itself can serve as a mechanosensing hub.

Where can I find out more?

Gregor, M., Osmanagic-Myers, S., Burgstaller, G., Wolfram, M., Fischer, I., Walko, G., Resch, G.P., Jörgl, A., Herrmann, H., and Wiche, G. (2014). Mechanosensing through focal adhesion-anchored intermediate filaments. FASEB J. *28*, 715–729.

Jirouskova, M., Nepomucka, K., Oyman-Eyrilmez, G., Kalendova, A., Havelkova, H., Sarnova, L., Chalupsky, K., Schuster, B., Benada, O., Miksatkova, P., *et al.* (2018). Plectin controls biliary tree architecture and stability in cholestasis. J. Hepatol. *68*, 1006–1017.

Krausova, A., Buresova, P., Sarnova, L., Oyman-Eyrilmez, G., Skarda, J., Wohl, P., Bajer, P., Sticova, E., Bartonova, L., Pacha, J., *et al.* (2021). Plectin ensures intestinal epithelial integrity and protects colon against colitis. Mucosal Immunol. *14*, 691–702.

Osmanagic-Myers, S., Gregor, M., Walko, G., Burgstaller, G., Reipert, S., and Wiche, G. (2006). Plectin-controlled keratin cytoarchitecture affects MAP kinases involved in cellular stress response and migration. J. Cell Biol. *174*, 557–568.

Prechova, M., Adamova, Z., Schweizer, A.L., Maninova, M., Bauer, A., Kah, D., Meier-Menches, S.M., Wiche, G., Fabry, B., and Gregor, M. (2022). Plectin-mediated cytoskeletal crosstalk controls cell tension and cohesion in epithelial sheets. J. Cell Biol. *221*, e202105146.

Wiche, G., Osmanagic-Myers, S., and Castañón, M.J. (2015). Networking and anchoring through plectin: a key to IF functionality and mechanotransduction. Curr. Opin. Cell Biol. *32*, 21–29.

Wiche, G. (2021). Plectin-mediated intermediate filament functions: why isoforms matter. Cells *10*, 2154.

Laboratory of Integrative Biology, Institute of Molecular Genetics of the Czech Academy of Sciences, Prague, Czech Republic.
*E-mail: martin.gregor@img.cas.cz

Primer

Taste

Alfredo Fontanini

In his book on the ecology of perception (*An Immense World: How Animal Senses Reveal the Hidden*, 2022), science writer Ed Yong emphasizes the simplicity of taste. He writes: "*Taste, then, is the simpler sense. As we've seen, smell covers a practically infinite selection of molecules with an indescribably vast range of characteristics, which the nervous system represents through a combinatorial code so fiendish that scientists have barely begun to crack it. Taste, by contrast, boils down to just five basic qualities in humans — salt, sweet, bitter, sour, and umami (savory) — and perhaps a few more in other animals, which are detected through a small number of receptors. And while smell can be put to complex uses — navigating the open oceans, finding prey, and coordinating herds or colonies — taste is almost always used to make binary decisions about food. Yes or no? Good or bad? Consume or spit? It's ironic that we associate taste with connoisseurship, subtlety and fine discrimination when it is among the coarsest of senses.*"

This perspective relies on a few fundamental assumptions. The first is that the gustatory system has a low bandwidth and is categorical — that is, taste categorizes a multitude of chemicals in only five perceptually distinct taste qualities. The second assumption is that, unlike olfaction, gustation does not rely on a complex combinatorial code, but rather uses a small number of receptors and cells representing individual taste qualities. Finally, the third assumption is that taste perception linearly maps onto simple, binary and hard-wired responses, with some tastes being innately palatable and consumed, and others aversive and rejected.

Current experimental evidence on the gustatory system *does not support* these widely held assumptions and points at a much more sophisticated role of taste in perception and behavior. The goal of this primer is to provide an account of taste based on the most recent research that dispels the myth of its linearity and simplicity.

Taste perception: Beyond the five taste qualities

As noted by Yong, it is widely acknowledged that humans can perceive five taste qualities: sweet, sour, bitter, salty and umami. With this knowledge often comes the assumption that each chemical that produces a taste sensation ('tastant') is exclusively categorized into one of these five qualities. While this may hold true for many chemicals, several others can evoke a combination of sensations. For instance, the salt LiCl is both salty and sour, and the sweetener saccharin has sweet and bitter components. This evidence challenges a strict categorical view of taste and suggests the presence of a combinatorial logic analogous to the one found for the olfactory system.

A second challenge to an oversimplified view of taste comes from the existence of more than five taste qualities and from additional oral sensations. The gustatory system may be responsible, at least partially, for the sensations associated with water, carbonation, metallic and fat. The latter, which derives from long and short chain fatty acids present in food as either triglycerides or free fatty acids, has been proposed as a sixth taste quality. As for other well-known qualities — such as the spiciness of chili peppers, the coolness of menthol, the astringency of tannins, the tingling of carbonation or temperature and texture — while they are detected by the trigeminal system and are not thought to involve taste cells, they profoundly affect gustatory perception.

Together with the notion of five basic taste qualities comes the idea of a simple and innate mapping between qualities, physiological value, palatability and binary ingestive decisions. For instance, it is commonly accepted that sweet, salty and umami are associated with nutrients, are palatable and promptly consumed. Similarly, bitter and sour are believed to be the qualities of toxic substances, thus they are aversive and avoided. However, the mapping between taste quality and palatability is far more nuanced and plastic. The palatability of sweet diminishes upon consumption

OPEN
BIOLOGY

In control of epithelial mechanics: Plectin as an integrator of epithelial cytoskeletal networks

Journal:	*Open Biology*
Manuscript ID	Draft
Article Type:	Review
Date Submitted by the Author:	n/a
Complete List of Authors:	Outla, Zuzana; Institute of Molecular Genetics Czech Academy of Sciences, Laboratory of Integrative Biology Prechova, Magdalena; Institute of Molecular Genetics Czech Academy of Sciences, Laboratory of Integrative Biology Korelova, Katerina; Institute of Molecular Genetics Czech Academy of Sciences, Laboratory of Integrative Biology Gemperle, Jakub; Institute of Molecular Genetics Czech Academy of Sciences, Laboratory of Integrative Biology Gregor, Martin; Institute of Molecular Genetics Czech Academy of Sciences, Laboratory of Integrative Biology
Subject:	cellular biology, molecular biology
Keywords:	plectin, cytoskeletal crosstalk, epithelia, mechanobiology

Author-supplied statements

Relevant information will appear here if provided.

Ethics

Does your article include research that required ethical approval or permits?:
This article does not present research with ethical considerations

Statement (if applicable):
CUST_IF_YES_ETHICS :No data available.

Data

It is a condition of publication that data, code and materials supporting your paper are made publicly available. Does your paper present new data?:
My paper has no data

Statement (if applicable):
CUST_IF_YES_DATA :No data available.

Conflict of interest

I/We declare we have no competing interests

Statement (if applicable):
CUST_STATE_CONFLICT :No data available.

In control of epithelial mechanics: Plectin as an integrator of epithelial cytoskeletal networks

Zuzana Outla*, Magdalena Prechova*, Katerina Korelova, Jakub Gemperle, Martin Gregor

Laboratory of Integrative Biology, Institute of Molecular Genetics of the Czech Academy of Sciences, Prague, Czech Republic.

*These authors contributed equally.

Author for correspondence: Martin Gregor, e-mail: martin.gregor@img.cas.cz

Subject Area: cellular biology, cellular biology

Keywords: plectin, cytoskeletal crosstalk, epithelia, mechanobiology

Abstract

Epithelia are multicellular sheets that form barriers defining the internal and external environments. The constant stresses acting at this interface require that epithelial sheets are mechanically robust and provide a selective barrier to the hostile exterior. These properties are mediated by cellular junctions, which are physically linked with heavily crosslinked cytoskeletal networks. Such hardwiring is facilitated by plakins, a family of giant modular proteins that serve as 'molecular bridges' between different cytoskeletal filaments and multiprotein adhesion complexes. Dysfunction of cytoskeletal crosslinking compromises epithelial biomechanics and structural integrity. Subsequent loss of the barrier function leads to disturbed tissue homeostasis and pathological consequences such as skin blistering or intestinal inflammation. In this review, we highlight the importance of cytolinker protein plectin for the functional organization of epithelial cytoskeletal networks. In particular, we focus on the ability of plectin to act as an integrator of the epithelial cytoarchitecture that defines biomechanics of the whole tissue. Finally, we also discuss the role of cytoskeletal crosslinking in emerging aspects of epithelial mechanobiology that are critical for the maintenance of epithelial homeostasis.

1. Introduction

Epithelia form layers of tightly linked epithelial cells, providing a selective physical barrier that is critical for metazoan homeostasis. Since epithelial sheets line the internal and external surfaces of the body and separate distinct compartments, epithelia are subject to considerable mechanical stress. The maintenance of the epithelial barrier function therefore requires mechanical resilience. This relies on cytoskeletal networks, consisting of actin fibers, microtubules (MTs), and intermediate filaments (IFs), that define the mechanical properties and functional organization of epithelial cells. Mechanical robustness is further provided by cytoskeleton-associated cell junctions that seal intercellular spaces and interlink epithelial cells with the underlying basement membrane (BM). While apical tight junctions (TJs) and subjacent adherens junctions (AJs) are linked to actin filaments, desmosomes (DSMs), together with BM-associated hemidesmosomes (HDs), are connected to keratin IFs (KFs). The textbook view is that cell junctions together with cytoskeletal networks integrate epithelial sheets with BM into a structural and functional continuum.

The spatiotemporal architecture of cytoskeletal networks is controlled by cytoskeletal crosslinkers (so-called cytolinkers) of the plakin family [1]. Owing to their multimodular structure, these giant proteins (amassing up-to 500 kDa) have the capacity to bind all three cytoskeletal filaments and anchor the resulting networks to various cell structures (such as organelles and cell junctions). The best-studied plakin, prototypical cytolinker plectin [2, 3], was isolated as vimentin IF (VF)-binding protein from glia-derived cells in 1980 [4]. The name 'plectin' originates from the Greek word 'πλεκτή' (plectae), which means mesh or net [4]. Over the past decades, plectin has been implicated in many epithelia-affecting pathologies, and multiple studies have highlighted the intimate relationship between plectin, cytoskeletal

networks, and epithelial physiology. Here, we review our current knowledge of plectin and of how its structure and binding versatility are adapted to its mechanical and non-mechanical functions in epithelia. We also focus on the molecular mechanisms underlying the major plectin-related, mechanical stress-driven pathological conditions. Finally, in the last chapters of this review, we provide an overview of the emerging concepts in epithelial mechanobiology such as cytoskeletal crosstalk, adaptive reconfiguration of epithelial cytoarchitecture, and mechanosignaling.

2. Plectin: a multifaceted crosslinker by design

Plectin molecules adopt the general plakin modular structure with the N-terminal plakin domain (PD), the central coiled rod domain, and the C-terminal globular domain (figure 1) (previously reviewed in [5, 6]). These domains enable plectin to interact with all the major cytoskeletal components: actin fibers, IFs, and MTs. The N-terminal segment contains the actin-binding domain (ABD) together with the canonical PD, which harbors the putative Src homology 3 (SH3) domain [7-9]. The IF-binding domain (IFBD) is located within a C-terminal region of six plakin repeat domains [10-14]. The additional VF-binding site is located within the ABD [15]. The end of the C-terminal region contains the MT-binding Gly-Ser-Arg-containing repeats [16]. In addition, an isoform-specific MT-interacting site that overlaps with ABD in the N-terminal region has recently been identified [17]. The central rod domain mediates the dimerization of plectin molecules through coiled-coil interactions, leading to the lateral association into plectin oligomers [18, 19]. In the early stages of apoptosis, the plectin rod domain is cleaved by caspase 8 [20]. Alternative splicing of exon 31 results in the rodless plectin variant [21]. All the plectin domains are multifunctional and interact with many proteins. For example, plectin recruits the cytoskeleton to cell junction complexes through association with integrin ß4 [22, 23], bullous pemphigoid antigens (BPAG)1 and 2 [24-26], periplakin [27], or zonula occludens 1 (ZO-1) [28]. The interactions of plectin with other cytoskeleton-associated proteins, namely nesprin-3 [29], ankyrin [30], endophilin B2 [31, 32], epithelial protein lost in neoplasm (EPLIN) [33], or MT-associated protein 2 (MAP2) [34] are also instrumental for the cytoskeletal configuration.

In addition to its organizational role, plectin is involved in signal transduction as a scaffolding protein, but also as a substrate of various serine/threonine protein kinases (such as Fer [35], AMPK [36], PKA, and MNK2 [37]), or non-receptor tyrosine kinases (such as Src [38, 39] and Pyk2 [38]). Furthermore, plectin can regulate kinase activity by sequestering its scaffolding proteins. For instance, plectin binding of RACK1 (the receptor and scaffolding protein of activated PKC) has been shown to regulate the PKCδ/Src/Erk2 pathway in keratinocytes [39, 40]. For detailed information on plectin interacting partners, see figure 1 and table 1.

The plectin locus [41] can generate at least 14 different protein isoforms (figure 1) by using alternative start sites and internal splicing. The alternative first exon sequences modulate the binding properties of subsequent ABD, thereby facilitating the targeting of individual plectin isoforms to diverse cellular structures [42-44]. In epithelia, the

predominantly expressed isoforms are plectin 1 (P1), 1a (P1a), 1f (P1f), and 1c (P1c) [45]. Isoform P1 localizes to the perinuclear region [46], where it links IFs to the nuclear envelope via nesprin-3 and endophilin B2 binding [29, 31, 47]. Isoform P1a interacts with integrin ß4 within HDs - the complexes that mediate cell adhesion to the underlying dense extracellular matrix (ECM) organized into BM [48] (figure 2). In stratified epithelia, P1a is therefore predominantly found in the basal cell layer, where its staining signal co-aligns with the BM [46]. In an isoform-specific manner, P1a was found to restore the HD formation and attachment to the BM in plectin-deficient keratinocytes [46]. Another membrane-enriched isoform, P1f, tethers VF precursors to focal adhesions (FAs) in fibroblasts [44, 49]. Such FA-associated KF assembly has also been documented in epithelial cells [50]. Remarkably, only re-expression of P1a and P1f isoforms restores the aberrant KF organization within the cell periphery in plectin-deficient epithelial monolayers [51]. In contrast to P1a, the P1c isoform is predominantly expressed in the suprabasal layers of stratified epithelia [46]. The P1c-specific exon, together with two additional exons 2α and 3α inserted into the ABD (figure 1), confers MT-binding ability on plectin [17]. P1c is involved in the regulation of MT stability, as its ablation in keratinocytes leads to higher MT resistance to nocodazole treatment and increased MT dynamics, thus affecting cell shape, division, and growth [34]. For an overview of the isoform-specific plectin functions in different experimental models, see table 2.

3. Keratin networks as safeguards of epithelial integrity

The major components of the epithelial cytoskeleton are KFs, which are believed to play a vital role in mechanical integrity at the cellular and tissue levels (previously reviewed in [52-54]). Keratins are encoded by 54 evolutionarily conserved genes. Based on their sequence, keratins are divided into two distinct gene families (Type I and Type II). The tripartite structure of keratins consists of a conserved central α-helical rod domain flanked by variable head and tail domains. The amphipathic properties of the central domain allow spontaneous heterodimerization of Type I and Type II keratins [55, 56]. These highly stable heterodimers associate laterally into four nonpolar antiparallel tetramers, which anneal longitudinally into filaments to be further organized into bundles [57].

The structure of keratin provides keratin networks with unique physical properties. KFs are highly extensible and can be stretched almost three times without rupture [58]. Compared to MTs and F-actin, the shortest flexible length makes KFs the most flexible cytoskeletal polymers in epithelia [59, 60]. KFs also undergo strain stiffening upon mechanical load to absorb and dissipate energy [60]. As evidenced by the deformation of epithelial sheets, KFs enable the re-stiffening of epithelial cells under tension, thus contributing significantly to epithelial elasticity and tensile strength [61].

The importance of KFs for tissue integrity is highlighted by the severe skin, liver, and intestinal fragility that occurs in genetic diseases [62, 63]. These are closely mimicked in many genetic mouse models. For example, mice lacking K5 or K14, the major keratin pair of the epidermis, suffer from skin blistering [64, 65], resembling patients with epidermolysis bullosa simplex (EBS) [66, 67]. The K8 deficiency/mutations in the intestine of both mouse and human

result in epithelial defects associated with inflammatory bowel disease [68-71]. In the liver, the mutation of K8 or K18 results in compromised hepatocyte integrity and increased susceptibility to injury [72-76], corresponding to K8/K18-associated human liver diseases [77-80].

4. Plectin governs the epithelial keratin network architecture

The unique mechanical properties are functionalized by plectin (and other plakins), which ensure the arrangement of KFs into highly organized networks. In epithelial cells, KFs are arranged in a so-called rim-and-spoke configuration in a plectin-dependent manner [51, 81]. This consists of a subplasmalemmal circumferential keratin rim, which associates with another subset of KFs that are aligned in dense radial spokes spanning the cytoplasmic space between the nucleus and the peripheral compartments of the cell (figure 3) [81-83].

Our recent study [51] has shown that plectin-mediated crosslinking between keratin and actin peripheral networks is required for the formation of the circumferential keratin rim in epithelial monolayers. Furthermore, plectin stabilizes the epithelial cytoarchitecture by anchoring KFs to cell adhesions (HDs and DSMs) and to the nucleus [84], while condensing the keratin network via orthogonal crosslinking of individual filaments [39]. This is reflected in the collapse of the keratin network into more bundled and less flexible filaments upon plectin loss [39, 51, 85-88]. Overall, plectin inactivation results in circumferential keratin rim ablation, KF bundling, cell adhesion defects, and general destabilization of aberrant keratin networks in epithelial cells [39, 51, 86, 89, 90].

Distinct populations of epithelial cells are characterized by unique keratin expression profiles. For instance, the basal layer of the epidermis expresses the keratin pair K5/K14, which is sequentially replaced by K1/K10 in the suprabasal layers [91, 92]. Similarly, biliary epithelial cells (BECs) in the liver express five different types of keratins: K7, K8, K18, K19, and K23 [93, 94]. Such redundancy prevents the assessment of the contribution of individual keratins to different cell/tissue properties (including mechanical properties), as suggested in the case of K10-, K19-, or K17-deficient mouse models [95-97].

The critical role of functional KF architecture is underscored by the phenotype of a liver-specific mouse model, in which plectin deletion was found to affect all keratin isotypes to the same extent [86]. In these mice, aberrant keratin networks in plectin-deficient BECs resulted in prominent biliary epithelial instability under cholestatic conditions. Such defects were not evident when only the K19 isotype was ablated [95]. Thus, plectin can be used as a unique tool to identify the role of keratins in complex systems. In contrast, other epithelial cells do not express such a broad spectrum of keratin isotypes. In these cases, the plectin-targeting phenotype mimics the keratin-related effects, as demonstrated by the destabilized keratin architecture of plectin-deficient hepatocytes expressing only the K8/K18 pair [86, 98]. Similar changes have also been identified following plectin or keratin inactivation in the intestinal epithelium with K8, K18, and K19 expression and structure [69, 90, 99].

5. Plectin in adhesion and cohesion of epithelial cells

The structural and functional integrity of epithelial sheets is secured by their coupling to the subjacent BM. Cell-ECM coupling is facilitated by HDs, multiprotein adhesion complexes that also play a crucial role in KF nucleation and anchorage [100, 101]. In (pseudo)stratified epithelia, type I HDs are located in the basal cell layer and consist of integrin α6ß4, tetraspanin CD151, and plakins BPAG1c (also known as BP230), BPAG2 (also known as BP180 or collagen XVII), and P1a [102]. In simple epithelia, type II HDs link the cells to the BM via the integrin α6ß4 and P1a only [103, 104] (figure 2).

As a major component of HDs, plectin is highly expressed in all types of epithelia [105]. Therefore, the tissue-specific ablation of plectin in mice leads to rearrangement of KFs, dramatic reduction of HDs, and increased susceptibility to mechanical injury. As a result, compromised intestinal barrier [90], collapsed bile ducts and ductules [86], or detachment of the skin basal layer from the BM [46, 106] have been found in plectin-deficient models. Plectin mechanically stabilizes epithelia not only through KF-HD coupling and KF configuration but also by stabilizing HDs through self-association of its rod domain into more stable oligomers [19].

Functional epithelial barriers and tissue homeostasis also require robust sealing of the intercellular spaces. This is achieved by a joint effort of cytoskeleton-bound cell-cell junctions: F-actin-linked TJs and AJs and KF-linked DSMs, distributed along the border of neighboring epithelial cells (figure 2). Apically located TJs consist of transmembrane junctional adhesion molecules, occludins, and claudins, which are linked to the actin cytoskeleton by ZO proteins [107-110]. The cohesion of AJs is ensured by trans-dimerization of E-cadherin transmembrane proteins that bind to p120-catenin or ß-catenin. The F-actin-AJ linkage is facilitated by α-catenin [111]. DSMs comprise the transmembrane adhesion proteins desmogleins and desmocollins, the DSM plaque of plakoglobin and plakophilin proteins, and the KF-linked desmoplakin [112-114] (figure 2B).

Multiple studies have recently converged on identifying the indispensable role of plectin in intercellular adhesion function and cell-cell cohesion [51, 86, 90, 115]. In the mouse endothelium, plectin depletion leads to AJ and TJ distortion paralleled by increased vascular permeability [115]. Impaired epithelial barrier function and dilation of intercellular spaces have also been described in mouse plectin-deficient biliary and intestinal epithelia, where defects in TJs, AJs, and DSMs have been noted. Therefore, dysfunctional cell cohesion, together with aberrant KF architecture and weakened cell-ECM adhesion, favors epithelial fragility, which manifests in pathologies such as ulcerative colitis or cholestasis [86, 90]. Furthermore, less effective upregulation of desmoplakin in a plectin-deficient model of liver injury suggests a role for plectin in maintaining DSM homeostasis [86]. As shown in Madin-Darby Canine Kidney (MDCK) cells, ablation of plectin leads to increased tensile loading on DSMs and compromises the mechanical integrity of epithelial sheets [51].

It is well recognized that plectin exerts numerous non-mechanical functions that are essential for maintaining epithelial homeostasis. For instance, plectin may influence TJ

stability and epithelial barrier properties by acting as a regulatory scaffold for AMPK regulatory subunit γ [36, 116].

6. Clinical manifestation of plectin mutations

More than 100 mapped mutations in the human plectin gene (*PLEC*) result in plectinopathies [117, 118], a group of complex multisystem disorders that primarily affect tissues exposed to mechanical stress. The most common plectinopathy is EBS, which manifests clinically with early onset severe epidermal blistering. The autosomal recessive variant of EBS is associated with muscular dystrophy (EBS-MD), myasthenic syndrome (EBS-MD-MyS), pyloric atresia (EBS-PA), or congenital myasthenia (EBS-CMS). These plectinopathies are often caused by mutations in exon 31, which encodes the rod domain, leading to nonsense-mediated mRNA decay (reviewed in [119, 120]). In contrast, the autosomal dominant EBS-Ogna disease is caused by a site-specific missense plectin mutation in exon 31 and manifests exclusively as skin fragility [119, 121]. Progressive familial intrahepatic cholestasis has also been reported [122, 123].

Only five mutations have been so far identified within the alternative first exon of a specific plectin isoform [118]. For example, homozygous deletion of P1f causes autosomal recessive limb-girdle muscular dystrophy (LGMD) associated with progressive muscle weakness without any dermatological component [124]. A similar phenotype was reported for another P1f-specific mutation (c.58G > T, p.E20X), with patients suffering from LGMD and respiratory symptoms [125]. Several other *PLEC* mutations have been linked to cardiomyopathy and malignant arrhythmias [118, 126]. The homozygous nonsense mutation in P1a (c.46C>T; p.Arg16X) causes autosomal recessive skin-only EBS with no effect on mucous membranes, heart, and muscles [127]. Recently, novel missense mutations in the P1-specific N-terminal sequence, exon 31, and exon 32 were identified in patients suffering from hearing loss, without any additional clinical conditions [128].

7. Mouse models of plectinopathies

In recent years, several different mouse models of plectin deficiency have been generated and have been instrumental in our efforts to investigate the role of plectin in the tissue and cell mechanobiology. Mice deficient in all plectin isoforms (plectin-null) die early in postnatal development due to internal blistering of the oral cavity that prevents food intake [106, 129]. At the cellular level, plectin-null mice exhibit rupture of basal keratinocytes, reduced number of HDs, and impaired stability of the keratin networks. In addition, plectin-null mice exhibit structural abnormalities in the heart and skeletal muscle [129]. The severity of the phenotype prevents any in-depth analysis, and therefore this model is not useful for studying human diseases caused by mutations in the plectin gene.

To circumvent the neonatal lethality of plectin-null mice, four types of isoform-specific knockout mice, lacking either P1, P1d, P1c, or P1b, have been generated [130-132] (reviewed

in [133]), significantly broadening the basis for dissecting the isoform-specific roles of plectin in epithelia. A plectin knock-in mouse model has been established to mimic the EBS-Ogna disease [19]. The EBS-Ogna mutation increases the susceptibility of the P1a rod domain to proteolytic cleavage in the epidermis, resulting in reduced P1a protein levels in basal keratinocytes. Furthermore, the mice expressing a rodless variant of plectin, which has been identified in a subset of EBS-MD patients with milder prognosis [134], develop without signs of skin blistering or HD changes. This finding suggests a compensatory effect of rodless plectin in the setting of full-length plectin deficiency [135]. Taken together, analyses of these models suggest that sufficient levels of plectin expression, as well as its interaction with HDs in keratinocytes, are critical for maintaining epidermal integrity.

Apart from isoform-specific and knock-in mouse models, several conditional tissue-specific models have been used in complex studies of the role of plectin in epithelia. For example, models of both constitutive and tamoxifen-induced plectin ablation in intestinal epithelial cells exhibit detachment of the epithelial sheet from the BM, loss of intestinal barrier integrity, and subsequent spontaneous development of a colitic phenotype [90]. It is therefore not surprising that the plectin expression levels were found to negatively correlate with the severity of ulcerative colitis in human patients [90]. Liver-specific plectin knockout mice revealed disruption of apicobasal KF polarity and compromised cell-cell junctions in BECs, accompanied by the collapse of the ductular lumen and misshapen bile canaliculi [86]. When challenged in a model of obstructive cholestasis, plectin ablation exacerbated biliary damage and resulted in markedly dilated bile ducts with more frequent ruptures and increased number of biliary infarcts in a bile duct ligation model. This model resembles the condition of patients who carry the compound mutation in the plectin SH3 domain and rod domain and suffer from intrahepatic cholestasis [122, 123].

8. Novel perspectives on epithelial mechanobiology

Over the past few decades, we have begun to understand the molecular basis of the high mechanical resistance of epithelial tissues. We now recognize that this is primarily achieved through the cytoskeletal networks and cell junctions, which are physically and functionally integrated by cytolinker proteins. In the following paragraphs, we discuss the emerging concepts of epithelial biomechanics, including the significance of the interplay among distinct cytoskeletal networks, the role of cytoskeletal crosslinking in the maintenance of tensional homeostasis, and the adaptive response of epithelia to mechanical stress. Finally, as increasing evidence suggests that plectin can regulate signaling pathways in response to mechanical cues, we propose a concept in which plectin represents a new class of versatile mechanosensors that allow the control of tensional homeostasis required for epithelial integrity.

8.1. Interplay between epithelial actin and keratin cytoskeletal networks

Previous attempts to define the role of cytoskeletal networks in the mechanical homeostasis of epithelial sheets have mainly been limited to their individual components (i.e., actin fibers,

KFs, and MTs), and have therefore provided only a fragmentary insight into the complexity of epithelial mechanics. In recent years, there has been increasing evidence that key features of complex networks arise from the cooperativity of structurally and functionally distinct cytoskeletal subsets that are physically integrated by cytoskeletal crosslinkers [5, 51, 136-138]. Such an interconnectedness is currently proposed for the plectin-mediated crosstalk between F-actin and IFs in motile vimentin-expressing cells, where the VFs provide a load-bearing 'meshwork' that supports the contractile actomyosin system [139-143]. This raises the question of whether a similar functional coupling exists between epithelial keratin and actin networks.

In polarized epithelial cells, KFs and F-actin are tightly intertwined within the circumferential cytoskeletal network [51, 144]. The subplasmalemmal space is dominated by a prominent actin belt, which is closely associated with mature AJs [145, 146] (figure 2). The cortical actin belt (so-called actin cortex) is composed of thick bundles of F-actin that are associated with non-muscle myosin II filaments and running parallel to the cell membrane [145]. This organization of the actin cytoskeleton enables force generation and controls the integrity of intercellular junctions [147-149]. Aligned parallel to cortical F-actin, the subset of interdesmosomal KFs assemble into a keratin circumferential rim [51, 81], thus forming a mechanically robust KF-DSM network. We have found that plectin decorates F-actin structures and colocalizes with circumferential keratin in MDCK cell monolayers [51]. Recently, similar organization has also been described in bladder umbrella cells [150]. Based on these findings, we have proposed a model [3, 51] in which plectin, by virtue of its structure, interacts simultaneously with KFs (via C-terminal IFBD) and cortical F-actin (via N-terminal ABD), thus securing close apposition of both circumferential structures (figure 3).

In the proposed model, plectin integrates keratin and actin subplasmalemmal networks to provide mechanical support for the plasma membrane and cell-cell contacts. Such a hardwired circumferential network has been reported in many epithelial sheet-forming cell types, including keratinocytes [83], intestinal epithelial cells [151], pancreatic exocrine acinar cells [152], bladder umbrella cells [150], or hepatocytes [153, 154] (for review, see [81]). The structural dependence of the keratin circumferential rim on the actin belt became apparent upon removal of plectin-mediated interlinkage. Hence, both genetic (CRISPR/Cas9 system) and pharmacological (plecstatin-1 [155]) inactivation of plectin led to complete disruption of subplasmalemmal keratin structures [51] in epithelial monolayers grown from MDCK cells, BECs, and mammary epithelial cells. Disruption of the actin belt by low doses of actin-depolymerizing drug latrunculin A had a similar effect [51]. As the keratin circumferential rim is closely associated with DSMs, ablation of interdesmosomal KFs resulted in their uneven patterning. Furthermore, DSM-anchored radial keratin spokes collapsed and laterally aligned into thick keratin bundles, as previously observed in various plectin-deficient cell types [39, 85-87, 156]. Together, these observations identified the keratin circumferential rim as a cortical actin belt-dependent framework responsible for the spatial organization of KF-DSM networks.

The physical engagement between peripheral actin and keratin networks has important consequences for cytoskeleton-linked cell-cell junctions, which in turn affect

cytoskeletal networks. For instance, it has recently been shown that KFs coupled to DSMs and the actin cytoskeleton linked to AJs cooperate to enable efficient mechanotransduction in epithelia, where DSM-anchored DP is required to activate RhoA at AJs in a response to tensile stimulation [157]. This is consistent with the previously reported increase in actomyosin contractility in cells where the DSM-KF linkage was strengthened, while disruption of DSM-KF interaction resulted in reduced cellular forces [158]. Since the keratin network itself is required for mechanosignaling [87], and a loss of several DSM components, such as desmoglein 1 [159], desmoglein 2 [160], desmoplakin [161, 162], or plakophilins [163, 164], has been associated with a perturbed actomyosin network, it is evident that the interconnection of KFs and DSMs is important for the organization of the actin cytoskeleton in epithelia.

The state of the actomyosin network simultaneously affects the DSM-KF networks. Partial inhibition of actomyosin contractility in keratinocytes and MDCK cells has been shown to reduce DSM protein turnover, affecting DSM formation and growth [165]. Meanwhile, increased actomyosin contractility, caused by the absence of aPKCλ, resulted in reorganization and reinforcement of KFs and increased mechanical resilience in stratified epithelia [166]. Notably, increased actomyosin contractility conveyed by subplasmalemmal networks to junctions has been proposed as one of the key mechanisms driving epithelial barrier disruption during various pathophysiological conditions, such as mucosal inflammation [51, 167, 168].

Functional cooperativity of peripheral cytoskeletal networks is particularly required in cellular processes that load membranes with internally generated mechanical stress, such as phagocytosis or cytokinesis. Recently, K8 has been reported to interact with F-actin via plectin, to mechanically support the actin fibers and enable successful autophagosome-lysosome fusion [169]. Strikingly, VFs were also shown to form a plectin-dependent subcortical layer to control organization of the actin cortex and the mechanics of the cortex during mitosis [170]. This suggests that the overall concept presented here is not limited to KFs and epithelia. Thus, plectin-mediated crosslinking of peripheral networks is expected to play a central role in the cellular events that require increased mechanical support of the plasma membrane (such as invagination, immune response, cell division, or synapse development).

Although the first lines of evidence suggest cooperativity of the subplasmalemmal KF and actin networks in regulating epithelial mechanics, the direct evidence that physical coupling with KFs determines properties of the actomyosin network at the nanoscale level is currently lacking. This is a surprising gap in the knowledge, as both in vitro and theoretical studies suggest that the actin network architecture and crosslinking levels are key regulators of contractile tension generation (for review, see [171]). While minimal crosslinking is required for contraction, excessive crosslinking limits contractile tension generation [172]. Therefore, the same actin crosslinker (such as α-actinin, fascin, filamin, or fimbrin [173]) can either promote or inhibit the contractility of the actomyosin network [174]. Spatiotemporal changes in the ‘network connectivity‘ [174] facilitate the switching between contraction modes (sarcomeric versus buckling mechanisms [171]) and determine the length scale of

contractions with the magnitude of the developed stresses [171]. Further studies are needed to investigate whether plectin-mediated integration of subplasmalemmal networks can play an analogous role, where local stabilization of F-actin by plectin would allow local modulation of contractility and tension.

8.2. Cytoskeletal crosslinking and tensional homeostasis

Plectin-mediated crosslinking integrates cortical keratin and actin networks to orchestrate the formation of epithelial keratin into a rim-and-spoke configuration [51, 81]. The coupling of mechanically distinct polymers allows a dynamic balance between the contractile forces generated by actomyosin and the mechanical resistance provided by the KFs and is a physical prerequisite for the generation of an isometric tension within the network [175] (figure 3). The crosslinker hardwiring thus facilitates the establishment of a tensional homeostasis that stabilizes cell structures and maintains cell integrity [175-177].

As the actin and keratin networks of neighboring cells within the epithelial sheet are interconnected via intercellular junctions, intrinsically generated forces can propagate on a multicellular scale to generate tissue-scale tensions [178, 179]. Tissue can be considered a so-called ‘tensegrity structure‘ (from tensional integrity [175]), where tensional homeostasis governs the structure of living systems [175-177]. Not surprisingly, several studies have identified plectin-controlled cortical networks as central to tension distribution and maintenance of tensional homeostasis at both the cellular and tissue levels (for review, see [179, 180]). Exposure of epithelial sheets to externally generated forces (for instance, during physical trauma, wound healing, or epithelial morphogenesis) places high demands on the stability of well-formed (i.e., properly crosslinked) cytoskeletal networks and cytoskeleton-linked intercellular junctions.

Experimental techniques for measuring tension in epithelial sheets have expanded dramatically in recent years. Among these, the laser ablation technique has proven to be a very convenient method to study epithelial mechanics without direct contact with the sample. A laser beam is used to cut subcellular, cellular, or supracellular structures (including contractile ring [181], intercellular adhesions [182], ventral stress fibers [183], or cell cortex [184]), where the dynamics of the recoil of the ablated structure is indicative of its tensile properties [185]. Traction force microscopy [186] can be used to determine the force patterns exerted by individual cells, cell colonies, as well as monolayers of epithelial cells. From the force balance between cell-substrate and cell-cell interactions, tensile stress at the cell-cell borders can be calculated using monolayer force microscopy [187-192]. In an alternative approach, Förster resonance energy transfer (FRET)-based tension sensors [193] (mostly derived from cell junction constituents) can be used to quantify tension across intercellular junctions. Such measurements rely on the tension-induced unfolding of the inserted tension module and can provide a single-molecule, pN-scale readouts [194]). Currently, the growing number of junctional tension sensors includes vinculin [193], talin [195], E-cadherin [196], desmoplakin [197], desmoglein [198], or ZO-1 [199]. This rapidly expanding toolbox provides an opportunity for combinatorial experiments, allowing researchers to measure and compare

forces at different cell junction types (such as AJs and DSMs [51]), providing a more detailed insight into the distribution of tension within epithelial sheets.

Only little is known about the forces acting across intercellular junctions in epithelial sheets. However, intrinsic tension at junctions arises when adhesions are coupled to the contractile cytoskeleton. For instance, using the E-cadherin FRET tension sensor, Nicolas Borghi and colleagues [196] demonstrated that the actomyosin cytoskeleton constitutively exerts pN-scale tension on individual E-cadherin molecules at the plasma membrane. When exposed to externally applied stretch, E-cadherin tension increased specifically at intercellular junctions, supporting the hypothesis that AJs transmit both intracellular and extracellular forces. An increase in the tensional loading on E-cadherin was later described not only upon externally applied stretch but also in between epithelial cells within spheroids, spontaneously formed 3D structures with a fluid-filled central lumen [200]. In contrast to actin-associated AJs [179, 196], KF-linked DSMs appear to experience only little (desmoglein FRET sensor [198]) or no (desmoplakin FRET sensor, [197]) strain under steady-state conditions. Under externally applied mechanical stretch, DSMs experience significant tensile stress [197], supporting the widely accepted view that the KF-DSM network is designed to absorb tensile stress and protect the mechanical integrity of epithelial sheets.

Disruption of tensional homeostasis often acts as a major trigger/driver of the biomechanical traits of numerous diseases. Probably the best-documented pathology in which dysregulation of biomechanical properties is associated with the disease onset and progression is cancer [201]. Cortical tension influences several aspects of cancer progression, including cancer cell extrusion [202, 203], epithelial-mesenchymal transition [204], and cell migration plasticity [205]. Furthermore, a tight control of the biomechanics of the cell cortex is required for proper cell division [170, 206, 207]. Further studies have implicated dysregulation of cortical contractility in developmental defects [208] or immunodeficiency [209]. Unsurprisingly, epithelial instability, which is closely associated with several plectinopathic disorders (including skin blistering, obstructive cholestasis, and ulcerative colitis [117]), arises from aberrant cytoskeletal architecture in which tension imbalance may be perceived as causative rather than consequential.

In previous chapters of this review, we reported that the loss of the circumferential keratin rim upon plectin inactivation is associated with prominent bundling of KFs, leading to a reduced number of radial spokes. Interestingly, this pathological reconfiguration of KFs can be alleviated by experimentally reducing actomyosin contractility by blocking myosin II or inhibiting upstream Rho-associated kinase [51]. This suggests that tensile stress rather than the loss of orthogonal filament cross-linking [39] drives the collapse of keratin networks in epithelia with disabled plectin. Furthermore, using the E-cadherin and desmoplakin FRET sensors, we have shown that collapsed keratin spokes with actin fibers transmit increased and unevenly distributed cytoskeletal tension to DSMs and AJs [51]. This then leads to profound destabilization of the cell/tissue mechanics and prevents long-range force propagation [210], which is required for coordinated cytoskeletal stress adaptation [176]. As apparently tensed KFs have also been found in ß4 integrin-inactivated keratinocytes [156], the loss of tensional equilibrium may also account for other cytoskeletal defects such as the

keratin 'fragile network' [211, 212] and the 'sparse network' [213], which were previously linked to skin fragility in EBS patients.

8.3. Adaptive response to mechanical stress

Epithelial sheets are designed to withstand substantial, dynamic external forces in the form of tensile, compressive, and shear stresses. These can be tensile and compressive forces during morphogenesis or organ growth, mechanical friction that affects the epidermis, or shear stresses within internal organs (previously reviewed in [179, 214]). Unlike cancer cells, where mechanical stress often leads to nuclear ruptures associated with DNA damage [215, 216], epithelial monolayers can withstand extreme mechanical stresses that lead to large deformations without signs of damage [61, 217]. This is achieved thanks to an adaptive process, which consists of several layers of protective responses including supracellular alignment, cytoskeletal rearrangement and reinforcement, and nuclear adaptation (mainly chromatin reorganization) [218]. Each level of this adaptive response requires coordinated cytoskeletal regulation and the interplay of well-formed cytoskeletal networks.

When exposed to sustained uniaxial stretching, confluent epithelial sheets undergo supracellular monolayer reorganization, with cells rearranging their longer axes perpendicular to the direction of stretch [218, 219]. Such reorganization is also associated with gradual, time-dependent reorientation of F-actin and nuclei perpendicular to the direction of stretch, and reorientation of AJs at an angle of 45° to the stretch axis [218]. Single cells exposed to two-dimensional stretching also reorient their body axes perpendicular to the applied stretch [220, 221]. This reorientation is both preceded and dependent on cytoskeletal reorientation and reinforcement [222]. Interestingly, all three cytoskeletal networks reorient in response to cyclic stretching with different dynamics. Actin filaments, as the most dynamic cytoskeletal network, reorient first, followed by MTs, and IFs reorient last [222, 223]. When comparing the extent of cytoskeletal reorganization between individual networks, cyclic stretching most affects the actin cytoskeleton, much less MTs, and VFs are mostly only affected by whole-cell reorientation [224]. Surprisingly, while MTs do reorient in response to cyclic stretch, the cell reorientation does not depend on them [225, 226], but rather relies on the integrity of the actomyosin network [225, 227]. Such reorganization and alignment of cytoskeletal networks is thought to minimize passively stored elastic energy, thereby reducing mechanical strain on the cytoskeleton and preventing mechanical damage [228].

The strain-induced spatial reorganization of cytoskeletal networks is complemented by a biochemical response. Cell stiffening and increased mechanical resilience are largely regulated by the polymerization/depolymerization rate of actin fibers, the degree of cytoskeletal crosslinking (both between filaments the of same type and between filaments of different cytoskeletal networks), or changes in the expression level of cytoskeletal components [229]. Mechanical stress, including cyclic stretching, activates the RhoA signaling pathway, leading to the assembly of actin stress fibers and reinforcement of the actomyosin cytoskeleton [148, 218, 230-232]. Remarkably, K18 and the keratin-associated Rho GEF Solo have been shown to be required for efficient force-induced activation of RhoA [233],

demonstrating the interdependence of cytoskeletal networks for efficient adaptation to mechanical stress. Strain-induced activation of RhoA signaling associated with increased cytoskeletal tension and actin polymerization then initiates mechanosensitive transcription through the YAP/TEAD, AP-1, and MRTF/SRF pathways [230, 234, 235]. While MRTF (transcriptional coactivators of SRF transcription factor) activation requires low levels of G-actin, as their interaction with G-actin retains these coactivators in the cytoplasm ([236, 237], reviewed in [238]), nuclear accumulation of YAP is primarily regulated by increased actomyosin contractility [239, 240]. Since the target genes of the YAP/TEAD and MRTF/SRF pathways are mostly cytoskeletal components, the activation of such tension-sensitive transcriptional programs results in the reinforcement of cytoskeletal networks and long-term adaptation to mechanical stress.

Previous studies on stretch-induced cytoskeletal rearrangement have mainly focused on actin stress fibers [213, 222, 232], while the adaptation of KFs [212, 222, 223] has received only little attention. Both increased expression of KF-DSM network components and their reorganization have been described. Remarkably, the stretch-induced expression of KF-DSM network components is dependent on the actomyosin cytoskeleton, as several proteins of the KF-DSM network (including keratin, desmoplakin, desmoglein, and plakophilin) are regulated by mechanosensitive transcription pathways, activated by increased actomyosin tension [241-244]. Mechanical stress also induces reorganization of the KF-DSM network. In keratinocytes, cyclic stretching has been shown to cause the thickening and compaction of keratin spokes [212]. Similarly, in a subset of extremely stretched MDCK cells, KFs form unusually straight and thick spokes that span between the perinuclear region and the plasma membrane [61]. Furthermore, MDCK monolayers in response to stretch substantially enrich KFs at the plasma membrane, where they co-align with DSMs [51]. Subplasmalemmal KF enrichment was accompanied by redistribution of the cytoplasmic pool of plectin towards the circumferential cytoskeleton at cell-cell borders. Taken together, these data suggest that upon stretch, the more abundant plectin integrates newly recruited KFs with the pre-existing circumferential rim and cortical F-actin to reinforce the peripheral cytoskeleton and mechanically challenged intercellular junctions. These experiments also provide the first evidence that plectin-mediated crosslinking of actin and keratin networks is essential for strain-induced cytoskeletal reorganization and reinforcement of cell cohesion, both of which are required for effective epithelial mechanoprotection.

The interconnected network of three distinct cytoskeletal systems, each with unique viscoelastic properties, forms a complex network that must respond to mechanical stress in a coordinated manner. All three cytoskeletal networks contribute to tissue resilience, even under low levels of mechanical stress. However, it is the network of IFs, in particular KFs and lamins, that is responsible for resilience under higher stresses, as both actin filaments and MTs disassemble under strain [245, 246]. Compared to F-actin and MTs, IFs are much more flexible due to the shorter persistence length of the filaments [247, 248]. Keratins are also highly extensible and can be stretched up to three times before breaking [249]. In addition, IFs stiffen under strain [250, 251], which is a key factor in mechanoprotective adaptation. To prevent mechanical damage, the hyperelastic and resilient KFs need to be interconnected with cytoskeletal components that can rapidly recover and restructure (such as the actin

cytoskeleton). Such an interconnected network can dissipate local deformation and slow down the viscoelastic relaxation to protect organelles, including nuclei that encapsulate the genetic material, from mechanical damage, such as membrane rupture or DNA damage. Overall, the multiple layers of adaptive responses to mechanical stress, which include supracellular patterning, cytoskeletal reorganization and stiffening, as well as changes in gene expression and nuclear adaptation, require a coordinated response from the interconnected cytoskeletal networks to effectively protect epithelia from mechanical damage.

8.4. Plectin as a mechanosensor

The adaptive response of epithelia to mechanical stress requires epithelial cells to sense a wide range of both extrinsic and intrinsic forces. These mechanical stimuli typically elicit mechanotransduction responses through stretch-sensitive channels or junction-associated proteins that act as mechanosensors. Mechanosensing involves the ability to translate physical stimuli into biochemical signaling via force-induced modifications or conformational changes (for a general review, see [252, 253]. The capacity of plectin to transmit tension and serve as a scaffolding platform for a multitude of signaling molecules, together with its location within mechanosensitive hubs (such as FAs and HDs), makes plectin an ideal candidate for a highly versatile mechanosensor. Furthermore, the mechanosensitive versatility of plectin could be further extended in an isoform-dependent manner.

The efforts to identify mechanosensitive and mechanotransductive structural elements within the plectin molecule have primarily focused on the evolutionarily conserved PD, consisting of nine spectrin repeats (SR1-SR9), and in particular on the SH3 domain embedded within spectrin repeats [8, 254]. Unlike other SH3 domains that mediate protein-protein interactions, this unique SH3 domain forms an intramolecular autoinhibitory interaction with SR4, blocking its accessibility. However, molecular dynamics simulations showed that physiological pulling forces (~500 pN) lead to the unfolding of SR4 and SR5 repeats, exposing the cryptic SH3 domain for binding [255] (figure 4). Similar results were provided by an analysis of the SH3 domain harbored by PD of *C. elegans* plectin homolog VAB-10A [256]. Interestingly, the force required for SR unfolding is significantly decreased in the absence of the SH3 domain, suggesting that the SH3 domain itself stabilizes the folded conformation [255]. Deletion or mutagenesis of the VAB-10A SH3 domain attenuated mechanosensitive recruitment of adaptor protein GIT-1 and induced embryonic elongation arrest [256]. *In vitro* analysis revealed that the plectin SH3 domain interacts with MT-associated protein 2c (MAP2c), with consequences for MT stabilization and assembly [34]. As no other interactors of this domain have been identified, it is plausible that an alternative mechanism of binding to the plectin SH3 domain requires the involvement of one or more SRs [8]. This is of particular interest for putative mechanosensing since plectin SRs, including SR4-SH3-SH5, participate in the interactions with junctional proteins such as HD integrin β4 [48, 257] and BPAG2 [258] in the epithelia and β-dystroglycan [259] and β-synemin in the skeletal muscle [260].

In this review, we propose a simple concept where plectin crosslinks actin fibers with IFs and recruits them to supramolecular assemblies at the sites of cell attachment either to

the underlying substrate (cell-ECM junctions) or to its neighbor (cell-cell junctions). Upon stretch, the SR4/SH3 interface is released from intramolecular interaction, allowing ligand binding to the unmasked SH3 domain (figure 4). Such interaction can lead to ligand sequestration and reduced availability for downstream signaling events. The scaffolding function of plectin has been well described for the receptor for activated C kinase 1 (RACK1), where it was shown to reduce membrane-associated PKCδ and c-Src activities [39, 40]. In a similar fashion, the SH3 domain of plectin may participate in ligand activation by inducing conformational changes upon binding. It is likely, however, that the same tension-sensitive interactions with modulators of the actin dynamics may be responsible for the signaling crosstalk between the IF and the actin cytoskeletal networks.

Indeed, several studies have implicated plectin in the regulation of cytoskeletal tension, with manipulations of plectin often resulting in altered actin cytoskeleton dynamics. For example, plectin deficiency was shown to increase the actomyosin contractility in various cell lines, including endothelial cells [261], fibroblasts [49], MDCK cells [51], and mouse [87] or human [156] keratinocytes. The signaling cascade affected by plectin depletion, leading to elevated actomyosin contractility, has not yet been identified. However, it is likely to involve activation of the Rho-ROCK signaling pathway, as plectin depletion has been associated with increased RhoA activation [49] and MLC phosphorylation [49, 156]. These findings reflect the ability of plectin to control signaling pathways that regulate actomyosin contractility, potentially providing a feedback loop to control tensional homeostasis with defective IF networks caused by plectin mutation/ablation.

9. Concluding remarks and outlook

Over the last four decades, our understanding of how cytoskeletal crosslinking governs fundamental principles of epithelial mechanobiology has significantly evolved. The development of both constitutive and tissue- or cell type-specific conditional knockout and knock-in mouse models has facilitated the elucidation of the pathophysiology of plectinopathies affecting both simple and (pseudo)stratified epithelia. The combination of high-resolution imaging and force/tension measurements (see Chapters 8.1 and 8.2) have uncovered the relationship between the structural organization of cytoskeletal networks/cell junctions and the spatiotemporal distribution of actomyosin-generated tension. Furthermore, the molecular identity of key players engaged in the cytoskeletal-junctional crosstalk has been identified in endogenous settings by proximity labelling- and FRET-based approaches. In light of these advances, we are only just beginning to appreciate the complexity of the intricate dance between so many molecular interactors that is required to sustain mechanical homeostasis of epithelial sheets.

However, despite all these efforts, there are many interesting challenges for the future. It is essential to elucidate whether and how plectin (and other cytolinkers)-mediated connectivity between KFs and actomyosin networks modulates modes of contraction and local force generation. The identification of a mechanosensitive SR/SH3 plectin module has opened up another intriguing direction for future studies, with mechanosensitive ligands and

downstream signaling pathways yet to be uncovered. Moreover, it seems probable that similar principles of mechanotransduction will apply to other members of the plakin family. This new class of mechanosensors would benefit from the residency among all three cytoskeletal networks, as well as from selective targeting to mechanosensitive hubs such as cell-cell and cell-ECM junctions. Equally important is to decipher the specific functions of plectin isoforms that are (or at least some of them are) recruited to different cellular structures in a tension-dependent manner. This leads to the engaging hypothesis that tension-sensitive plectin isoform patterning would allow fine-tuning of signaling hubs and provide a framework for mechanical memory of the cell. In this scenario, the engagement of diverse isoform subsets, in conjunction with isoform-specific cytoskeletal components and downstream effectors, would help with distinguishing between continuous and sudden mechanical cues, thereby enabling the cell to adapt to repetitive mechanical inputs (such as breathing or peristalsis). Finally, given the critical role plectin plays in cell/tissue mechanics, which is a key aspect of epithelial carcinogenesis, it is surprising that only a few studies aiming at elucidating the role of plectin in cancer have been published so far.

Ethics. This work did not require ethical approval from a human subject or animal welfare committee.

Data accessibility. This article has no additional data.

Declaration of AI use. We have not used AI-assisted technologies in creating this article.

Authors' contributions. M.G.: conceptualization, funding acquisition, project administration, supervision, writing—original draft, visualization, writing—review and editing; Z.O.: writing—original draft, visualization, writing—review and editing; M.P.: writing—original draft, visualization, writing—review and editing; K.K.: visualization, writing—review and editing; J.G.: writing—original draft, visualization, writing—review and editing. All authors gave final approval for publication and agreed to be held accountable for the work performed therein.

Competing interests. We declare we have no competing interests.

Funding. This work was supported by the Czech Science Foundation (GA21-21736S); Institutional Research Project of the Czech Academy of Sciences (RVO 68378050); and National Institute for Cancer Research (Programme EXCELES, LX22NPO5102) - Funded by the European Union - Next Generation EU.

The funding source was not involved in the study design, collection, analysis and interpretation of data, in the writing of the report and in the decision to submit the article for publication.

Tables

Name	Protein function	Described function of interaction	Method	Ref
N-terminal region				
Calmodulin (P1a-specific)	calcium-binding messenger protein	integrin α6β4-plectin complex disruption F-actin-plectin binding inhibition	CaM-Sepharose pulldown, actin co-sedimentation assay, SAXS	[262, 263]
ABD				
ß-dystroglycan	cell adhesion	desmin filament anchorage at sarcolemma	microtiter plate-binding assay	[264]
Dystrophin (Utrophin)	cell adhesion	desmin filament anchorage at sarcolemma	Co-IP, GST pull-down	[264]
F-actin	actin cytoskeleton	F-actin network organization	actin-binding assay	[265]
Integrin ß4	cell adhesion	HD assembly and stability, KF-HD linkage	crystallization, *in vitro* binding assays	[22, 48]
Nesprin-3	actin cytoskeleton	IF-outer nuclear membrane linkage	Co-IP, EM	[29]
PIP2	cell signaling	modulation of plectin-actin binding		[266]
Rapsyn (P1f-specific)	AchR scaffolding protein	IF-AchR linkage, neuromuscular junction organization	Co-IP, GST pull-down, EM	[34]
MT (P1c-specific)	MT cytoskeleton	MT dynamics regulation	MT co-sedimentation assay	[17]
Vimentin	IF cytoskeleton	vimentin network organization	affinity chromatography, crystallization	[15]
Plakin domain				
ß-dystroglycan	cell adhesion	desmin filament anchorage at sarcolemma	microtiter plate-binding assay	[259]
BPAG 1 - BP230 - dystonin	cell adhesion, IF cytoskeleton	HD assembly	Co-IP	[26, 258]
BPAG 2 - BP180 - collagen XVII	cell adhesion	BP180-β4 linkage support, epidermal BMZ organization	Protein-protein binding assay	[25, 258]
CXCR4	chemokine receptor	CXCR4 trafficking and HIV-1 infection promotion	Co-IP, GST pull-down	[267]
Endophilin B2 (P1-specific)	endosome maturation	perinuclear vimentin network organization, nuclear positioning	GST pull-down	[32]
Integrin ß4	cell adhesion	stabilization of KF-HD linkage	yeast two-hybrid binding assay, Co-IP	[48, 257]
MAP1, 2 (SH3 domain)	MT cytoskeleton	prevention of MT-MAPs binding	*in vitro* binding assays	[268, 269]
Fer kinase	receptor Tyr kinase, proto-oncogene	negative regulation of Fer activity	Co-IP	[35]
Rod domain				
Caspase 8	apoptotic process	apoptosis-induced actin cytoskeleton reorganization	*in vitro* cleavage by recombinant caspases	[20]
C-terminal domain				
BRCA-2	DNA repair	prevention of micronuclei formation, centrosomal positioning	GST pull-down	[270]
MNK2	Ser/Thr protein kinase, MAPK signaling	plectin-IF binding modulation	yeast two-hybrid assay, CGP 57380 treatment	[37]

PKA	Ser/Thr protein kinase	plectin-IF binding modulation	yeast two-hybrid assay, H-89 and 8-Br-cAMP treatment	[37]
MT	MT cytoskeleton	MT destabilization	MT binding assay	[16]
Ankyrin	actin cytoskeleton	costamere organization	yeast two-hybrid assay, GST pull-down	[30]
IFBD				
AMPK	Ser/Thr protein kinase, energy sensor	stabilization of AMPK γ1 regulatory subunit complex	yeast two-hybrid assay, Co-IP	[271]
Desmin	IF cytoskeleton	desmin network organization	yeast two-hybrid assay, GST pull-down	[272]
GFAP	IF cytoskeleton	GFAP network organization	Co-IP, *in vitro* overlay assay	[11, 273]
Lamin B	IF cytoskeleton		solid-phase binding assay	[12]
K5/14	IF cytoskeleton	K5/14 network organization	yeast two- and three-hybrid assay, FluoBACE assays	[13, 274]
RACK1	PKC regulation	PKC signaling regulation	yeast two-hybrid assay, Co-IP	[40]
Vimentin	IF cytoskeleton	vimentin network organization	solid-phase binding assay	[11-13]
Unspecified				
Desmoplakin	cell adhesion, IF cytoskeleton	IF-DSM linkage	Co-IP, *in vitro* binding assay	[275]
Dishevelled-2	Wnt signaling	Dishevelled-2 stabilization	IP	[276]
Dlc1	GTPase-activating protein, tumor suppressor		HaloTag pulldown/LC-MS screen, IP	[277]
α-dystrobrevin (P1-specific)	IF cytoskeleton, DGC component	costamere organization	Co-IP, blot overlay assay	[260]
EPLIN	actin cytoskeleton	apical extrusion regulation	Co-IP	[278]
Fer kinase	receptor Tyr kinase, proto-oncogene	negative regulation of Fer activity	Co-IP	[35]
Fodrin	actin and MT cytoskeleton		Co-IP	[275]
FUS	DNA/RNA-binding protein	FUS localization and function regulation	GST pull-down	[279]
GPR56	cell adhesion		MS screen, Co-IP	[280]
K18	IF cytoskeleton	keratin network organization	Co-IP	[281]
K8	IF cytoskeleton	K8-mitochondria linkage, mitophagy promotion	Co-IP	[10]
KPNA2	nuclear importin subunit	lung metastatic potential promotion	SILAC-MS screen	[282]
MT (P1c-specific)	MT cytoskeleton	MT destabilization	MT co-sedimentation assay	[34]
NR3a	glutamate receptor subunit		yeast two-hybrid screen, GST pull-down	[283]

Periplakin	cell adhesion, IF cytoskeleton	keratin network reorganization, cell migration promotion	Co-IP	[27]
Pyk2	non-receptor Tyr kinase	Pyk2 activation via Src, actin ring formation and bone resorption	IP	[38]
RON – MST1R	receptor tyrosine kinase	disruption of plectin-integrin B4 interaction, cell migration promotion	LC-MS screen, IP	[14]
Siah (P1-specific)	E3 ubiquitin-protein ligase		surface plasmon resonance analysis	[284]
α-spectrin	actin cytoskeleton		solid-phase binding assay	[269]
Src	non-receptor kinase, proto-oncogene	Src activation (plectin is in turn phosphorylated by activated Src)	LCMS screen, Halo-tag pull-down	[38, 285]
SNRPA1	alternative splicing mediator	breast cancer promotion via Δexon 31 plectin	EMSA, RBNS	[286]
ß-synemin (P1-specific)	IF cytoskeleton	costamere organization	GST pull-down	[260]
ZO-1	cell adhesion, actin cytoskeleton		MALDI-MS screen	[287]

Table 1. Summary of plectin interacting proteins. CaM, calmodulin; SAXS, small-angle X-ray scattering; Co-IP, co-immunoprecipitation; GST, glutathione S-transferase; EM, electron microscopy; AchR, acetylcholine receptor; BMZ, basement membrane zone; FluoBACE, fluorescent protein-binding assay; LC-MS, liquid chromatography-mass spectrometry; IP, immunoprecipitation; MS, mass spectrometry; SILAC -MS, stable isotope labeling by amino acids in cell culture-mass spectrometry; EMSA, electrophoresis mobility shift assay; RBNS, RNA Bind-n-Seq; MALDI-MS, matrix-assisted laser desorption/ionization-mass spectrometry; DGC, dystrophin glycoprotein complex.

Isoform Uniprot	Transcript name Transcript ID	Isoform-specific model	localization	phenotype	references
P1 *Q15149-1*	*PLEC-201* ENST00000322810.8	P1 knockout mouse; myoblasts	perinuclear	perimyonuclear desmin network integrity, positioning and mobility of myonuclei, mechanotransduction	[31]
		P1 knockout mouse; dermal fibroblasts and T cells		cell migration	[131]
P1a *Q15149-4*	*PLEC-202* *ENST00000345136.8*	P1a-re-expressing plectin-null immortalized keratinocytes	HDs	HD-like protein complexes formation and stabilization	[46]
		EBS-Ogna knock-in mouse; epidermis	HDs	HDs formation and function, HD-KF linkage	[19]
		EBS-Ogna knock-in mouse; primary keratinocytes	HDs	HD-like protein complexes formation and stabilization	[19]
		P1a-re-expressing plectin knockout MDCK cells	cell-cell borders	circumferential keratin rim formation	[51]
P1b *Q15149-5*	*PLEC-203* *ENST00000354589.7*	P1b knockout mouse; primary myoblasts and fibroblasts	mitochondria	mitochondrial morphology, mitochondrion-KF linkage,	[130]
		P1b knockout mouse; dorsal root ganglion neurons	mitochondria	mitochondrial subcellular positioning, mobility and morphology	[17]
		P1b knockout mouse; muscle fibers	mitochondria	mitochondrial fusion-fission machinery	[288]
P1c *Q15149-2*	*PLEC-208* *ENST00000436759.6*	P1c-re-expressing plectin-null immortalized primary keratinocytes	cell periphery, MTs		[46]
		P1c knockout mouse; dorsal root ganglia and hippocampal neurons	MTs	axonal MT dynamics regulation, neuritogenesis regulation, MT-mediated mitochondrial and vesicular transport, growth cone morphology; effect on long-term memory, cognitive functions and pain sensitivity of P1c knockout mice	[17]
		P1c knockout mouse; sciatic nerves	MTs	number and thickness of motor nerve fibers, motor nerve conduction velocity	[132]
P1d *Q15149-7*	*PLEC-207* *ENST00000398774.6*	P1d knockout mouse; muscles	Z-discs	costamere alignment	[289]
		P1d knockout mouse; muscles		mitochondrial distribution, desmin networks arrangement	[288]
P1f *Q15149-9*	*PLEC-205* *ENST00000356346.7*	P1f-re-expressing plectin knockout MDCK cells	cell-cell borders	circumferential keratin rim formation	[51]
		P1f-re-expressing plectin knockout fibroblasts	FAs	FA dynamics regulation, VF precursor anchorage	[49]
P1k *A0A8I5KUE3*	PLEC-215 ENST00000693060.1	P1k-expressing plectin knockdown SW480 colon carcinoma cells	podosome-like adhesions	F-actin assembly and podosome-like adhesion site formation	[290]

Table 2. Summary of key features of plectin isoforms and their functions.

Figure legends

Figure 1. Schematic representation of plectin transcripts and encoded protein domains. **(A)** Schematics of the plectin transcripts. Twelve first exons spliced into exon 2 are shown. Untranslated regions (light gray) and two optionally spliced exons, 2a and 3a (red), are indicated. **(B)** Schematics of the plectin protein. The N-termini of isoforms predominantly expressed in epithelia are indicated (black). The N -terminal domain contains the actin-binding domain (ABD; yellow) and plakin domain (PD; light blue), which contains the non-canonical SH3 domain (dark blue). Alternative splicing of exon 31 encoding the rod domain of plectin (pink) generates the rodless isoform. The C -terminal domain consists of six plectin repeat domains (PRD; gray), with the linker region of the fifth PRD containing an IF-binding domain (IFBD, green). The corresponding interacting partners are indicated below. The figure is not drawn to scale.

Figure 2. Schematic representation of plectin localization and plectin -mediated organization of cytoskeletal networks in epithelial cells. Plectin (black) crosslinks KFs (green) with the actin fibers (orange). Plectin also anchors cytoskeletal networks to cell junctions, such as hemidesmosomes (HDs, blue; cell-ECM adhesion) and desmosomes (DSMs, purple; cell-cell adhesion), shown in more detail on the right. The localization of major plectin isoforms (black circles) is indicated. TJ, tight junction (orange); AJ, adherens junction (red).

Figure 3. Schematic representation of the proposed model for plectin -mediated cytoskeletal organization and tensional homeostasis. In epithelial monolayers, the perinuclear KFs connect to the cell periphery via keratin radial spokes (light green) that are anchored to the membrane at DSMs (purple). Contractile actomyosin networks (orange) closely align with the plasma membrane. Plectin (black) interacts (via its N -terminus) with cortical F-actin and facilitates the formation of a circumferential keratin rim (dark green) that interconnects individual DSMs. Together, the interlinked web of cytoskeletal networks has the ability to dissipate local deformations, support the plasma membrane, and protect the epithelial sheets from mechanical d amage.

Figure 4. Schematic representation of plectin as a new class of cytolinker -based mechanosensors. Plectin crosslinks IFs and contractile actomyosin networks and recruits them to tension-sensitive junctions (such as FAs, HDs, or DSMs; not shown, for details see Chapters 2, 5, and 8.4). Increased tension resulting from intrinsic and extrinsic forces leads to unfolding of SR4 and SR5 within the plectin PD (middle box; PDB: 3PE0 [8]), releasing the SR4/SH3 interface from inhibitory intramolecular interactions. The unmasked SR4/SH3 interface allows the binding of ligands (such as MAP2) that regulate the dynamics of individual cytoskeletal networks (right box). Theoretically, a similar mechanism can be envisaged for the regulation of actomyosin contractility or flexibility/stiffness of IFs.

References

1 Ruhrberg, C., Watt, F. M. 1997 The plakin family: versatile organizers of cytoskeletal architecture. *Curr Opin Genet Dev*. **7**, 392-397. (10.1016/s0959-437x(97)80154-2)

2 Wiche, G., Osmanagic-Myers, S., Castanon, M. J. 2015 Networking and anchoring through plectin: a key to IF functionality and mechanotransduction. *Curr Opin Cell Biol*. **32**, 21-29. (10.1016/j.ceb.2014.10.002)

3 Prechova, M., Korelova, K., Gregor, M. 2023 Plectin. *Curr Biol*. **33**, R128-R130. (10.1016/j.cub.2022.12.061)

4 Wiche, G., Herrmann, H., Leichtfried, F., Pytela, R. 1982 Plectin: a high-molecular-weight cytoskeletal polypeptide component that copurifies with intermediate filaments of the vimentin type. *Cold Spring Harb Symp Quant Biol*. **46 Pt 1**, 475-482. (10.1101/sqb.1982.046.01.044)

5 Bouameur, J. E., Favre, B., Borradori, L. Plakins, a versatile family of cytolinkers: Roles in skin integrity and in human diseases. *Journal of Investigative Dermatology*: Nature Publishing Group 2014:885-894.

6 Leung, C. L., Green, K. J., Liem, R. K. H. Plakins: A family of versatile cytolinker proteins. *Trends in Cell Biology*: Elsevier 2002:37-45.

7 Jefferson, J. J., Ciatto, C., Shapiro, L., Liem, R. K. H. 2007 Structural Analysis of the Plakin Domain of Bullous Pemphigoid Antigen1 (BPAG1) Suggests that Plakins Are Members of the Spectrin Superfamily. *Journal of Molecular Biology*. **366**, 244-257. (10.1016/j.jmb.2006.11.036)

8 Ortega, E., Buey, R. M., Sonnenberg, A., De Pereda, J. M. 2011 The structure of the plakin domain of plectin reveals a non-canonical SH3 domain interacting with its fourth spectrin repeat. *Journal of Biological Chemistry*. **286**, 12429-12438. (10.1074/jbc.M110.197467)

9 Sonnenberg, A., Rojas, A. M., de Pereda, J. M. 2007 The Structure of a Tandem Pair of Spectrin Repeats of Plectin Reveals a Modular Organization of the Plakin Domain. *Journal of Molecular Biology*. **368**, 1379-1391. (10.1016/j.jmb.2007.02.090)

10 Baek, A., Son, S., Baek, Y. M., Kim, D. E. 2021 KRT8 (keratin 8) attenuates necrotic cell death by facilitating mitochondrial fission-mediated mitophagy through interaction with PLEC (plectin). *Autophagy*. (10.1080/15548627.2021.1897962)

11 Foisner, R., Leichtfried, F. E., Herrmann, H., Small, J. V., Lawson, D., Wiche, G. 1988 Cytoskeleton-associated plectin: In situ localization, in vitro reconstitution, and binding to immobilized intermediate filament proteins. *Journal of Cell Biology*. **106**, 723-733. (10.1083/jcb.106.3.723)

12 Foisner, R., Traub, P., Wiche, G. 1991 Protein kinase A- And protein kinase C-regulated interaction of plectin with lamin B and vimentin. *P Natl Acad Sci USA*. **88**, 3812-3816. (10.1073/pnas.88.9.3812)

13 Steinböck, F. A., Nikolic, B., Coulombe, P. A., Fuchs, E., Traub, P., Wiche, G. 2000 Dose-dependent linkage, assembly inhibition and disassembly of vimentin and cytokeratin 5/14 filaments through plectin's intermediate filament-binding domain. *Journal of Cell Science*. **113**, 483-491. (10.1242/jcs.113.3.483)

14 Yu, P. T., Babicky, M., Jaquish, D., French, R., Marayuma, K., Mose, E., Niessen, S., Hoover, H., Shields, D., Cheresh, D*., et al.* 2012 The RON-receptor regulates pancreatic cancer cell migration through phosphorylation-dependent breakdown of the hemidesmosome. *International Journal of Cancer*. **131**, 1744-1754. (10.1002/ijc.27447)

15 Sevcik, J., Urbanikova, L. U., Kostan, J., Janda, L., Wiche, G. 2004 Actin-binding domain of mouse plectin: Crystal structure and binding to vimentin. *European Journal of Biochemistry*. **271**, 1873-1884. (10.1111/j.1432-1033.2004.04095.x)

16 Sun, D., Leung, C. L., Liem, R. K. H. 2001 Characterization of the microtubule binding domain of microtubule actin crosslinking factor (MACF): Identification of a novel group of microtubule associated proteins. *Journal of Cell Science*. **114**, 161-172. (10.1242/jcs.114.1.161)

17 Valencia, R. G., Mihailovska, E., Winter, L., Bauer, K., Fischer, I., Walko, G., Jorgacevski, J., Potokar, M., Zorec, R., Wiche, G. 2021 Plectin dysfunction in neurons leads to tau accumulation on microtubules affecting neuritogenesis, organelle trafficking, pain sensitivity and memory. *Neuropathol Appl Neurobiol*. **47**, 73-95. (10.1111/nan.12635)

18 Foisner, R., Wiche, G. 1987 Structure and hydrodynamic properties of plectin molecules. *J Mol Biol*. **198**, 515-531. (10.1016/0022-2836(87)90297-x)

19 Walko, G., Vukasinovic, N., Gross, K., Fischer, I., Sibitz, S., Fuchs, P., Reipert, S., Jungwirth, U., Berger, W., Salzer, U*., et al.* 2011 Targeted proteolysis of plectin isoform 1a accounts for hemidesmosome dysfunction in mice mimicking the dominant skin blistering disease EBS-Ogna. *PLoS Genet*. **7**, e1002396. (10.1371/journal.pgen.1002396)

20 Stegh, A. H., Herrmann, H., Lampel, S., Weisenberger, D., Andrä, K., Seper, M., Wiche, G., Krammer, P. H., Peter, M. E. 2000 Identification of the Cytolinker Plectin as a Major Early In Vivo Substrate for Caspase 8 during CD95- and Tumor Necrosis Factor Receptor-Mediated Apoptosis. *Molecular and Cellular Biology*. **20**, 5665-5679. (10.1128/mcb.20.15.5665-5679.2000)

21 Elliott, C. E., Becker, B., Oehler, S., Castanon, M. J., Hauptmann, R., Wiche, G. 1997 Plectin transcript diversity: identification and tissue distribution of variants with distinct first coding exons and rodless isoforms. *Genomics*. **42**, 115-125. (10.1006/geno.1997.4724)

22 de Pereda, J. M., Lillo, M. P., Sonnenberg, A. 2009 Structural basis of the interaction between integrin alpha6beta4 and plectin at the hemidesmosomes. *EMBO J*. **28**, 1180-1190. (10.1038/emboj.2009.48)

23 Rezniczek, G. A., De Pereda, J. M., Reipert, S., Wiche, G. 1998 Linking integrin α6β4-based cell adhesion to the intermediate filament cytoskeleton: Direct interaction between the β4 subunit and plectin at multiple molecular sites. *Journal of Cell Biology*. **141**, 209-225. (10.1083/jcb.141.1.209)

24 Koster, J., Geerts, D., Favre, B., Borradori, L., Sonnenberg, A. 2003 Analysis of the interactions between BP180, BP230, plectin and the integrin α6β4 important for hemidesmosome assembly. *Journal of Cell Science*. **116**, 387-399. (10.1242/jcs.00241)

25 Natsuga, K., Nishie, W., Nishimura, M., Shinkuma, S., Watanabe, M., Izumi, K., Nakamura, H., Hirako, Y., Shimizu, H. 2017 Loss of interaction between plectin and type XVII collagen results in epidermolysis bullosa simplex. *Human Mutation*. **38**, 1666-1670. (10.1002/humu.23344)

26 Steiner-Champliaud, M. F., Schneider, Y., Favre, B., Paulhe, F., Praetzel-Wunder, S., Faulkner, G., Konieczny, P., Raith, M., Wiche, G., Adebola, A*., et al.* 2010 BPAG1 isoform-b: Complex distribution pattern in striated and heart muscle and association with plectin and α-actinin. *Experimental Cell Research*. **316**, 297-313. (10.1016/j.yexcr.2009.11.010)

27 Boczonadi, V., McInroy, L., Maatta, A. 2007 Cytolinker cross-talk: periplakin N-terminus interacts with plectin to regulate keratin organisation and epithelial migration. *Exp Cell Res*. **313**, 3579-3591. (10.1016/j.yexcr.2007.07.005)

28 Chen, V. C., Li, X., Perreault, H., Nagy, J. I. 2006 Interaction of zonula occludens-1 (ZO-1) with α-actinin-4: Application of functional proteomics for identification of PDZ domain-associated proteins. *Journal of Proteome Research*. **5**, 2123-2134. (10.1021/pr060216l)

29 Wilhelmsen, K., Litjens, S. H., Kuikman, I., Tshimbalanga, N., Janssen, H., van den Bout, I., Raymond, K., Sonnenberg, A. 2005 Nesprin-3, a novel outer nuclear membrane protein, associates with the cytoskeletal linker protein plectin. *J Cell Biol*. **171**, 799-810. (10.1083/jcb.200506083)

30 Maiweilidan, Y., Klauza, I., Kordeli, E. 2011 Novel interactions of ankyrins-G at the costameres: The muscle-specific Obscurin/Titin-Binding-related Domain (OTBD) binds plectin and filamin C. *Experimental Cell Research*. **317**, 724-736. (10.1016/j.yexcr.2011.01.002)

31 Staszewska, I., Fischer, I., Wiche, G. 2015 Plectin isoform 1-dependent nuclear docking of desmin networks affects myonuclear architecture and expression of mechanotransducers. *Hum Mol Genet*. **24**, 7373-7389. (10.1093/hmg/ddv438)

32 Vannier, C., Pesty, A., San-Roman, M. J., Schmidt, A. A. 2013 The Bin/amphiphysin/Rvs (BAR) domain protein endophilin B2 interacts with plectin and controls perinuclear cytoskeletal architecture. *J Biol Chem*. **288**, 27619-27637. (10.1074/jbc.M113.485482)

33 Kasai, N., Kadeer, A., Kajita, M., Saitoh, S., Ishikawa, S., Maruyama, T., Fujita, Y. 2018 The paxillin-plectin-EPLIN complex promotes apical elimination of RasV12-transformed cells by modulating HDAC6-regulated tubulin acetylation. *Sci Rep*. **8**, 2097. (10.1038/s41598-018-20146-1)

34 Valencia, R. G., Walko, G., Janda, L., Novacek, J., Mihailovska, E., Reipert, S., Andrä-Marobela, K., Wiche, G. 2013 Intermediate filament-associated cytolinker plectin 1c destabilizes microtubules in keratinocytes. *Molecular Biology of the Cell*. **24**, 768-784. (10.1091/mbc.E12-06-0488)

35 Lunter, P. C., Wiche, G. 2002 Direct binding of plectin to Fer kinase and negative regulation of its catalytic activity. *Biochemical and Biophysical Research Communications*. **296**, 904-910. (10.1016/S0006-291X(02)02007-7)

36 Gregor, M., Zeöld, A., Oehler, S., Marobela, K. A., Fuchs, P., Weigel, G., Hardie, D. G., Wiche, G. 2006 Plectin scaffolds recruit energy-controlling AMP-activated protein kinase (AMPK) in differentiated myofibres. *Journal of Cell Science*. **119**, 1864-1875. (10.1242/jcs.02891)

37 Bouameur, J. E., Schneider, Y., Begre, N., Hobbs, R. P., Lingasamy, P., Fontao, L., Green, K. J., Favre, B., Borradori, L. 2013 Phosphorylation of serine 4,642 in the C-terminus of plectin by MNK2 and PKA modulates its interaction with intermediate filaments. *J Cell Sci*. **126**, 4195-4207. (10.1242/jcs.127779)

38 Matsubara, T., Yaginuma, T., Addison, W. N., Fujita, Y., Watanabe, K., Yoshioka, I., Hikiji, H., Maki, K., Baron, R., Kokabu, S. 2020 Plectin stabilizes microtubules during osteoclastic bone resorption by acting as a scaffold for Src and Pyk2. *Bone*. **132**, 115209-115209. (10.1016/j.bone.2019.115209)

39 Osmanagic-Myers, S., Gregor, M., Walko, G., Burgstaller, G., Reipert, S., Wiche, G. 2006 Plectin-controlled keratin cytoarchitecture affects MAP kinases involved in cellular stress response and migration. *J Cell Biol*. **174**, 557-568. (10.1083/jcb.200605172)

40 Osmanagic-Myers, S., Wiche, G. 2004 Plectin-RACK1 (receptor for activated C kinase 1) scaffolding: A novel mechanism to regulate protein kinase C activity. *Journal of Biological Chemistry*. **279**, 18701-18710. (10.1074/jbc.M312382200)

41 Liu, C. G., Maercker, C., Castanon, M. J., Hauptmann, R., Wiche, G. 1996 Human plectin: organization of the gene, sequence analysis, and chromosome localization (8q24). *Proc Natl Acad Sci U S A*. **93**, 4278-4283. (10.1073/pnas.93.9.4278)

42 Rezniczek, G. A., Abrahamsberg, C., Fuchs, P., Spazierer, D., Wiche, G. 2003 Plectin 5′-transcript diversity: Short alternative sequences determine stability of gene products, initiation of translation and subcellular localization of isoforms. *Human Molecular Genetics*. **12**, 3181-3194. (10.1093/hmg/ddg345)

43 Kostan, J., Gregor, M., Walko, G., Wiche, G. 2009 Plectin isoform-dependent regulation of keratin-integrin α6β4 anchorage via Ca2+/calmodulin. *Journal of Biological Chemistry*. **284**, 18525-18536. (10.1074/jbc.M109.008474)

44 Burgstaller, G., Gregor, M., Winter, L., Wiche, G. 2010 Keeping the vimentin network under control: cell-matrix adhesion-associated plectin 1f affects cell shape and polarity of fibroblasts. *Mol Biol Cell*. **21**, 3362-3375. (10.1091/mbc.E10-02-0094)

45 Fuchs, P., Zorer, M., Rezniczek, G. A., Spazierer, D., Oehler, S., Castanon, M. J., Hauptmann, R., Wiche, G. 1999 Unusual 5' transcript complexity of plectin isoforms: novel tissue-specific exons modulate actin binding activity. *Hum Mol Genet*. **8**, 2461-2472. (10.1093/hmg/8.13.2461)

46 Andrä, K., Kornacker, I., Jörgl, A., Zörer, M., Spazierer, D., Fuchs, P., Fischer, I., Wiche, G. 2003 Plectin-isoform-specific rescue of hemidesmosomal defects in plectin (-/-) keratinocytes. *Journal of Investigative Dermatology*. **120**, 189-197. (10.1046/j.1523-1747.2003.12027.x)

47 Ketema, M., Wilhelmsen, K., Kuikman, I., Janssen, H., Hodzic, D., Sonnenberg, A. 2007 Requirements for the localization of nesprin-3 at the nuclear envelope and its interaction with plectin. *Journal of Cell Science*. **120**, 3384-3394. (10.1242/jcs.014191)

48 Rezniczek, G. A., de Pereda, J. M., Reipert, S., Wiche, G. 1998 Linking integrin alpha6beta4-based cell adhesion to the intermediate filament cytoskeleton: direct interaction between the beta4 subunit and plectin at multiple molecular sites. *J Cell Biol*. **141**, 209-225. (10.1083/jcb.141.1.209)

49 Gregor, M., Osmanagic-Myers, S., Burgstaller, G., Wolfram, M., Fischer, I., Walko, G., Resch, G. P., Jorgl, A., Herrmann, H., Wiche, G. 2014 Mechanosensing through focal adhesion-anchored intermediate filaments. *FASEB J*. **28**, 715-729. (10.1096/fj.13-231829)

50 Windoffer, R., Kölsch, A., Wöll, S., Leube, R. E. 2006 Focal adhesions are hotspots for keratin filament precursor formation. *Journal of Cell Biology*. **173**, 341-348. (10.1083/jcb.200511124)

51 Prechova, M., Adamova, Z., Schweizer, A. L., Maninova, M., Bauer, A., Kah, D., Meier-Menches, S. M., Wiche, G., Fabry, B., Gregor, M. 2022 Plectin-mediated cytoskeletal crosstalk controls cell tension and cohesion in epithelial sheets. *J Cell Biol*. **221**, (10.1083/jcb.202105146)

52 Salas, P. J., Forteza, R., Mashukova, A. 2016 Multiple roles for keratin intermediate filaments in the regulation of epithelial barrier function and apico-basal polarity. *Tissue Barriers*. **4**, e1178368. (10.1080/21688370.2016.1178368)

53 Hatzfeld, M., Keil, R., Magin, T. M. 2017 Desmosomes and Intermediate Filaments: Their Consequences for Tissue Mechanics. *Cold Spring Harb Perspect Biol*. **9**, (10.1101/cshperspect.a029157)

54 Jacob, J. T., Coulombe, P. A., Kwan, R., Omary, M. B. 2018 Types I and II Keratin Intermediate Filaments. *Cold Spring Harb Perspect Biol*. **10**, (10.1101/cshperspect.a018275)

55 Quinlan, R. A., Hatzfeld, M., Franke, W. W., Lustig, A., Schulthess, T., Engel, J. 1986 Characterization of dimer subunits of intermediate filament proteins. *Journal of Molecular Biology*. **192**, 337-349. (10.1016/0022-2836(86)90369-4)

56 Steinert, P. M., Gullino, M. I. 1976 Bovine epidermal keratin filament assembly in vitro. *Biochemical and Biophysical Research Communications*. **70**, 221-227. (10.1016/0006-291X(76)91131-1)

57 Herrmann, H., Wedig, T., Porter, R. M., Lane, B., Aebi, U. Year Characterization of early assembly intermediates of recombinant human keratins. Journal of Structural Biology; 2002: Academic Press Inc.; 2002. p. 82-96.

58 Kreplak, L., Bär, H., Leterrier, J. F., Herrmann, H., Aebi, U. 2005 Exploring the mechanical behavior of single intermediate filaments. *Journal of Molecular Biology*. **354**, 569-577. (10.1016/j.jmb.2005.09.092)

59 Lichtenstern, T., Mücke, N., Aebi, U., Mauermann, M., Herrmann, H. 2012 Complex formation and kinetics of filament assembly exhibited by the simple epithelial keratins K8 and K18. *Journal of Structural Biology*. **177**, 54-62. (10.1016/j.jsb.2011.11.003)

60 Pawelzyk, P., Mücke, N., Herrmann, H., Willenbacher, N. 2014 Attractive interactions among intermediate filaments determine network mechanics in vitro. *PLoS ONE*. **9**, (10.1371/journal.pone.0093194)

61 Latorre, E., Kale, S., Casares, L., Gomez-Gonzalez, M., Uroz, M., Valon, L., Nair, R. V., Garreta, E., Montserrat, N., Del Campo, A.*, et al.* 2018 Active superelasticity in three-dimensional epithelia of controlled shape. *Nature*. **563**, 203-208. (10.1038/s41586-018-0671-4)

62 Christopher Chamcheu, J., Siddiqui, I. A., Syed, D. N., Adhami, V. M., Liovic, M., Mukhtar, H. 2011 Keratin gene mutations in disorders of human skin and its appendages. *Archives of Biochemistry and Biophysics*. **508**, 123-137. (10.1016/j.abb.2010.12.019)

63 Omary, M. B., Ku, N. O., Strnad, P., Hanada, S. 2009 Toward unraveling the complexity of simple epithelial keratins in human disease. *J Clin Invest*. **119**, 1794-1805. (10.1172/JCI37762)

64 Lloyd, C., Yu, Q. C., Cheng, J., Turksen, K., Degenstein, L., Hutton, E., Fuchs, E. 1995 The basal keratin network of stratified squamous epithelia: Defining K15 function in the absence of K14. *Journal of Cell Biology*. **129**, 1329-1344. (10.1083/jcb.129.5.1329)

65 Peters, B., Kirfel, J., Büssow, H., Vidal, M., Magin, T. M. 2001 Complete cytolysis and neonatal lethality in keratin 5 knockout mice reveal its fundamental role in skin integrity and in epidermolysis bullosa simplex. *Molecular Biology of the Cell*. **12**, 1775-1789. (10.1091/mbc.12.6.1775)

66 Coulombe, P. A., Kerns, M. L., Fuchs, E. Epidermolysis bullosa simplex: A paradigm for disorders of tissue fragility. *Journal of Clinical Investigation*: The American Society for Clinical Investigation 2009:1784-1793.

67 Lane, E. B., McLean, W. H. I. 2004 Keratins and skin disorders. *The Journal of Pathology*. **204**, 355-366. (10.1002/path.1643)

68 Baribault, H., Penner, J., Iozzo, R. V., Wilson-Heiner, M. 1994 Colorectal hyperplasia and inflammation in keratin 8-deficient FVB/N mice. *Genes and Development*. **8**, 2964-2973. (10.1101/gad.8.24.2964)

69 Misiorek, J. O., Lähdeniemi, I. A. K., Nyström, J. H., Paramonov, V. M., Gullmets, J. A., Saarento, H., Rivero-Müller, A., Husøy, T., Taimen, P., Toivola, D. M. 2016 Keratin 8-deletion induced colitis predisposes to murine colorectal cancer enforced by the inflammasome and IL-22 pathway. *Carcinogenesis*. **37**, 777-786. (10.1093/carcin/bgw063)

70 Owens, D. W., Wilson, N. J., Hill, A. J. M., Rugg, E. L., Porter, R. M., Hutcheson, A. M., Quinlan, R. A., van Heel, D., Parkes, M., Jewell, D. P*., et al.* 2004 Human keratin 8 mutations that disturb filament assembly observed in inflammatory bowel disease patients. *Journal of Cell Science*. **117**, 1989-1999. (10.1242/jcs.01043)

71 Zupancic, T., Stojan, J., Lane, E. B., Komel, R., Bedina-Zavec, A., Liovic, M. 2014 Intestinal cell barrier function in vitro is severely compromised by keratin 8 and 18 mutations identified in patients with inflammatory bowel disease. *PLoS ONE*. **9**, (10.1371/journal.pone.0099398)

72 Ku, N. O., Michie, S., Oshima, R. G., Omary, M. B. 1995 Chronic hepatitis, hepatocyte fragility, and increased soluble phosphoglycokeratins in transgenic mice expressing a keratin 18 conserved arginine mutant. *Journal of Cell Biology*. **131**, 1303-1314. (10.1083/jcb.131.5.1303)

73 Ku, N. O., Michie, S. A., Soetikno, R. M., Resurreccion, E. Z., Broome, R. L., Oshima, R. G., Omary, M. B. 1996 Susceptibility to hepatotoxicity in transgenic mice that express a dominant-negative human keratin 18 mutant. *Journal of Clinical Investigation*. **98**, 1034-1046. (10.1172/JCI118864)

74 Loranger, A., Duclos, S., Grenier, A., Price, J., Wilson-Heiner, M., Baribault, H., Marceau, N. 1997 Simple epithelium keratins are required for maintenance of hepatocyte integrity - PubMed. *Am J Pathol.* **151**, 1673-1683.

75 Magin, T. M., Schröder, R., Leitgeb, S., Wanninger, F., Zatloukal, K., Grund, C., Melton, D. W. 1998 Lessons from keratin 18 knockout mice: Formation of novel keratin filaments, secondary loss of keratin 7 and accumulation of liver-specific keratin 8-positive aggregates. *Journal of Cell Biology*. **140**, 1441-1451. (10.1083/jcb.140.6.1441)

76 Toivola, D. M., Omary, M. B., Ku, N. O., Peltola, O., Baribault, H., Eriksson, J. E. 1998 Protein phosphatase inhibition in normal and keratin 8/18 assembly- incompetent mouse strains supports a functional role of keratin intermediate filaments in preserving hepatocyte integrity. *Hepatology*. **28**, 116-128. (10.1002/hep.510280117)

77 Ku, N.-O., Gish, R., Wright, T. L., Omary, M. B. 2001 Keratin 8 Mutations in Patients with Cryptogenic Liver Disease. *New England Journal of Medicine*. **344**, 1580-1587. (10.1056/nejm200105243442103)

78 Schöniger-Hekele, M., Petermann, D., Müller, C. 2006 Mutation of keratin 8 in patients with liver disease. *Journal of Gastroenterology and Hepatology (Australia)*. **21**, 1466-1469. (10.1111/j.1440-1746.2006.04392.x)

79 Usachov, V., Urban, T. J., Fontana, R. J., Gross, A., Iyer, S., Omary, M. B., Strnad, P. 2015 Prevalence of genetic variants of keratins 8 and 18 in patients with drug-induced liver injury. *BMC Medicine*. **13**, (10.1186/s12916-015-0418-0)

80 Zierden, M., Penner, A. H., Manuel, M. R., Weferling, M., Drebber, U., Stift, J., Fries, J. W. U., Odenthal, M., Rosenkranz, S., Dienes, H. P. 2012 Keratin 8 variants are associated with cryptogenic hepatitis. *Virchows Archiv*. **460**, 389-397. (10.1007/s00428-012-1216-0)

81 Quinlan, R. A., Schwarz, N., Windoffer, R., Richardson, C., Hawkins, T., Broussard, J. A., Green, K. J., Leube, R. E. 2017 A rim-and-spoke hypothesis to explain the biomechanical roles for cytoplasmic intermediate filament networks. *J Cell Sci*. **130**, 3437-3445. (10.1242/jcs.202168)

82 Farquhar, M. G., Palade, G. E. 1963 Junctional complexes in various epithelia. *J Cell Biol*. **17**, 375-412. (10.1083/jcb.17.2.375)

83 Troyanovsky, S. M., Eshkind, L. G., Troyanovsky, R. B., Leube, R. E., Franke, W. W. 1993 Contributions of cytoplasmic domains of desmosomal cadherins to desmosome assembly and intermediate filament anchorage. *Cell*. **72**, 561-574. (10.1016/0092-8674(93)90075-2)

84 Ketema, M., Kreft, M., Secades, P., Janssen, H., Sonnenberg, A. 2013 Nesprin-3 connects plectin and vimentin to the nuclear envelope of Sertoli cells but is not required for Sertoli cell function in spermatogenesis. *Molecular Biology of the Cell*. **24**, 2454-2466. (10.1091/mbc.E13-02-0100)

85 Moch, M., Windoffer, R., Schwarz, N., Pohl, R., Omenzetter, A., Schnakenberg, U., Herb, F., Chaisaowong, K., Merhof, D., Ramms, L*., et al.* 2016 Effects of Plectin Depletion on Keratin Network Dynamics and Organization. *PLoS One*. **11**, e0149106. (10.1371/journal.pone.0149106)

86 Jirouskova, M., Nepomucka, K., Oyman-Eyrilmez, G., Kalendova, A., Havelkova, H., Sarnova, L., Chalupsky, K., Schuster, B., Benada, O., Miksatkova, P*., et al.* 2018 Plectin controls biliary tree architecture and stability in cholestasis. *J Hepatol*. **68**, 1006-1017. (10.1016/j.jhep.2017.12.011)

87 Laly, A. C., Sliogeryte, K., Pundel, O. J., Ross, R., Keeling, M. C., Avisetti, D., Waseem, A., Gavara, N., Connelly, J. T. 2021 The keratin network of intermediate filaments regulates keratinocyte rigidity sensing and nuclear mechanotransduction. *Sci Adv*. **7**, (10.1126/sciadv.abd6187)

88 Wang, W., Zuidema, A., Molder, L. t., Nahidiazar, L., Hoekman, L., Schmidt, T., Coppola, S., Sonnenberg, A. 2020 Hemidesmosomes modulate force generation via focal adhesions. *Journal of Cell Biology*. **219**, (10.1083/jcb.201904137)

89 Kah, D., Winterl, A., Přechová, M., Schöler, U., Schneider, W., Friedrich, O., Gregor, M., Fabry, B. 2021 A low-cost uniaxial cell stretcher for six parallel wells. *HardwareX*. **9**, e00162. (10.1016/j.ohx.2020.e00162)

90 Krausova, A., Buresova, P., Sarnova, L., Oyman-Eyrilmez, G., Skarda, J., Wohl, P., Bajer, L., Sticova, E., Bartonova, L., Pacha, J.*, et al.* 2021 Plectin ensures intestinal epithelial integrity and protects colon against colitis. *Mucosal Immunol*. **14**, 691-702. (10.1038/s41385-021-00380-z)

91 Fuchs, E., Green, H. 1980 Changes in keratin gene expression during terminal differentiation of the keratinocyte. *Cell*. **19**, 1033-1042. (10.1016/0092-8674(80)90094-X)

92 Moll, R., Franke, W. W., Schiller, D. L., Geiger, B., Krepler, R. The catalog of human cytokeratins: Patterns of expression in normal epithelia, tumors and cultured cells. *Cell*: Cell 1982:11-24.

93 Guldiken, N., Kobazi Ensari, G., Lahiri, P., Couchy, G., Preisinger, C., Liedtke, C., Zimmermann, H. W., Ziol, M., Boor, P., Zucman-Rossi, J.*, et al.* 2016 Keratin 23 is a stress-inducible marker of mouse and human ductular reaction in liver disease. *Journal of Hepatology*. **65**, 552-559. (10.1016/j.jhep.2016.04.024)

94 Omary, M. B., Ku, N.-O., Toivola, D. M. 2002 Keratins: Guardians of the liver. *Hepatology*. **35**, 251-257. (10.1053/jhep.2002.31165)

95 Chen, Y., Guldiken, N., Spurny, M., Mohammed, H. H. A., Haybaeck, J., Pollheimer, M. J., Fickert, P., Gassler, N., Jeon, M. K., Trautwein, C.*, et al.* 2015 Loss of keratin 19 favours the development of cholestatic liver disease through decreased ductular reaction. *Journal of Pathology*. **237**, 343-354. (10.1002/path.4580)

96 McGowan, K. M., Tong, X., Colucci-Guyon, E., Langa, F., Babinet, C., Coulombe, P. A. 2002 Keratin 17 null mice exhibit age- and strain-dependent alopecia. *Genes Dev*. **16**, 1412-1422. (10.1101/gad.979502)

97 Reichelt, J., Bussow, H., Grund, C., Magin, T. M. 2001 Formation of a normal epidermis supported by increased stability of keratins 5 and 14 in keratin 10 null mice. *Mol Biol Cell*. **12**, 1557-1568. (10.1091/mbc.12.6.1557)

98 Gilbert, S., Loranger, A., Daigle, N., Marceau, N. 2001 Simple epithelium keratins 8 and 18 provide resistance to Fas-mediated apoptosis. The protection occurs through a receptor-targeting modulation. *Journal of Cell Biology*. **154**, 763-773. (10.1083/jcb.200102130)

99 Liu, C., Liu, E. D., Meng, Y. X., Dong, X. M., Bi, Y. L., Wu, H. W., Jin, Y. C., Zhao, K., Li, J. J., Yu, M.*, et al.* 2017 Keratin 8 reduces colonic permeability and maintains gut microbiota homeostasis, protecting against colitis and colitisassociated tumorigenesis. *Oncotarget*. **8**, 96774-96790. (10.18632/oncotarget.18241)

100 Moch, M., Leube, R. E. 2021 Hemidesmosome-related keratin filament bundling and nucleation. *International Journal of Molecular Sciences*. **22**, 1-24. (10.3390/ijms22042130)

101 Walko, G., Castanon, M. J., Wiche, G. 2015 Molecular architecture and function of the hemidesmosome. *Cell Tissue Res*. **360**, 529-544. (10.1007/s00441-015-2216-6)

102 Owaribe, K., Kartenbeck, J., Stumpp, S., Magin, T. M., Krieg, T., Diaz, L. A., Franke, W. W. 1990 The hemidesmosomal plaque. I. Characterization of a major constituent protein as a differentiation marker for certain forms of epithelia. *Differentiation*. **45**, 207-220. (10.1111/j.1432-0436.1990.tb00475.x)

103 Fontao, L., Stutzmann, J., Gendry, P., Launay, J. F. 1999 Regulation of the type II hemidesmosomal plaque assembly in intestinal epithelial cells. *Experimental Cell Research*. **250**, 298-312. (10.1006/excr.1999.4549)

104 Uematsu, J., Nishizawa, Y., Sonnenberg, A., Owaribe, K. 1994 Demonstration of type II hemidesmosomes in a mammary gland epithelial cell line, BMGE-H. *Journal of Biochemistry*. **115**, 469-476. (10.1093/oxfordjournals.jbchem.a124361)

105 Wiche, G. 2021 Plectin-Mediated Intermediate Filament Functions: Why Isoforms Matter. *Cells*. **10**, 2154-2154. (10.3390/cells10082154)

106 Ackerl, R., Walko, G., Fuchs, P., Fischer, I., Schmuth, M., Wiche, G. 2007 Conditional targeting of plectin in prenatal and adult mouse stratified epithelia causes keratinocyte fragility and lesional epidermal barrier defects. *J Cell Sci*. **120**, 2435-2443. (10.1242/jcs.004481)

107 Hartmann, C., Schwietzer, Y. A., Otani, T., Furuse, M., Ebnet, K. Physiological functions of junctional adhesion molecules (JAMs) in tight junctions. *Biochimica et Biophysica Acta - Biomembranes*: Elsevier B.V. 2020.

108 Itoh, M., Furuse, M., Morita, K., Kubota, K., Saitou, M., Tsukita, S. 1999 Direct binding of three tight junction-associated MAGUKs, ZO-1, ZO-2, and ZO-3, with the COOH termini of claudins. *Journal of Cell Biology*. **147**, 1351-1363. (10.1083/jcb.147.6.1351)

109 Otani, T., Nguyen, T. P., Tokuda, S., Sugihara, K., Sugawara, T., Furuse, K., Miura, T., Ebnet, K., Furuse, M. 2019 Claudins and JAM-A coordinately regulate tight junction formation and epithelial polarity. *Journal of Cell Biology*. **218**, 3372-3396. (10.1083/JCB.201812157)

110 Umeda, K., Ikenouchi, J., Katahira-Tayama, S., Furuse, K., Sasaki, H., Nakayama, M., Matsui, T., Tsukita, S., Furuse, M., Tsukita, S. 2006 ZO-1 and ZO-2 Independently Determine Where Claudins Are Polymerized in Tight-Junction Strand Formation. *Cell*. **126**, 741-754. (10.1016/j.cell.2006.06.043)

111 Niessen, C. M., Gottardi, C. J. Molecular components of the adherens junction. *Biochimica et Biophysica Acta - Biomembranes*: Elsevier 2008:562-571.

112 Al-Amoudi, A., Castaño-Diez, D., Devos, D. P., Russell, R. B., Johnson, G. T., Frangakis, A. S. 2011 The three-dimensional molecular structure of the desmosomal plaque. *P Natl Acad Sci USA*. **108**, 6480-6485. (10.1073/pnas.1019469108)

113 Harrison, O. J., Brasch, J., Lasso, G., Katsamba, P. S., Ahlsen, G., Honig, B., Shapiro, L. 2016 Structural basis of adhesive binding by desmocollins and desmogleins. *P Natl Acad Sci USA*. **113**, 7160-7165. (10.1073/pnas.1606272113)

114 Kowalczyk, A. P., Green, K. J. 2013 Structure, function, and regulation of desmosomes. *Prog Mol Biol Transl Sci*. **116**, 95-118. (10.1016/B978-0-12-394311-8.00005-4)

115 Osmanagic-Myers, S., Dechat, T., Foisner, R. 2015 Lamins at the crossroads of mechanosignaling. *Genes Dev*. **29**, 225-237. (10.1101/gad.255968.114)

116 Zheng, B., Cantley, L. C. 2007 Regulation of epithelial tight junction assembly and disassembly by AMP-activated protein kinase. *P Natl Acad Sci USA*. **104**, 819-822. (10.1073/pnas.0610157104)

117 Wiche, G. 2022 Plectin in Health and Disease. *Cells*. **11**, (10.3390/cells11091412)

118 Vahidnezhad, H., Youssefian, L., Harvey, N., Tavasoli, A. R., Saeidian, A. H., Sotoudeh, S., Varghaei, A., Mahmoudi, H., Mansouri, P., Mozafari, N.*, et al.* 2022 Mutation update: The spectra of PLEC sequence variants and related plectinopathies. *Hum Mutat*. **43**, 1706-1731. (10.1002/humu.24434)

119 Castañón, M. J., Walko, G., Winter, L., Wiche, G. Plectin-intermediate filament partnership in skin, skeletal muscle, and peripheral nerve. *Histochemistry and Cell Biology*: Histochem Cell Biol 2013:33-53.

120 Winter, L., Wiche, G. 2013 The many faces of plectin and plectinopathies: pathology and mechanisms. *Acta Neuropathol*. **125**, 77-93. (10.1007/s00401-012-1026-0)

121 Pfendner, E., Rouan, F., Uitto, J. Progress in epidermolysis bullosa: The phenotypic spectrum of plectin mutations. *Experimental Dermatology*: Exp Dermatol 2005:241-249.

122 Wu, S. H., Hsu, J. S., Chen, H. L., Chien, M. M., Wu, J. F., Ni, Y. H., Liou, B. Y., Ho, M. C., Jeng, Y. M., Chang, M. H.*, et al.* 2019 Plectin Mutations in Progressive Familial Intrahepatic Cholestasis. *Hepatology*. **70**, 2221-2224. (10.1002/hep.30841)

123 Thebaut, A., Aumar, M., Gardin, A., Almes, M., Davit-Spraul, A., Jacquemin, E. 2024 Failure of cholic acid therapy in a child with a bile acid synthesis defect and harboring plectin mutations. *J Pediatr Gastroenterol Nutr*. **78**, 1203-1204. (10.1002/jpn3.12171)

124 Zrelski, M. M., Kustermann, M., Winter, L. 2021 Muscle-Related Plectinopathies. *Cells*. **10**, (10.3390/cells10092480)

125 Gundesli, H., Talim, B., Korkusuz, P., Balci-Hayta, B., Cirak, S., Akarsu, N. A., Topaloglu, H., Dincer, P. 2010 Mutation in exon 1f of PLEC, leading to disruption of plectin isoform 1f, causes autosomal-recessive limb-girdle muscular dystrophy. *Am J Hum Genet*. **87**, 834-841. (10.1016/j.ajhg.2010.10.017)

126 Deev, R. V., Bardakov, S. N., Mavlikeev, M. O., Yakovlev, I. A., Umakhanova, Z. R., Akhmedova, P. G., Magomedova, R. M., Chekmaryeva, I. A., Dalgatov, G. D., Isaev, A. A. 2017 Glu20Ter Variant in PLEC 1f Isoform Causes Limb-Girdle Muscle Dystrophy with Lung Injury. *Front Neurol*. **8**, 367. (10.3389/fneur.2017.00367)

127 Gostyńska, K. B., Nijenhuis, M., Lemmink, H., Pas, H. H., Pasmooij, A. M. G., Lang, K. K., Castañón, M. J., Wiche, G., Jonkman, M. F. 2014 Mutation in exon 1a of PLEC, leading to disruption of plectin isoform 1a, causes autosomal-recessive skin-only epidermolysis bullosa simplex. *Human Molecular Genetics*. **24**, 3155-3162. (10.1093/hmg/ddv066)

128 Zhang, T., Xu, Z., Zheng, D., Wang, X., He, J., Zhang, L., Zallocchi, M. 2023 Novel biallelic variants in the PLEC gene are associated with severe hearing loss. *Hear Res*. **436**, 108831. (10.1016/j.heares.2023.108831)

129 Andra, K., Lassmann, H., Bittner, R., Shorny, S., Fassler, R., Propst, F., Wiche, G. 1997 Targeted inactivation of plectin reveals essential function in maintaining the integrity of skin, muscle, and heart cytoarchitecture. *Genes Dev*. **11**, 3143-3156. (10.1101/gad.11.23.3143)

130 Winter, L., Abrahamsberg, C., Wiche, G. 2008 Plectin isoform 1b mediates mitochondrion - Intermediate filament network linkage and controls organelle shape. *Journal of Cell Biology*. **181**, 903-911. (10.1083/jcb.200710151)

131 Abrahamsberg, C., Fuchs, P., Osmanagic-Myers, S., Fischer, I., Propst, F., Elbe-Bürger, A., Wiche, G. 2005 Targeted ablation of plectin isoform 1 uncovers role of cytolinker proteins in leukocyte recruitment. *P Natl Acad Sci USA*. **102**, 18449-18454. (10.1073/pnas.0505380102)

132 Fuchs, P., Zörer, M., Reipert, S., Rezniczek, G. A., Propst, F., Walko, G., Fischer, I., Bauer, J., Leschnick, M. W., Lüscher, B.*, et al.* 2009 Targeted inactivation of a developmentally regulated neural plectin isoform (plectin 1c) in mice leads to reduced motor nerve conduction velocity. *Journal of Biological Chemistry*. **284**, 26502-26509. (10.1074/jbc.M109.018150)

133 Castanon, M. J., Wiche, G. 2021 Identifying Plectin Isoform Functions through Animal Models. *Cells*. **10**, (10.3390/cells10092453)

134 Natsuga, K., Nishie, W., Shinkuma, S., Arita, K., Nakamura, H., Ohyama, M., Osaka, H., Kambara, T., Hirako, Y., Shimizu, H. 2010 Plectin Deficiency Leads to Both Muscular Dystrophy and Pyloric Atresia in Epidermolysis Bullosa Simplex. *Human Mutation*. **31**, (10.1002/humu.21330)

135 Ketema, M., Secades, P., Kreft, M., Nahidiazar, L., Janssen, H., Jalink, K., De Pereda, J. M., Sonnenberg, A. 2015 The rod domain is not essential for the function of plectin in maintaining tissue integrity. *Molecular Biology of the Cell*. **26**, 2402-2417. (10.1091/mbc.E15-01-0043)

136 Broussard, J. A., Jaiganesh, A., Zarkoob, H., Conway, D. E., Dunn, A. R., Espinosa, H. D., Janmey, P. A., Green, K. J. 2020 Scaling up single-cell mechanics to multicellular tissues

- the role of the intermediate filament-desmosome network. *J Cell Sci*. **133**, (10.1242/jcs.228031)

137 Dogterom, M., Koenderink, G. H. 2019 Actin-microtubule crosstalk in cell biology. *Nat Rev Mol Cell Biol*. **20**, 38-54. (10.1038/s41580-018-0067-1)

138 Wiche, G. 2021 Plectin-Mediated Intermediate Filament Functions: Why Isoforms Matter. *Cells*. **10**, (10.3390/cells10082154)

139 Alisafaei, F., Mandal, K., Saldanha, R., Swoger, M., Yang, H., Shi, X., Guo, M., Hehnly, H., Castaneda, C. A., Janmey, P. A*., et al.* 2024 Vimentin is a key regulator of cell mechanosensing through opposite actions on actomyosin and microtubule networks. *Commun Biol*. **7**, 658. (10.1038/s42003-024-06366-4)

140 Beedle, A. E. M., Jaganathan, A., Albajar-Sigales, A., Yavitt, F. M., Bera, K., Andreu, I., Granero-Moya, I., Zalvidea, D., Kechagia, Z., Wiche, G*., et al.* 2023 Fibrillar adhesion dynamics govern the timescales of nuclear mechano-response via the vimentin cytoskeleton. *bioRxiv*. (10.1101/2023.11.08.566191)

141 Jiu, Y., Lehtimaki, J., Tojkander, S., Cheng, F., Jaalinoja, H., Liu, X., Varjosalo, M., Eriksson, J. E., Lappalainen, P. 2015 Bidirectional Interplay between Vimentin Intermediate Filaments and Contractile Actin Stress Fibers. *Cell Rep*. **11**, 1511-1518. (10.1016/j.celrep.2015.05.008)

142 Strouhalova, K., Prechova, M., Gandalovicova, A., Brabek, J., Gregor, M., Rosel, D. 2020 Vimentin Intermediate Filaments as Potential Target for Cancer Treatment. *Cancers (Basel)*. **12**, (10.3390/cancers12010184)

143 Battaglia, R. A., Delic, S., Herrmann, H., Snider, N. T. 2018 Vimentin on the move: new developments in cell migration. *F1000Res*. **7**, (10.12688/f1000research.15967.1)

144 Lechuga, S., Ivanov, A. I. 2021 Actin cytoskeleton dynamics during mucosal inflammation: a view from broken epithelial barriers. *Curr Opin Physiol*. **19**, 10-16. (10.1016/j.cophys.2020.06.012)

145 Ebrahim, S., Fujita, T., Millis, B. A., Kozin, E., Ma, X., Kawamoto, S., Baird, M. A., Davidson, M., Yonemura, S., Hisa, Y*., et al.* 2013 NMII forms a contractile transcellular sarcomeric network to regulate apical cell junctions and tissue geometry. *Curr Biol*. **23**, 731-736. (10.1016/j.cub.2013.03.039)

146 Yonemura, S., Itoh, M., Nagafuchi, A., Tsukita, S. 1995 Cell-to-cell adherens junction formation and actin filament organization: similarities and differences between non-polarized fibroblasts and polarized epithelial cells. *J Cell Sci*. **108 (Pt 1)**, 127-142. (10.1242/jcs.108.1.127)

147 Efimova, N., Svitkina, T. M. 2018 Branched actin networks push against each other at adherens junctions to maintain cell-cell adhesion. *J Cell Biol*. **217**, 1827-1845. (10.1083/jcb.201708103)

148 Acharya, B. R., Nestor-Bergmann, A., Liang, X., Gupta, S., Duszyc, K., Gauquelin, E., Gomez, G. A., Budnar, S., Marcq, P., Jensen, O. E*., et al.* 2018 A Mechanosensitive RhoA Pathway that Protects Epithelia against Acute Tensile Stress. *Dev Cell*. **47**, 439-452 e436. (10.1016/j.devcel.2018.09.016)

149 Stephenson, R. E., Higashi, T., Erofeev, I. S., Arnold, T. R., Leda, M., Goryachev, A. B., Miller, A. L. 2019 Rho Flares Repair Local Tight Junction Leaks. *Dev Cell*. **48**, 445-459 e445. (10.1016/j.devcel.2019.01.016)

150 Ruiz, W. G., Clayton, D. R., Parakala-Jain, T., Dalghi, M. G., Franks, J., Apodaca, G. 2024 The umbrella cell keratin network: organization as a tile-like mesh, formation of a girded layer in response to bladder filling, and dependence on the plectin cytolinker. *bioRxiv*. (10.1101/2024.06.11.598498)

151 Brunser, O., Luft, H. J. 1970 Fine structure of the apex of absorptive cell from rat small intestine. *J Ultrastruct Res*. **31**, 291-311. (10.1016/s0022-5320(70)90133-4)

152 Toivola, D. M., Baribault, H., Magin, T., Michie, S. A., Omary, M. B. 2000 Simple epithelial keratins are dispensable for cytoprotection in two pancreatitis models. *Am J Physiol Gastrointest Liver Physiol*. **279**, G1343-1354. (10.1152/ajpgi.2000.279.6.G1343)

153 Baffet, G., Loyer, P., Glaise, D., Corlu, A., Etienne, P. L., Guguen-Guillouzo, C. 1991 Distinct effects of cell-cell communication and corticosteroids on the synthesis and distribution of cytokeratins in cultured rat hepatocytes. *J Cell Sci*. **99 (Pt 3)**, 609-615. (10.1242/jcs.99.3.609)

154 Iwatsuki, H., Suda, M. 2007 Keratin 20 expressed in the endocrine and exocrine cells of the rabbit duodenum. *Acta Histochem Cytochem*. **40**, 123-130. (10.1267/ahc.07007)

155 Meier, S. M., Kreutz, D., Winter, L., Klose, M. H. M., Cseh, K., Weiss, T., Bileck, A., Alte, B., Mader, J. C., Jana, S*., et al.* 2017 An Organoruthenium Anticancer Agent Shows Unexpected Target Selectivity For Plectin. *Angew Chem Int Ed Engl*. **56**, 8267-8271. (10.1002/anie.201702242)

156 Wang, W., Zuidema, A., Te Molder, L., Nahidiazar, L., Hoekman, L., Schmidt, T., Coppola, S., Sonnenberg, A. 2020 Hemidesmosomes modulate force generation via focal adhesions. *J Cell Biol*. **219**, (10.1083/jcb.201904137)

157 Nanavati, B. N., Noordstra, I., Verma, S., Duszyc, K., Green, K. J., Yap, A. S. 2023 Desmosome-anchored intermediate filaments facilitate tension-sensitive RhoA signaling for epithelial homeostasis. *bioRxiv*. (10.1101/2023.02.23.529786)

158 Broussard, J. A., Yang, R., Huang, C., Nathamgari, S. S. P., Beese, A. M., Godsel, L. M., Hegazy, M. H., Lee, S., Zhou, F., Sniadecki, N. J*., et al.* 2017 The desmoplakin-intermediate filament linkage regulates cell mechanics. *Mol Biol Cell*. **28**, 3156-3164. (10.1091/mbc.E16-07-0520)

159 Nekrasova, O., Harmon, R. M., Broussard, J. A., Koetsier, J. L., Godsel, L. M., Fitz, G. N., Gardel, M. L., Green, K. J. 2018 Desmosomal cadherin association with Tctex-1 and

cortactin-Arp2/3 drives perijunctional actin polymerization to promote keratinocyte delamination. *Nat Commun*. **9**, 1053. (10.1038/s41467-018-03414-6)

160 Kant, S., Freytag, B., Herzog, A., Reich, A., Merkel, R., Hoffmann, B., Krusche, C. A., Leube, R. E. 2019 Desmoglein 2 mutation provokes skeletal muscle actin expression and accumulation at intercalated discs in murine hearts. *J Cell Sci*. **132**, (10.1242/jcs.199612)

161 Hatsell, S., Cowin, P. 2001 Deconstructing desmoplakin. *Nat Cell Biol*. **3**, E270-272. (10.1038/ncb1201-e270)

162 Vasioukhin, V., Bowers, E., Bauer, C., Degenstein, L., Fuchs, E. 2001 Desmoplakin is essential in epidermal sheet formation. *Nat Cell Biol*. **3**, 1076-1085. (10.1038/ncb1201-1076)

163 Keil, R., Rietscher, K., Hatzfeld, M. 2016 Antagonistic Regulation of Intercellular Cohesion by Plakophilins 1 and 3. *J Invest Dermatol*. **136**, 2022-2029. (10.1016/j.jid.2016.05.124)

164 Godsel, L. M., Dubash, A. D., Bass-Zubek, A. E., Amargo, E. V., Klessner, J. L., Hobbs, R. P., Chen, X., Green, K. J. 2010 Plakophilin 2 couples actomyosin remodeling to desmosomal plaque assembly via RhoA. *Mol Biol Cell*. **21**, 2844-2859. (10.1091/mbc.E10-02-0131)

165 Moch, M., Schieren, J., Leube, R. E. 2022 Cortical tension regulates desmosomal morphogenesis. *Front Cell Dev Biol*. **10**, 946190. (10.3389/fcell.2022.946190)

166 Rubsam, M., Pullen, R., Tellkamp, F., Bianco, A., Peskoller, M., Bloch, W., Green, K. J., Merkel, R., Hoffmann, B., Wickstrom, S. A*., et al.* 2023 Polarity signaling balances epithelial contractility and mechanical resistance. *Sci Rep*. **13**, 7743. (10.1038/s41598-023-33485-5)

167 Buckley, A., Turner, J. R. 2018 Cell Biology of Tight Junction Barrier Regulation and Mucosal Disease. *Cold Spring Harb Perspect Biol*. **10**, (10.1101/cshperspect.a029314)

168 Ruder, B., Atreya, R., Becker, C. 2019 Tumour Necrosis Factor Alpha in Intestinal Homeostasis and Gut Related Diseases. *Int J Mol Sci*. **20**, (10.3390/ijms20081887)

169 Son, S., Baek, A., Lee, J. H., Kim, D. E. 2022 Autophagosome-lysosome fusion is facilitated by plectin-stabilized actin and keratin 8 during macroautophagic process. *Cell Mol Life Sci*. **79**, 95. (10.1007/s00018-022-04144-1)

170 Serres, M. P., Samwer, M., Truong Quang, B. A., Lavoie, G., Perera, U., Gorlich, D., Charras, G., Petronczki, M., Roux, P. P., Paluch, E. K. 2020 F-Actin Interactome Reveals Vimentin as a Key Regulator of Actin Organization and Cell Mechanics in Mitosis. *Dev Cell*. **52**, 210-222 e217. (10.1016/j.devcel.2019.12.011)

171 Koenderink, G. H., Paluch, E. K. 2018 Architecture shapes contractility in actomyosin networks. *Curr Opin Cell Biol*. **50**, 79-85. (10.1016/j.ceb.2018.01.015)

172 Janson, L. W., Kolega, J., Taylor, D. L. 1991 Modulation of contraction by gelation/solation in a reconstituted motile model. *J Cell Biol*. **114**, 1005-1015. (10.1083/jcb.114.5.1005)

173 Matsudaira, P. 1994 Actin crosslinking proteins at the leading edge. *Semin Cell Biol*. **5**, 165-174. (10.1006/scel.1994.1021)

174 Ennomani, H., Letort, G., Guerin, C., Martiel, J. L., Cao, W., Nedelec, F., De La Cruz, E. M., Thery, M., Blanchoin, L. 2016 Architecture and Connectivity Govern Actin Network Contractility. *Curr Biol*. **26**, 616-626. (10.1016/j.cub.2015.12.069)

175 Ingber, D. E. 2008 Tensegrity and mechanotransduction. *J Bodyw Mov Ther*. **12**, 198-200. (10.1016/j.jbmt.2008.04.038)

176 Ingber, D. E. 2003 Tensegrity I. Cell structure and hierarchical systems biology. *J Cell Sci*. **116**, 1157-1173. (10.1242/jcs.00359)

177 Ingber, D. E. 2003 Tensegrity II. How structural networks influence cellular information processing networks. *J Cell Sci*. **116**, 1397-1408. (10.1242/jcs.00360)

178 Angulo-Urarte, A., van der Wal, T., Huveneers, S. 2020 Cell-cell junctions as sensors and transducers of mechanical forces. *Biochim Biophys Acta Biomembr*. **1862**, 183316. (10.1016/j.bbamem.2020.183316)

179 Charras, G., Yap, A. S. 2018 Tensile Forces and Mechanotransduction at Cell-Cell Junctions. *Curr Biol*. **28**, R445-R457. (10.1016/j.cub.2018.02.003)

180 Chugh, P., Paluch, E. K. 2018 The actin cortex at a glance. *J Cell Sci*. **131**, (10.1242/jcs.186254)

181 Bellingham-Johnstun, K., Tyree, Z. L., Martinez-Baird, J., Thorn, A., Laplante, C. 2023 Actin-Microtubule Crosstalk Imparts Stiffness to the Contractile Ring in Fission Yeast. *Cells*. **12**, (10.3390/cells12060917)

182 Liang, X., Michael, M., Gomez, G. A. 2016 Measurement of Mechanical Tension at Cell-cell Junctions Using Two-photon Laser Ablation. *Bio Protoc*. **6**, (10.21769/BioProtoc.2068)

183 Tojkander, S., Gateva, G., Husain, A., Krishnan, R., Lappalainen, P. 2015 Generation of contractile actomyosin bundles depends on mechanosensitive actin filament assembly and disassembly. *Elife*. **4**, e06126. (10.7554/eLife.06126)

184 Tinevez, J. Y., Schulze, U., Salbreux, G., Roensch, J., Joanny, J. F., Paluch, E. 2009 Role of cortical tension in bleb growth. *Proc Natl Acad Sci U S A*. **106**, 18581-18586. (10.1073/pnas.0903353106)

185 Zulueta-Coarasa, T., Fernandez-Gonzalez, R. 2015 *Integrative Mechanobiology: Micro- and Nano- Techniques in Cell Mechanobiology*. Cambridge: Cambridge University Press.

186 Style, R. W., Boltyanskiy, R., German, G. K., Hyland, C., MacMinn, C. W., Mertz, A. F., Wilen, L. A., Xu, Y., Dufresne, E. R. 2014 Traction force microscopy in physics and biology. *Soft Matter*. **10**, 4047-4055. (10.1039/c4sm00264d)

187 Bauer, A., Prechova, M., Fischer, L., Thievessen, I., Gregor, M., Fabry, B. 2021 pyTFM: A tool for traction force and monolayer stress microscopy. *PLoS Comput Biol*. **17**, e1008364. (10.1371/journal.pcbi.1008364)

188 Trepat, X., Wasserman, M. R., Angelini, T. E., Millet, E., Weitz, D. A., Butler, J. P., Fredberg, J. J. 2009 Physical forces during collective cell migration. *Nat Phys*. **5**, 426-430. (10.1038/Nphys1269)

189 Tang, X., Tofangchi, A., Anand, S. V., Saif, T. A. 2014 A novel cell traction force microscopy to study multi-cellular system. *PLoS Comput Biol*. **10**, e1003631. (10.1371/journal.pcbi.1003631)

190 Dembo, M., Wang, Y. L. 1999 Stresses at the cell-to-substrate interface during locomotion of fibroblasts. *Biophys J*. **76**, 2307-2316. (10.1016/S0006-3495(99)77386-8)

191 Lekka, M., Gnanachandran, K., Kubiak, A., Zielinski, T., Zemla, J. 2021 Traction force microscopy - Measuring the forces exerted by cells. *Micron*. **150**, 103138. (10.1016/j.micron.2021.103138)

192 Hur, S. S., Jeong, J. H., Ban, M. J., Park, J. H., Yoon, J. K., Hwang, Y. 2020 Traction force microscopy for understanding cellular mechanotransduction. *BMB Rep*. **53**, 74-81. (10.5483/BMBRep.2020.53.2.308)

193 Grashoff, C., Hoffman, B. D., Brenner, M. D., Zhou, R., Parsons, M., Yang, M. T., McLean, M. A., Sligar, S. G., Chen, C. S., Ha, T*., et al.* 2010 Measuring mechanical tension across vinculin reveals regulation of focal adhesion dynamics. *Nature*. **466**, 263-266. (10.1038/nature09198)

194 Cost, A. L., Khalaji, S., Grashoff, C. 2019 Genetically Encoded FRET-Based Tension Sensors. *Curr Protoc Cell Biol*. **83**, e85. (10.1002/cpcb.85)

195 Kumar, A., Ouyang, M., Van den Dries, K., McGhee, E. J., Tanaka, K., Anderson, M. D., Groisman, A., Goult, B. T., Anderson, K. I., Schwartz, M. A. 2016 Talin tension sensor reveals novel features of focal adhesion force transmission and mechanosensitivity. *J Cell Biol*. **213**, 371-383. (10.1083/jcb.201510012)

196 Borghi, N., Sorokina, M., Shcherbakova, O. G., Weis, W. I., Pruitt, B. L., Nelson, W. J., Dunn, A. R. 2012 E-cadherin is under constitutive actomyosin-generated tension that is increased at cell-cell contacts upon externally applied stretch. *Proc Natl Acad Sci U S A*. **109**, 12568-12573. (10.1073/pnas.1204390109)

197 Price, A. J., Cost, A. L., Ungewiss, H., Waschke, J., Dunn, A. R., Grashoff, C. 2018 Mechanical loading of desmosomes depends on the magnitude and orientation of external stress. *Nat Commun*. **9**, (ARTN 5284

10.1038/s41467-018-07523-0)

198 Baddam, S. R., Arsenovic, P. T., Narayanan, V., Duggan, N. R., Mayer, C. R., Newman, S. T., Abutaleb, D. A., Mohan, A., Kowalczyk, A. P., Conway, D. E. 2018 The Desmosomal Cadherin Desmoglein-2 Experiences Mechanical Tension as Demonstrated by a FRET-Based Tension Biosensor Expressed in Living Cells. *Cells*. **7**, (10.3390/cells7070066)

199 Haas, A. J., Zihni, C., Ruppel, A., Hartmann, C., Ebnet, K., Tada, M., Balda, M. S., Matter, K. 2020 Interplay between Extracellular Matrix Stiffness and JAM-A Regulates Mechanical Load on ZO-1 and Tight Junction Assembly. *Cell Rep*. **32**, 107924. (10.1016/j.celrep.2020.107924)

200 Narayanan, V., Schappell, L. E., Mayer, C. R., Duke, A. A., Armiger, T. J., Arsenovic, P. T., Mohan, A., Dahl, K. N., Gleghorn, J. P., Conway, D. E. 2020 Osmotic Gradients in Epithelial Acini Increase Mechanical Tension across E-cadherin, Drive Morphogenesis, and Maintain Homeostasis. *Curr Biol*. **30**, 624-633 e624. (10.1016/j.cub.2019.12.025)

201 Kumar, S., Weaver, V. M. 2009 Mechanics, malignancy, and metastasis: the force journey of a tumor cell. *Cancer Metastasis Rev*. **28**, 113-127. (10.1007/s10555-008-9173-4)

202 Hogan, C., Dupre-Crochet, S., Norman, M., Kajita, M., Zimmermann, C., Pelling, A. E., Piddini, E., Baena-Lopez, L. A., Vincent, J. P., Itoh, Y.*, et al.* 2009 Characterization of the interface between normal and transformed epithelial cells. *Nat Cell Biol*. **11**, 460-467. (10.1038/ncb1853)

203 Kajita, M., Hogan, C., Harris, A. R., Dupre-Crochet, S., Itasaki, N., Kawakami, K., Charras, G., Tada, M., Fujita, Y. 2010 Interaction with surrounding normal epithelial cells influences signalling pathways and behaviour of Src-transformed cells. *J Cell Sci*. **123**, 171-180. (10.1242/jcs.057976)

204 Yilmaz, M., Christofori, G. 2009 EMT, the cytoskeleton, and cancer cell invasion. *Cancer Metastasis Rev*. **28**, 15-33. (10.1007/s10555-008-9169-0)

205 Friedl, P., Wolf, K. 2010 Plasticity of cell migration: a multiscale tuning model. *J Cell Biol*. **188**, 11-19. (10.1083/jcb.200909003)

206 Taubenberger, A. V., Baum, B., Matthews, H. K. 2020 The Mechanics of Mitotic Cell Rounding. *Front Cell Dev Biol*. **8**, 687. (10.3389/fcell.2020.00687)

207 Salbreux, G., Charras, G., Paluch, E. 2012 Actin cortex mechanics and cellular morphogenesis. *Trends Cell Biol*. **22**, 536-545. (10.1016/j.tcb.2012.07.001)

208 Escuin, S., Vernay, B., Savery, D., Gurniak, C. B., Witke, W., Greene, N. D., Copp, A. J. 2015 Rho-kinase-dependent actin turnover and actomyosin disassembly are necessary for mouse spinal neural tube closure. *J Cell Sci*. **128**, 2468-2481. (10.1242/jcs.164574)

209 Moulding, D. A., Record, J., Malinova, D., Thrasher, A. J. 2013 Actin cytoskeletal defects in immunodeficiency. *Immunol Rev*. **256**, 282-299. (10.1111/imr.12114)

210 Na, S., Chowdhury, F., Tay, B., Ouyang, M., Gregor, M., Wang, Y., Wiche, G., Wang, N. 2009 Plectin contributes to mechanical properties of living cells. *Am J Physiol Cell Physiol*. **296**, C868-877. (10.1152/ajpcell.00604.2008)

211 Werner, N. S., Windoffer, R., Strnad, P., Grund, C., Leube, R. E., Magin, T. M. 2004 Epidermolysis bullosa simplex-type mutations alter the dynamics of the keratin cytoskeleton and reveal a contribution of actin to the transport of keratin subunits. *Mol Biol Cell*. **15**, 990-1002. (10.1091/mbc.e03-09-0687)

212 Russell, D., Andrews, P. D., James, J., Lane, E. B. 2004 Mechanical stress induces profound remodelling of keratin filaments and cell junctions in epidermolysis bullosa simplex keratinocytes. *J Cell Sci*. **117**, 5233-5243. (10.1242/jcs.01407)

213 Shirinsky, V. P., Antonov, A. S., Birukov, K. G., Sobolevsky, A. V., Romanov, Y. A., Kabaeva, N. V., Antonova, G. N., Smirnov, V. N. 1989 Mechano-chemical control of human endothelium orientation and size. *J Cell Biol*. **109**, 331-339. (10.1083/jcb.109.1.331)

214 Chen, T., Saw, T. B., Mege, R. M., Ladoux, B. 2018 Mechanical forces in cell monolayers. *J Cell Sci*. **131**, (10.1242/jcs.218156)

215 Denais, C. M., Gilbert, R. M., Isermann, P., McGregor, A. L., te Lindert, M., Weigelin, B., Davidson, P. M., Friedl, P., Wolf, K., Lammerding, J. 2016 Nuclear envelope rupture and repair during cancer cell migration. *Science*. **352**, 353-358. (10.1126/science.aad7297)

216 Xia, Y., Ivanovska, I. L., Zhu, K., Smith, L., Irianto, J., Pfeifer, C. R., Alvey, C. M., Ji, J., Liu, D., Cho, S.*, et al.* 2018 Nuclear rupture at sites of high curvature compromises retention of DNA repair factors. *J Cell Biol*. **217**, 3796-3808. (10.1083/jcb.201711161)

217 Le, H. Q., Ghatak, S., Yeung, C. Y., Tellkamp, F., Gunschmann, C., Dieterich, C., Yeroslaviz, A., Habermann, B., Pombo, A., Niessen, C. M.*, et al.* 2016 Mechanical regulation of transcription controls Polycomb-mediated gene silencing during lineage commitment. *Nat Cell Biol*. **18**, 864-875. (10.1038/ncb3387)

218 Nava, M. M., Miroshnikova, Y. A., Biggs, L. C., Whitefield, D. B., Metge, F., Boucas, J., Vihinen, H., Jokitalo, E., Li, X., Garcia Arcos, J. M.*, et al.* 2020 Heterochromatin-Driven Nuclear Softening Protects the Genome against Mechanical Stress-Induced Damage. *Cell*. **181**, 800-817 e822. (10.1016/j.cell.2020.03.052)

219 Gérémie, L., Ilker, E., Bernheim-Dennery, M., Cavaniol, C., Viovy, J.-L., Vignjevic, D. M., Joanny, J.-F., Descroix, S. 2022 Evolution of a confluent gut epithelium under on-chip cyclic stretching. *Physical Review Research*. **4**, 023032. (10.1103/PhysRevResearch.4.023032)

220 Buck, R. C. 1980 Reorientation response of cells to repeated stretch and recoil of the substratum. *Exp Cell Res*. **127**, 470-474. (10.1016/0014-4827(80)90456-5)

221 Lien, J. C., Wang, Y. L. 2021 Cyclic stretching-induced epithelial cell reorientation is driven by microtubule-modulated transverse extension during the relaxation phase. *Sci Rep*. **11**, 14803. (10.1038/s41598-021-93987-y)

222 Zielinski, A., Linnartz, C., Pleschka, C., Dreissen, G., Springer, R., Merkel, R., Hoffmann, B. 2018 Reorientation dynamics and structural interdependencies of actin,

microtubules and intermediate filaments upon cyclic stretch application. *Cytoskeleton (Hoboken)*. **75**, 385-394. (10.1002/cm.21470)

223 Kreplak, L., Fudge, D. 2007 Biomechanical properties of intermediate filaments: from tissues to single filaments and back. *Bioessays*. **29**, 26-35. (10.1002/bies.20514)

224 Springer, R., Zielinski, A., Pleschka, C., Hoffmann, B., Merkel, R. 2019 Unbiased pattern analysis reveals highly diverse responses of cytoskeletal systems to cyclic straining. *PLoS One*. **14**, e0210570. (10.1371/journal.pone.0210570)

225 Goldyn, A. M., Kaiser, P., Spatz, J. P., Ballestrem, C., Kemkemer, R. 2010 The kinetics of force-induced cell reorganization depend on microtubules and actin. *Cytoskeleton (Hoboken)*. **67**, 241-250. (10.1002/cm.20439)

226 Wang, J. H., Goldschmidt-Clermont, P., Wille, J., Yin, F. C. 2001 Specificity of endothelial cell reorientation in response to cyclic mechanical stretching. *J Biomech*. **34**, 1563-1572. (10.1016/s0021-9290(01)00150-6)

227 Iba, T., Sumpio, B. E. 1991 Morphological response of human endothelial cells subjected to cyclic strain in vitro. *Microvasc Res*. **42**, 245-254. (10.1016/0026-2862(91)90059-k)

228 Livne, A., Bouchbinder, E., Geiger, B. 2014 Cell reorientation under cyclic stretching. *Nat Commun*. **5**, 3938. (10.1038/ncomms4938)

229 Galie, P. A., Georges, P. C., Janmey, P. A. 2022 How do cells stiffen? *Biochem J*. **479**, 1825-1842. (10.1042/BCJ20210806)

230 Cui, Y., Hameed, F. M., Yang, B., Lee, K., Pan, C. Q., Park, S., Sheetz, M. 2015 Cyclic stretching of soft substrates induces spreading and growth. *Nat Commun*. **6**, 6333. (10.1038/ncomms7333)

231 Faust, U., Hampe, N., Rubner, W., Kirchgeßner, N., Safran, S., Hoffmann, B., Merkel, R. 2011 Cyclic stress at mHz frequencies aligns fibroblasts in direction of zero strain. *PLoS ONE*. **6**, (10.1371/journal.pone.0028963)

232 Kaunas, R., Nguyen, P., Usami, S., Chien, S. 2005 Cooperative effects of Rho and mechanical stretch on stress fiber organization. *Proc Natl Acad Sci U S A*. **102**, 15895-15900. (10.1073/pnas.0506041102)

233 Fujiwara, S., Ohashi, K., Mashiko, T., Kondo, H., Mizuno, K. 2016 Interplay between Solo and keratin filaments is crucial for mechanical force-induced stress fiber reinforcement. *Mol Biol Cell*. **27**, 954-966. (10.1091/mbc.E15-06-0417)

234 Aragona, M., Sifrim, A., Malfait, M., Song, Y., Van Herck, J., Dekoninck, S., Gargouri, S., Lapouge, G., Swedlund, B., Dubois, C*., et al.* 2020 Mechanisms of stretch-mediated skin expansion at single-cell resolution. *Nature*. **584**, 268-273. (10.1038/s41586-020-2555-7)

235 Benham-Pyle, B. W., Pruitt, B. L., Nelson, W. J. 2015 Cell adhesion. Mechanical strain induces E-cadherin-dependent Yap1 and beta-catenin activation to drive cell cycle entry. *Science*. **348**, 1024-1027. (10.1126/science.aaa4559)

236 Miralles, F., Posern, G., Zaromytidou, A. I., Treisman, R. 2003 Actin dynamics control SRF activity by regulation of its coactivator MAL. *Cell*. **113**, 329-342. (10.1016/s0092-8674(03)00278-2)

237 Vartiainen, M. K., Guettler, S., Larijani, B., Treisman, R. 2007 Nuclear actin regulates dynamic subcellular localization and activity of the SRF cofactor MAL. *Science*. **316**, 1749-1752. (10.1126/science.1141084)

238 Posern, G., Treisman, R. 2006 Actin' together: serum response factor, its cofactors and the link to signal transduction. *Trends Cell Biol*. **16**, 588-596. (10.1016/j.tcb.2006.09.008)

239 Dupont, S., Morsut, L., Aragona, M., Enzo, E., Giulitti, S., Cordenonsi, M., Zanconato, F., Le Digabel, J., Forcato, M., Bicciato, S*., et al.* 2011 Role of YAP/TAZ in mechanotransduction. *Nature*. **474**, 179-183. (10.1038/nature10137)

240 Panciera, T., Azzolin, L., Cordenonsi, M., Piccolo, S. Mechanobiology of YAP and TAZ in physiology and disease. *Nature Reviews Molecular Cell Biology*: Nature Publishing Group 2017:758-770.

241 Yamada, K., Green, K. G., Samarel, A. M., Saffitz, J. E. 2005 Distinct pathways regulate expression of cardiac electrical and mechanical junction proteins in response to stretch. *Circ Res*. **97**, 346-353. (10.1161/01.RES.0000178788.76568.8a)

242 Liu, S., Liu, L., Ye, W., Ye, D., Wang, T., Guo, W., Liao, Y., Xu, D., Song, H., Zhang, L*., et al.* 2016 High Vimentin Expression Associated with Lymph Node Metastasis and Predicated a Poor Prognosis in Oral Squamous Cell Carcinoma. *Sci Rep*. **6**, 38834. (10.1038/srep38834)

243 Leitner, L., Shaposhnikov, D., Mengel, A., Descot, A., Julien, S., Hoffmann, R., Posern, G. 2011 MAL/MRTF-A controls migration of non-invasive cells by upregulation of cytoskeleton-associated proteins. *Journal of Cell Science*. **124**, 4318-4331. (10.1242/jcs.092791)

244 Yates, S., Rayner, T. E. 2002 Transcription factor activation in response to cutaneous injury: role of AP-1 in reepithelialization. *Wound Repair Regen*. **10**, 5-15. (10.1046/j.1524-475x.2002.10902.x)

245 Janmey, P. A. 1991 Mechanical properties of cytoskeletal polymers. *Curr Opin Cell Biol*. **3**, 4-11. (10.1016/0955-0674(91)90159-v)

246 van Bodegraven, E. J., Etienne-Manneville, S. 2021 Intermediate Filaments from Tissue Integrity to Single Molecule Mechanics. *Cells*. **10**, (10.3390/cells10081905)

247 Block, J., Schroeder, V., Pawelzyk, P., Willenbacher, N., Koster, S. 2015 Physical properties of cytoplasmic intermediate filaments. *Biochim Biophys Acta*. **1853**, 3053-3064. (10.1016/j.bbamcr.2015.05.009)

248 Koster, S., Weitz, D. A., Goldman, R. D., Aebi, U., Herrmann, H. 2015 Intermediate filament mechanics in vitro and in the cell: from coiled coils to filaments, fibers and networks. *Curr Opin Cell Biol*. **32**, 82-91. (10.1016/j.ceb.2015.01.001)

249 Sapra, K. T., Medalia, O. 2021 Bend, Push, Stretch: Remarkable Structure and Mechanics of Single Intermediate Filaments and Meshworks. *Cells*. **10**, (10.3390/cells10081960)

250 Ackbarow, T., Sen, D., Thaulow, C., Buehler, M. J. 2009 Alpha-helical protein networks are self-protective and flaw-tolerant. *PLoS One*. **4**, e6015. (10.1371/journal.pone.0006015)

251 Block, J., Witt, H., Candelli, A., Peterman, E. J., Wuite, G. J., Janshoff, A., Koster, S. 2017 Nonlinear Loading-Rate-Dependent Force Response of Individual Vimentin Intermediate Filaments to Applied Strain. *Phys Rev Lett*. **118**, 048101. (10.1103/PhysRevLett.118.048101)

252 Uray, I. P., Uray, K. 2021 Mechanotransduction at the Plasma Membrane-Cytoskeleton Interface. *Int J Mol Sci*. **22**, (10.3390/ijms222111566)

253 Martino, F., Perestrelo, A. R., Vinarsky, V., Pagliari, S., Forte, G. 2018 Cellular Mechanotransduction: From Tension to Function. *Front Physiol*. **9**, 824. (10.3389/fphys.2018.00824)

254 Ortega, E., Manso, J. A., Buey, R. M., Carballido, A. M., Carabias, A., Sonnenberg, A., de Pereda, J. M. 2016 The Structure of the Plakin Domain of Plectin Reveals an Extended Rod-like Shape. *J Biol Chem*. **291**, 18643-18662. (10.1074/jbc.M116.732909)

255 Daday, C., Kolšek, K., Gräter, F. 2017 The mechano-sensing role of the unique SH3 insertion in plakin domains revealed by Molecular Dynamics simulations. *Scientific Reports*. **7**, (10.1038/s41598-017-11017-2)

256 Suman, S. K., Daday, C., Ferraro, T., Vuong-Brender, T., Tak, S., Quintin, S., Robin, F., Gräter, F., Labouesse, M. 2019 The plakin domain of C. Elegans VAB-10/plectin acts as a hub in a mechanotransduction pathway to promote morphogenesis. *Development (Cambridge)*. **146**, (10.1242/dev.183780)

257 Koster, J., van Wilpe, S., Kuikman, I., Litjens, S. H., Sonnenberg, A. 2004 Role of binding of plectin to the integrin beta4 subunit in the assembly of hemidesmosomes. *Mol Biol Cell*. **15**, 1211-1223. (10.1091/mbc.e03-09-0697)

258 Koster, J., Geerts, D., Favre, B., Borradori, L., Sonnenberg, A. 2003 Analysis of the interactions between BP180, BP230, plectin and the integrin alpha6beta4 important for hemidesmosome assembly. *J Cell Sci*. **116**, 387-399. (10.1242/jcs.00241)

259 Rezniczek, G. A., Konieczny, P., Nikolic, B., Reipert, S., Schneller, D., Abrahamsberg, C., Davies, K. E., Winder, S. J., Wiche, G. 2007 Plectin 1f scaffolding at the sarcolemma of dystrophic (mdx) muscle fibers through multiple interactions with beta-dystroglycan. *J Cell Biol*. **176**, 965-977. (10.1083/jcb.200604179)

260 Hijikata, T., Nakamura, A., Isokawa, K., Imamura, M., Yuasa, K., Ishikawa, R., Kohama, K., Takeda, S., Yorifuji, H. 2008 Plectin 1 links intermediate filaments to costameric sarcolemma through beta-synemin, alpha-dystrobrevin and actin. *J Cell Sci*. **121**, 2062-2074. (10.1242/jcs.021634)

261 Osmanagic-Myers, S., Rus, S., Wolfram, M., Brunner, D., Goldmann, W. H., Bonakdar, N., Fischer, I., Reipert, S., Zuzuarregui, A., Walko, G.*, et al.* 2015 Plectin reinforces vascular integrity by mediating crosstalk between the vimentin and the actin networks. *J Cell Sci*. **128**, 4138-4150. (10.1242/jcs.172056)

262 Kostan, J., Gregor, M., Walko, G., Wiche, G. 2009 Plectin isoform-dependent regulation of keratin-integrin alpha6beta4 anchorage via Ca2+/calmodulin. *J Biol Chem*. **284**, 18525-18536. (10.1074/jbc.M109.008474)

263 Song, J. G., Kostan, J., Drepper, F., Knapp, B., de Almeida Ribeiro, E., Jr., Konarev, P. V., Grishkovskaya, I., Wiche, G., Gregor, M., Svergun, D. I.*, et al.* 2015 Structural insights into Ca2+-calmodulin regulation of Plectin 1a-integrin beta4 interaction in hemidesmosomes. *Structure*. **23**, 558-570. (10.1016/j.str.2015.01.011)

264 Rezniczek, G. A., Konieczny, P., Nikolic, B., Reipert, S., Schneller, D., Abrahamsberg, C., Davies, K. E., Winder, S. J., Wiche, G. 2007 Plectin 1f scaffolding at the sarcolemma of dystrophic (mdx) muscle fibers through multiple interactions with β-dystroglycan. *Journal of Cell Biology*. **176**, 965-977. (10.1083/jcb.200604179)

265 Fontao, L., Geerts, D., Kulkman, I., Koster, J., Kramer, D., Sonnenberg, A. 2001 The interaction of plectin with actin: Evidence for cross-linking of actin filaments by dimerization of the actin-binding domain of plectin. *Journal of Cell Science*. **114**, 2065-2076. (10.1242/jcs.114.11.2065)

266 Andra, K., Nikolic, B., Stocher, M., Drenckhahn, D., Wiche, G. 1998 Not just scaffolding: plectin regulates actin dynamics in cultured cells. *Genes Dev*. **12**, 3442-3451.

267 Ding, Y., Zhang, L., Goodwin, J. S., Wang, Z., Liu, B., Zhang, J., Fan, G. H. 2008 Plectin regulates the signaling and trafficking of the HIV-1 co-receptor CXCR4 and plays a role in HIV-1 infection. *Experimental Cell Research*. **314**, 590-602. (10.1016/j.yexcr.2007.10.032)

268 Valencia, R. G., Walko, G., Janda, L., Novacek, J., Mihailovska, E., Reipert, S., Andra-Marobela, K., Wiche, G. 2013 Intermediate filament-associated cytolinker plectin 1c destabilizes microtubules in keratinocytes. *Mol Biol Cell*. **24**, 768-784. (10.1091/mbc.E12-06-0488)

269 Herrmann, H., Wiche, G. 1987 Plectin and IFAP-300K are homologous proteins binding to microtubule-associated proteins 1 and 2 and to the 240-kilodalton subunit of spectrin. *J Biol Chem*. **262**, 1320-1325.

270 Niwa, T., Saito, H., Imajoh-ohmi, S., Kaminishi, M., Seto, Y., Miki, Y., Nakanishi, A. 2009 BRCA2 interacts with the cytoskeletal linker protein plectin to form a complex controlling centrosome localization. *Cancer Science*. **100**, 2115-2125. (10.1111/j.1349-7006.2009.01282.x)

271 Gregor, M., Zeold, A., Oehler, S., Marobela, K. A., Fuchs, P., Weigel, G., Hardie, D. G., Wiche, G. 2006 Plectin scaffolds recruit energy-controlling AMP-activated protein kinase (AMPK) in differentiated myofibres. *J Cell Sci*. **119**, 1864-1875. (10.1242/jcs.02891)

272 Favre, B., Schneider, Y., Lingasamy, P., Bouameur, J. E., Begré, N., Gontier, Y., Steiner-Champliaud, M. F., Frias, M. A., Borradori, L., Fontao, L. 2011 Plectin interacts with the rod domain of type III intermediate filament proteins desmin and vimentin. *European Journal of Cell Biology*. **90**, 390-400. (10.1016/j.ejcb.2010.11.013)

273 Tian, R., Gregor, M., Wiche, G., Goldman, J. E. 2006 Plectin regulates the organization of glial fibrillary acidic protein in Alexander disease. *American Journal of Pathology*. **168**, 888-897. (10.2353/ajpath.2006.051028)

274 Bouameur, J. E., Favre, B., Fontao, L., Lingasamy, P., Begre, N., Borradori, L. 2014 Interaction of plectin with keratins 5 and 14: dependence on several plectin domains and keratin quaternary structure. *J Invest Dermatol*. **134**, 2776-2783. (10.1038/jid.2014.255)

275 Eger, A., Stockinger, A., Wiche, G., Foisner, R. 1997 Polarisation-dependent association of plectin with desmoplakin and the lateral submembrane skeleton in MDCK cells. *J Cell Sci*. **110 (Pt 11)**, 1307-1316.

276 Yin, H., Han, S., Cui, C., Wang, Y., Li, D., Zhu, Q. 2021 Plectin regulates Wnt signaling mediated-skeletal muscle development by interacting with Dishevelled-2 and antagonizing autophagy. *Gene*. **783**, 145562-145562. (10.1016/j.gene.2021.145562)

277 Sabbir, M. G., Dillon, R., Mowat, M. R. 2016 Dlc1 interaction with non-muscle myosin heavy chain II-A (Myh9) and Rac1 activation. *Biol Open*. **5**, 452-460. (10.1242/bio.015859)

278 Kadeer, A., Maruyama, T., Kajita, M., Morita, T., Sasaki, A., Ohoka, A., Ishikawa, S., Ikegawa, M., Shimada, T., Fujita, Y. 2017 Plectin is a novel regulator for apical extrusion of RasV12-transformed cells. *Sci Rep*. **7**, 44328. (10.1038/srep44328)

279 Thomsen, C., Udhane, S., Runnberg, R., Wiche, G., Ståhlberg, A., Åman, P. 2012 Fused in sarcoma (FUS) interacts with the cytolinker protein plectin: Implications for FUS subcellular localization and function. *Experimental Cell Research*. **318**, 653-661. (10.1016/j.yexcr.2011.12.019)

280 Ackerman, S. D., Luo, R., Poitelon, Y., Mogha, A., Harty, B. L., D'Rozario, M., Sanchez, N. E., Lakkaraju, A. K. K., Gamble, P., Li, J.*, et al.* 2018 GPR56/ADG RG1 regulates development and maintenance of peripheral myelin. *Journal of Experimental Medicine*. **215**, 941-961. (10.1084/jem.20161714)

281 Liu, Y. H., Cheng, C. C., Ho, C. C., Chao, W. T., Pei, R. J., Hsu, Y. H., Yeh, K. T., Ho, L. C., Tsai, M. C., Lai, Y. S. 2008 Degradation of plectin with modulation of cytokeratin 18 in human liver cells during staurosporine-induced apoptosis. *In Vivo*. **22**, 543-548.

282 Wang, C. I., Wang, C. L., Wu, Y. C., Feng, H. P., Liu, P. J., Chang, Y. S., Yu, J. S., Yu, C. J. 2015 Quantitative proteomics reveals a novel role of karyopherin alpha 2 in cell migration

through the regulation of vimentin-pErk protein complex levels in lung cancer. *J Proteome Res*. **14**, 1739-1751. (10.1021/pr501097a)

283 Eriksson, M., Nilsson, A., Samuelsson, H., Samuelsson, E. B., Mo, L., Akesson, E., Benedikz, E., Sundstrom, E. 2007 On the role of NR3A in human NMDA receptors. *Physiol Behav*. **92**, 54-59. (10.1016/j.physbeh.2007.05.026)

284 House, C. M., Frew, I. J., Huang, H. L., Wiche, G., Traficante, N., Nice, E., Catimel, B., Bowtell, D. D. L. 2003 A binding motif for Siah ubiquitin ligase. *P Natl Acad Sci USA*. **100**, 3101-3106. (10.1073/pnas.0534783100)

285 Matsubara, T., Kinbara, M., Maeda, T., Yoshizawa, M., Kokabu, S., Takano Yamamoto, T. 2017 Regulation of osteoclast differentiation and actin ring formation by the cytolinker protein plectin. *Biochem Biophys Res Commun*. **489**, 472-476. (10.1016/j.bbrc.2017.05.174)

286 Fish, L., Khoroshkin, M., Navickas, A., Garcia, K., Culbertson, B., Hanisch, B., Zhang, S., Nguyen, H. C. B., Soto, L. M., Dermit, M.*, et al.* 2021 A prometastatic splicing program regulated by SNRPA1 interactions with structured RNA elements. *Science*. **372**, (10.1126/science.abc7531)

287 Chen, V. C., Li, X., Perreault, H., Nagy, J. I. 2006 Interaction of zonula occludens-1 (ZO-1) with alpha-actinin-4: application of functional proteomics for identification of PDZ domain-associated proteins. *J Proteome Res*. **5**, 2123-2134. (10.1021/pr060216l)

288 Winter, L., Kuznetsov, A. V., Grimm, M., Zeöld, A., Fischer, I., Wiche, G. 2015 Plectin isoform P1b and P1d deficiencies differentially affect mitochondrial morphology and function in skeletal muscle. *Human Molecular Genetics*. **24**, 4530-4544. (10.1093/hmg/ddv184)

289 Konieczny, P., Fuchs, P., Reipert, S., Kunz, W. S., Zeöld, A., Fischer, I., Paulin, D., Schröder, R., Wiche, G. 2008 Myofiber integrity depends on desmin network targeting to Z-disks and costameres via distinct plectin isoforms. *Journal of Cell Biology*. **181**, 667-681. (10.1083/jcb.200711058)

290 McInroy, L., Maatta, A. 2011 Plectin regulates invasiveness of SW480 colon carcinoma cells and is targeted to podosome-like adhesions in an isoform-specific manner. *Exp Cell Res*. **317**, 2468-2478. (10.1016/j.yexcr.2011.07.013)

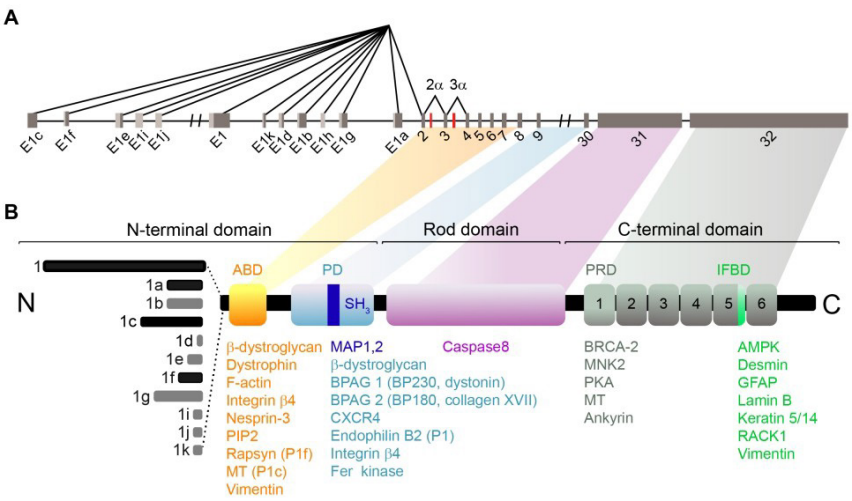

Figure 1

Figure 1. Schematic representation of plectin transcripts and encoded protein domains. (A) Schematics of the plectin transcripts. Twelve first exons spliced into exon 2 are shown. Untranslated regions (light gray) and two optionally spliced exons, 2a and 3a (red), are indicated. (B) Schematics of the plectin protein. The N-termini of isoforms predominantly expressed in epithelia are indicated (black). The N-terminal domain contains the actin-binding domain (ABD; yellow) and plakin domain (PD; light blue), which contains the non-canonical SH3 domain (dark blue). Alternative splicing of exon 31 encoding the rod domain of plectin (pink) generates the rodless isoform. The C-terminal domain consists of six plectin repeat domains (PRD; gray), with the linker region of the fifth PRD containing an IF-binding domain (IFBD, green). The corresponding interacting partners are indicated below. The figure is not drawn to scale.

534x732mm (118 x 118 DPI)

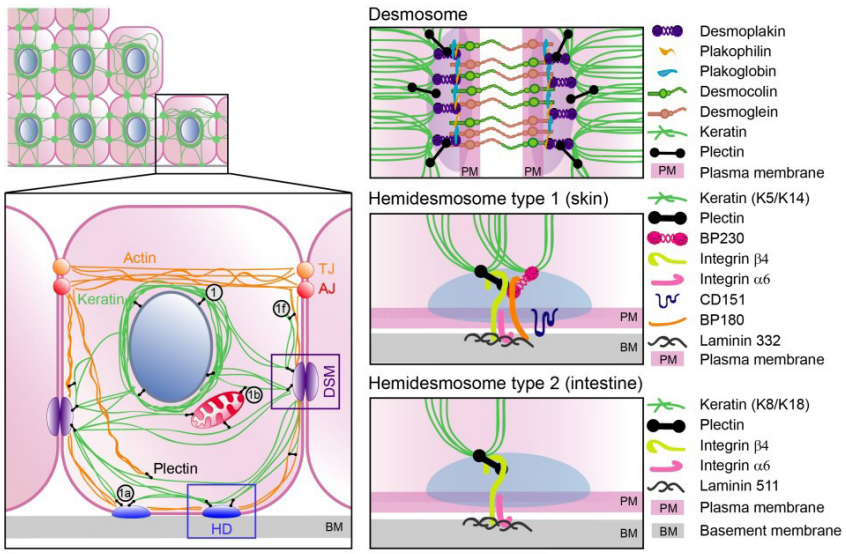

Figure 2

Figure 2. Schematic representation of plectin localization and plectin-mediated organization of cytoskeletal networks in epithelial cells. Plectin (black) crosslinks KFs (green) with the actin fibers (orange). Plectin also anchors cytoskeletal networks to cell junctions, such as hemidesmosomes (HDs, blue; cell-ECM adhesion) and desmosomes (DSMs, purple; cell-cell adhesion), shown in more detail on the right. The localization of major plectin isoforms (black circles) is indicated. TJ, tight junction (orange); AJ, adherens junction (red).

534x731mm (118 x 118 DPI)

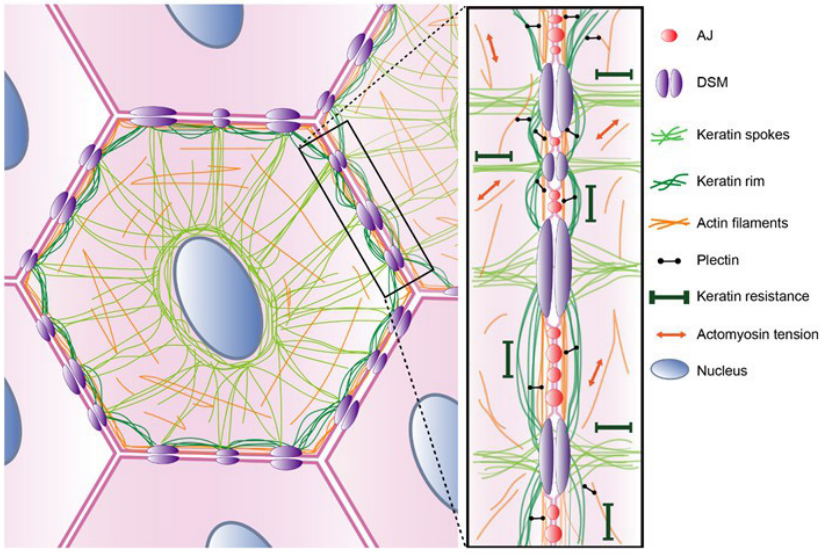

Figure 3

Figure 3. Schematic representation of the proposed model for plectin-mediated cytoskeletal organization and tensional homeostasis. In epithelial monolayers, the perinuclear KFs connect to the cell periphery via keratin radial spokes (light green) that are anchored to the membrane at DSMs (purple). Contractile actomyosin networks (orange) closely align with the plasma membrane. Plectin (black) interacts (via its N-terminus) with cortical F-actin and facilitates the formation of a circumferential keratin rim (dark green) that interconnects individual DSMs. Together, the interlinked web of cytoskeletal networks has the ability to dissipate local deformations, support the plasma membrane, and protect the epithelial sheets from mechanical damage.

481x695mm (38 x 38 DPI)

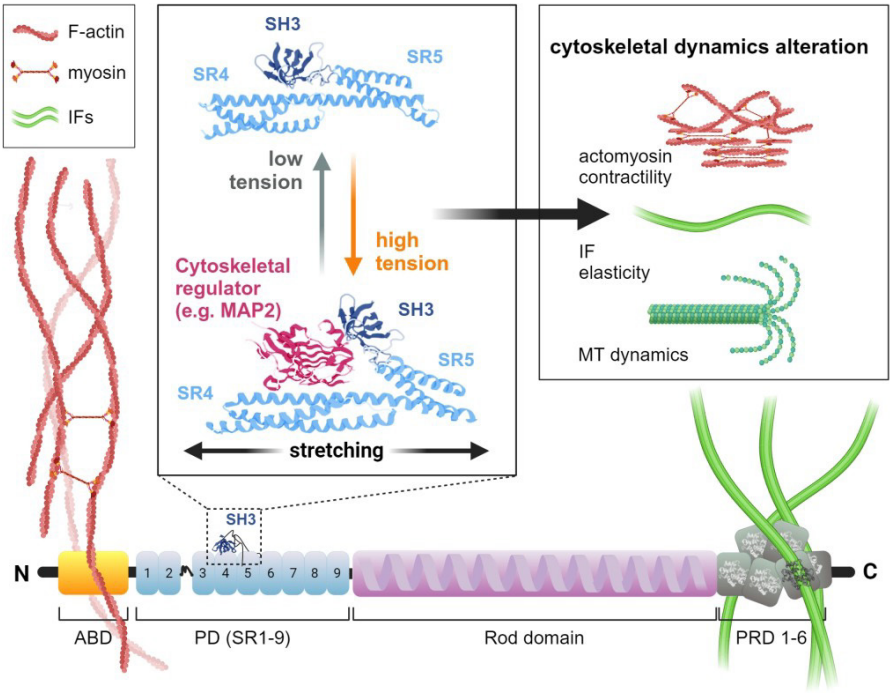

Figure 4

Figure 4. Schematic representation of plectin as a new class of cytolinker-based mechanosensors. Plectin crosslinks IFs and contractile actomyosin networks and recruits them to tension-sensitive junctions (such as FAs, HDs, or DSMs; not shown, for details see Chapters 2, 5, and 8.4). Increased tension resulting from intrinsic and extrinsic forces leads to unfolding of SR4 and SR5 within the plectin PD (middle box; PDB: 3PE0 [8]), releasing the SR4/SH3 interface from inhibitory intramolecular interactions. The unmasked SR4/SH3 interface allows the binding of ligands (such as MAP2) that regulate the dynamics of individual cytoskeletal networks (right box). Theoretically, a similar mechanism can be envisaged for the regulation of actomyosin contractility or flexibility/stiffness of IFs.

457x396mm (118 x 118 DPI)

Plectin-mediated cytoskeletal crosstalk as a target for inhibition of hepatocellular carcinoma growth and metastasis.

Zuzana Outla[1], Gizem Oyman-Eyrilmez[1], Katerina Korelova[1], Magdalena Prechova[1], Lukas Frick[2], Lenka Sarnova[1], Piyush Bisht[1], Petra Novotna[1], Jan Kosla[1,3], Patricia Bortel[4], Yasmin Borutzki[5], Andrea Bileck[4,6], Christopher Gerner[4,6], Mohammad Rahbari[3,7], Nuh Rahbari[8], Emrullah Birgin[8], Bibiana Kvasnicova[9], Andrea Galisova[10], Katerina Sulkova[10], Andreas Bauer[11], Njainday Jobe[12], Ondrej Tolde[12], Eva Sticova[13,14], Daniel Rosel[12], Tracy O'Connor[15], Martin Otahal[9], Daniel Jirak[10], Mathias Heikenwälder[3], Gerhard Wiche[16], Samuel M. Meier-Menches[4,5,6], Martin Gregor[1]

[1]Laboratory of Integrative Biology, Institute of Molecular Genetics of the Czech Academy of Sciences, Prague, Czech Republic

[2]Institute of Molecular Cancer Research, University of Zurich, Zurich, Switzerland

[3]Division of Chronic Inflammation and Cancer, German Cancer Research Center, Im Neuenheimer Feld 242, 69120, Heidelberg, Germany

[4]Department of Analytical Chemistry, University of Vienna, Waehringer Str. 38, 1090 Vienna, Austria

[5]Institute of Inorganic Chemistry, University of Vienna, Waehringer Str. 42, 1090 Vienna, Austria

[6]Joint Metabolome Facility, Medical University of Vienna and University of Vienna, Waehringer Str. 38, 1090 Vienna, Austria

[7]Department of Surgery, University Hospital Mannheim, Medical Faculty Mannheim, University of Heidelberg, Theodor-Kutzer-Ufer 1-3, 68167, Mannheim, Germany

[8]Department of General and Visceral Surgery, Ulm University Hospital, Ulm, Germany

[9]Department of Natural Sciences, Faculty of Biomedical Engineering, Czech Technical University in Prague, Kladno, Czech Republic

[10]Department of Radiodiagnostic and Interventional Radiology, Institute for Clinical and Experimental Medicine, Prague, Czech Republic

[11]Department of Physics, University of Erlangen-Nuremberg, Erlangen, Germany

[12]Department of Cell Biology, Faculty of Science, Charles University, BIOCEV, Prumyslova 595, 25242, Vestec, Czech Republic.

[13]Department of Clinical and Transplant Pathology, Institute for Clinical and Experimental Medicine, Prague, Czech Republic

[14]Department of Pathology, Third Faculty of Medicine, Charles University, Prague, Czech Republic

[15]Department of Biology, North Park University, Chicago, USA.

[16]Department of Biochemistry and Cell Biology, Max F. Perutz Laboratories, University of Vienna, Vienna, Austria

Correspondence to:

Martin Gregor, PhD

Laboratory of Integrative Biology, Institute of Molecular Genetics of the Czech Academy of Sciences

Videnska 1083, Prague 4, CZ-14220, Czech Republic

Phone: +420 241 063 461

Email: martin.gregor@img.cas.cz

Abstract

The most common primary malignancy of the liver, hepatocellular carcinoma (HCC), is a heterogeneous tumor entity with high metastatic potential and complex pathophysiology. Increasing evidence suggests that tissue mechanics plays a critical role in tumor onset and progression. Here we show that plectin, a major cytoskeletal crosslinker protein, plays a crucial role in mechanical homeostasis and mechanosensitive oncogenic signaling that drives hepatocarcinogenesis. Our expression analyses revealed elevated plectin levels in liver tumors, which correlated with poor prognosis for HCC patients. Using autochthonous and orthotopic mouse models we demonstrated that genetic and pharmacological inactivation of plectin potently suppressed the initiation and growth of HCC. Moreover, plectin targeting potently inhibited the invasion potential of human HCC cells and reduced their metastatic outgrowth in the lung. Proteomic and phosphoproteomic profiling linked plectin-dependent disruption of cytoskeletal networks to attenuation of oncogenic FAK, MAPK/Erk, and PI3K/AKT signatures. Importantly, by combining cell line-based and murine HCC models, we show that plectin inhibitor plecstatin-1 (PST) is well-tolerated and potently inhibits HCC progression. In conclusion, our study demonstrates that plectin-controlled cytoarchitecture is a key determinant of HCC development and suggests that pharmacologically induced disruption of mechanical homeostasis may represent a new therapeutic strategy for HCC treatment.

Introduction

Mounting evidence indicates that tissue mechanics plays a pivotal role in cancer cell and stromal cell behavior. Tumor progression is typically associated with a pathological increase of tissue stiffness caused by excessive deposition, crosslinking, and aberrant organization of dense extracellular matrix (ECM) fibers. Increasing tissue rigidity drives tumor invasion and malignancy and correlates with poor patient survival[1,2].

At the cellular level, both tumor and stromal cells respond to altered mechanical properties of the extracellular milieu by translating physical cues into mechanosensitive signaling pathways. This conversion relies on focal adhesions (FAs), clusters of integrin receptors facilitating the link between the ECM and the cytoskeleton. Integrin-mediated adhesion induces the activation of FAK, MAPK/Erk, and PI3K/AKT pathways, leading to increased cell survival, migration, and invasion[3-5]. Subsequent activation of Rho-dependent pathways results in higher cytoskeletal tension and force transmission across FAs, thus establishing a mechanical reciprocity between ECM viscoelasticity and actomyosin-generated cytoskeletal tension. Importantly, many genes encoding components of the ECM-cytoskeletal axis and their regulators (e.g. *αSMA*, *ITGβ*, *LMNA*, *ROCK*, and *COL*) are controlled by tension-dependent transcription[6,7]. This creates a difficult-to-break positive feedback loop leading to cellular and matrix stiffening, further promoting the aggressive, pro-proliferative, and invasive tumor cell phenotype.

Emerging therapeutic strategies aimed at tumor mechanics and mechanotransduction include the targeting of the ECM and ECM modulators (e.g. lysyl oxidase and angiotensin), depletion of stromal myofibroblasts, and integrin receptors[2,3]. Other approaches target cytoskeleton-mediated downstream cellular response to tissue stiffening (e.g. Rho-dependent actomyosin-generated contractile forces[8]). We hypothesized that another efficacious strategy could be inactivation of cytoskeletal crosslinker proteins (so-called cytolinkers)[9,10], large proteins of the plakin protein family, responsible for maintaining cellular architecture. The best-studied example, a prototypical cytolinker plectin is a well-established regulator of cellular tensional homeostasis and mechanotransduction[10] which is upregulated in various tumors[11,12]. Through its canonical actin-binding domain (ABD[13]) and intermediate filament (IF)-binding domain (IFBD[14]), plectin crosslinks actin with IF networks and recruits them to cell adhesions, including FAs. Plectin deletion or mutation results in cytoskeletal reconfiguration accompanied by altered mechanical properties, such as cellular stiffness, stress propagation, and traction force generation[15-18]. In addition, plectin-dependent changes in cell adhesions[18-21] and cytoskeletal tension[17,18,20-22] are associated with aberrant integrin-mediated mechanosignaling[20,21]. Although multiple reports have linked plectin with tumor malignancy[12] and

other pathologies[10,23], mechanistic insights into how plectin functionally contributes to carcinogenesis remain largely unknown.

A malignancy with a well-known link to overproduction of ECM components is hepatocellular carcinoma (HCC), the most common type of liver cancer. Repeated rounds of hepatocyte damage and renewal due to a number of etiologies, most commonly chronic viral infection, alcohol abuse, or a diet rich in fats and sugars, creates a pro-inflammatory environment in the liver. Activated hepatic stellate cells adopt a myofibroblast phenotype and increase production and deposition of ECM components leading to liver fibrosis which can eventually progress to liver cirrhosis. Up to 90% of HCC cases occur on a background of liver fibrosis or cirrhosis, suggesting a causal link between increased deposition of ECM components and liver carcinogenesis. Consistent with this idea, plectin mRNA has been found to be upregulated in liver carcinomas, especially in later stages of disease[11]. Thus, changes in the interactions between the cytoskeleton and ECM may be important in HCC progression, particularly during the transition from local to metastatic malignancy.

Here we explore the role of plectin in the development and dissemination of HCC. Using publicly available HCC sequencing data and biopsies from HCC patients we identify plectin as a novel HCC marker associated with a malignant phenotype and poor survival. To explore the role of plectin in hepatocarcinogenesis, we use a genetic mouse model with liver-specific plectin ablation ($Ple^{\Delta Alb}$). In this model, plectin deficiency suppresses tumor initiation and growth. We further demonstrate that CRISPR/Cas9-engineered human HCC cell lines with inactivated plectin display limited migration, invasion, and anchorage-independent proliferation which correlates with their reduced metastatic outgrowth in the lung. By comprehensive proteomic analysis, we show that plectin inactivation attenuates oncogenic FAK, MAPK/Erk, and PI3K/AKT signaling signatures. Finally, our work identifies the ruthenium-based plecstatin-1 (PST), as a candidate drug that can mimic the genetic ablation of plectin, thus providing a robust pre-clinical proof-of-concept for PST in the treatment of HCC. Our study implicates plectin as a potent driver of HCC, highlights its importance in metastatic spread, and points to potential novel treatment options.

Results

Plectin levels are elevated in HCC and predict a poor prognosis

Using 17 distinct HCC patient datasets, we confirmed that *plectin* expression is consistently and significantly increased in HCC samples when compared to non-tumor (NT) liver tissues (Fig. 1A). The analysis of data from The Cancer Genome Atlas (TCGA) confirmed elevated *plectin* expression in HCC, irrespective of HCC etiology or gender (Figure 1—figure supplement 1A-D). To assess whether high plectin expression is typical for a specific subpopulation of HCC patients, we created t-SNE plots and compared plectin expression patterns with those of molecular subclasses of Dr. Chang´s and Dr. Boyault´s classification[24,25]. Although we observed local clusters of patients with higher or lower plectin expression levels, they did not seem to be associated with any of the largest clusters or subgroups (Figure 1—figure supplement 1E). Strikingly, using higher tertile expression as the cut-off, higher *plectin* mRNA levels were associated with a significant decrease in recurrence-free survival (Fig. 1B). A similar trend was observed across 8 distinct HCC datasets (Figure 1—figure supplement 1F).

Consistent with expression analysis, quantitative immunofluorescence microscopy of 19 human HCC tissue sections revealed a significant increase of plectin fluorescence intensities in tumor (T) compared to adjacent non-tumor (NT) tissue, with plectin perimembraneous enrichment in tumor hepatocytes (Fig. 1C; Figure 1—figure supplement 1G). Next, we compared plectin expression levels by immunoblotting in a panel of human HCC cell lines, which represent distinct stages of HCC development[24]. Consistent with mRNA and immunofluorescence analyses, poorly differentiated mesenchymal-like HCC cell lines (characterized by low E-cadherin and high vimentin levels) displayed elevated plectin levels, coinciding with higher migration speed when compared to well-differentiated HCC cell lines (Fig. 1D,E).

To validate our findings in a well-established chemical carcinogen murine HCC model, we analyzed plectin expression in hepatic tumors formed 46 weeks after diethylnitrosamine (DEN) injection in C57Bl/6J mice (Fig. 1F). Both quantitative immunofluorescence and immunoblot analyses indicated elevated plectin levels in T versus NT liver tissue (Fig. 1C,G,H; Figure 1—figure supplement 1H). Moreover, enhanced plectin signal along hepatocyte membranes closely resembled the staining pattern found in patient HCC sections (Fig. 1C), suggesting reliable translation from the human setting. Together, these results show that elevated plectin is associated with HCC progression both in human patients and animal model and indicates robust prognostic potential for patient survival.

Plectin promotes hepatocarcinogenesis

To determine the functional consequences of plectin loss in liver tumor development, we analyzed the formation of DEN-induced HCCs in mice lacking plectin expression in the liver using magnetic resonance imaging (MRI). To achieve liver-specific plectin deletion, mice carrying a floxed plectin sequence (*Ple*$^{fl/fl}$) were crossed to mice expressing the Cre recombinase under the liver-specific albumin promoter (*Alb-Cre*). The resulting mice (*Ple*$^{\Delta Alb}$) lack plectin expression in the liver[26]. Remarkably, MRI screening 32 and 44 weeks post-injection revealed a significant reduction of tumor number and volume in *Ple*$^{\Delta Alb}$ mice compared to *Ple*$^{fl/fl}$ controls (Fig. 2A-C). Decreased tumor burden in the second cohort of *Ple*$^{\Delta Alb}$ mice was confirmed macroscopically 44 weeks after DEN administration (Fig. 2D,E). Notably, *Ple*$^{\Delta Alb}$ mice more frequently formed larger tumors, as reflected by overall tumor size increase (Fig. 2F; Figure 2—figure supplement 1A), possibly implying reduced migration or increased cohesion of plectin-depleted cells[26,27].

To address plectin´s role in HCC at a cellular level, we genetically manipulated endogenous plectin in well-differentiated Huh7 and poorly differentiated SNU-475 human HCC cell lines[24]. Using the CRISPR/Cas-9 system we generated either knockouts (KO) or cells harboring endogenous plectin with deletion of the IF-binding domain (ΔIFBD) as functional knockouts[18] (Figure 2—figure supplement 1B-D). Gene editing was complemented by treatment with organoruthenium-based compound PST that inactivates plectin function[18,28]. If not stated otherwise, we applied PST in the final concentration of 8 µM, which corresponds to the 25% of IC_{50} for Huh7 cells (Figure 2—figure supplement 1E). Consistent with the murine model, plectin inactivation resulted in a reduced number of Huh7 and SNU-475 colonies in a soft agar colony formation assay, with PST treatment closely mimicking the effect of genetic targeting (Fig. 2G). Moreover, KO and ΔIFBD SNU-475 colonies were significantly smaller when compared to wild-type (WT) controls, with a similar trend observed for Huh7 cells (Figure 2—figure supplement 1F). Collectively, these data demonstrate the inhibitory effect of plectin inactivation on HCC progression in adhesion-independent conditions.

To further assess whether plectin is required for human HCC progression, we investigated the growth of subcutaneous Huh7 xenografts in immunodeficient NSG mice (Fig. 2H; Figure 2—figure supplement 1G). Cells with disabled plectin developed significantly smaller tumors when compared with untreated WT cells (Fig. 2H), mirroring the results of the colony forming assay. The percentage of $Ki67^+$ cells on immunolabeled xenograft sections, however, did not differ between experimental conditions (Figure 2—figure supplement 1G). These results show the reduced tumorigenic potential of human HCC cells when plectin is disabled either by CRISPR/Cas9-mediated gene ablation or

pharmacologically with PST. Hence, by combining *in vivo* and *in vitro* approaches, we provide evidence that plectin promotes hepatocarcinogenesis.

Plectin controls oncogenic FAK, MAPK/Erk, and PI3K/Akt signaling in HCC cells

To identify potential molecular effectors and signaling pathways mediating the tumor suppressive effects of plectin inactivation, we profiled the proteomes of WT, KO, and PST-treated WT SNU-475 cells using MS-based shotgun proteomics and phosphoproteomics (Fig. 3A-C; Figure 3—figure supplement 1A,B). Using a label free quantification strategy, a total of 5440 protein groups and 3573 phosphosites were detected. We found 265 protein groups significantly regulated (FDR < 0.05; s0 = 0.01) upon plectin ablation when comparing WT and KO SNU-475 proteomes (Fig. 3B). Ingenuity Pathway Analysis (IPA) revealed major plectin-dependent regulation of signaling pathways related to the actin cytoskeleton, such as “RhoA signaling”, “Actin cytoskeleton signaling”, “Integrin signaling”, and “Signaling by Rho family GTPases” (Fig. 3B). Similarly, 313 regulated phosphosites indicated a major impact on actin, as well as “ILK signaling”, “FAK signaling”, and “Molecular mechanisms of cancer” among the most altered pathways (Fig. 3B).

Analysis of proteome differences between WT and PST-treated cells identified abundance changes (FDR < 0.05; s0 = 0.01) in 1178 proteins and 290 phosphoproteins (Fig. 3C). A comparison of KO and PST signatures using IPA revealed an overlap (Figure 3—figure supplement 1A). Consistently, the IPA annotation linked also PST signature to integrin- and cytoskeleton-related signaling pathways such as “ILK signaling”, “Integrin signaling”, “RhoA signaling”, and “Actin cytoskeleton signaling” (Fig. 3C). Taken together, our proteomic analyses suggest a regulatory role for plectin in the mechanosensitive, cell adhesion-linked signaling which is critical for cancer development and dissemination[3-5].

To independently confirm our MS findings, we performed extensive immunoblot analysis of WT, KO, ΔIFBD, and PST-treated Huh7 and SNU-475 cells with a focus on integrin-associated adhesome network (Fig. 3D; Figure 3—figure supplement 1C). In agreement with our proteomic analyses, plectin inactivation resulted in considerable changes in expression levels of integrin adhesion receptors (integrins αV and β1) as well as other FA constituents (i.e. talin, vinculin, and paxillin). Moreover, immunoblotting revealed in cells with disabled plectin either generally altered expression (FAK, AKT, Erk1/2, ILK, and PI3K) and/or reduced phosphorylation (AKT, Erk1/2, and PI3K) of key effectors downstream of integrin-mediated adhesion. Although these alterations were not found systematically in both cell lines and condition (reflecting thus presumably their distinct differentiation grade and

plectin inactivation efficacy), collectively these data confirmed plectin-dependent adhesome remodeling together with attenuation of oncogenic FAK, MAPK/Erk, and PI3K/Akt pathways upon plectin inactivation (Fig. 3E).

Plectin-dependent disruption of cytoarchitecture accounts for hampered migration of HCC cells

As plectin acts as a major organizer of cytoskeletal networks[10], we next investigated cytoskeletal organization in HCC cells by immunofluorescence microscopy. To circumvent considerable variability in cellular morphology, which largely obscures quantitative assessment of cytoarchitecture, we seeded WT, KO, ΔIFBD, and PST-treated SNU-475 cells on crossbow-shaped micropatterns[29]. Reminiscent of plectin-deficient fibroblasts[20,30], plectin inactivation in SNU-475 cells produced less delicate vimentin networks compared to WT cells, with filaments often bundled and sometimes collapsing into vimentin clumps (Fig. 4A,B). A quantitative analysis revealed uneven distribution of vimentin filaments throughout the cytoplasm of KO, ΔIFBD, and PST-treated WT cells as evidenced by the distance between the position of the center of vimentin intensity mass and the cell center (Figure 4—figure supplement 1A-C). In addition to the aberrant vimentin phenotype, we noticed a dramatic reduction in longitudinal dorsal actin stress fibers and transversal arcs, as well as pronounced ventral stress fibers in plectin-disabled cells (Fig. 4A,C,D). Moreover, we detected a reduction in F-actin fluorescence intensity in both Huh7 and SNU-475 KO cells, as well as a decrease of atomic force microscopy (AFM)-inferred cellular stiffness as a functional readout for a well-formed cytoskeleton[16] (Figure 4—figure supplement 1D-G).

Given the extent of plectin-dependent adhesome remodeling (Fig. 3D,E; Figure 3—figure supplement 1C), we next assessed whether plectin inactivation affects the morphology and localization of FAs in vinculin-immunolabeled SNU-475 cells. Remarkably, while FAs of micropattern-seeded WT cells were mostly located at the cell periphery, FAs of plectin-disabled cells were frequently found within the cell interior (Fig. 4A,E). Moreover, plectin inactivation resulted in an overall reduced number of FAs, and the FAs that remained were larger and more elongated than in WT cells (Fig. 4F,G; Figure 4—figure supplement 1H,I). To test whether the changes in actin/FA configuration affected adhesion-transmitted forces, we performed traction force microscopy (TFM; Fig. 4H,I). The smaller FAs found in WT cells transmitted significantly higher contractile energy than KO, ΔIFBD, and PST-treated cells, indicating that FAs in plectin-deficient cells were less functional than in WT.

Functional transmission of actomyosin-generated forces across FAs constitutes a prerequisite for cellular locomotion[31]. Therefore, we examined the effect of plectin inactivation on the migration of HCC cells. As anticipated, both Huh7 and SNU-475 cells exhibited a decrease in migration speed upon plectin targeting in the scratch wound healing assay (Fig. 5A,B; Figure 5—figure supplement 1A). It is noteworthy that migrating plectin-disabled SNU-475 cells exhibited more cohesive, epithelial-like features while progressing collectively. By contrast, WT SNU-475 leader cells were more polarized and found to migrate into scratch areas more frequently than their plectin-deficient counterparts (Figure 5—figure supplement 1B). Consistent with this observation, individually seeded SNU-475 cells less frequently assumed a polarized, mesenchymal-like shape upon plectin inactivation in both 2D and 3D environments (Fig. 5C). Moreover, plectin-inactivated SNU-475 cells exhibited a decrease in N-cadherin and vimentin levels when compared to WT counterparts (Figure 5—figure supplement 1C).

In addition to slower general migration, we also found epithelial growth factor (EGF)-guided migration potential of individual KO, ΔIFBD, and PST-treated cells to be significantly reduced compared to WT cells. Consistent with previous findings[20], plectin-disabled cells traversed less linear trajectories in both random and directed scenarios (Fig. 5D,E; Figure 5—figure supplement 1D,E). To determine whether plectin is involved in migration-associated cellular shape dynamics, we further investigated protrusions of SNU-475 cells using morphodynamic contour analysis[32]. Our analysis revealed a higher protrusion frequency of randomly migrating WT compared to plectin-disabled cells (Figure 5—figure supplement 1F), while no differences in protrusion orientation were observed (Fig. 5F-H). In sharp contrast, plectin ablation dramatically reduced the capacity of KO and ΔIFBD cells to form stable protrusions in the direction of chemotactic motion (Fig. 5F-H), although only a marginal effect on the protrusivity was observed (Figure 5—figure supplement 1F). Collectively, these results show that plectin is essential for the proper cytoskeletal configuration of HCC cells and their cytoskeleton-linked FAs. Moreover, they provide evidence that aberrant cytoarchitecture of plectin-disabled cells accounts for the failure to effectively exert traction forces and actively reconfigure body shape, both of which are required for HCC cell migration.

Plectin inactivation reduces HCC cell invasion and lung colonization

To investigate whether disruption of cytoarchitecture in plectin-disabled HCC cells also affected 3D migratory behavior, we compared the activity of WT, KO, ΔIFBD, and PST-treated SNU-475 cells in transwell and spheroid invasion assays. In both assays, plectin inactivation significantly reduced invasion potential compared to WT cells (Fig. 6A-C; Figure 6—figure supplement 1A). Unexpectedly,

plectin-targeted cells also degraded dramatically less FITC-labeled gelatin, suggesting that slower invasion is accompanied by defects in ECM degradation (Fig. 6D; Figure 6—figure supplement 1B).

To monitor plectin effects on shape dynamics in a 3D environment, we recorded WT and KO SNU-475 cells by time-lapse video microscopy in a matrigel invasion assay. Invading WT cells exhibited polarized protrusions followed by cell body displacement in the direction of the nascent protrusion (Video 1; Fig. 6E). By contrast, randomly oriented thinner protrusions of KO cells were often retracted shortly after formation. Markedly thinner and branched KO protrusions were confirmed by subsequent immunofluorescence microscopy (Fig. 6E). Similar to what we observed in the 2D assay, KO cells failed to invade in the direction of these transient protrusions (Video 1; Fig. 6E). Hence, plectin-controlled cytoarchitecture facilitates both 2D and 3D HCC cell migration.

Tumor, node, metastasis (TNM) classification of an HCC meta-cohort with clinically annotated tumors from HCC patients (n = 978) demonstrated that high plectin mRNA expression is associated with advanced TNM stages (Fig. 6F). To elucidate the impact of plectin inactivation on HCC dissemination, we conducted the lung colonization assay using both Huh7 and SNU-475 cells (Fig. 6G-I; Figure 6—figure supplement 1C-F). To this end, we administered red firefly luciferase and GFP (RedFLuc-GFP)-expressing WT and KO cells intravenously (i.v.) in 5-week-old NSG mice. Whereas mice receiving WT Huh7 (but not SNU-475; data not shown) cells succumbed rapidly to disease, mice receiving KO cells exhibited prolonged survival (Fig. 6G). To identify early phase of metastasis formation, we next monitored the HCC cell retention in the lungs using *in vivo* bioluminescence imaging (Fig. 6H). This experimental cohort was expanded for WT-injected mice which were administered PST two times a day for 5 weeks (WT+PST). Mice were sacrificed 5 weeks post-injection when the first luminescence-positive chest areas were detected (Fig. 6H) and cleared whole lung lobes were analyzed by lattice light sheet fluorescence microscopy (Fig. 6I). Although no macroscopic Huh7 nodules were visible, we found a prominent reduction in the number and volume of GFP-positive KO- and WT+PST-derived metastatic nodules. Thus, both CRISPR/Cas9-based and pharmacological plectin inactivation in HCC potently inhibits metastatic load in the lungs, identifying plectin as a potential target against tumor dissemination *in vivo*.

Genetic and pharmacological plectin targeting prevents hepatocarcinogenesis through signatures shared by animal models and patients

To further investigate the translational potential of PST treatment, we evaluated the effects of PST administration on hepatocarcinogenesis in additional murine model. To this end, we induced

multifocal HCC tumors by hydrodynamic delivery of a *c-myc* (Myc)-encoding element together with a CRISPR/Cas9 construct targeting *Tp53* (sgTp53)[33]. To test whether HCC onset and progression are sensitive to pharmacological targeting of plectin, we monitored Myc;sgTp53-driven tumor development in $Ple^{fl/fl}$, $Ple^{\Delta Alb}$, and PST-treated $Ple^{fl/fl}$ male mice using MRI (Fig. 7A). Consistent with our *in vitro* observations, MRI analysis at 4, 6, and 9 weeks post-induction revealed that both genetic and pharmacological plectin inactivation results in a substantial reduction in the average tumor number per mouse and the tumor incidence (Fig. 7A). Stalled development of $Ple^{\Delta Alb}$ and PST-treated $Ple^{fl/fl}$ tumors was also reflected by a decrease in liver/body weight ratio in another male cohort sacrificed at 6 weeks post-induction (Fig. 7B,C). The quantitative immunofluorescence microscopy revealed comparable rates of proliferation and apoptosis in Myc;sgTp53-induced tumors across experimental conditions (Figure 7 —figure supplement 1A,B). Comparable trends in liver/body weight ratio and tumor incidence were also found in a female cohort sacrificed 8 weeks post-induction (Figure 7—figure supplement 1C,D).

To better understand the antitumor effects observed in PST-treated mice, we performed proteomics on Myc;sgTp53-treated $Ple^{fl/fl}$, $Ple^{\Delta Alb}$, and PST-treated $Ple^{fl/fl}$ livers. Consistent with (phospho)proteomic and immunoblot analyses of HCC cell lines (Fig. 3A-E) we found a high level of similarity between $Ple^{\Delta Alb}$ and PST-treated $Ple^{fl/fl}$ signatures (Fig. 7D; Figure 7—figure supplement 2A,B). In addition, gene set enrichment analysis (GSEA)[34] revealed enrichment in “PI3K/Akt” or “Hippo/YAP signaling” pathways (Fig. 7D). Although the data from liver tissue proteomics showed some degree of variation, enrichment of tension-dependent signatures points toward similar trends found in *in vitro* scenarios. To further translate our findings to the human setting, we correlated plectin transcript levels with differentially expressed signatures identified in proteomic analysis of HCC cells (Fig. 3B-D). Through analysis of 1268 HCC patients, we found gene sets annotated as “Integrin pathway”, “FAK pathway”, “PI3K Akt/mTOR signaling” or “Erk pathway” to positively correlate with elevated plectin expression (Fig. 7E; Figure 7—figure supplement 2C; Figure 7—figure supplement 3). Collectively, these data connect plectin with well-characterized pro-oncogenic signaling pathways which were previously identified as prime candidates for therapeutic intervention in cancer[3-5].

Discussion

HCC represents a leading cause of cancer-related death, characterized by poor long-term prognosis, high postoperative recurrence, and a high rate of metastasis[35,36]. As chemotherapy, surgical resection, radiation, and local ablation are not effective in a large group of patients[35,37], there is an urgent need to develop effective therapeutic strategies to target HCC. By combining comprehensive analysis of CRISPR/Cas9-engineered HCC cell lines with (phospho)proteomics, mouse modeling as well as human patient data, we identified the plakin family member plectin as a novel HCC marker and druggable target upstream of FAK, MAPK/Erk, and PI3K/AKT signaling. Thus, our data link plectin, a cytolinker implicated in cytoskeletal tension and mechanotransduction with a major oncogenic signaling hub controlling growth and metastasis of HCC.

We began this work by assessing plectin expression in publicly available HCC patient datasets. Our meta-analyses revealed plectin transcript levels to be considerably elevated in HCC irrespective of etiology or gender, whereas previous findings in HCC were inconsistent[11,38]. Notably, we found that patients with higher *PLEC* mRNA levels had significantly shorter recurrence-free survival times than those with lower *PLEC* mRNA levels. Strikingly, *PLEC* expression in publicly available datasets was significantly associated with gene signatures related to „cell survival and proliferation“, „angiogenesis“, and „hypoxia“ (Figure 7—figure supplement 3) indicating that the *PLEC* level was associated with more aggressive cancer traits in HCC patients. In addition, plectin expression levels were associated with TNM staging, underscoring plectin´s prognostic value for HCC patient survival. Although HCC transcriptomes appears to differ from other cancers[39], our findings are in line with higher *PLEC* expression in other cancer entities such as oral squamous cell carcinoma[40,41], testicular cancer[42], or pancreatic cancer[43], and identify plectin as a specific marker for both early and advanced stages of HCC.

We and others have proposed that plectin plays a central role in tumor growth and dissemination[12,44]. Here, using liver-specific $Ple^{\Delta Alb}$ knockout mice[26], we show that plectin ablation in hepatocytes significantly reduced tumor burden in a model of DEN-induced HCC[45], which mimics fundamental aspects of human disease[46]. These mice also showed decreased hepatocarcinogenesis in a powerful model of multifocal HCC formation following hydrodynamic delivery of Myc;sgTp53[33,47]. In this model, both genetic and PST-mediated pharmacological inactivation of plectin not only reduced the number of HCC tumors formed but ultimately resulted in significantly improved survival of $Ple^{\Delta Alb}$ female mice. Complementing the data from both HCC models, we found that plectin inactivation resulted in the reduced tumorigenic potential of human HCC cells, as evidenced by reduced colony growth under adhesion-independent conditions or subcutaneous xenografts in immunodeficient NSG

mice. While several approaches (such as genetic manipulation[48], PST treatment[28] or blocking peptides[49] and antibodies[50]) decreasing the levels of functional plectin also lead to limited xenograft growth, to our knowledge, this is the first study showing that plectin inactivation prevents tumor progression in well-established preclinical mouse models.

Our previous studies demonstrated that plectin inactivation abrogates physical crosstalk between actin and IF networks[18,20], leading to the redistribution of internal tension[18], and ultimately resulting in defects in cell adhesions[20]. Indeed, plectin-dependent cytoskeletal disruption and aberrant adhesions have been previously linked to compromised migration and invasion of many non-cancerous[19,20,22,51,52] as well as cancerous cell types[48,53-56], including HCC cells[27]. In support of this concept, we report the collapse of actin and vimentin IF networks in Huh7 and SNU-475 cells with disabled plectin. Cytoskeletal disruption was accompanied by redistribution of misshapen FAs, which exerted reduced traction forces onto the underlying substrates. As anticipated, aberrant cytoarchitecture resulted in significantly slower motility of HCC cells in both 2D and 3D environments. Consistent with *in vitro* findings, plectin inactivation reduced metastatic outgrowth of HCC cells in the lung. Intriguingly, morphodynamic contour analysis revealed in these cells reduced capacity to form stable protrusions implicated in driving path finding and cellular locomotion[31]. Collectively, our data suggest that plectin is essential for spatiotemporal cytoskeletal rearrangement, cell shape stabilization, and effective transmission of traction forces, and place plectin-mediated cytoskeletal crosstalk at the center of the processes that control the metastatic cascade.

Plectin-mediated cytoskeletal crosstalk at FAs facilitates their essential features such as dynamics[20], adhesion strength[57], and mechanotransduction capacity[20]. Loss of vimentin filament-FA linkage upon plectin deletion in highly migratory dermal fibroblasts was shown to uncouple the activation of FAK from actomyosin-generated tension and attenuate downstream effectors such as Src, Erk1/2, and p38[20]. Here we show that plectin-dependent perturbation of the cytoskeleton-FAs interplay in invasive SNU-475 HCC cells profoundly altered (phospho)proteomic signatures of cytoskeleton- and cell adhesion-annotated proteins, thereby modulating mechanosensitive integrin-associated signaling events. Importantly, our (phospho)proteomic and immunoblot analyses identified attenuated signaling along FAK, MAPK/Erk, and PI3K/Akt axes as a consequence of plectin inactivation in both Huh7 and SNU-475 HCC cells. Plectin´s control of cytoskeletal crosstalk and its interplay with pro-oncogenic signaling pathways thus emerges as a critical determinant of the initiation and progression of HCC. It is noteworthy that plectin-dependent effects on PI3K/Akt and FAK/Erk signaling were recently described for prostate cancer[53,56] and head and neck squamous carcinoma cells[58], indicating that these observations have broader implications beyond liver cancer.

Finally, we were able to translate our findings from HCC cell lines and mouse models to HCC patients. By mining data from a large human patient cohort, we found a positive correlation between plectin expression and FA-associated FAK, Erk, and PI3K/Akt pathway gene sets. However, it is conceivable that dysregulated cytoskeletal crosstalk could affect HCC through multiple mechanisms independent from FA-associated signaling. Indeed, we and others[26,27] have shown that upon plectin inactivation, liver cells acquire epithelial characteristics that promote increased intercellular cohesion and reduced migration. Further studies will be required to identify and investigate synergistic adhesion-independent effects of plectin inactivation on HCC growth and metastasis.

Current systemic therapies for advanced HCC rely on a combination of multikinase inhibitors (such as sorafenib) or anti-VEGF /VEGF inhibitor (such as bevacizumab) treatment with immunotherapy[59]. Multikinase inhibitors provide only moderate survival benefit[60,61] due to primary resistance and the plasticity of signaling networks[62], and only a subset of patients benefits from addition of immunotherapy in HCC treatment[63]. Therefore, the most translationally impactful finding of this work is the ability of a small organoruthenium compound PST, a high-affinity plectin ligand, to effectivelly limit hepatocarcinogenesis in Myc;sgTp53-driven HCC mouse model as well as xenografted human HCCs, leading to the dampening of HCC burden. Using PST, we further report a marked effect on metastatic HCC outgrowth in the lung along with a reduction of the migratory potential of human HCC cells in 2D and 3D settings. Most notably, our animal models show improvement in local and metastatic survival rates. Similar to other ruthenium-based metallodrugs[64-66], PST was well-tolerated by mice and human cells, suggesting good potential for clinical utilization. We and others have previously demonstrated that PST treatment closely mimics phenotypes fostered by ablation of the plectin gene[18,28,67,68]. Consistently, PST-mediated inhibition of plectin attenuates FAK, MAPK/Erk, and PI3K/Akt pathways in HCC cells with efficacy comparable to CRISPR/Cas-9-engineered functional (ΔIFBD) or full (KO) knockouts. However, despite high PST target selectivity for plectin[67], our data do not rule out pleiotropic effects of PST in the liver and further studies will be required to investigate whether PST mode-of-action in HCC entails molecular mechanisms other than engaging prooncogenic signaling cascades.

Materials and methods

Patient tissue samples

Formalin-fixed paraffin-embedded (FFPE) human liver tissue specimens were prepared at the Department of Surgery of the University Hospital Mannheim. The cohort consisted of 21 patients diagnosed with HCC (for details, see Supplementary file 1). Tissue collection and analysis were performed in accordance with institutional review board guidelines (reference no. 2012-293N-MA), and written informed consent was obtained from all included patients.

Animals

Liver-specific deletion of the plectin (Plec) gene was achieved by crossing *Plectin*$^{flox/flox}$ mice (*Ple*$^{fl/fl}$)[69] with *Alb-Cre* transgenic mice (MGI 2176228; The Jackson Laboratory, Bar Harbor, ME) to generate *Plectin*$^{lox/lox/Alb\text{-}Cre}$ (*Ple*$^{\Delta Alb}$) mice[26]. Immunodeficient NOD.Cg-Prkdcscid Il2rgtm1Wjl/SzJ (NSG) mice were purchased from the Czech Centre for Phenogenomics (BIOCEV – Institute of Molecular Genetics Academy of Sciences, Prague, Czechia)

Animals were housed under specific pathogen-free conditions with regular access to chow and drinking water and 12 h light/12 h dark conditions. All animal studies were performed in accordance with European Directive 86/609/EEC and were approved by the Czech Central Commission for Animal Welfare. Age-matched littermate mice were used in all experiments. The details regarding animal treatments can be found in the following sections.

DEN-induced HCC mouse model

2-week-old *Ple*$^{fl/fl}$ and *Ple*$^{\Delta Alb}$ mice received intraperitoneal injection of 25 mg/kg diethylnitrosamine (DEN; Sigma-Aldrich, St. Louis, MO, USA) diluted in PBS. Mice were monitored for tumor formation 30 and 42 weeks after the DEN injection by magnetic resonance imaging (MRI) and tumor volumes were calculated from MRI images (for details see Magnetic resonance imaging section). Mice were sacrificed at 44 weeks post-injection, livers were dissected, and tumors were measured using a caliper.

Lung colonization assay

Huh7 and SNU-475 cell lines stably expressing Red Firefly Luciferase reporter and GFP were prepared by lentiviral transfection of LentiGlo™ pLenti-CMV-RedFluc-IRES-EGFP plasmid (LP-31, Targeting Systems, El Cajon, CA, USA) according to the manufacturer´s protocol. Next, 2×10^6 Huh7 or SNU-475 cells suspended in serum-free Dulbecco's modified Eagle medium (DMEM, Sigma-Aldrich) were injected into the tail vein of 5-week-old NSG mice. The mice were monitored for survival analysis or monitored using bioluminescence imaging for the presence of lung metastasis after 5 weeks. Prior to

imaging, mice were anesthetized with isoflurane and injected intraperitoneally with D-luciferin potassium salt (Promega, Madison, WI, USA). Ten to fifteen min after injection, luciferase activity was measured using LagoX (Spectral Instruments Imaging, Tuscon, AZ, USA).

HDTVi-induced HCC mouse model

For hydrodynamic tail vein injections, a mixture of plasmid mix containing 5 µg/ml of px330 expressing Tp53 sgRNA, 5 µg/ml of pT3-EF1a MYC DNA (92046, Addgene, Watertown, MA, USA), and 0.5 µg/ml pCMV HSB2 sleeping beauty transponase was prepared in a sterile 0.9% sodium chloride (NaCl) solution. 7-week-old $Ple^{fl/fl}$ and $Ple^{\Delta Alb}$ mice were pre-warmed for 15 min using two infrared lamps (IL 11, Beuer GmbH, Ulm, Germany), placed in a restrainer (TV-RED-150_STD, Braintree Scientific INC., Braintree, MA, USA) and injected intravenously via the lateral tail vein with a total volume corresponding to 10% of body weight over 5–7 s. All animals were monitored daily, and animal experiments were performed in compliance with all relevant ethical regulations outlined in the animal permit. After mice were sacrificed, livers and lungs were visually inspected, excised, and photographed. Tumor samples were taken to obtain protein, and the remaining liver tissue was incubated in 4% PFA for at least 24 h for FFPE tissue preparation.

Statistical analyses

All data mining with the exception of patient analysis, proteomics on mouse tissue samples, and proteomics of SNU-475 cell cultures (see details in corresponding sections), all graphs and statistical tests were performed using GraphPad Prism (GraphPad Software, Inc., La Jolla, CA). In the boxplots, the box margins represent the 25th and 75th percentile with the midline indicates the median. Whiskers reach the last data point. Data comparison of adjacent tumor and non-tumor tissue was performed using a paired *t*-test. Data comparison of individual experimental groups with the control group was performed using a two-tailed *t*-test. Growth curves were analyzed using Two-way ANOVA. Survival curves were analyzed using the Mantel-Cox test. Data distributions were assumed to be normal, but this was not formally tested. Statistical significance was determined at the level of $*P < 0.05$, $**P < 0.01$, $\dagger P < 0.001$. The number of independent experiments (N), number of data points (n), and statistical tests used are specified for individual experiments in the figure legends.

For further details regarding the materials used, please refer to the supplementary information.

Acknowledgement

We would like to thank D. Tschaharganeh (DKFZ, Heidelberg) for generously providing the px330 (Tp53 sgRNA) and pT3-EF1a MYC plasmids, and B. Schuster (IMG CAS, Prague) for pX330 Cas9-Venus plasmid; D. Heide and J. Hetzer (DKFZ, Heidelberg) for their outstanding technical assistance; B. Fabry (FAU Erlangen-Nürnberg), K. Volz (DKFZ, Heidelberg), J. Prochazka (Czech Centre for Phenogenomics, Vestec), M. Maninova, M. K. Adamcova, M. Burocziova, M. Capek, and J. Valecka (all IMG CAS, Prague) for their expertise. We acknowledge the Light Microscopy Core Facility, IMG CAS, Prague, Czech Republic, for support with advanced microscopy imaging.

Competing interests The authors have declared that no conflict of interest exists.

Funding This work was supported by the Grant Agency of the Czech Republic (GA21-21736S and GA24-10672S); the Institutional Research Project of the Czech Academy of Sciences (RVO 68378050); National Institute for Cancer Research (Programme EXCELES, LX22NPO5102) - Funded by the European Union - Next Generation EU; MEYS CR projects (LM2023050, LM2018126, LQ1604 NPU II, LO1419, and LM2015040); and MEYS CR/ERDF projects (OP RDI CZ.1.05/2.1.00/19.0395 and CZ.1.05/1.1.00/02.0109).

Author contributions Study concept and design: M.G. Acquisition of data: Z.O., G.O.-E., K.K., M.P., L.S., P.B., P.N., P.B., Y.B., A.B., C.G., B.K., A.G., K.S., M.O., O.T., N.J. Analysis and interpretation of data: Z.O., K.K., M.P., L.F., J.K., E.S., D.J., O.T., N.J., D.R., S.M.M., M.G. Drafting of the manuscript: Z.O., M.G. Critical revision of the manuscript for important intellectual content: all authors. Funding: M.G., S.M.M., D.R. Technical and material support: J.K., M.J., M.R., N.R., E.B., A.B., T.O., D.J., M.H., G.W., S.M.M.

References

1 Broders-Bondon, F., Nguyen Ho-Bouldoires, T. H., Fernandez-Sanchez, M. E. & Farge, E. Mechanotransduction in tumor progression: The dark side of the force. *J Cell Biol* **217**, 1571-1587, doi:10.1083/jcb.201701039 (2018).

2 Piersma, B., Hayward, M. K. & Weaver, V. M. Fibrosis and cancer: A strained relationship. *Biochim Biophys Acta Rev Cancer* **1873**, 188356, doi:10.1016/j.bbcan.2020.188356 (2020).

3 Cooper, J. & Giancotti, F. G. Integrin Signaling in Cancer: Mechanotransduction, Stemness, Epithelial Plasticity, and Therapeutic Resistance. *Cancer Cell* **35**, 347-367, doi:10.1016/j.ccell.2019.01.007 (2019).

4 Hoxhaj, G. & Manning, B. D. The PI3K-AKT network at the interface of oncogenic signalling and cancer metabolism. *Nat Rev Cancer* **20**, 74-88, doi:10.1038/s41568-019-0216-7 (2020).

5 Sun, Z., Guo, S. S. & Fassler, R. Integrin-mediated mechanotransduction. *J Cell Biol* **215**, 445-456, doi:10.1083/jcb.201609037 (2016).

6 Dupont, S. *et al.* Role of YAP/TAZ in mechanotransduction. *Nature* **474**, 179-183, doi:10.1038/nature10137 (2011).

7 Esnault, C. *et al.* Rho-actin signaling to the MRTF coactivators dominates the immediate transcriptional response to serum in fibroblasts. *Genes Dev* **28**, 943-958, doi:10.1101/gad.239327.114 (2014).

8 Bustelo, X. R. RHO GTPases in cancer: known facts, open questions, and therapeutic challenges. *Biochem Soc Trans* **46**, 741-760, doi:10.1042/BST20170531 (2018).

9 Bouameur, J. E., Favre, B. & Borradori, L. Plakins, a versatile family of cytolinkers: roles in skin integrity and in human diseases. *J Invest Dermatol* **134**, 885-894, doi:10.1038/jid.2013.498 (2014).

10 Prechova, M., Korelova, K. & Gregor, M. Plectin. *Curr Biol* **33**, R128-R130, doi:10.1016/j.cub.2022.12.061 (2023).

11 Gundesli, H., Kori, M. & Arga, K. Y. The Versatility of Plectin in Cancer: A Pan-Cancer Analysis on Potential Diagnostic and Prognostic Impacts of Plectin Isoforms. *OMICS* **27**, 281-296, doi:10.1089/omi.2023.0053 (2023).

12 Perez, S. M., Brinton, L. T. & Kelly, K. A. Plectin in Cancer: From Biomarker to Therapeutic Target. *Cells* **10**, doi:10.3390/cells10092246 (2021).

13 Andra, K., Nikolic, B., Stocher, M., Drenckhahn, D. & Wiche, G. Not just scaffolding: plectin regulates actin dynamics in cultured cells. *Genes Dev* **12**, 3442-3451, doi:10.1101/gad.12.21.3442 (1998).

14 Nikolic, B., Mac Nulty, E., Mir, B. & Wiche, G. Basic amino acid residue cluster within nuclear targeting sequence motif is essential for cytoplasmic plectin-vimentin network junctions. *J Cell Biol* **134**, 1455-1467, doi:10.1083/jcb.134.6.1455 (1996).

15 Eisenberg, J. L. *et al.* Plectin-containing, centrally localized focal adhesions exert traction forces in primary lung epithelial cells. *J Cell Sci* **126**, 3746-3755, doi:10.1242/jcs.128975 (2013).

16 Na, S. *et al.* Plectin contributes to mechanical properties of living cells. *Am J Physiol Cell Physiol* **296**, C868-877, doi:10.1152/ajpcell.00604.2008 (2009).

17 Osmanagic-Myers, S. *et al.* Plectin reinforces vascular integrity by mediating crosstalk between the vimentin and the actin networks. *J Cell Sci* **128**, 4138-4150, doi:10.1242/jcs.172056 (2015).

18 Prechova, M. *et al.* Plectin-mediated cytoskeletal crosstalk controls cell tension and cohesion in epithelial sheets. *The Journal of cell biology* **221**, doi:10.1083/jcb.202105146 (2022).

19 De Pascalis, C. *et al.* Intermediate filaments control collective migration by restricting traction forces and sustaining cell-cell contacts. *J Cell Biol* **217**, 3031-3044, doi:10.1083/jcb.201801162 (2018).

20 Gregor, M. *et al.* Mechanosensing through focal adhesion-anchored intermediate filaments. *FASEB J* **28**, 715-729, doi:10.1096/fj.13-231829 (2014).

21 Wang, W. *et al.* Hemidesmosomes modulate force generation via focal adhesions. *J Cell Biol* **219**, doi:10.1083/jcb.201904137 (2020).
22 Marks, P. C., Hewitt, B. R., Baird, M. A., Wiche, G. & Petrie, R. J. Plectin linkages are mechanosensitive and required for the nuclear piston mechanism of three-dimensional cell migration. *Mol Biol Cell* **33**, ar104, doi:10.1091/mbc.E21-08-0414 (2022).
23 Vahidnezhad, H. *et al.* Mutation update: The spectra of PLEC sequence variants and related plectinopathies. *Human mutation* **43**, 1706-1731, doi:10.1002/humu.24434 (2022).
24 Boyault, S. *et al.* Transcriptome classification of HCC is related to gene alterations and to new therapeutic targets. *Hepatology* **45**, 42-52, doi:10.1002/hep.21467 (2007).
25 Chiang, D. Y. *et al.* Focal gains of VEGFA and molecular classification of hepatocellular carcinoma. *Cancer Res* **68**, 6779-6788, doi:10.1158/0008-5472.CAN-08-0742 (2008).
26 Jirouskova, M. *et al.* Plectin controls biliary tree architecture and stability in cholestasis. *Journal of hepatology* **68**, 1006-1017, doi:10.1016/j.jhep.2017.12.011 (2018).
27 Xu, R. *et al.* Plectin Downregulation Inhibits Migration and Suppresses Epithelial Mesenchymal Transformation of Hepatocellular Carcinoma Cells via ERK1/2 Signaling. *Int J Mol Sci* **24**, doi:10.3390/ijms24010073 (2022).
28 Meier, S. M. *et al.* An Organoruthenium Anticancer Agent Shows Unexpected Target Selectivity For Plectin. *Angewandte Chemie (International ed. in English)* **56**, 8267-8271, doi:10.1002/anie.201702242 (2017).
29 Jiu, Y. *et al.* Bidirectional Interplay between Vimentin Intermediate Filaments and Contractile Actin Stress Fibers. *Cell Rep* **11**, 1511-1518, doi:10.1016/j.celrep.2015.05.008 (2015).
30 Burgstaller, G., Gregor, M., Winter, L. & Wiche, G. Keeping the vimentin network under control: cell-matrix adhesion-associated plectin 1f affects cell shape and polarity of fibroblasts. *Mol Biol Cell* **21**, 3362-3375, doi:10.1091/mbc.E10-02-0094 (2010).
31 Bodor, D. L., Ponisch, W., Endres, R. G. & Paluch, E. K. Of Cell Shapes and Motion: The Physical Basis of Animal Cell Migration. *Dev Cell* **52**, 550-562, doi:10.1016/j.devcel.2020.02.013 (2020).
32 Yolland, L. *et al.* Persistent and polarized global actin flow is essential for directionality during cell migration. *Nat Cell Biol* **21**, 1370-1381, doi:10.1038/s41556-019-0411-5 (2019).
33 Revia, S. *et al.* Histone H3K27 demethylase KDM6A is an epigenetic gatekeeper of mTORC1 signalling in cancer. *Gut* **71**, 1613-1628, doi:10.1136/gutjnl-2021-325405 (2022).
34 Subramanian, A. *et al.* Gene set enrichment analysis: a knowledge-based approach for interpreting genome-wide expression profiles. *Proc Natl Acad Sci U S A* **102**, 15545-15550, doi:10.1073/pnas.0506580102 (2005).
35 Llovet, J. M. *et al.* Hepatocellular carcinoma. *Nat Rev Dis Primers* **7**, 6, doi:10.1038/s41572-020-00240-3 (2021).
36 Singal, A. G. *et al.* AASLD Practice Guidance on prevention, diagnosis, and treatment of hepatocellular carcinoma. *Hepatology* **78**, 1922-1965, doi:10.1097/HEP.0000000000000466 (2023).
37 Ladd, A. D., Duarte, S., Sahin, I. & Zarrinpar, A. Mechanisms of drug resistance in HCC. *Hepatology* **79**, 926-940, doi:10.1097/HEP.0000000000000237 (2024).
38 Liu, Y. H. *et al.* Cytokeratin 18-mediated disorganization of intermediate filaments is induced by degradation of plectin in human liver cells. *Biochem Biophys Res Commun* **407**, 575-580, doi:10.1016/j.bbrc.2011.03.066 (2011).
39 Uhlen, M. *et al.* A pathology atlas of the human cancer transcriptome. *Science* **357**, doi:10.1126/science.aan2507 (2017).
40 Flores, I. L. *et al.* EEF1D modulates proliferation and epithelial-mesenchymal transition in oral squamous cell carcinoma. *Clin Sci (Lond)* **130**, 785-799, doi:10.1042/CS20150646 (2016).
41 Yang, Z. *et al.* Putative biomarkers of malignant transformation of sinonasal inverted papilloma into squamous cell carcinoma. *J Int Med Res* **47**, 2371-2380, doi:10.1177/0300060519838385 (2019).

42 Paumard-Hernandez, B. *et al.* Whole exome sequencing identifies PLEC, EXO5 and DNAH7 as novel susceptibility genes in testicular cancer. *Int J Cancer* **143**, 1954-1962, doi:10.1002/ijc.31604 (2018).

43 Yin, X., Kong, L. & Liu, P. Identification of prognosis-related molecular subgroups based on DNA methylation in pancreatic cancer. *Clin Epigenetics* **13**, 109, doi:10.1186/s13148-021-01090-w (2021).

44 Strouhalova, K. *et al.* Vimentin Intermediate Filaments as Potential Target for Cancer Treatment. *Cancers (Basel)* **12**, doi:10.3390/cancers12010184 (2020).

45 Tolba, R., Kraus, T., Liedtke, C., Schwarz, M. & Weiskirchen, R. Diethylnitrosamine (DEN)-induced carcinogenic liver injury in mice. *Lab Anim* **49**, 59-69, doi:10.1177/0023677215570086 (2015).

46 Lee, J. S. *et al.* Application of comparative functional genomics to identify best-fit mouse models to study human cancer. *Nat Genet* **36**, 1306-1311, doi:10.1038/ng1481 (2004).

47 Moon, S. H. *et al.* p53 Represses the Mevalonate Pathway to Mediate Tumor Suppression. *Cell* **176**, 564-580 e519, doi:10.1016/j.cell.2018.11.011 (2019).

48 Buckup, M. *et al.* Plectin is a regulator of prostate cancer growth and metastasis. *Oncogene* **40**, 663-676, doi:10.1038/s41388-020-01557-9 (2021).

49 Pal, K. *et al.* Multifaceted peptide assisted one-pot synthesis of gold nanoparticles for plectin-1 targeted gemcitabine delivery in pancreatic cancer. *Nanoscale* **9**, 15622-15634, doi:10.1039/c7nr03172f (2017).

50 Perez, S. M., Dimastromatteo, J., Landen, C. N., Jr. & Kelly, K. A. A Novel Monoclonal Antibody Targeting Cancer-Specific Plectin Has Potent Antitumor Activity in Ovarian Cancer. *Cells* **10**, doi:10.3390/cells10092218 (2021).

51 Abrahamsberg, C. *et al.* Targeted ablation of plectin isoform 1 uncovers role of cytolinker proteins in leukocyte recruitment. *Proc Natl Acad Sci U S A* **102**, 18449-18454, doi:10.1073/pnas.0505380102 (2005).

52 Zrelski, M. M. *et al.* Plectin Deficiency in Fibroblasts Deranges Intermediate Filament and Organelle Morphology, Migration, and Adhesion. *J Invest Dermatol* **144**, 547-562 e549, doi:10.1016/j.jid.2023.08.020 (2024).

53 Katada, K. *et al.* Plectin promotes migration and invasion of cancer cells and is a novel prognostic marker for head and neck squamous cell carcinoma. *J Proteomics* **75**, 1803-1815, doi:10.1016/j.jprot.2011.12.018 (2012).

54 McInroy, L. & Maatta, A. Plectin regulates invasiveness of SW480 colon carcinoma cells and is targeted to podosome-like adhesions in an isoform-specific manner. *Exp Cell Res* **317**, 2468-2478, doi:10.1016/j.yexcr.2011.07.013 (2011).

55 Sutoh Yoneyama, M. *et al.* Vimentin intermediate filament and plectin provide a scaffold for invadopodia, facilitating cancer cell invasion and extravasation for metastasis. *Eur J Cell Biol* **93**, 157-169, doi:10.1016/j.ejcb.2014.03.002 (2014).

56 Wenta, T. *et al.* Disassembly of alpha6beta4-mediated hemidesmosomal adhesions promotes tumorigenesis in PTEN-negative prostate cancer by targeting plectin to focal adhesions. *Oncogene* **41**, 3804-3820, doi:10.1038/s41388-022-02389-5 (2022).

57 Bhattacharya, R. *et al.* Recruitment of vimentin to the cell surface by beta3 integrin and plectin mediates adhesion strength. *J Cell Sci* **122**, 1390-1400, doi:10.1242/jcs.043042 (2009).

58 Burch, T. C., Watson, M. T. & Nyalwidhe, J. O. Variable metastatic potentials correlate with differential plectin and vimentin expression in syngeneic androgen independent prostate cancer cells. *PLoS One* **8**, e65005, doi:10.1371/journal.pone.0065005 (2013).

59 Cappuyns, S., Corbett, V., Yarchoan, M., Finn, R. S. & Llovet, J. M. Critical Appraisal of Guideline Recommendations on Systemic Therapies for Advanced Hepatocellular Carcinoma: A Review. *JAMA oncology* **10**, 395-404, doi:10.1001/jamaoncol.2023.2677 (2024).

60 Llovet, J. M., Montal, R., Sia, D. & Finn, R. S. Molecular therapies and precision medicine for hepatocellular carcinoma. *Nat Rev Clin Oncol* **15**, 599-616, doi:10.1038/s41571-018-0073-4 (2018).

61 Llovet, J. M. *et al.* Sorafenib in advanced hepatocellular carcinoma. *N Engl J Med* **359**, 378-390, doi:10.1056/NEJMoa0708857 (2008).

62 Yau, T., Chan, P., Epstein, R. & Poon, R. T. Evolution of systemic therapy of advanced hepatocellular carcinoma. *World J Gastroenterol* **14**, 6437-6441, doi:10.3748/wjg.14.6437 (2008).

63 Yau, T. *et al.* Nivolumab in advanced hepatocellular carcinoma: Sorafenib-experienced Asian cohort analysis. *J Hepatol* **71**, 543-552, doi:10.1016/j.jhep.2019.05.014 (2019).

64 Bakewell, S. J. *et al.* Suppression of stress induction of the 78-kilodalton glucose regulated protein (GRP78) in cancer by IT-139, an anti-tumor ruthenium small molecule inhibitor. *Oncotarget* **9**, 29698-29714, doi:10.18632/oncotarget.25679 (2018).

65 Burris, H. A. *et al.* Safety and activity of IT-139, a ruthenium-based compound, in patients with advanced solid tumours: a first-in-human, open-label, dose-escalation phase I study with expansion cohort. *ESMO Open* **1**, e000154, doi:10.1136/esmoopen-2016-000154 (2016).

66 Flocke, L. S., Trondl, R., Jakupec, M. A. & Keppler, B. K. Molecular mode of action of NKP-1339 - a clinically investigated ruthenium-based drug - involves ER- and ROS-related effects in colon carcinoma cell lines. *Invest New Drugs* **34**, 261-268, doi:10.1007/s10637-016-0337-8 (2016).

67 Meier-Menches, S. M. *et al.* Time-dependent shotgun proteomics revealed distinct effects of an organoruthenium prodrug and its activation product on colon carcinoma cells. *Metallomics* **11**, 118-127, doi:10.1039/c8mt00152a (2019).

68 Wernitznig, D. *et al.* Plecstatin-1 induces an immunogenic cell death signature in colorectal tumour spheroids. *Metallomics* **12**, 2121-2133, doi:10.1039/d0mt00227e (2020).

69 Ackerl, R. *et al.* Conditional targeting of plectin in prenatal and adult mouse stratified epithelia causes keratinocyte fragility and lesional epidermal barrier defects. *Journal of cell science* **120**, 2435-2443, doi:10.1242/jcs.004481 (2007).

Figures & Figure legends

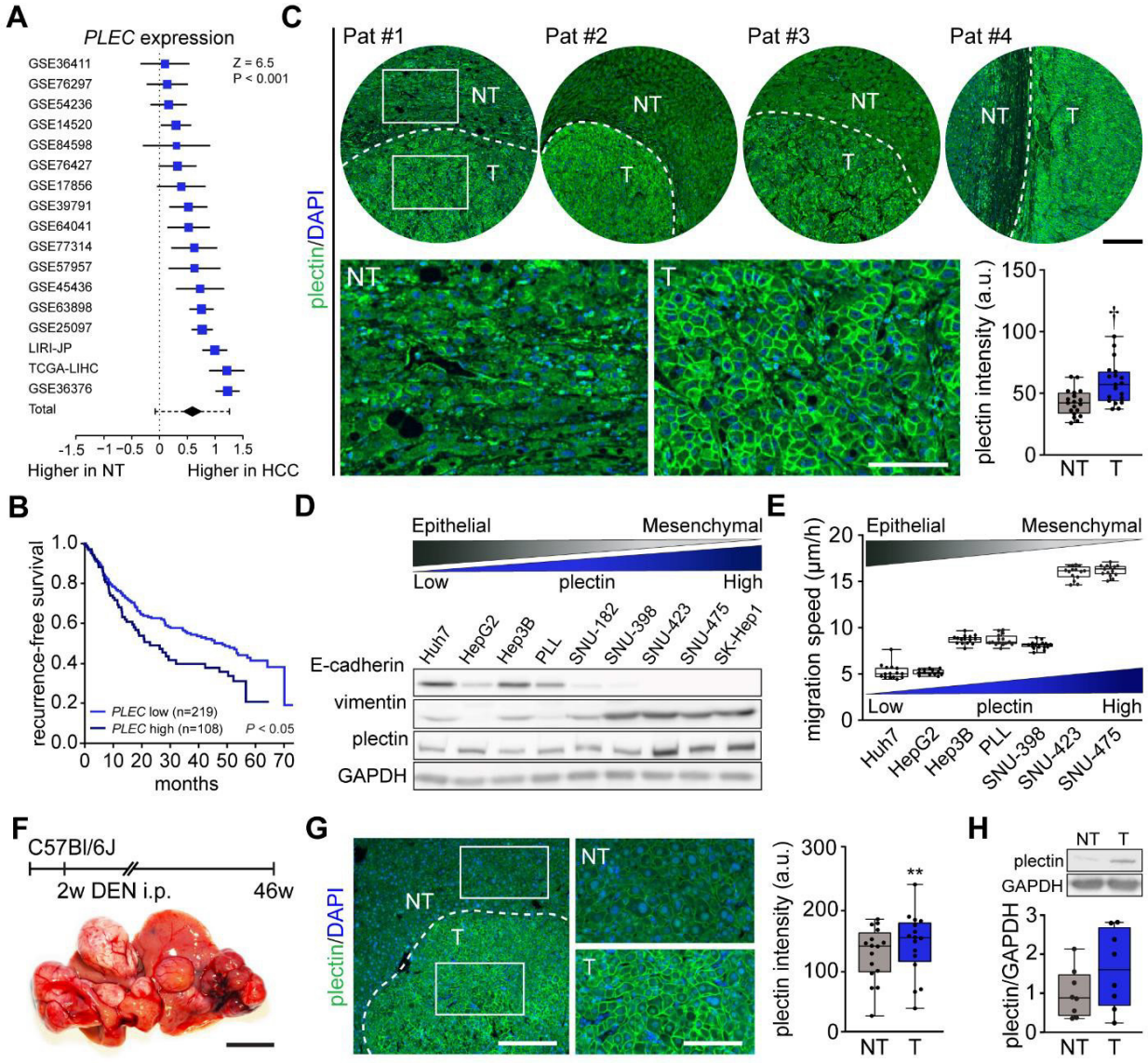

Figure 1. Plectin elevation in tumor hepatocytes is associated with HCC progression and poor prognosis. (A) Meta-analysis of differential *plectin* (*PLEC*) mRNA expression in non-tumor (NT) liver and hepatocellular carcinoma (HCC) patients. Blue squares indicate the standardized mean difference (SMD) and 95% confidence interval of individual datasets. The black diamond shows the mean and 95% confidence interval for the combined SMD, while the whiskers indicate the 95% prediction interval. **(B)** Kaplan-Meier curve of recurrence-free survival of HCC patients with low *PLEC* (lower 2 tertiles, *n* = 219) and high *PLEC* (top tertile, *n* = 108) mRNA expression. Log-rank test; $P < 0.05$. **(C)** Representative images of human HCC tissue sections immunolabeled for plectin (green). Nuclei, DAPI (blue). Dashed line, the borderline between non-tumor (NT) and tumor (T) area. Boxed areas, x4 images. Scale bars, 200 and 100 µm (boxed areas). Boxplot shows quantification of plectin fluorescence intensities in NT and T areas. The box represents the median, 25th, and 75th percentile;

whiskers reach the last data point; dots, individual patients; $N = 19$. Paired two-tailed *t*-test; ǂ$P < 0.001$. **(D)** Immunoblot analysis of indicated HCC cell lines with antibodies to plectin, E-cadherin, and vimentin. GAPDH, loading control. **(E)** Quantification of the speed of indicated HCC cell lines migrating in the scratch-wound assay. Boxplots show the median, 25th, and 75th percentile with whiskers reaching the last data point; dots, fields of view; $n = 15$ (Huh7), 13 (HepG2), 15 (Hep3B), 15 (PLL), 15 (SNU-398), 15 (SNU-423), 15 (SNU-475) fields of view; $N = 3$. **(F)** Hepatocarcinogenesis was induced in two-week-old C57Bl/6J mice by intraperitoneal injection of DEN. Representative image of the livers with multifocal HCC at 46 weeks post-induction. Scale bar, 1 cm. **(G)** Representative image of DEN-induced HCC section immunolabeled for plectin (green). Nuclei, DAPI (blue). Dashed line, the borderline between non-tumor (NT) and tumor (T) area. Boxed areas, x2 images. Scale bars, 200 and 100 µm (boxed areas). Quantification of plectin fluorescence intensities in NT and T areas. Boxplot shows the median, 25th, and 75th percentile with whiskers reaching the last data point; dots, fields of view; $n = 16$ fields of view; $N = 4$. Paired two-tailed *t*-test; $^{**}P < 0.01$. **(H)** Immunoblot analysis of NT and T liver lysates. The boxplot shows relative plectin band intensities normalized to GAPDH. The box represents the median, 25th, and 75th percentile; whiskers reach the last data point; dots, individual mice; $N = 8$.

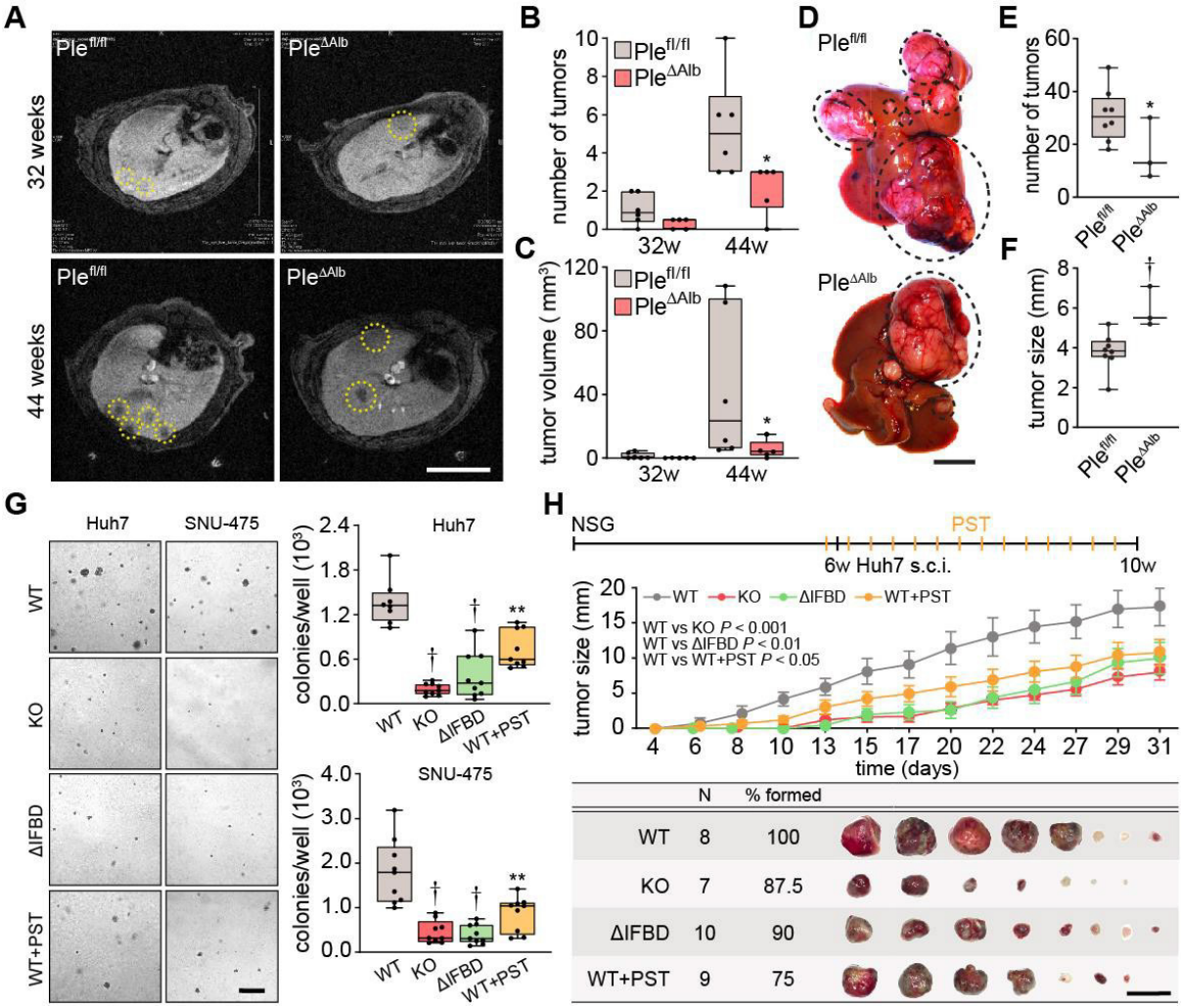

Figure 2. Plectin promotes HCC growth. (A) Representative MRI images of *Ple*$^{fl/fl}$ and *Ple*$^{\Delta Alb}$ livers at 32 and 44 weeks post-DEN injection. Dashed circles, tumors. Scale bar, 500 µm. **(B, C)** Quantification of tumor number (B) and volume (C) in *Ple*$^{fl/fl}$ and *Ple*$^{\Delta Alb}$ livers shown in (A). Boxplot shows the median, 25th, and 75th percentile with whiskers reaching the last data point; dots, individual mice; N = 6 (*Ple*$^{fl/fl}$), 5 (*Ple*$^{\Delta Alb}$). Two-tailed t-test; *$P < 0.05$. **(D)** Representative images of *Ple*$^{fl/fl}$ and *Ple*$^{\Delta Alb}$ livers at 44 weeks post-induction. Dashed circles, tumors. Scale bar, 1 cm. **(E, F)** Quantification of the number (E) and size (F) of *Ple*$^{fl/fl}$ and *Ple*$^{\Delta Alb}$ tumors shown in (D). Boxplot shows the median, 25th, and 75th percentile with whiskers reaching the last data point; dots, individual mice; N = 8 (*Ple*$^{fl/fl}$), 3 (*Ple*$^{\Delta Alb}$). Two-tailed t-test; *$P < 0.05$; †$P < 0.001$. **(G)** Representative images of colonies from WT, KO, ΔIFBD, and PST-treated WT (WT+PST) Huh7 and SNU-475 cells grown in soft agar. Scale bar, 500 µm. Boxplots show the number of Huh7 (upper graph) and SNU-475 (lower graph) cell colonies. The box represents the median, 25th, and 75th percentile with whiskers reaching the last data point; dots, agar wells; n = 9 agar wells; N = 3. Two-tailed t-test; **$P < 0.01$; †$P < 0.001$. **(H)** Six-week-old NSG mice were subcutaneously injected with indicated Huh7 cells into both hind flanks and were kept either untreated (WT, KO, and ΔIFBD) or daily treated by orogastric gavage of plecstatin (WT+PST) as

indicated in upper bar. Mice were sacrificed 4 weeks post-injection and xenografts were dissected. The graph shows the time course of xenograft growth. Data are shown as mean ± SEM; n = 8 (WT), 7 (KO), 10 (ΔIFBD) and 9 (WT+PST) tumors; *N* = 4 (WT), 4 (KO), 5 (ΔIFBD) and 6 (WT+PST). Two-way ANOVA. The table shows the number (N), percentage, and representative images of formed xenografts. Scale bar, 2 cm.

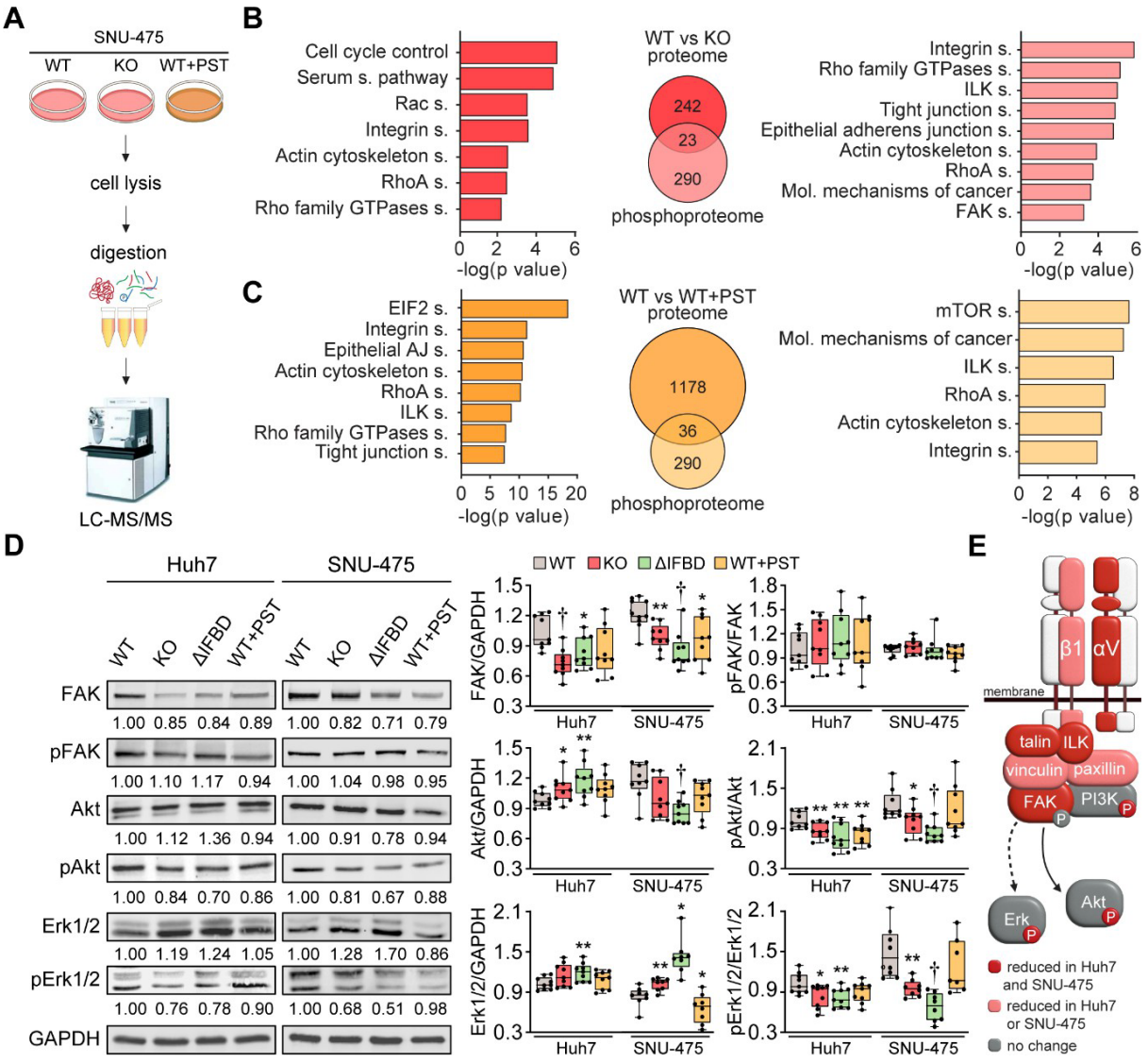

Figure 3. CRISPR/Cas9- or PST-mediated plectin inactivation attenuates HCC oncogenic potential through FAK, Erk1/2, and PI3K/Akt axis. (A) Schematic of MS-based proteomic analysis of WT, KO, and PST-treated WT (WT+PST) SNU-475 cells. **(B,C)** Ingenuity Pathway Analysis (IPA) canonical signaling pathways predicted from differentially expressed proteins identified by proteomics (left) and phosphoproteomics (right) in WT vs. KO (B) and WT vs. WT+PST (C) proteomes. Venn diagrams show relative proportions of differentially expressed proteins. Two-sided Student´s *t*-test with multiple testing correction: FDR < 0.05; s0 = 0.1; triplicates. **(D)** Quantification of FAK, phospho-Tyr397-FAK (pFAK), Akt, phospho-Ser473-Akt (pAkt), Erk1/2, and phospho-Thr202/Tyr204-Erk (pErk) in indicated Huh7 and SNU-475 cell lines by immunoblotting. GAPDH, loading control. The numbers below lines indicate relative band intensities normalized to average WT values. Boxplots show relative band intensities normalized to GAPDH or non-phosphorylated protein. The box represents the median, 25th, and 75th percentile with whiskers reaching the last data point; dots, individual experiments; *N*

= 9. Two-tailed *t*-test; **P* < 0.05; ***P* < 0.01; †*P* < 0.001. **(E)** Schematic representation of immunoblot analyses of adhesome-associated signaling shown in (F) and (Extended Data Fig. 2h). Proteins with significantly reduced expression levels and/or phosphorylation status (P) upon plectin inactivation in both HCC cell lines are highlighted in red, proteins with significantly reduced expression levels upon plectin inactivation in either Huh7 or SNU-475 cells are highlighted in pink.

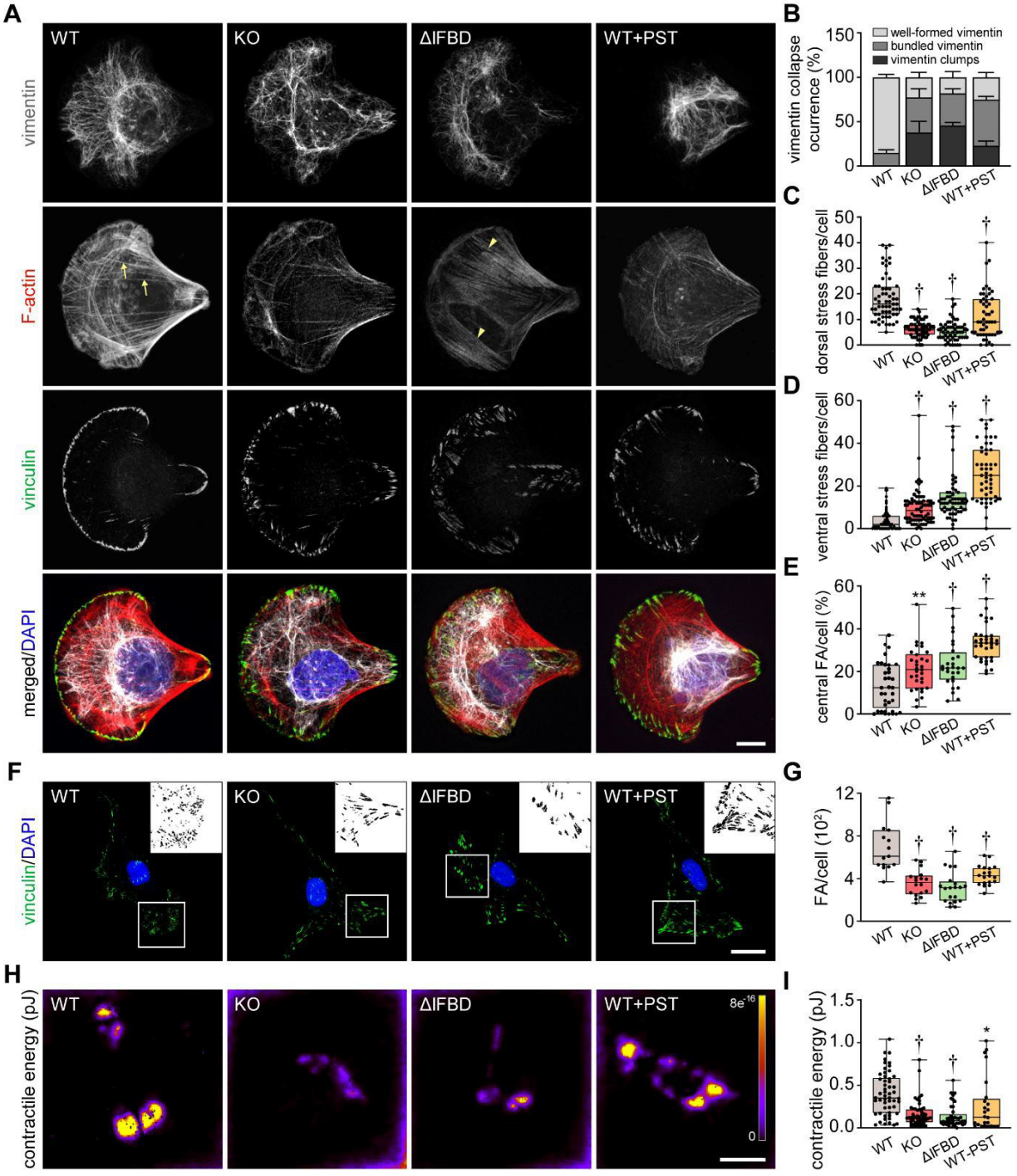

Figure 4. Disruption of cytoskeletal networks upon plectin inactivation accounts for reduced contractility and aberrant adhesions in HCC cells. (A) Representative confocal images of crossbow-shaped fibronectin micropattern-seeded WT, KO, ΔIFBD, and PST-treated WT (WT+PST) SNU-475 cells stained for F-actin (red), vinculin (green), and vimentin (grey). Nuclei, DAPI (blue). Arrows, dorsal stress fibers; arrowheads, ventral stress fibers. Scale bar, 10 µm. **(B)** Quantification of the percentage of cells (shown in (A)) with well-formed, bundled, and clump-containing vimentin networks. Data are shown as mean ± SEM; *n* = 60 (WT), 68 (KO), 55 (ΔIFBD), 50 (WT+PST) cells; *N* = 4 (WT, KO, IFBD), 3 (WT+PST).

(C,D) Quantification of the number of dorsal (C) and ventral (D) actin stress fibers in cells shown in (A). Boxplots show the median, 25th, and 75th percentile with whiskers reaching the last data point; dots, individual cells; n = 60 (WT), 68 (KO), 55 (ΔIFBD), 50 (WT+PST); N = 4 (WT, KO, IFBD), 3 (WT+PST). Two-tailed t-test; †$P < 0.001$. **(E)** Quantification of FAs located within the interior of cells (central) shown in (A). Boxplot shows the median, 25th and 75th percentile with whiskers reaching the last data point; dots, individual cells; n = 25 (WT), 26 (KO), 23 (ΔIFBD), 28 (WT+PST); N = 3. **$P < 0.01$; †$P < 0.001$. **(F)** Representative confocal images of WT, KO, ΔIFBD, and PST-treated WT (WT+PST) SNU-475 cells immunolabeled for vinculin (green). Nuclei, DAPI (blue). Boxed areas, representative FA clusters shown as segmented binary maps in x2 enlarged insets. Scale bar, 30 µm. **(G)** Quantification of FA number in cells shown in (F). Boxplot shows the median, 25th, and 75th percentile with whiskers reaching the last data point; dots, individual cells; n = 15 (WT), 18 (KO), 20 (ΔIFBD), 19 (WT+PST); N = 3. Two-tailed t-test; †$P < 0.001$. **(H)** Pseudocolor spatial maps of contractile energy determined by TFM in WT, KO, ΔIFBD, and PST-treated WT (WT+PST) SNU-475 cells. Scale bar, 50 µm. **(I)** Quantification of contractile energy in cells shown in (H). Boxplots show the median, 25th, and 75th percentile with whiskers reaching the last data point; dots, individual cells; n = 54 (WT), 53 (KO), 41 (ΔIFBD), 24 (WT+PST) cells; N = 4. Two-tailed t test; *$P < 0.05$; **$P < 0.01$; †$P < 0.001$.

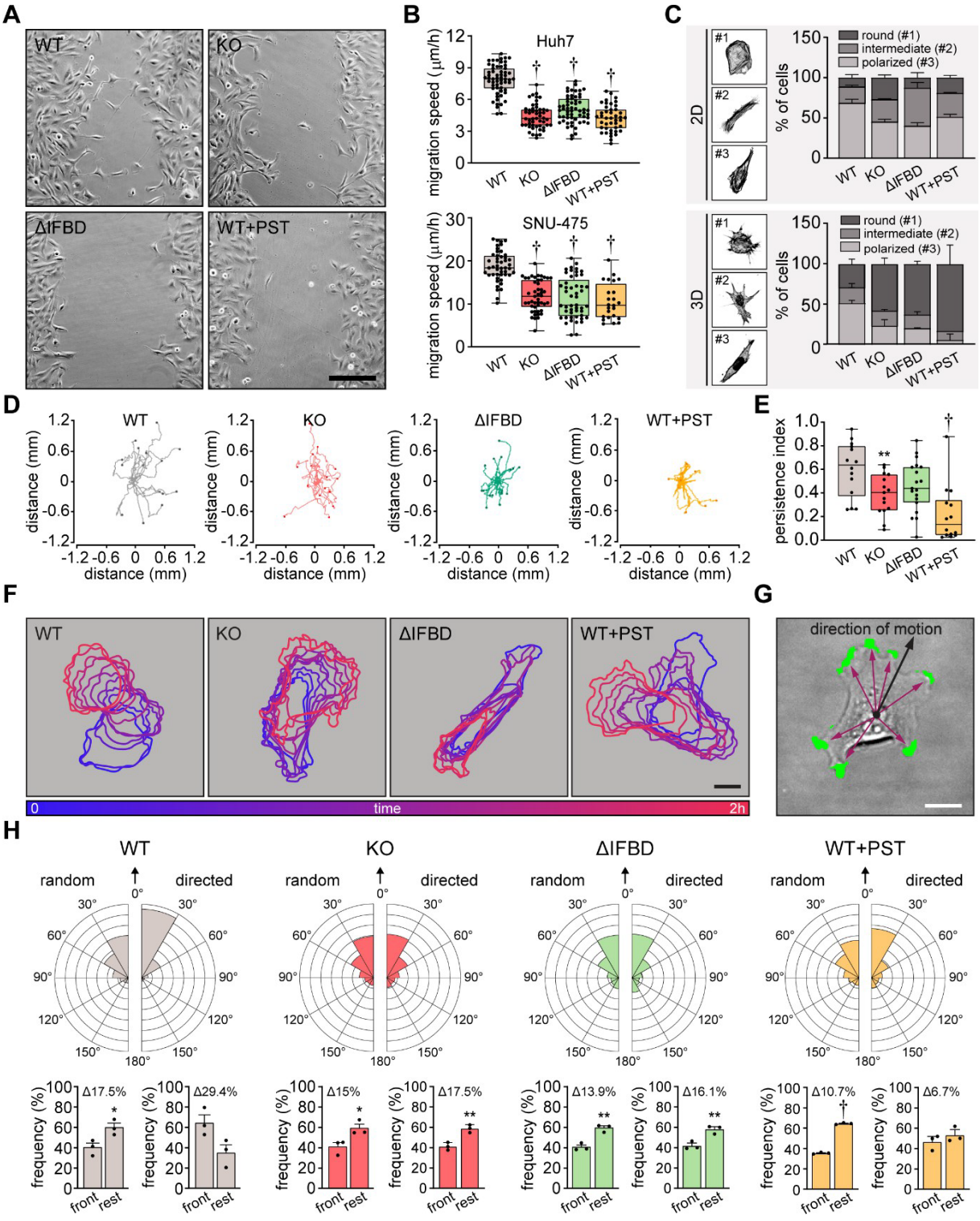

Figure 5. Plectin links migration potential of HCC cells to cell shape dynamics. (A) Representative phase contrast images of WT, KO, ΔIFBD, and PST-treated WT (WT+PST) SNU-475 cells migrating in the scratch-wound assay for 14 hours. Note individual, highly polarized WT cells frequently migrating into scratch areas. Scale bar, 200 µm. **(B)** Quantification of migration speed of indicated Huh7 (upper graph) and SNU-475 (lower graph) cells. Boxplots show the median, 25th, and 75th percentile with

whiskers reaching the last data point; dots, fields of view; *n* (Huh7) = 59 (WT), 51 (KO), 58 (ΔIFBD), 43 (WT+PST); *n* (SNU-475) = 47 (WT), 47 (KO), 50 (ΔIFBD), 24 (WT+PST); *N* (Huh7) = 3; *N* (SNU-475) = 5 (WT, KO, ΔIFBD), 3 (WT+PST). Two-tailed *t*-test;† $P < 0.001$. **(C)** Representative confocal images of F-actin stained WT, KO, ΔIFBD, and PST-treated WT (WT+PST) SNU-475 cells grown on fibronectin-coated coverslips (2D) or in collagen (3D) and classified as round (#1), intermediate (#2), and polarized (#3) shape. Quantification of the percentage of cell shape categories in indicated 2D and 3D SNU-475 cell cultures. Data are shown as mean ± SEM; *N* (2D) = 3; *N* (3D) = 5 (WT), 3 (KO, ΔIFBD), 2 (WT+PST). **(D)** Spider plots with migration trajectories of WT, KO, ΔIFBD, and PST-treated WT (WT+PST) SNU-475 cells tracked during 16 hours of EGF-guided migration; dots, the final position of each single tracked cell. **(E)** Quantification of processivity indices of WT, KO, ΔIFBD, and PST-treated WT (WT+PST) SNU-475 cells. Boxplot shows the median, 25th, and 75th percentile with whiskers reaching the last data point; dots, individual cells; *n* = 15 (WT), 15 (KO), 19 (ΔIFBD), 14 (WT+PST); *N* = 3. Two-tailed *t*-test; **$P < 0.01$;† $P < 0.001$. **(F)** Representative time sequences of the WT, KO, ΔIFBD, and PST-treated WT (WT+PST) SNU-475 cell contours during EGF-guided migration. Color coding indicates the time of cell position acquired in 10-minute intervals. Scale bar, 20 µm. **(G)** Representative phase contrast image of SNU-475 cell with protrusions (green) segmented from superimposed contours used in morphodynamic analysis. Extension vectors (purple arrows) were drawn from the center of the cell nucleus towards individual protrusions and related to the direction of cell motion (black arrow). Scale bar, 20 µm. **(H)** Rose graphs show the percentage of extension vector directions in 30° cones, normalized to the directions of random and EGF-guided (directed) motions (0°; arrows) of WT, KO, ΔIFBD, and PST-treated WT (WT+PST) SNU-475 cells. *n* = 9752 extensions in 22 cells (WT random), 4167 extensions in 15 cells (WT directed), 8394 extensions in 19 cells (KO random), 5107 extensions in 15 cells (KO directed), 8362 extensions in 21 cells (ΔIFBD random), 5809 extensions in 19 cells (ΔIFBD directed), 9450 extensions in 20 cells (WT+PST random), 4350 extensions in 14 cells (WT+PST directed); *N* = 3. Bar graphs show the percentage of cell extensions formed either in the direction of motion (frontal, 30° to -30° cones) or along the rest of the cell perimeter (rest). Data are shown as mean ± SEM; dots, biological replicates; *N* = 3. Two-tailed *t*-test; *$P < 0.05$; **$P < 0.01$;† $P < 0.001$.

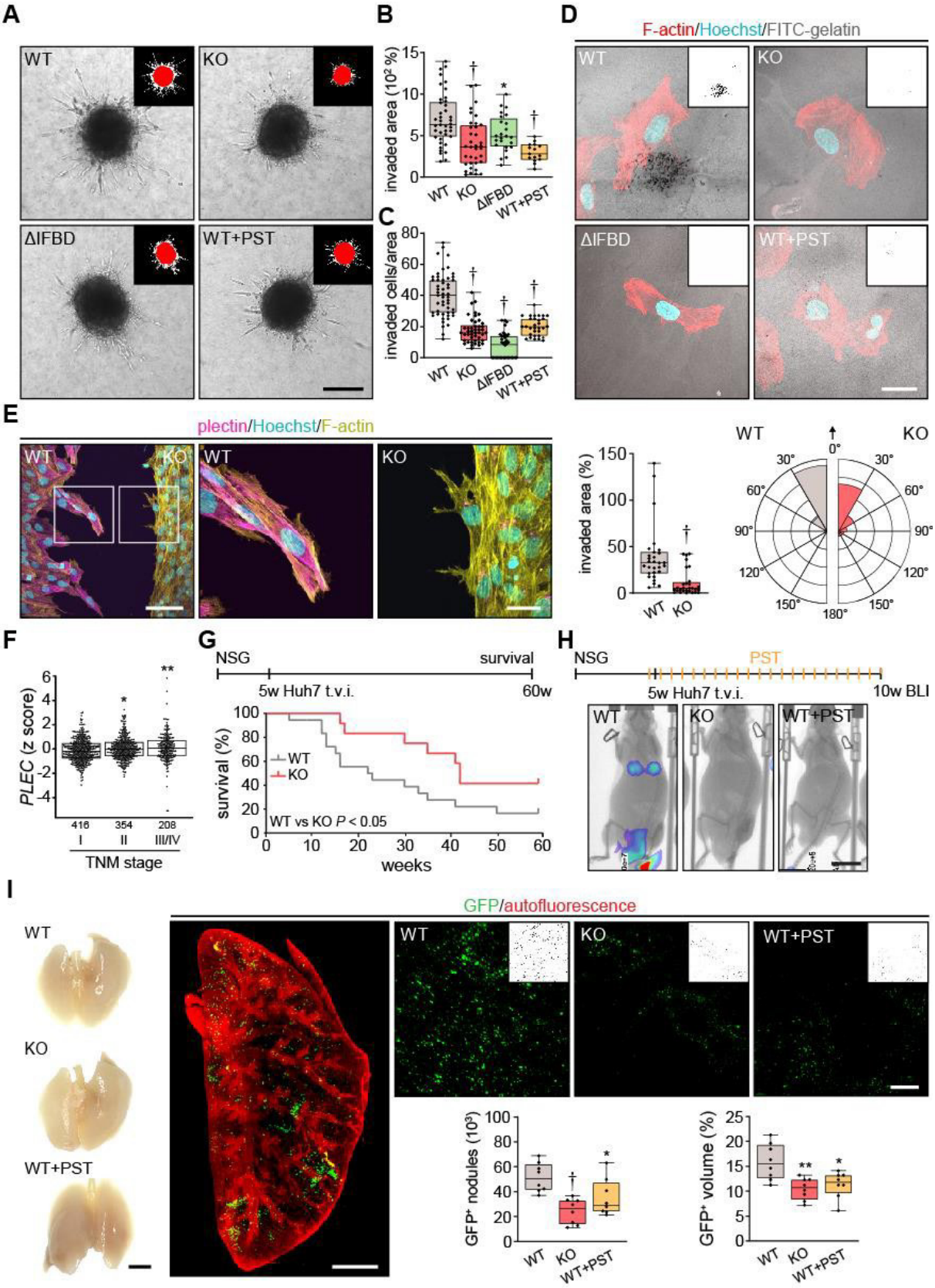

Figure 6. Plectin inactivation inhibits HCC invasion and metastasis. (A) Representative images of WT, KO, ΔIFBD, and PST-treated WT (WT+PST) SNU-475 spheroids grown for 3 days in collagen mixture. Insets, superimposed binary masks of initial (red) and final (white) spheroid area. Scale bar, 200 µm.

(B) Quantification of the invaded area calculated as the percentage of the initial spheroid area from day 0. Boxplots show the median, 25th, and 75th percentile with whiskers reaching the last data point; dots, individual spheroids; *n* = 47 (WT), 44 (KO), 34 (ΔIFBD), 25 (WT+PST) spheroids; *N* = 5 (WT, KO), 4 (ΔIFBD), 3 (WT+PST). Two-tailed *t*-test; $^{**}P < 0.01$; $\dagger P < 0.001$. **(C)** Quantification of the number of indicated cells invaded in Matrigel transwell assay. Boxplots show the median, 25th, and 75th percentile with whiskers reaching the last data point; dots, fields of view; *n* = 51 (WT), 45 (KO), 38 (ΔIFBD), 31 (WT+PST) fields of view; *N* = 4 (WT, KO), 3 (ΔIFBD, WT+PST). Two-tailed *t*-test; $\dagger P < 0.001$. **(D)** Representative confocal micrographs of WT, KO, ΔIFBD, and PST-treated WT (WT+PST) SNU-475 cells grown on FITC-labeled gelatin (grey) for 24 hours and stained for F-actin (red). Nuclei, Hoechst (blue). Insets, segmented binary masks of FITC-gelatin signal. Black regions correspond to gelatin areas degraded by individual cells. Scale bar, 30 µm. **(E)** Representative confocal images of WT and KO SNU-475 cells during the Matrigel invasion assay, stained for plectin (magenta) and F-actin (yellow). Nuclei, Hoechst (blue). See Video 1. Boxed areas, x3 images. Scale bars, 100 and 30 µm (boxed areas). Boxplot shows the invaded area calculated as the percentage of the initial area covered by WT and KO cells. The box represents the median, 25th, and 75th percentile with whiskers reaching the last data point; dots, fields of view; *n* = 29 fields of view; *N* = 2. Rose graphs show the percentage of extension vector directions in 30° cones, normalized to the directions of cell motions (0°; arrow) during matrigel invasion. *n* = 857 extensions in 18 cells (WT), 623 extensions in 12 cells (KO); *N* = 2. Two-tailed *t*-test; $\dagger P < 0.001$. **(F)** Relative *plectin* (*PLEC*) mRNA expression in samples collected from HCC patient meta-cohort clustered based on TNM classification (stage I-IV). The meta-cohort includes 6 different datasets from 5 platforms (for details, see Materials and methods section). The numbers of participants per stage are indicated in the graph. Scattered boxplots show individual data points, median, 25th, and 75th percentile; *N* = 978. Wilcoxon rank-sum test; $^{*}P < 0.05$; $^{**}P < 0.01$. **(G)** The 5-week-old NSG mice were injected (t.v.i.) with WT and KO RedFLuc-GFP-expressing Huh7 cells generated for lung colonization assay. Kaplan-Meier curves show the overall survival of mice injected with the cells indicated. *N* = 14 (WT), 13 (KO). Long-rank test, $P < 0.05$. **(H)** The 5-week-old NSG mice were injected (t.v.i.) with indicated RedFLuc-GFP-expressing Huh7 cells. WT cell-bearing mice were kept either untreated or every second day provided with orogastric gavage of plecstatin (WT+PST) as indicated. Five weeks post-injection mice were screened by whole-body bioluminescence imaging (BLI). Representative BLI images of WT, KO, and PST-treated WT (WT+PST) Huh7 cells-bearing mice are shown. Scale bar, 2 cm. **(I)** Representative images of lungs dissected from mice shown in (H). Scale bar, 1 cm. Representative lattice light sheet fluorescence image of clear, unobstructed brain imaging cocktails (CUBIC)-cleared lung lobe immunolabeled with antibodies against GFP (green). Autofluorescence visualizing the lobe structures is shown in red. Scale bar, 2 mm. Representative

magnified images from lung lobes with GFP-positive WT, KO, and WT+PST Huh7 nodules. Insets, segmented binary masks of GFP-positive metastatic nodules. Scale bar, 400 µm. Boxplots show metastatic load in the lungs expressed as the number (left graph) and relative volume (right graph) of indicated GFP-positive (GFP^+) nodules. The box represents the median, 25th, and 75th percentile with whiskers reaching the last data point; dots, lung lobes; n = 8 lung lobes; N = 4. Two-tailed t-test; *P < 0.05; **P < 0.01; †P < 0.001.

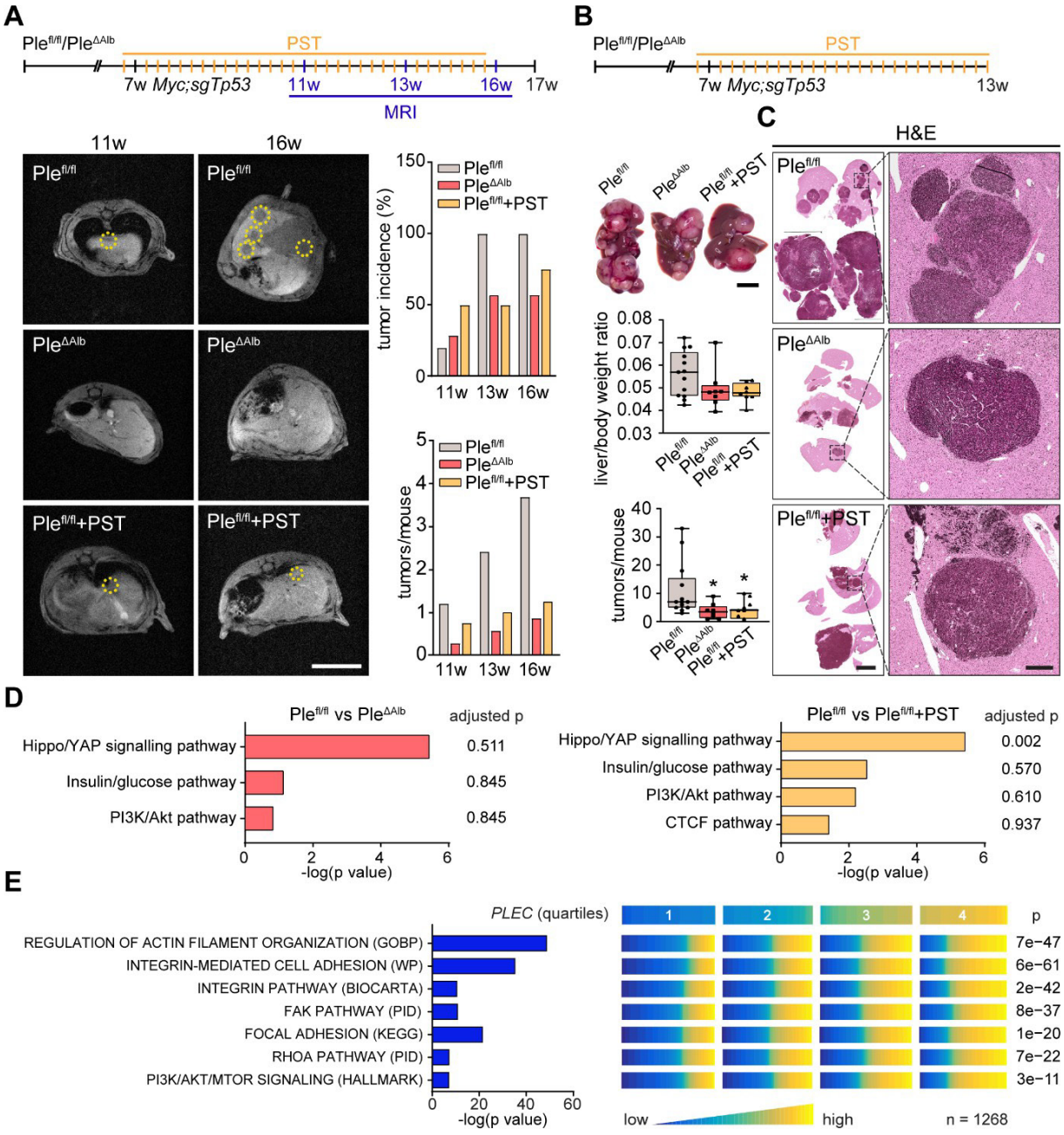

Figure 7. Genetic and pharmacological plectin targeting prevents hepatocarcinogenesis through signatures shared by animal models and patients. (A) HCC-predisposing lesions were introduced by hydrodynamic gene delivery via tail vein injection (HDTVi) of transposon vector encoding cMyc in conjunction with CRISPR/Cas9 construct targeting *Tp53* (Myc;sgTp53) in *Ple*$^{fl/fl}$ and *Ple*$^{\Delta Alb}$ cohorts of 7-week-old male mice. *Ple*$^{fl/fl}$ mice were kept either untreated or every second day provided with orogastric gavage of plecstatin (*Ple*$^{fl/fl}$+PST) and the development of HCC was monitored by MRI at 11, 13, and 16 week, as indicated. Representative MRI images of *Ple*$^{fl/fl}$ and *Ple*$^{\Delta Alb}$ and *Ple*$^{fl/fl}$+PST tumors acquired at indicated time points. Dashed circles, tumors. Scale bar, 2 cm. Graphs show the average number of tumors (lower graph) and percentual tumor incidence (upper graph) inferred from MRI

images. *N* = 5 (*Ple*$^{fl/fl}$), 7 (*Ple*$^{\Delta Alb}$), 4 (*Ple*$^{fl/fl}$+PST). **(B)** Myc;sgTp53 HCC was induced in *Ple*$^{fl/fl}$, *Ple*$^{\Delta Alb}$, and PST-treated *Ple*$^{fl/fl}$ (*Ple*$^{fl/fl}$+PST) male mice as in (A). Shown are representative images of *Ple*$^{fl/fl}$, *Ple*$^{\Delta Alb}$, and *Ple*$^{fl/fl}$+PST livers from mice with fully developed multifocal HCC sacrificed 6 weeks post-induction. Scale bar, 1 cm. Boxplots show tumor burden in the livers expressed as the liver/body weight ratio (upper graph) and number of tumors per mouse (lower graph). The box represents the median, 25th, and 75th percentile with whiskers reaching the last data point; dots, mice; *N* = 12 (*Ple*$^{fl/fl}$), 9 (*Ple*$^{\Delta Alb}$), 10 (*Ple*$^{fl/fl}$+PST). Two-tailed *t*-test; **P* < 0.05. **(C)** Representative images of H&E-stained *Ple*$^{fl/fl}$, *Ple*$^{\Delta alb}$, and *Ple*$^{fl/fl}$+PST liver sections. Note darker areas corresponding to HCC lesions. Boxed areas, x12 images. Scale bars, 5 and 1 mm (boxed areas). **(D)** Gene set enrichment analysis of differentially regulated proteins in *Ple*$^{fl/fl}$ vs *Ple*$^{\Delta Alb}$ and *Ple*$^{fl/fl}$ vs *Ple*$^{fl/fl}$ + PST livers from the cohort shown in (A). Prediction of canonical signaling pathways in *Ple*$^{fl/fl}$ vs *Ple*$^{\Delta Alb}$ (left) and *Ple*$^{fl/fl}$ vs *Ple*$^{fl/fl}$ + PST (right) proteomes. **(E)** Association of plectin-dependent signatures compiled from human HCC-derived cells (see Fig. 3B-E) and mouse models (see Fig. 7D) with *plectin* (*PLEC*) mRNA expression in HCC patients. Right panel shows the levels of selected signatures in patients grouped into quartiles of *PLEC* expression level. *N* = 1268. *P* values were generated from an analysis of variance (ANOVA).

Supplemental Material

Plectin-mediated cytoskeletal crosstalk as a target for inhibition of hepatocellular carcinoma growth and metastasis.

Zuzana Outla, Gizem Oyman-Eyrilmez, Katerina Korelova, Magdalena Prechova, Lukas Frick, Lenka Sarnova, Piyush Bisht, Petra Novotna, Jan Kosla, Patricia Bortel, Yasmin Borutzki, Andrea Bileck, Christopher Gerner, Mohammad Rahbari, Nuh Rahbari, Emrullah Birgin, Bibiana Kvasnicova, Andrea Galisova, Katerina Sulkova, Andreas Bauer, Njainday Jobe, Ondrej Tolde, Eva Sticova, Daniel Rosel, Tracy O'Connor, Martin Otahal, Daniel Jirak, Mathias Heikenwälder, Gerhard Wiche, Samuel M. Meier-Menches, Martin Gregor

Supplemental Materials and Methods

Patient tissue samples

Formalin-fixed paraffin-embedded (FFPE) human liver tissue specimens were prepared at the Department of Surgery of the University Hospital Mannheim. The cohort consisted of 21 patients diagnosed with HCC (for details, see Supplementary file 1). Tissue collection and analysis were performed in accordance with institutional review board guidelines (reference no. 2012-293N-MA), and written informed consent was obtained from all included patients.

Animals

Liver-specific deletion of the plectin (Plec) gene was achieved by crossing *Plectin*$^{flox/flox}$ mice (*Ple*$^{fl/fl}$)[1] with *Alb-Cre* transgenic mice (MGI 2176228; The Jackson Laboratory, Bar Harbor, ME) to generate *Plectin*$^{lox/lox/Alb\text{-}Cre}$ (*Ple*$^{\Delta Alb}$) mice[2]. Immunodeficient NOD.Cg-Prkdcscid Il2rgtm1Wjl/SzJ (NSG) mice were purchased from the Czech Centre for Phenogenomics (BIOCEV – Institute of Molecular Genetics Academy of Sciences, Prague, Czechia)

Animals were housed under specific pathogen-free conditions with regular access to chow and drinking water and 12 h light/12 h dark conditions. All animal studies were performed in accordance with European Directive 86/609/EEC and were approved by the Czech Central Commission for Animal Welfare. Age-matched littermate mice were used in all experiments. The details regarding animal treatments can be found in the following sections.

Xenograft tumorigenesis

6-week-old NSG male mice were kept in a pathogen-free environment, and procedures were performed in a laminar airflow cabinet. 2.5×10^6 Huh7 cells in 250 µl PBS mice were administered subcutaneously in the left and right hind flanks. Animals were treated by orogastric gavage with plecstatin-1 every other day at a dose of 30 mg/kg. Before administration, plecstatin-1 was dissolved in olive oil. Tumor development was monitored by caliper measurement over 28 days before the mice were sacrificed and tissue samples were collected.

DEN-induced HCC mouse model

2-week-old *Ple*$^{fl/fl}$ and *Ple*$^{\Delta Alb}$ mice received intraperitoneal injection of 25 mg/kg diethylnitrosamine (DEN; Sigma-Aldrich, St. Louis, MO, USA) diluted in PBS. Mice were monitored for tumor formation 30 and 42 weeks after the DEN injection by magnetic resonance imaging (MRI), and tumor volumes were calculated from MRI images (for details see Magnetic resonance imaging

section). Mice were sacrificed at 44 weeks post-injection, livers were dissected and tumors were measured using a caliper.

Lung colonization assay

Huh7 and SNU-475 cell lines stably expressing Red Firefly Luciferase reporter and GFP were prepared by lentiviral transfection of LentiGlo™ pLenti-CMV-RedFluc-IRES-EGFP plasmid (LP-31, Targeting Systems, El Cajon, CA, USA) according to manufacturer´s protocol. Next, 2×10^6 Huh7 or SNU-475 cells suspended in serum-free Dulbecco's modified Eagle medium (DMEM, Sigma-Aldrich) were injected into the tail vein of 5-week-old NSG mice. Mice were monitored for survival, and bioluminescence imaging was used to test for the presence of lung metastasis after 5 weeks. Prior to imaging, mice were anesthetized with isoflurane and injected intraperitoneally with D-luciferin potassium salt (Promega, Madison, WI, USA). Ten to fifteen min after injection, luciferase activity was measured using LagoX (Spectral Instruments Imaging, Tuscon, AZ, USA).

To prepare lung clearing samples, mice were injected with heparin (500 UI, Zentiva, Prague, Czechia) and after 15 min, mice were sacrificed by cervical dislocation and then perfused with 20 ml of PBS (pH 7.4) followed by 30 ml of 4% (w/v) paraformaldehyde (PFA) in PBS via the left ventricle of the heart. The excised organs were post-fixed in 4% (w/v) PFA at 4 °C for 24 h. The lungs were washed with PBS twice for 3 h and one time for 16 h to remove PFA just before clearing. The fixed lungs were immersed in 50% (v/v) clear, unobstructed brain imaging cocktails and computational analysis (CUBIC-1; 35w% water, 25 w% urea, 25w% N,N,N',N'-tetrakis(2-hydroxypropyl)ethylenediamine and 15w% Triton X-100; 1:1 mixture of H_2O and CUBIC-1) for more than 12 h and further immersed in CUBIC-1 with gentle shaking at 37 °C for 14 days. CUBIC-1 solution was refreshed every 2 days during the procedure. After decolorization and de-lipidation, the lungs were washed with PBS three times for 2 h. Lung samples after decolorization and de-lipidation were subjected to indirect immunostaining with anti-GFP antibody (1:100, A-11122, Invitrogen, Waltham, MA, USA) diluted in the staining buffer composed of 0.5% (v/v) Triton X-100, 0.4% BSA (BSA-1, Capricorn Scientific GmbH, Ebsdorfergrund, Germany) and 0.01% sodium azide for 5 days at room temperature (RT) with gentle shaking. The stained samples with primary antibody were washed with PBS three times for 3 h at RT and subsequently incubated for 5 days with secondary antibody anti-rabbit-AlexaFluor-594 (1:400, A11037, Life Technologies, Thermo-Fisher Scientific, Carslbad, CA, USA) at RT with gentle shaking. The stained samples with secondary antibody were washed with PBS three times for 3 h at RT.

Lung lobes were imaged using a Carl Zeiss Lightsheet Z1 microscope (Carl Zeiss AG, Oberkochen, Germany) with 5×/NA 0.15 objective with digital zoom 2. Lasers of 488 nm Solid-state laser 30 mW and 561 nm Solid-state laser 20 mW, were used for acquisition. The images were visualized and

captured with Imaris software (version 10.1.0, Bitplane AG, Schlieren, Switzerland). The number of GFP positive foci was analyzed using a custom-made macro in ImageJ (NIH, USA) created by Martin Capek, Imaging Methods Core Facility (IMCF), Institute of Molecular Genetics (IMG).

HDTVi-induced HCC mouse model

For hydrodynamic tail vein injections, a mixture of plasmid containing 5 µg/ml of px330-expressing Tp53 sgRNA, 5 µg/ml of pT3-EF1a MYC DNA (92046, Addgene, Watertown, MA, USA), and 0.5 µg/ml pCMV HSB2 sleeping beauty transponase was prepared in sterile 0.9% sodium chloride (NaCl). 7-weeks-old $Ple^{fl/fl}$ and $Ple^{\Delta Alb}$ mice were pre-warmed for 15 min using two infrared lamps (IL 11, Beuer GmbH, Ulm, Germany), placed in a restrainer (TV-RED-150_STD, Braintree Scientific INC., Braintree, MA, USA) and injected into the lateral tail vein with a total volume corresponding 10% of body weight over 5–7 s. All animals were monitored daily, and animal experiments were performed in compliance with all relevant ethical regulations described in the animal permit. After mice were sacrificed, livers and lungs were visually inspected, excised, and photographed. Tumor samples were taken to obtain protein and the remaining liver tissue was incubated in 4% PFA for at least 24 h for FFPE tissue preparation.

Proteomics on mouse tissue - sample preparation

PBS-washed, snap-frozen livers were cut on dry ice and an aliquot of approximately 30 mg was suspended in 100 µl of lysis buffer (64 mM DTT, 8 M urea, 20% SDS, 1 M TEAB at pH 7.55). Each sample was homogenized using an ultra-sonicator. The samples were centrifuged (5000 g, 10 min, 4 °C), and the supernatant was transferred to a labeled Eppendorf tube and denatured at 95 °C for 5 min. Lysed tissues were stored at –20 °C.

Magnetic resonance imaging

Mice were anesthetized by inhalation of 1-2% isoflurane (Aerrane, Sigma-Aldrich) in atmospheric air. Animals were kept on a water tube heating pad to maintain constant body temperature. Breathing rate (~80 bpm) was monitored (ECG Trigger Unit, Rapid Biomedical, Rimpar, Germany). Imaging experiments were performed on a 4.7T horizontal bore MRI experimental system (Bruker Biospec 47/20, Ettlingen, Germany). A self-made wide-tunable 1H volume surface coil was used, which was optimized for whole-body mouse MRI (coil diameter = 35 mm). The livers were localized using axial T2*-weighted gradient echo sequence (repetition time (TR) 112 ms; echo time (TE) 3.7 ms; flip angle 30 °; averages = 4; field of view (FOV) 35×35 mm; plane resolution = 137x137 µm; slice thickness = 1.5 mm; scan time 1 min 54 s). Axial 1H T1-weighted anatomical images

were acquired by gradient echo sequence (repetition time (TR) = 130 ms; echo time (TE) = 3.7 ms; flip angle = 70 °; averages =32; field of view (FOV) 35×35 mm; plane resolution = 137x137 µm; slice thickness 0.75 mm; scan time 17 min 44 s) to cover the whole liver. The pulse program and data processing were managed by Paravision 4.0 (Paravision, Bruker); then all data were post-processed and evaluated in ImageJ.

Cell culture

The human Huh7, Hep3B, PLC/PRF/5, SNU-398, SNU-423, and SNU-475 HCC cell lines were maintained in DMEM supplemented with 10% fetal bovine serum (FBS, Gibco, Thermo-Fisher Scientific) and 1% penicillin-streptomycin (Sigma-Aldrich) in 5% CO_2/air humidified atmosphere at 37 °C.

CRISPR-mediated targeting of plectin

Plectin KO cell lines were generated using the CRISPR/Cas9 system, by targeting exon 6 of *plectin* (Ensembl Plec-205), which encodes the essential actin-binding domain (ABD) and is shared among plectin isoforms. Single DNA sequence coding gRNA targeting sequence (AGTTGTCGCATCGCAGGCCC) was designed. To generate ΔIFBD mutant cell lines, an array of crRNA targeting sequences within exon 32 flanking the IFBD (5'-ACCCTAACACGGAGGAGAACCTC-3' and 5'-CGCTCCCGTTCCTCCTCGGTGGG-3') linked with short spacer sequence was designed (5'-AgatACCCTAACACGGAGGAGAACCTCAATTTCTACTCTTGTAGATCGCTCCCGTTCCTCCTCGGTGGG-3'). DNA sequences coding guide RNA targeting sequences and crRNA array were synthesized and subcloned into a modified version of a px330-Cas9-Venus[2] using *BbsI* restriction site, where Cas9 was fused to monomeric Venus as a selection marker. For WT cell generation, the px330-Cas9-Venus vector lacking the guide RNA targeting sequence was used. The vectors were transiently transfected into cells using Lipofectamine® LTX with Plus™ Reagent (Life Technologies) according to the manufacturer's instructions. Cells were incubated with the transfection complexes for 48 h, followed by fluorescence-activated cell sorting (FACS). Single-cell clones were FACS sorted into 96-well plates, and plectin knockout or mutation was confirmed by DNA sequencing and immunoblot analysis.

Plecstatin treatment in vitro

Plecstatin-1 (PST) was synthesized at the Faculty of Chemistry, University of Vienna, as previously described[3]. To determine IC_{50} of PST, Huh7 and SNU-475 cells were seeded at a density of 5×10^4 cells/ml in a 96-well plate and incubated under standard conditions overnight. Next, the PST was diluted with culture medium to the desired concentration and cancer cells were treated for 96 h.

The cell viability was measured by absorbance using (3-(4, 5-dimethylthiazolyl-2)-2, 5-diphenyltetrazolium bromide) (MTT) viability assay (Sigma-Aldrich) according to the manufacturer´s protocol.

If not stated otherwise, PST was used at a concentration of 8 µM for 4 h. Stocks were dissolved in dimethylsulfoxide to a concentration of 4 mM and diluted in complete medium.

Anchorage-independent growth in soft agar

The wells of a 6-well plate were coated with 1.5 ml of 0.5% low-gelling temperature agarose (Sigma-Aldrich) solution dissolved in a standard culture medium. After solidification, 2×10^3 cells were suspended in 1 ml of 0.35% agarose in culture medium seeded on top of 0.5% agarose and overlaid with 200 µl culture medium. Cells were cultured for 28 days at 37 °C and 5% CO_2, and culture medium was exchanged once a week. For PST treatment, PST was added to 0.35% agarose mixture and into the overlaying medium in a final concentration of 8 µM. The colonies were stained and fixed with 0.01% crystal violet in 4% PFA in PBS and captured by Carl Zeiss Axio.Zoom V.16 microscope with PlanNeoFluar Z 1.0×/0.25 NA objective. The size and area of colonies were analyzed from binary masks created using a custom-made ImageJ macro.

Micropatterning

Cells were seeded on coverslips with crossbow-shaped micropatterns (CYTOOchips CW-L-A x18, CYTOO, Grenoble, France) according to the manufacturer´s protocol. In brief, micropatterns were coated with fibronectin overnight at 4 °C. After washing with PBS and complete medium, 3×10^4 cells were plated on coverslips, placed into 6-well plates, and allowed to adhere for 10 h before fixation. For PST treatment, PST was added 6 h after seeding to a final concentration of 8 µM. Cells were fixed with 4% formaldehyde (FA) in PBS for vimentin analysis or with 4% PFA in PBS for actin stress fiber analysis for 10 min at RT and permeabilized with 2% Triton in PBS for 5 min. Cells were imaged using a confocal Leica sp8 microscope (Leica Microsystems, Wetzlar, Germany) with HC PL APO 63×/1.4 NA immersion oil objective. Images were acquired as Z-stacks and deconvolved with Huygens Essential 4.0.0 software (Huygens; Scientific Volume Imaging, Hilversum, The Netherlands) using blind deconvolution. In vimentin networks analysis, the bundles were defined as a prominent signal of thickened vimentin filaments of more than approx. 0.5 µm, the clumps present condensed vimentin signal no longer resembling filamentous pattern. The vimentin fluorescence intensity distribution and focal adhesion distribution were analyzed using custom-made ImageJ macros. The peripheral region of the cell was defined as a 3 µm-wide border of the cell edge.

Scratch wound-healing assay

1×10^5 Huh7 or SNU-475 cells were plated onto a well of 24-well plates in triplicate and incubated under standard conditions overnight to achieve 100% confluence. Prior to imaging, PST was added to a final concentration of 8 µM for 4 h. Using a 200-µl pipette tip, a linear scratch was made, running the length of each well. Subsequently, cells were washed with PBS and complete medium. To assess collective cell migration kinetics, 24-h movies for Huh7 and 18-h movies for SNU-475 with a 20-min time-lapse interval were recorded using brightfield video microscopy obtained with a Leica DMi8 with HCX PL FLUOTAR L 20×/0.40 NA objective (37 °C and 5% CO_2 in a humidified atmosphere; OKOlab, Naples, Italy). Individual fields of view were monitored in each well. The migration speed was calculated from the change of wound area between the initial and final timepoint, measured using ImageJ.

Morphology in 3D collagen

SNU-475 cells were trypsinized, washed in complete medium, and counted. 1×10^5 cells were mixed with 500 µl of 3 mg/ml Collagen R in complete medium. For PST treatment, the collagen mixture included PST at a final concentration of 8 µM. The suspension of cells in collagen (500 µl) was loaded onto a well of a 12-well plate, the gel was allowed to polymerize for 30 min at 37 °C and was subsequently overlaid with complete medium. After 24 h the cells were fixed with 4% PFA and stained with phalloidin, nuclei were counterstained with DAPI. The morphology of cells in 3D collagen was inspected using a Leica DMi8 microscope.

Single cell random and chemotaxis migration assays

SNU-475 cells were seeded at a total number of 1×10^3 onto a well of 6-well plate. Recordings of migration started 16 h after plating, and frames were taken with a Leica DMi8 with HCX PL FLUOTAR L 20×/0.4 NA objective in 5-min intervals over 20 h.

For chemotaxis experiments, 5×10^3 SNU-475 cells were seeded into Chemotaxis µ-slide (ibidi GmbH, Gräfelfing, Germany) according to the manufacturer´s protocol. Briefly, cells were incubated in 1% FBS-containing DMEM for 8 h after seeding, and chemo-attractant medium contained 20% FBS and 100 nM EGF. For plecstatin treatment, cells were treated with 8 uM PST 4 h after seeding.

The representative cell contours were generated by segmentation using ImageJ. The motion of cells was tracked using the ImageJ plugin Manual Tracking and the tracking results were analyzed using the ibidi Chemotaxis and Migration tool to generate Spider plots and processive indexes. The angle between cell protrusion and the direction of future cell motion was analyzed using a custom-made

macro, using cell trajectories from Manual tracking analysis as an input for future movement calculation.

Traction force microscopy

Fibronectin-coated 7% polyacrylamide (PAA) gels (Young's modulus 25.5 kPa, thickness 130 µm), with embedded 0.2-µm fluorescent beads were prepared as described previously[4]. Briefly, the glass-bottom dishes were pre-treated with the 1:1:14 solution of acetic acid, bind-silane, and ethanol for 15 min at RT, washed with 95% ethanol, H_2O and dried. Poly-L-lysine coated coverslips were incubated with 150 µm of 1:500 Fluorescent beads/mQH_2O (505/515, Invitrogen) for 20 min at 4 °C, subsequently washed with mQH_2O and dried. 11.8 µl of PAA gel was applied to the glass-bottomed dish, covered with a bead-coated coverglass, and incubated for 4 h at RT. After coverslip removal with tweezers and PBS wash, the gel was treated with 2 mg/ml Sulfo-SANPAH/H_2O for 5 min under UV light and coated with 10 µg/ml fibronectin overnight at 4 °C.

3×10^4 SNU-475 cells were seeded on the gels and incubated under standard conditions overnight. Prior to imaging, PST was added at a final concentration of 8 µM for 4 h. TFM imaging was performed using a Dragonfly (Andor Technology Ltd., Belfast, UK) spinning disc confocal microscope with Zyla 4.2 PLUS sCMOS camera and HC PL APO 63×/1.2 NA multi-immersion objective with water used as an immersion medium. During measurements, cells were kept in a life-cell imaging chamber (37 °C and 5% CO_2 in a humidified atmosphere; OKOlab). Gels were imaged both with the cells attached and in a relaxed state after cell trypsinization. Image acquisition was performed by Andor Technology software. Cell tractions were computed using pyTFM software[5] from images taken before and after trypsin-based cell removal.

Atomic force microscopy (AFM)

2.5×10^5 Huh7 or SNU-475 cells were seeded onto fibronectin-coated glass coverslip placed in a 35 mm well 16 h before imaging. The cell elastic modulus was measured using AFM NanoWizard Sense (JPK Instruments AG, Berlin, Germany) with cantilever HYDRA-6R-200NG (AppNano, Mountain View, CA, USA; sensitivity = 76 nm/V, force constant = 30.13 N/m), with a spherical tip of 5.2 µm diameter. The cantilever was calibrated using the indentation of a microscope slide and using thermal noise. The measurement was performed using the force spectroscopy method in contact mode, using a sampling rate of 2046 Hz, a contact force of 4.186 nN, a loading speed of 1 µm/s, and a maximal indentation z-length of 5 µm. The cell elastic modulus was measured in an area of 16x16 µm, with a force map resolution of 8x8. The fitting of the force curves was performed using the Hertz-Sneddon model, and Young's modulus values were extracted using statistical parametric mapping (SPM) Data Processing

software (JPK Instruments AG) when Poisson's ratio value of 0.5 was assumed. Young´s modulus of nuclear and cytosolic area was discerned based on the height profile, where the nucleus was defined as the area above 80% of the total cell height.

Spheroid invasion assay

5×10^5 SNU-475 cells were grown for 2 days in Microtissues® 3D Petri Dish® (Sigma-Aldrich) according to the manufacturer's protocol. Formed spheroids were then embedded in 1.5 mg/ml Collagen I (Thermo-Fisher Scientific) solution containing DMEM, 5 % $NaHCO_3$ and 10% FBS. For PST treatment, PST was added to the collagen mixture and into the overlaying medium in a final concentration of 8 µM. Using a 96-well plate, one spheroid was embedded per well in 100 µl of collagen mixture, and once collagen polymerized, 80 µl of DMEM was added to the wells. Images were taken after 3 days using a Leica DMi8 microscope with HC PL FLUOTAR 5×/0.25 NA objective. The invaded area was calculated as the percentage of the initial spheroid area using ImageJ.

Matrigel transwell invasion assay

Matrigel Basement Membrane Matrix (Corning, Corning, NY, USA) diluted 1:3 in PBS was added to 6.5-mm transwell with 8-µm pore polycarbonate membrane inserts (Corning) and allowed to solidify at 37 °C for 2 h. Next, 3×10^4 SNU-475 cells in 180 µl total volume of serum-free medium were gently seeded on the top of the gel. For PST treatment, a serum-free medium mixture contained PST in a final concentration of 8 µM. The lower chamber was filled with 800 µl of medium containing 10% FBS as an attractant. After 20 h, cells were fixed using 4% PFA in PBS and stained with 0.02% crystal violet solution in 10% ethanol. Noninvasive cells in the upper matrix layer were discarded using a cotton swab and the cells on the bottom surface of the inserts were imaged using Leica DMi8 microscope with N PLAN 10×/0.25 NA objective.

Gelatin degradation assay

Dry coverslips were coated with a chilled poly-D-lysine (50 µg/ml) for 20 min at RT, washed 3 times with PBS, and subsequently coated with 0.5% glutaraldehyde for 15 min at RT. After washing 3 times with PBS, coverslips were coated with the mixture of 1% unlabeled gelatin and 488-conjugated gelatin (G13186, Thermo-Fisher Scientific) 1:30 for 30 min at 37 °C. 3×10^4 SNU-475 cells were seeded on fluorescent gelatin-coated coverslip placed onto a well of a 12-well plate in complete medium and allowed to adhere under standard conditions overnight. After 24 h, the coverslips were washed, fixed with 4% PFA in PBS for 10 min at RT, and permeabilized with 0.2% Triton X-100 in PBS for 5 min. F-actin was stained with Alexa Fluor 594-conjugated phalloidin (Thermo-Fisher Scientific), and nuclei

were counterstained with DAPI. Cells were imaged using a Leica sp8 confocal microscope with HC PL APO 63×/1.40 NA immersion oil objective. 488-conjugated gelatin degraded area was segmented and measured using ImageJ.

Matrigel invasion assay

A biocompatible silicon self-stick cellular stopper (ibidi, 80209) was placed in the center of a 35-mm glass bottom dish (ibidi) before seeding 6×10^5 SNU-475 cells. After cells adhered, the stopper was removed and 250 µl of 50% BD Matrigel™ (4.5 mg/ml) in PBS was overlaid onto the cell monolayer to create a matrix barrier and allowed to polymerize for 2 h at 37 °C before adding growth medium on the top of the set Matrigel. Monolayers with overlaid Matrigel were then imaged with a Nikon time-lapse microscope or incubated for 24 h in a humidified atmosphere of 5% CO_2 at 37 °C before fixation and immunofluorescence. For time-lapse imaging, frames were taken using Leica DMi8 with HCX PL FLUOTAR L 20×/0.40 NA objective in 15-min intervals over 20 h. The motion of invading leader cells was tracked using the ImageJ plugin Manual Tracking. The angle between cell protrusion and the direction of future cell motion was analyzed using a custom-made ImageJ macro, using cell trajectories from Manual tracking analysis as an input for future movement calculation.

Proteomic analyses of SNU-475 cell culture – sample preparation

All steps for the sample collection process were performed on ice. 1.5×10^6 SNU-475 cells were seeded in P100 plates.

Proteomics: The cells were processed according to a nucleocytoplasmic fractionation protocol as previously described[3]. All steps were performed on ice. The medium was removed and the cells were washed twice with 1×PBS (3 mL). Then, PBS was thoroughly removed. Isotonic lysis buffer (10 mM HEPES, 10 mM NaCl, 3.5 mM MgCl2, 1 mM EGTA, 0.25 M Sucrose, 0.5% Triton X-100) containing protease inhibitors (1% PMSF, Sigma, and 1% protease and phosphatase inhibitor cocktail, Roche) was added to the wells, the cells were scraped off and transferred into labeled 15 mL Falcon tubes. The cellular membrane was ruptured using shear stress by pressing the cell suspension through a syringe 9–12 times. Membrane rupture with intact nuclei was monitored under a microscope. After centrifugation (960 g, 5 min), the supernatant containing the cytoplasmic (CYT) proteins was transferred into ice-cold ethanol (1:5, HPLC grade) and precipitated overnight at –20 °C. The pellet containing the nuclei was incubated with a hypertonic solution (10 mM Tris-HCl, 1 mM EDTA and 0.5 M NaCl) and subsequently with NP-40 buffer (10 mm Tris-HCl, 1 mm EDTA and 0.5% Triton X-100) containing protease inhibitors (1% PMSF, Sigma, and 1% protease and phosphatase inhibitor cocktail, Roche). Solubilization was assisted by an ultrasonic rod. After centrifugation (960 g, 5 min), the soluble

nuclear (NE) proteins were also transferred into ice-cold ethanol (1:5, HPLC grade) and precipitated overnight at –20 °C. The precipitated proteins were finally pelleted by centrifugation (5000 g, 30 min, 4 °C), the solution was decanted and the pellet dried under vacuum.

Phosphoproteomics: The cells were washed twice with 2 ml cold Tris-buffered saline (TBS; 25 mM Tris·HCl, 150 mM NaCl, pH 7.4). The wash buffer was completely removed. A volume of 250 µl of 4% [wt/vol] sodium deoxycholate buffer (SDC; 0.4 g SDC, 500 µl Tris·HCl (pH 8.8) in 9.5 ml H2O) was added to the well. The cells were scraped off and the whole cell lysate (WCL) was transferred to an Eppendorf® tube, which was subsequently heated to 95 °C for 5 min. WCLs were stored at –20 °C until processing.

Image acquisition and processing

If not stated otherwise, immunofluorescence images were acquired at RT using a Leica DM6000 wide-field microscope (Leica Microsystems) with Leica DFC 9000 sCMOS camera and an APO 100×/1.4 NA immersion oil objective with Type F Immersion liquid (Leica Microsystems). The acquisition was performed by LasX software (Leica Microsystems). Immunofluorescence confocal images were acquired at RT using a Leica TCS SP8 confocal fluorescence microscope (Leica Microsystems) with photomultiplier tubes (PMTs), supersensitive hybrid detectors (HyDs), and HC PL APO 63×/1.4 NA immersion oil objective, using Type F Immersion liquid (Leica Microsystems). The acquisition was performed by LasX software (Leica Microsystems). Unless stated otherwise, representative maximal projections of z-stacks, acquired from whole cell volumes are shown. Post-acquisition processing (such as formation of maximal projections, linear adjustments of brightness and contrast, inversion of grayscale images, changes in lookup tables, cropping or resizing) was performed using an open-source ImageJ image processing package[6]. Soft agar colony number and size, focal adhesion distribution, vimentin fluorescence intensity distribution, and direction of protrusion formation, were analyzed using custom-made ImageJ macros created by Jan Valecka, IMCF IMG.

Immunoblot analysis

7×10^5 cells were seeded on a P100 plate coated with fibronectin (Sigma-Aldrich) and incubated for 24 h. For PST treatment, PST in a final concentration of 8 µM was added 4 h after cell seeding. Cells were rinsed with PBS and lysed in RIPA buffer (20 mM Tris pH 7.4, 150 mM NaCl, 0.1% sodium dodecyl sulfate, 0.5% Na-Deoxycholate, 1% Triton X-100), supplemented with protease and phosphatase inhibitors (Roche, Basel, Switzerland). For liver tissue lysate preparation, snap-frozen liver tissue samples were homogenized in ice-cold RIPA buffer supplemented with a protease and phosphatase inhibitor cocktail (Roche) using the Tissue Lyzer II (Qiagen, Hilden, Germany). Protein concentrations

were determined using a BCA Protein Assay Kit (Thermo-Fisher Scientific). Proteins were separated by SDS-PAGE and transferred to nitrocellulose membranes. Membranes were incubated with 5% BSA in PBST to block non-specific antigen interactions and subsequently incubated with primary and secondary antibodies (see Supplementary file 2). Signals were detected and quantified using an Odyssey imaging system (LI-COR Biosciences, Lincoln, NE; Figure 2—figure supplement 1C, Fig. 3D, Figure 3—figure supplement 1C; Figure 5—figure supplement 1C) or using chemiluminescence *via* enhanced chemiluminescence (ECL) western blot substrates (Thermo-Fisher Scientific; Fig. 1D,H).

Immunohistochemistry and immunofluorescence of patient samples

Immunohistochemistry and immunofluorescence microscopy of patient samples were performed by Danijela Heide and Jenny Hetzer at the Department of Chronic Inflammation and Cancer, DKFZ, (Heidelberg). 2-µm sections were cut from paraffin blocks with a Microtome (Leica Biosystems, Nussloch, Germany), mounted on glass coverslips (Thermo-Fisher Scientific), and H&E stained using a Leica BOND-MAX automated staining machine. Plectin immunofluorescence staining was done with primary antibody (Progen, Heidelberg, Germany; GP21, dilution 1:500) followed by the AKOYA Biosciences Opal Fluorophore kit (Opal 620, FP1495001KT diluted 1:150) and counterstained with AKOYA 10× Spectral DAPI (FP1490) following the manufacturer's instructions. The slides were imaged with a NanoZoomer S60 Scanner (Hamamatsu, Japan) at 20× and analyzed with the NDP.view software (ver. 2.7.25, Hamamatsu).

Immunohistochemistry on murine samples

FA-fixed liver paraffin sections (4 µm) sections were subjected to heat-induced antigen retrieval in Tris-EDTA (pH 9) or citrate (pH 6) buffer and further permeabilized with 0.1 M glycine, 0.1% Triton X-100 in PBS for 15 min. Blocking of unspecific antigen interactions was performed with 5% BSA in PBS. Next, sections were incubated with primary antibodies at 4 °C overnight followed by incubation with secondary antibodies at RT for 120 min, nuclei were counterstained with DAPI. To evaluate the apoptosis rate in liver tumor samples, apoptotic cells were visualized on paraffin-embedded liver tissue sections using a Click-iT TUNEL Alexa Fluor 488 kit (ThermoFisher Scientific) according to the manufacturer's protocol. Immunofluorescence images were acquired using DM6000 (Leica Microsystems; with HC PL Apo 10×/0.40 NA and PH1 HC PLAN Apo 20×/0.70 NA objectives) and analyzed using ImageJ.

Patient analysis – data mining

To investigate the association of *plectin* mRNA expression with gene signatures and clinical parameters in HCC patients, mRNA expression datasets were obtained from online repositories including Gene Expression Omnibus (GEO), ArrayExpress, and the Cancer Genome Atlas. For Affymetrix whole-genome microarray data, raw .CEL files were processed using the SCAN (single channel array normalization) method[7], and samples with median GNUSE quality scores[8] above 1.25, as computed by the "frma" Bioconductor package, were excluded. For all other datasets, processed data from the original authors were used. Cases of fibrolamellar carcinoma were removed[9]. Across all platforms, probe or gene IDs were mapped to Entrez gene identifiers. For microarray platforms containing multiple alternative probes or probesets per gene, the probe showing the great variance in expression among HCC samples was selected. Meta-analyses across datasets were computed with the "metafor" R package[10] using a random-effects model and the DerSimonian-Laird estimator. The tumor node metastasis (TNM) analysis comprised datasets corresponding to Iizuka et al.[11], GSE14520, iCOD[12], GSE76427, GSE36376, and TCGA-LIHC from Affymetrix HuGeneFL, Affymetrix HT_HG-U133A, and Affymetrix HG-U133 Plus 2.0, Illumina HumanHT-12 V4.0, and Illumina HiSeq platforms. Collections of gene signatures were obtained from the Molecular Signatures Database (MSigDB)[13,14], and used to produce quantitative gene set enrichment scores with the "GSVA" (Gene Set Variation Analysis) Bioconductor package[15]. To assess the correlation of *PLEC* expression with various genes and pathways in human HCC, eleven datasets with extensive whole-genome RNA expression data were chosen (TCGA-LIHC[16], GSE65485, GSE50579, GSE45436, GSE62232, GSE9843[17], iCOD[18], GSE63898, GSE64041[19], GSE76297, GSE16757), and gene expression values were batch-adjusted using the ComBat method[20] as implemented by the "sva" R package. To generate t-SNE plots, the "Rtsne" package was applied to ComBat-adjusted data with a perplexity parameter of 50. The Nearest Template Prediction method[21] was used to assign HCC samples to the most likely predicted molecular subclass based on published gene lists[16,17,19,22,23]. The Kaplan-Meier survival analysis of *PLEC* expression was based on three datasets for which recurrence-free survival data was available: GSE17856, GSE14520, and GSE76427.

Proteomics on mouse tissue samples

Samples were thawed and the protein concentration was determined via bicinchoninic acid (BCA) assay and an aliquot of 20 µg of protein was used for proteomics. Proteins were reduced with dithiothreitol (DTT, 64 mM) and carbamidomethylated with iodoacetamide (148 mM). Proteolytic digestion was performed using the ProtiFi S-trap technology and samples were loaded onto S-trap mini cartridges. Trapping buffer (methanol 90% v/v, 0.1 M tetraethylammonium bromide was added.

Samples were thoroughly washed and digested with 0.5 µg trypsin/Lys-C mix (Promega) at 37 °C for 2 h (1:40 enzyme-to-protein ratio). Peptides were eluted, dried in glass inserts, and stored at -20 °C. Dried samples were reconstituted with 5 µl of a peptide standard mix consisting of the four synthetic peptides at 10 fmol in 30% formic acid (Glu1-fribrinopeptideB, EGVNDNEEGFFSAR; M28, TTPAVLDSDGSYFLYSK; HK0, VLETKSLYVR and HK1, VLETK(ε-Ac)SLYVR) and diluted with loading buffer (40 µl, acetonitrile 2% v/v, TFA 0.05% v/v; ddH2O 97.95% v/v). The glass inserts were transferred into 2 ml Eppendorf tubes filled with 400 µl ddH2O. The samples were sonicated for 5 min (20% power), centrifuged (5000 g, 7 min, RT), and transferred into labeled high-performance liquid chromatography vials.

LC-MS/MS data acquisition was performed employing a timsTOF Pro mass spectrometer (Bruker Daltonics, Bremen, Germany) hyphenated to a Dionex UltiMate™ 3000 RSLCnano system (Thermo Scientific, Bremen, Germany). Samples were analyzed in data-dependent acquisition mode by label-free quantification (LFQ) shotgun proteomics in PASEF mode[24]. Samples were loaded on an Acclaim™PepMap™ C18 HPLC pre-column (2 cm × 100 µm, 100 Å, Thermo-Fisher Scientific) at a flow rate of 10 µl/min. After trapping, peptides were eluted at a flow rate of 300 nL min^{-1} and separated on an Aurora series CSI UHPLC emitter column (25 cm × 75 µm, 1.6 µm C18, Ionopticks, Fitzroy, Australia) applying an 8–40% gradient of mobile phase B (79.9% ACN, 20% H_2O, 0.1% FA) in mobile phase A (99.9% H_2O, 0.1% FA). The injection volume was 2 µl. The gradient for the proteome profiling was selected to run over 85 min giving a total run time of 135 min per sample.

Protein identification was performed *via* MaxQuant (version 1.6.17.0) employing the Andromeda search engine against the UniProt Database (mus musculus, version 06/2021, 17'519 entries). A mass tolerance of 20 ppm for MS spectra and 40 ppm for MS/MS spectra, a PSM–, protein– and site-false discovery rate (FDR) of 0.01, and a maximum of two missed cleavages per peptide were allowed. Match-between-runs was enabled with a matching time window of 0.7 min and an alignment time window of 20 min. Oxidation of methionine and N-terminal protein acetylation were set as variable modifications. Carbamidomethylation of cysteine was set as a fixed modification. Data analysis was performed *via* Perseus software (version 1.6.14.0)[25]. Proteins with at least a 75% quantification rate in at least one group were considered for analysis. A two-sided Student's *t*-test with S0 = 0.1 and FDR cut-off of 0.05 was applied for identifying multiple testing-corrected significantly regulated proteins.

Proteomic analyses of SNU-475 cell culture

Proteomics: The protein fractions were pelleted, dried and solubilised in sample buffer (7.5 M urea, 1.5 M thiourea, 4% CHAPS, 0.05% SDS and 100 mM dithiothreitol) before the total protein

amount was determined by means of a colorimetric Bradford assay. A total of 20 µg protein per sample were then tryptically digested. This involved reduction with dithiothreitol, alkylation with iodoacetamide and digestion with trypsin/Lys-C according to a filter-assisted protein digestion (FASP) protocol[3]. The obtained peptide samples were dried in a speed-vac.

Phosphoproteomics: WCLs were thawed and lysed using the S220 Focused-ultrasonicator (Covaris, LLC., Woburn, MA, USA). Protein concentrations were determined via bicinchoninic acid assay (BCA)-assay. Between 130–220 µg of protein was reduced and alkylated with tris(2-carboxyethyl)phosphine (TCEP) and 2-chloroacetamide (2-CAM) for 5 min at 45 °C, followed by 18 h digestion with Trypsin/Lys-C (1:100 enzyme-to-substrate ratio) at 37 °C. An aliquot of 20 µg peptide was taken from each sample for global proteome analysis and dried in a vacuum concentrator. Then, the samples were reconstituted in styrenedivinylbenzene-reverse phase sulfonate (SDB-RPS) loading buffer (99% iPrOH, 1% TFA) and desalted via SDB-RPS StageTips. Desalted global proteome samples were reconstituted in 5 µL formic acid (30%) containing synthetic standard peptides at 10 fmol and diluted with 40 µL loading solvent (98% H2O, 2% ACN, 0.05% TFA). For phosphopeptide enrichment, the digested samples were mixed with enrichment buffer (52% H2O, 48% TFA, 8 mM KH2PO4) and incubated with TiO2 Titansphere beads (GL Sciences, Japan), followed by sample clean-up via C8-StageTips. Phosphopeptides were eluted and subsequently dried in a vacuum concentrator. Phosphopeptides were reconstituted in 15 µL MS loading buffer (97.7% H2O, 2% ACN, 0.3% TFA).

LC-MS/MS analyses were performed employing a timsTOF Pro mass spectrometer (Bruker Daltonics, Bremen, Germany) hyphenated with a Dionex UltiMateTM 3000 RSLCnano system (Thermo Scientific, Bremen, Germany). Samples were analyzed in data-dependent acquisition mode by label free quantification (LFQ) shotgun proteomics. The injection volume was 10 µL and 2 µL for analyzing phosphoproteomes and global proteomes, respectively. Samples were loaded on an AcclaimTMPepMapTM C18 HPLC pre-column (2 cm × 100 µm, 100 Å, Thermo Fisher Scientific™, Vienna, Austria) at a flow rate of 10 µL min-1 MS loading buffer. After trapping, peptides were eluted at a flow rate of 300 nL min-1 and separated on an Aurora series CSI UHPLC emitter column (25 cm × 75 µm, 1.6 µm C18, Ionopticks, Fitzroy, Australia) applying a gradient of 8–40% mobile phase B (79.9% ACN, 20% H2O, 0.1% FA) in mobile phase A (99.9% H2O, 0.1% FA) over 95 min.

Protein identification was performed via MaxQuant (version 1.6.17.0) employing the Andromeda search engine against the UniProt Database (version 11/2021, 20’375 entries). A mass tolerance of 20 ppm for MS spectra and 40 ppm for MS/MS spectra, a PSM–, protein– and site-false discovery rate (FDR) of 0.01, and a maximum of two missed cleavages per peptide were allowed. Match-between-runs was enabled with a matching time window of 0.7 min and an alignment time window of 20 min. Oxidation of methionine, N-terminal protein acetylation, and phosphorylation of

serine, threonine, and tyrosine were set as variable modifications. Carbamidomethylation of cysteine was set as a fixed modification. Global proteome data analysis was performed via Perseus (version 1.6.14.0). Proteins with at least 60% quantification rate in at least one group were considered for analysis. A two-sided Student's t-test with S0 = 0.1 and an FDR cut-off of 0.05 was applied for identifying multiple testing-corrected significantly regulated proteins or phosphosites.

Statistical analyses

Proteomics on mouse tissue samples proteomics of SNU-475 cell cultures (see details in corresponding sections), all graphs and statistical tests were performed using GraphPad Prism (GraphPad Software, Inc., La Jolla, CA). Rose graphs were generated using Microsoft Excel (Microsoft Corporation, Redmont, WA). In the boxplots the box margins represent the 25th and 75th percentile with the median indicated; whiskers reach the last data point. Data comparison of adjacent tumor and non-tumor tissue was performed using a paired *t*-test. Data comparison of individual experimental groups with the control group was performed using a two-tailed *t*-test. Growth curves were analyzed using two-way ANOVA. Survival curves were analyzed using the Mantel-Cox test. Data distribution was assumed to be normal, but this was not formally tested. Statistical significance was determined at the level of $*P < 0.05$, $**P < 0.01$, $\dagger P < 0.001$. The number of independent experiments (N), number of data points (n), and statistical tests used are specified for individual experiments in the figure legends.

Antibodies and reagents

For details on primary and secondary antibodies used in this study, see Supplementary file 2. The following reagents were used: AF-Phalloidin 594 (Invitrogen); low gelling temperature agarose (Sigma-Aldrich), Collagen I Rat Protein (Thermo-Fisher Scientific), Crystal Violet solution (Sigma-Aldrich), DAPI (AppliChem, Darmstadt, Germany), diethylnitrosamine (DEN; Sigma-Aldrich), mouse EGF recombinant protein (Invitrogen), Gelatin 488 Conjugate (Thermo-Fisher Scientific), Fibronectin (FN) from bovine plasma (Sigma), glutaraldehyde solution 25% (Sigma-Aldrich), heparin (Zentiva), isoflurane (Aerrane, Sigma-Aldrich), D-luciferin potassium salt (Promega), Matrigel Basement Membrane Matrix (Corning), Poly-D-Lysine solution (Sigma-Aldrich), Sulfo-SANPAH (Sigma-Aldrich), N,N,N',N'-Tetrakis (2-Hydroxypropyl)ethylenediamine (Sigma-Aldrich).

Supplemental Figures & Supplemental Figure legends

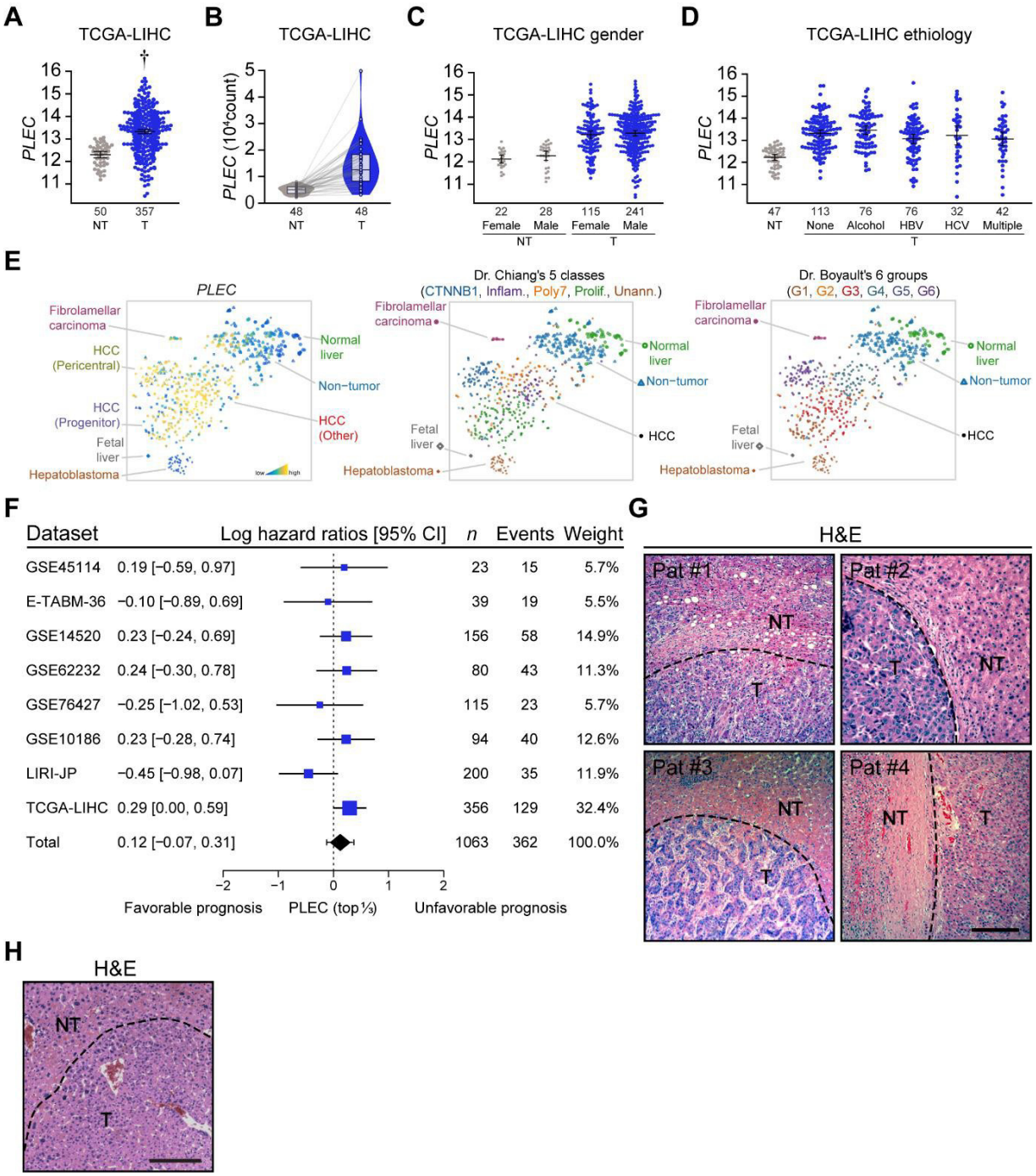

Figure 1—figure supplement 1. Plectin is elevatated in HCC across genders and etiologies. (A-D) TCGA-based analysis of *plectin* (*PLEC*) mRNA expression in non-tumor (NT) and tumor (T) tissue of liver hepatocellular carcinoma (LIHC). Graphs show differential *plectin* expression in the whole cohort (A), pair-matched samples (B), and samples sorted by gender (C) and etiology (D). The numbers of included participants per cohort are indicated in the graph. **(E)** t-SNE plots (left graph) show *plectin* (*PLEC*) mRNA expression in subgroups of HCC patients. Points, individual patient tissue samples. As a reference, t-SNE plots of Dr. Chiang's (middle graph) and Dr. Boyault's (right graph) classification are

shown. The HCC classes were predicted using the Nearest Template Prediction method. **(F)** Meta-analysis of the predictive value of *plectin* expression across different HCC datasets. Blue squares indicate the log hazard ratios and 95% confidence interval from a Cox proportional hazards model. The black diamond represents the mean and 95% confidence interval for the overall log hazard ratio, while the whiskers indicate the 95% prediction interval. **(G)** Representative images of H&E-stained human HCC tissue sections corresponding to immunofluorescence images shown in Fig. 1C. NT, non-tumor area; T, tumor area. Scale bar, 200 µm. **(H)** Representative image of H&E-stained section of DEN-induced HCC corresponding to immunofluorescence images shown in Fig. 1G. NT, non-tumor area; T, tumor area. Scale bar, 200 µm.

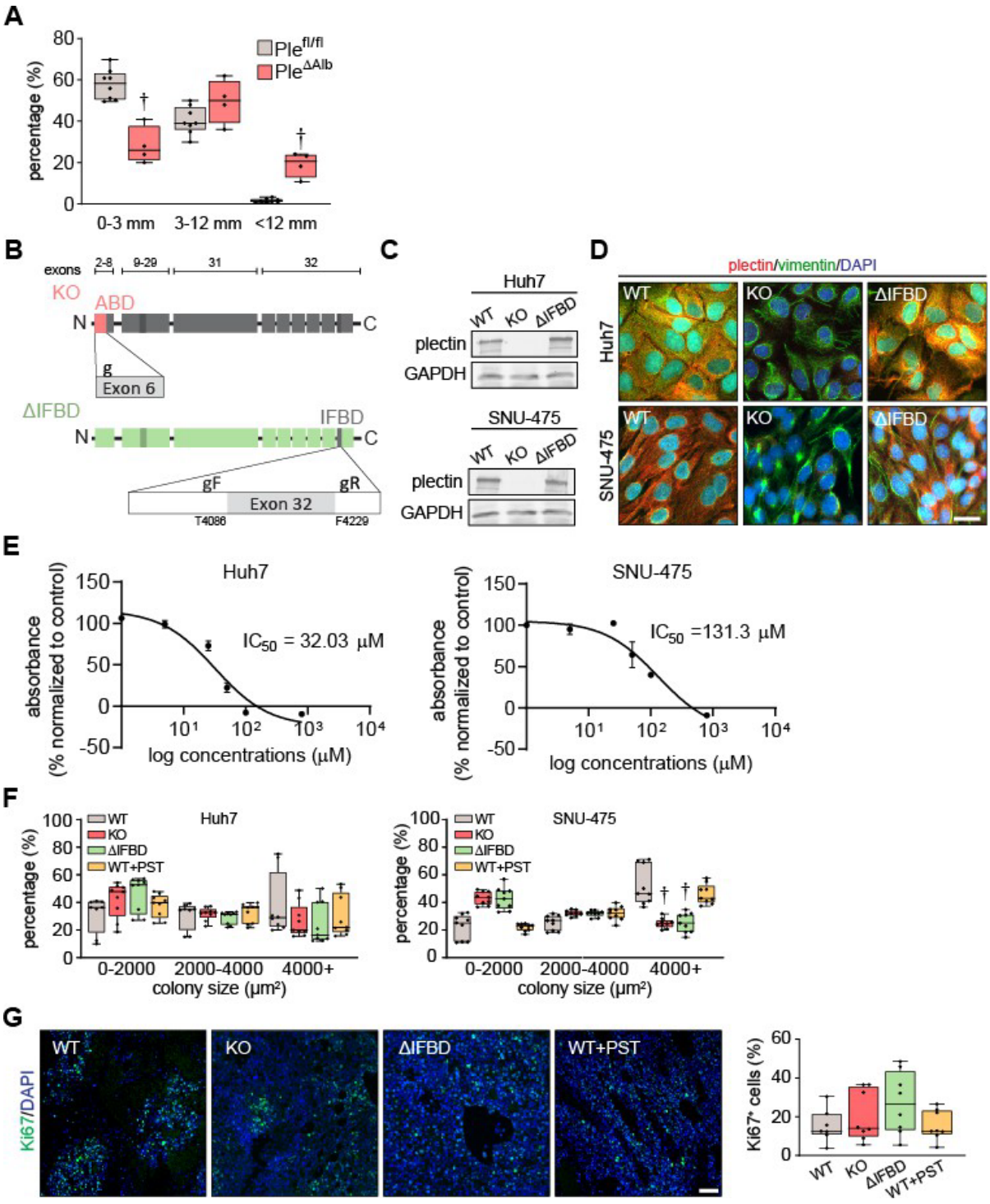

Figure 2—figure supplement 1. Plectin influences HCC progression *in vivo*. (A) Percentage of DEN-induced *Ple*$^{fl/fl}$ and *Ple*$^{\Delta Alb}$ HCCs corresponding to the indicated size intervals. Boxplot shows the median, 25th, and 75th percentile with whiskers reaching the last data point; dots, individual mice; *N* = 8 (*Ple*$^{fl/fl}$), 4 (*Ple*$^{\Delta Alb}$). Two-tailed *t*-test; †*P* < 0.001. **(B)** Schematic of CRISPR/Cas9-based strategy for the generation of plectin KO and ΔIFBD mutant HCC lines. To generate plectin KO, exon 6 of plectin was targeted by the single guide RNA (g) as previously described[26]. To generate the plectin ΔIFBD HCC lines, deletion between amino acid T4086-F4229 (Uniprot accession: Q15149-9) was introduced using

crRNA array targeting the sequences within the exon 32 flanking the IFBD. Upper bar indicates the exons encoding plectin domains shown below. For details, see the Materials and methods section. **(C)** Representative immunoblots for plectin in WT, KO, and ΔIFBD Huh7 and SNU-475 cell lines. GAPDH, loading control. **(D)** Representative images of WT, KO, and ΔIFBD Huh7 and SNU-475 cells immunolabeled for plectin (red) and vimentin (green). Nuclei, DAPI (blue). Scale bar, 10 µm. **(E)** IC_{50} curve of Huh7 and SNU-475 cells after treatment with plecstatin-1 (PST) for 96 hours. **(F)** Percentage of colonies grown from WT, KO, ΔIFBD, and PST-treated WT (WT+PST) Huh7 and SNU-475 cells within indicated size intervals. Boxplots show the median, 25th, and 75th percentile with whiskers reaching the last data point; dots, agar wells; *n* = 9 agar wells; *N* = 3. Two-way ANOVA; †*P* < 0.001. **(G)** Representative images of WT, KO, ΔIFBD, and WT+PST Huh7 xenograft sections immunolabeled for Ki67 (green). Nuclei, DAPI (blue). Scale bar, 150 µm. Quantification (percentage) of Ki67-positive cells in xenografts grown from WT, KO, ΔIFBD, and WT+PST Huh7 cells shown in Fig. 2H. Boxplot shows the median, 25th and 75th percentile with whiskers reaching the last data point; dots, individual tumors; *N* = 7 (WT), 8 (KO), 8 (ΔIFBD), 8 (WT+PST).

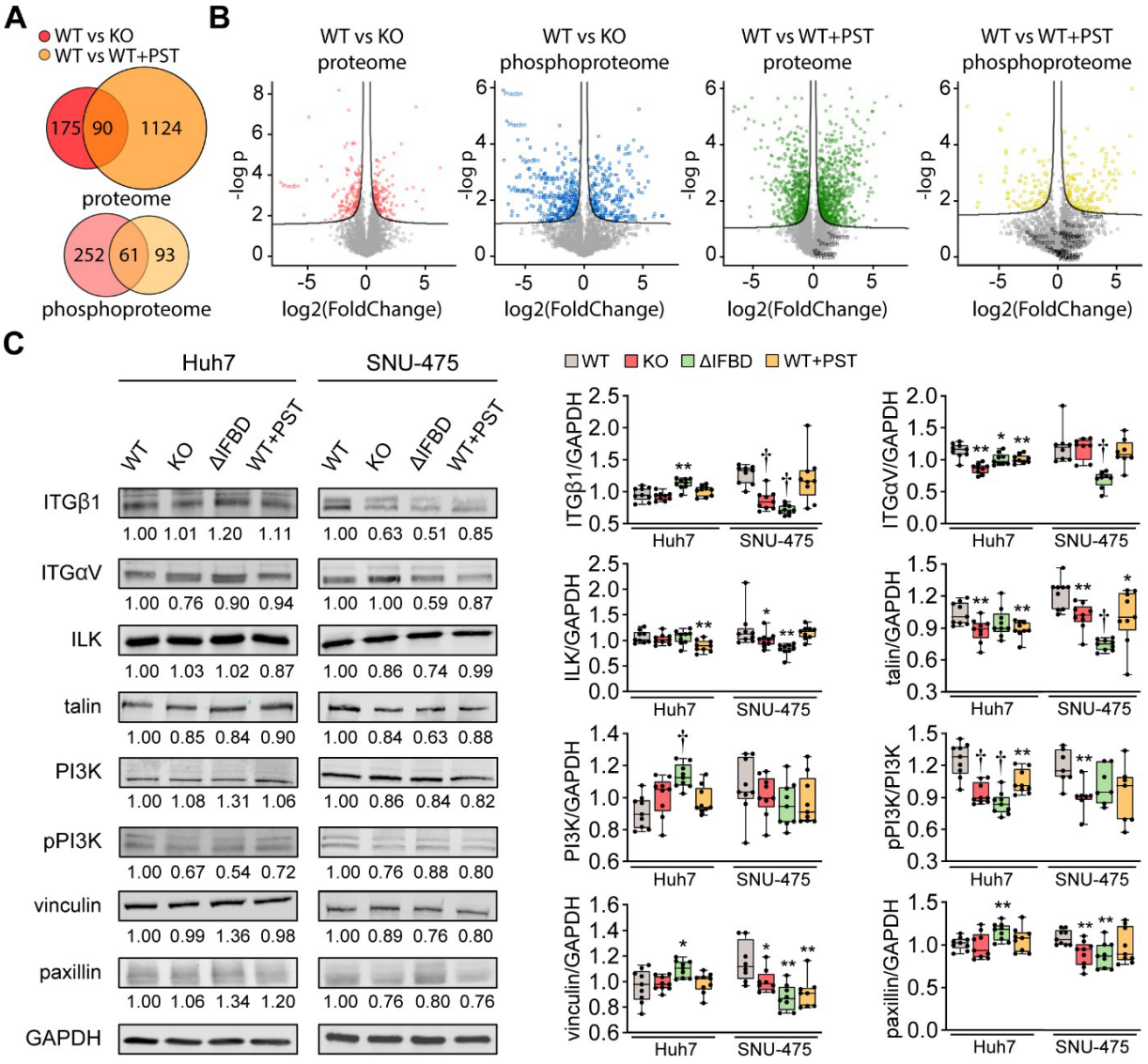

Figure 3—figure supplement 1. Integrin-associated signaling is altered in SNU-475 cells upon CRISPR/Cas9- or PST-mediated plectin inactivation. (A) Venn diagrams show relative proportions of differentially expressed/phosphorylated proteins identified by proteomic (proteome) and phospho-proteomic (phosphoproteome) analyses of WT vs KO and WT vs WT+PST SNU-475 cells shown in Fig. 3A-C. **(B)** Volcano plots show the fold change vs. *p*-value of differentially expressed/phosphorylated proteins of indicated comparisons of Snu475 cells. **(C)** Quantification of β1 integrin (ITGβ1), αV integrin (ITGαV), ILK, talin, PI3K, phospho-p85 (Tyr458)/p55(Tyr199)-PI3K (pPI3K), vinculin, and paxillin in indicated Huh7 and SNU-475 cell lines by immunoblotting. GAPDH, loading control. The numbers below lines indicate relative band intensities normalized to average WT values. Boxplots show relative band intensities normalized to GAPDH or non-phosphorylated protein. The box represents the median, 25th, and 75th percentile with whiskers reaching the last data point; dots, individual experiments; $N = 9$. Two-tailed *t*-test; $^{*}P < 0.05$; $^{**}P < 0.01$; †$P < 0.001$.

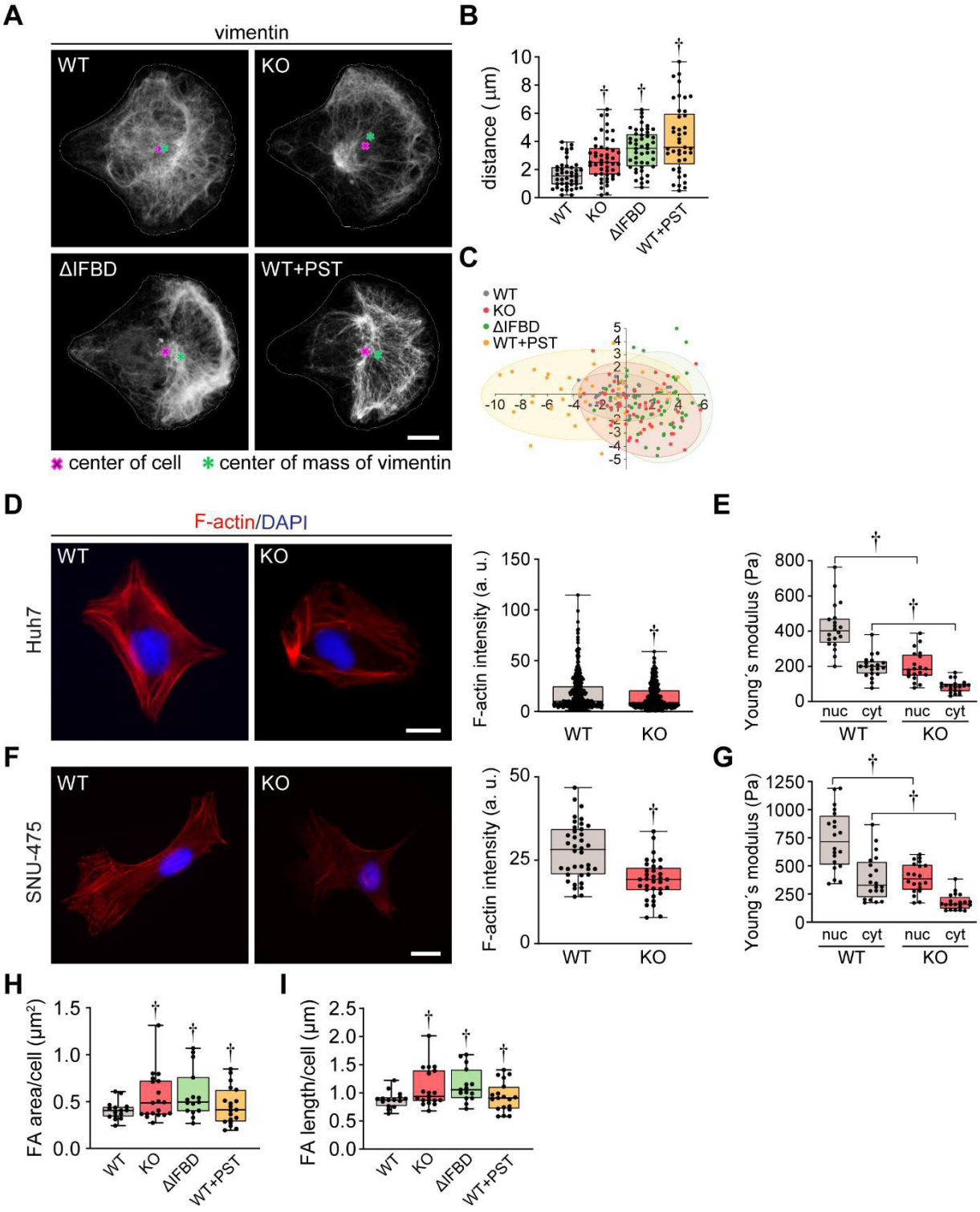

Figure 4—figure supplement 1. Cytoskeletal networks and cell stiffness are altered upon plectin inactivation. (A) Representative confocal images of micropattern-seeded WT, KO, ΔIFBD, and PST-treated WT (WT+PST) SNU-475 cells immunolabeled for vimentin. Line, cell contour; red cross, center of cell; green asterisk, center of mass of vimentin fluorescence signal. Scale bar, 10 µm. **(B,C)** Quantification of vimentin distribution in WT, KO, ΔIFBD, and PST-treated WT (WT+PST) SNU-475 cells shown in (A). Graphs show the distance between the cell center and the center of mass of the vimentin

signal (B) and the position of the center of mass of the vimentin signal (C). Boxplot shows the median, 25th and 75th percentile with whiskers reaching the last data point; dots, individual cells; *n* = 43 (WT), 48 (KO), 47 (ΔIFBD), 41 (WT+PST) cells; *N* = 3. Two-tailed *t*-test; ✝*P* < 0.001. **(D,F)** Representative images of WT and KO Huh7 (D) and SNU-475 (F) cells immunolabeled for F-actin (red). Nuclei, DAPI (blue). Scale bar, 20 µm. Graphs show the quantification of F-actin fluorescence intensity. Boxplots show the median, 25th, and 75th percentile with whiskers reaching the last data point; dots, individual cells; *n* (Huh7) = 169 (WT), 180 (KO); *n* (SNU-475) = 38 (WT), 34 (KO) cells; *N* (Huh7) = 3; *N* (SNU-475) = 3. Two-tailed *t*-test; ✝*P* < 0.001. **(E,G)** Quantification of average Young´s modulus values in nuclear (nuc) and cytosolic (cyt) area of WT and KO Huh7 (E) and SNU-475 (G) cells. Boxplot shows the median, 25th, and 75th percentile with whiskers reaching the last data point; dots, individual cells; *n* = 20 cells; *N* = 3. Two-tailed *t*-test; ✝*P* < 0.001. **(H,I)** Quantification of average FA length (H) and FA area (I) per cell for WT, KO, ΔIFBD, and PST-treated WT (WT+PST) SNU-475 cells shown in Fig. 4F. Boxplot shows the median, 25th, and 75th percentile with whiskers reaching the last data point; dots, individual cells; *n* = 15 (WT), 18 (KO), 20 (ΔIFBD), 19 (WT+PST) cells; *N* = 3. Two-tailed *t*-test; ✝*P* < 0.001.

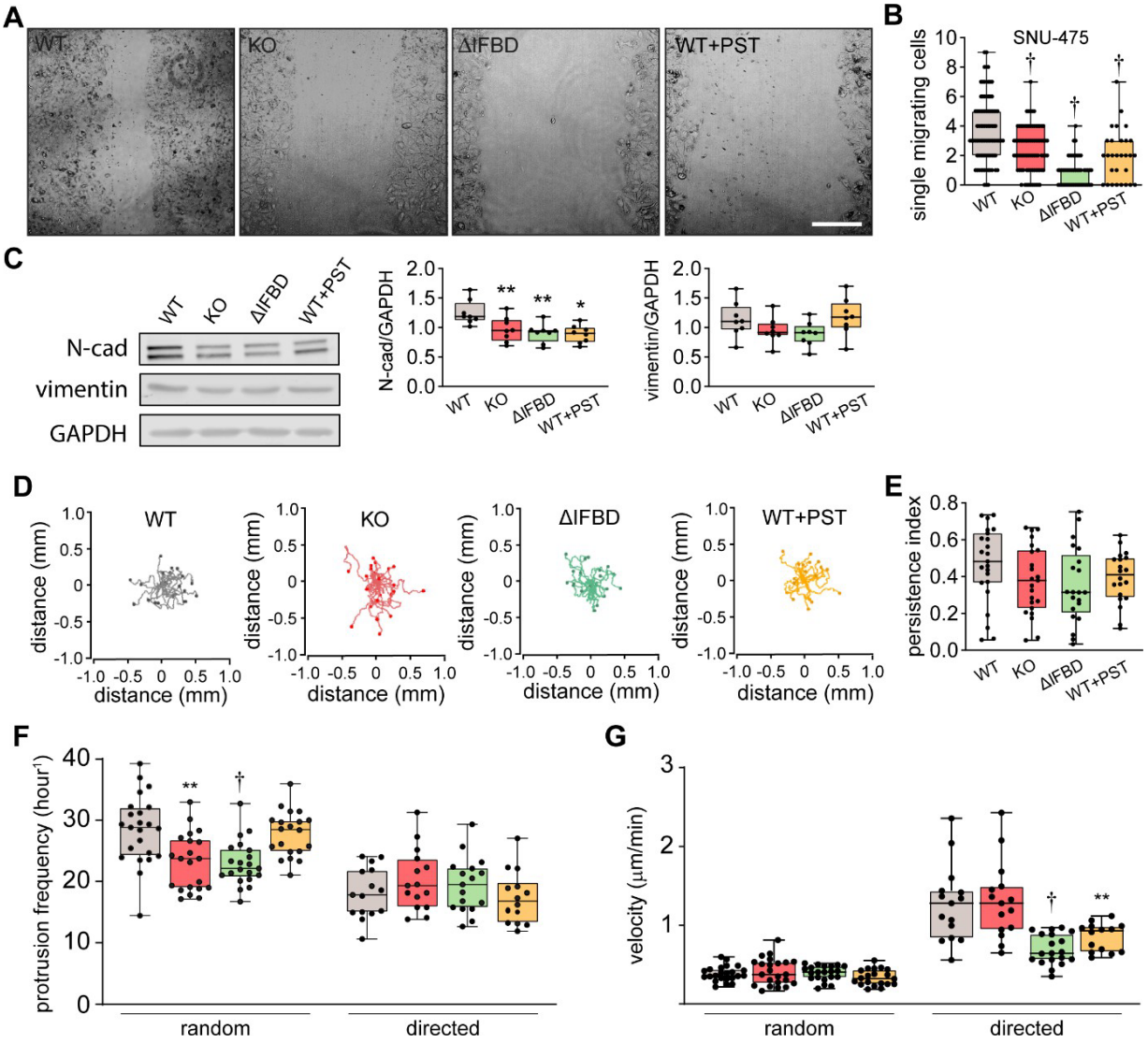

Figure 5—figure supplement 1. Plectin inactivation impairs migration of HCC cells. (A) Representative phase contrast images of WT, KO, ΔIFBD, and PST-treated WT (WT+PST) Huh7 cells migrating in the scratch-wound assay for 24 hours corresponding to the graph shown in Fig. 5B. Scale bar, 200 µm. **(B)** Quantification of the number of WT, KO, ΔIFBD, and PST-treated WT (WT+PST) leader SNU-475 cells migrating individually into the scratch wounds shown Fig. 5A. Boxplot shows the median, 25th, and 75th percentile with whiskers reaching the last data point; dots, fields of view; *n* = 47 (WT), 47 (KO), 50 (ΔIFBD), 24 (WT+PST) fields of view; *N* = 5 (WT, KO, ΔIFBD), 3 (WT+PST). Two-tailed *t*-test; †*P* < 0.001. **(C)** Quantification of N-cadherin (N-cad) and vimentin in indicated SNU-475 cell lines by immunoblotting. GAPDH, loading control. Boxplots show relative band intensities normalized to GAPDH. The box represents the median, 25th, and 75th percentile with whiskers reaching the last data point; dots, individual experiments; *N* = 8. Two-tailed *t*-test; **P* < 0.05, ***P* < 0.01. **(D)** Spider plots with migration trajectories of WT, KO, ΔIFBD, and PST-treated WT (WT+PST) SNU-475 cells tracked during 16 hours of random migration; dots, the final position of each single

tracked cell. **(E)** Quantification of persistence indices of WT, KO, ΔIFBD, and PST-treated WT (WT+PST) SNU-475 cells shown in (D). Boxplot shows the median, 25th, and 75th percentile with whiskers reaching the last data point; dots, individual cells; *n* = 15 (WT), 15 (KO), 19 (ΔIFBD), 14 (WT+PST); *N* = 3. **(F)** Quantification of average protrusion frequency of WT, KO, ΔIFBD, and PST-treated WT (WT+PST) SNU-475 cells during random and EGF-guided (directed) migrations. Boxplot shows the median, 25th, and 75th percentile with whiskers reaching the last data point; dots, individual cells; *n* (random) = 23 (WT), 21 (KO), 21 (ΔIFBD), 20 (WT+PST) cells; *n* (directed) = 15 (WT), 15 (KO), 17 (ΔIFBD), 14 (WT+PST) cells; *N* = 3. Two-tailed *t*-test; **P* < 0.05, ***P* < 0.01; ✝*P* < 0.001. **(G)** Quantification of migration velocity of WT, KO, ΔIFBD, and PST-treated WT (WT+PST) SNU-475 cells during random and EGF-guided (directed) migrations. Boxplot shows the median, 25th, and 75th percentile with whiskers reaching the last data point; dots, individual cells; *n* (random) = 23 (WT), 21 (KO), 21 (ΔIFBD), 20 (WT+PST) cells; *n* (directed) = 15 (WT), 15 (KO), 17 (ΔIFBD), 14 (WT+PST) cells; *N* = 3. Two-tailed *t*-test; ✝*P* < 0.001.

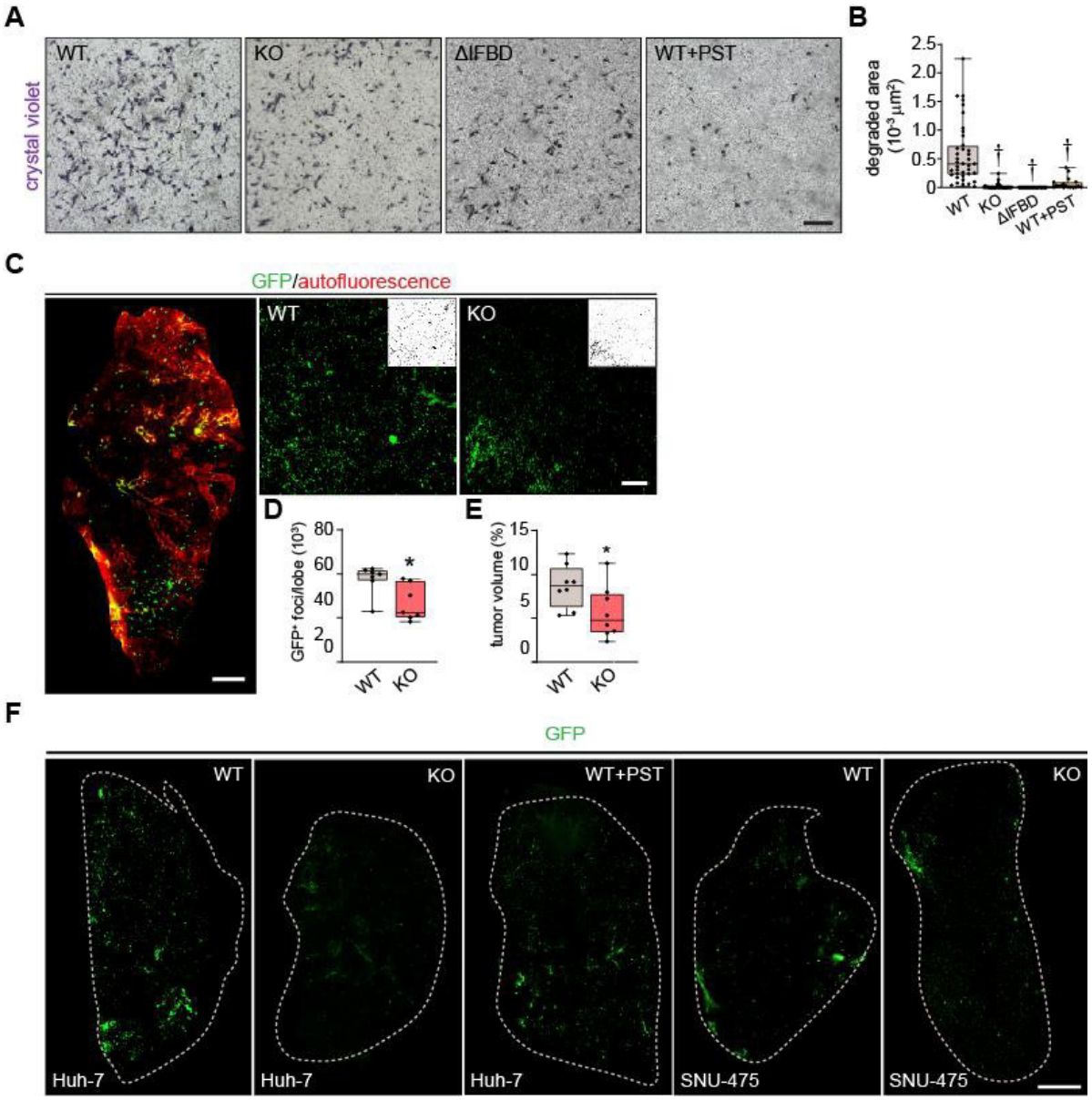

Figure 6—figure supplement 1. Plectin inactivation reduces invasiveness of HCC cells. (A) Representative images of crystal violet-stained WT, KO, ΔIFBD, and PST-treated WT (WT+PST) SNU-475 cells invading in Matrigel transwell assay shown in Fig. 6C. Scale bar, 300 µm. **(B)** Quantification of gelatin area degraded by WT, KO, ΔIFBD, and PST-treated WT (WT+PST) SNU-475 cells shown in Fig. 6D. Boxplot shows the median, 25th, and 75th percentile with whiskers reaching the last data point; dots, individual cells; *n* = 49 (WT), 36 (KO), 25 (ΔIFBD), 29 (WT+PST); *N* = 5 (WT), 4 (KO), 3 (IFBD, ΔWT+PST). Two-tailed *t*-test; †*P* < 0.001. **(C)** The 5-week-old NSG mice were injected (t.v.i.) with indicated RedFLuc-GFP-expressing SNU-475 cells. Representative lattice light sheet fluorescence image of CUBIC-cleared lung lobe immunolabeled with antibodies against GFP (green). Autofluorescence visualizing the lobe structures is shown in red. Scale bar, 1 mm. Representative magnified images from lung lobes with GFP-positive WT and KO nodules. Insets, segmented binary

masks of GFP-positive metastatic nodules. Scale bar, 200 µm. **(D,E)** Boxplots show metastatic load in the lungs expressed as the number (D) and relative volume (E) of GFP-positive (GFP^+) nodules indicated in (C). The box represents the median, 25th, and 75th percentile with whiskers reaching the last data point; dots, lung lobes; $n = 8$ lung lobes; $N = 4$. Two-tailed *t*-test; $*P < 0.05$ **(F)** Representative lattice light sheet fluorescence images of CUBIC-cleared lung lobes from (C) and Figure 6I, immunolabeled with antibodies against GFP (green). Dashed line, lobe contour. Scale bar, 1500 µm.

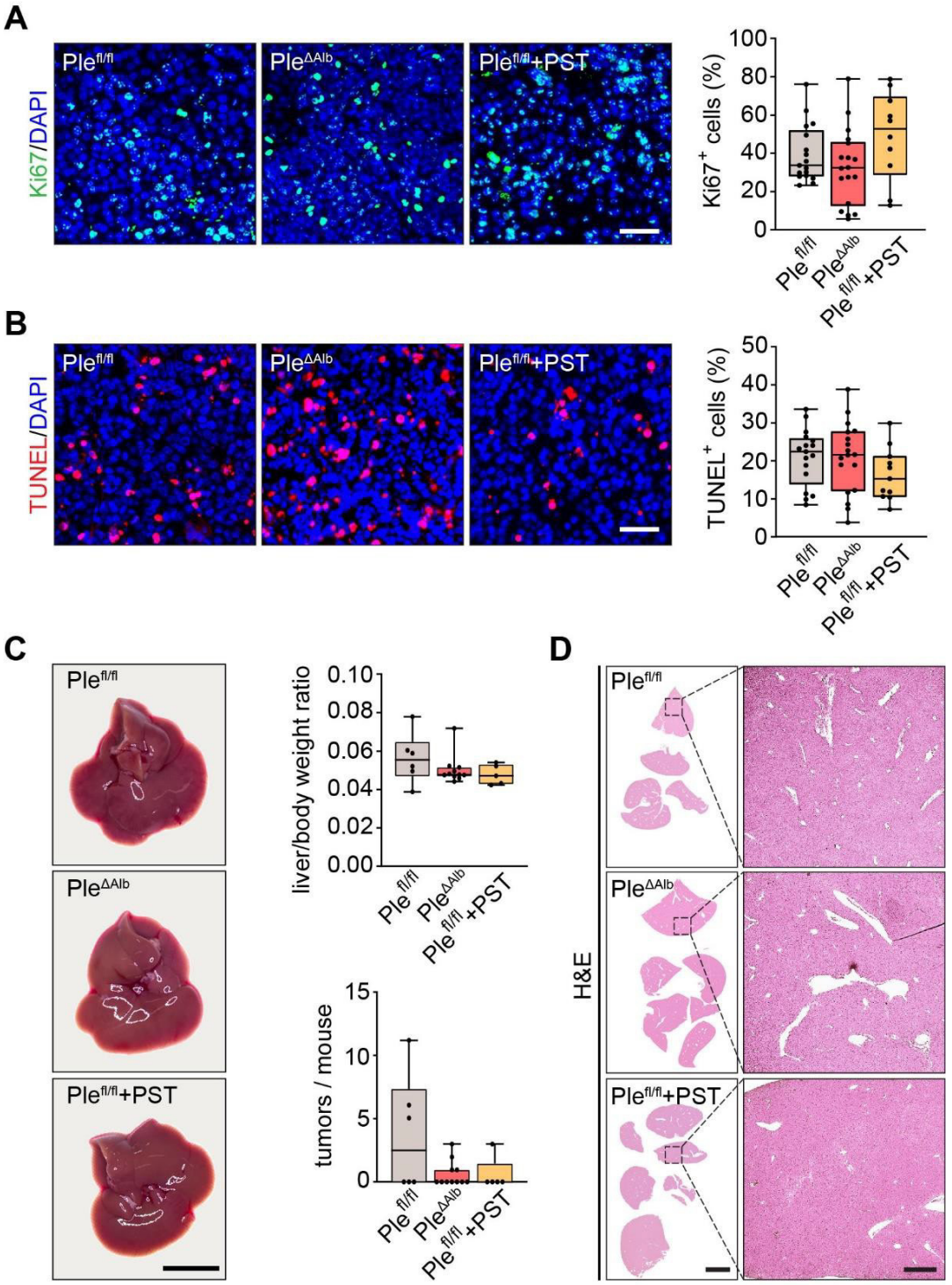

Figure 7—figure supplement 1. Effect of plectin inactivation on HCC proliferation, apoptosis, and development. (A,B) Representative images of Myc;sgTp53-induced liver tumor sections from *Ple*$^{fl/fl}$, *Ple*$^{\Delta Alb}$, and PST-treated *Ple*$^{fl/fl}$ (*Ple*$^{fl/fl}$ +PST) mice shown in Fig. 7B,C immunolabeled for Ki67 (green; A) and TUNEL (red;B). Nuclei, DAPI (blue). Scale bar, 50 µm. Quantification (percentage) of Ki67-positive cells (A) and TUNEL-positive cells (B). Boxplot shows the median, 25th and 75th percentile with whiskers reaching the last data point; dots, individual tumors; *n* = 17 (*Ple*$^{fl/fl}$), 18 (*Ple*$^{\Delta Alb}$), 10 (*Ple*$^{fl/fl}$+PST). **(C,D)** Myc;sgTp53 HCC was induced as before (see Fig. 7A,B) in 8-week-old *Ple*$^{fl/fl}$ and

Ple$^{\Delta Alb}$ female mice. *Ple*$^{fl/fl}$ mice were kept either untreated or every second day provided with orogastric gavage of plecstatin (*Ple*$^{fl/fl}$+PST). Animals were sacrificed 8 weeks post-induction. Representative images of *Ple*$^{fl/fl}$, *Ple*$^{\Delta Alb}$, and *Ple*$^{fl/fl}$+PST livers. Scale bar, 1 cm. Boxplots show tumor burden in the livers expressed as the liver/body weight ratio (upper graph) and number of tumors per mouse (lower graph). The box represents the median, 25th, and 75th percentile with whiskers reaching the last data point; dots, mice; *N* = 6 (*Ple*$^{fl/fl}$), 13 (*Ple*$^{\Delta Alb}$), 5 (*Ple*$^{fl/fl}$ + PST). **(D)** Representative images of H&E-stained *Ple*$^{fl/fl}$, *Ple*$^{\Delta Alb}$, and *Ple*$^{fl/fl}$+PST sections of livers shown in (C). Boxed areas, x12 images. Scale bars, 5 and 1 mm (boxed areas).

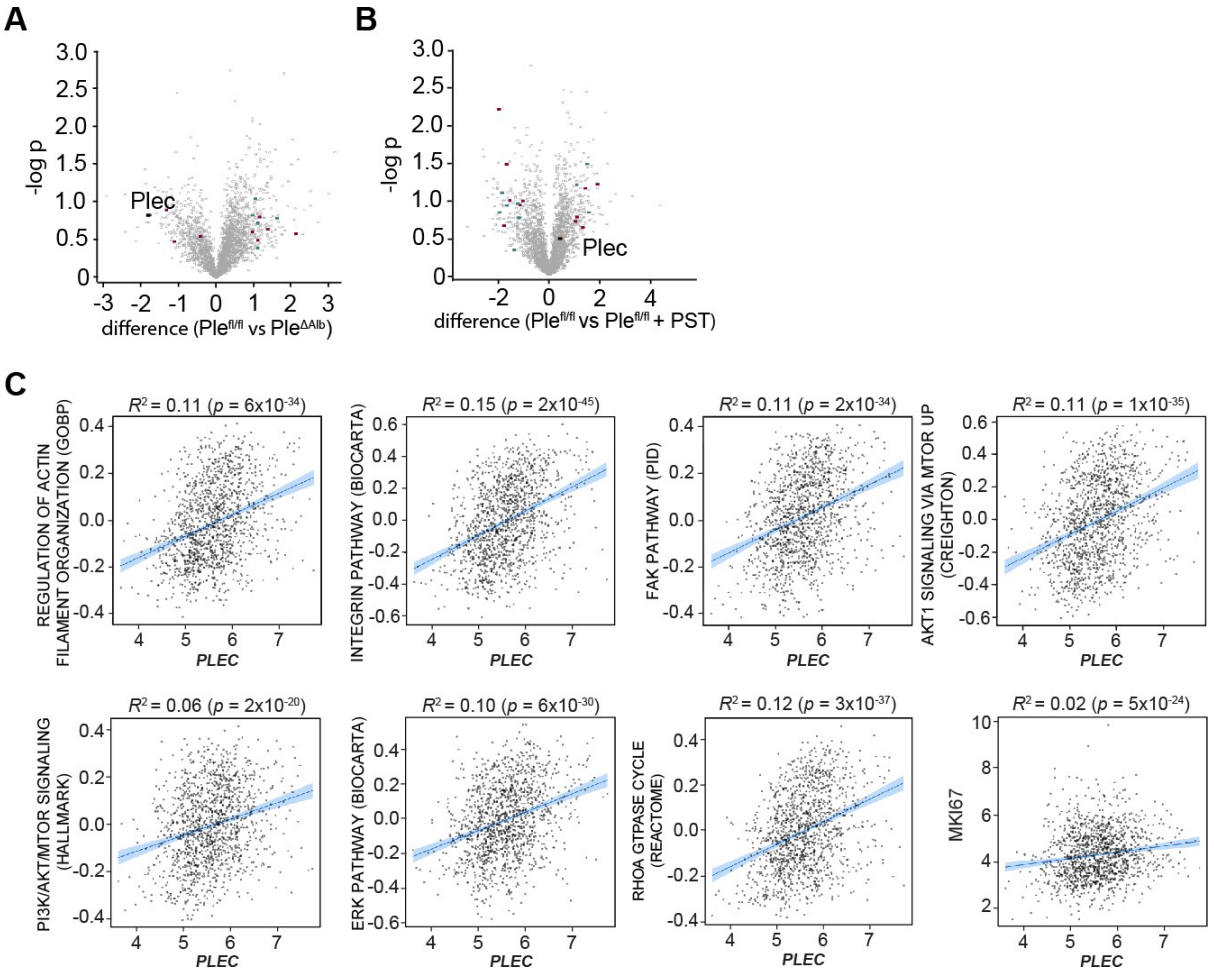

Figure 7—figure supplement 2. Plectin-related expression signatures HCC from animal models and patients. (A,B) Volcano plots show the fold change vs. *p*-value of differentially expressed proteins in livers of *Ple*$^{fl/fl}$ vs. *Ple*$^{\Delta Alb}$ (A) and *Ple*$^{fl/fl}$ vs. *Ple*$^{fl/fl}$ + PST (B) Myc;sgTp53-treated mice (see also Fig. 7B). Colored dots represent differentially expressed proteins identified in canonical signaling pathways shown in Fig. 7D. **(C)** Scatter plots show the correlation of *plectin* (*PLEC*) mRNA expression with indicated expression signatures. Line, linear regression line; blue area, 95% confidence intervals. Coefficient of determination (R^2) and *P* values are indicated above the graphs.

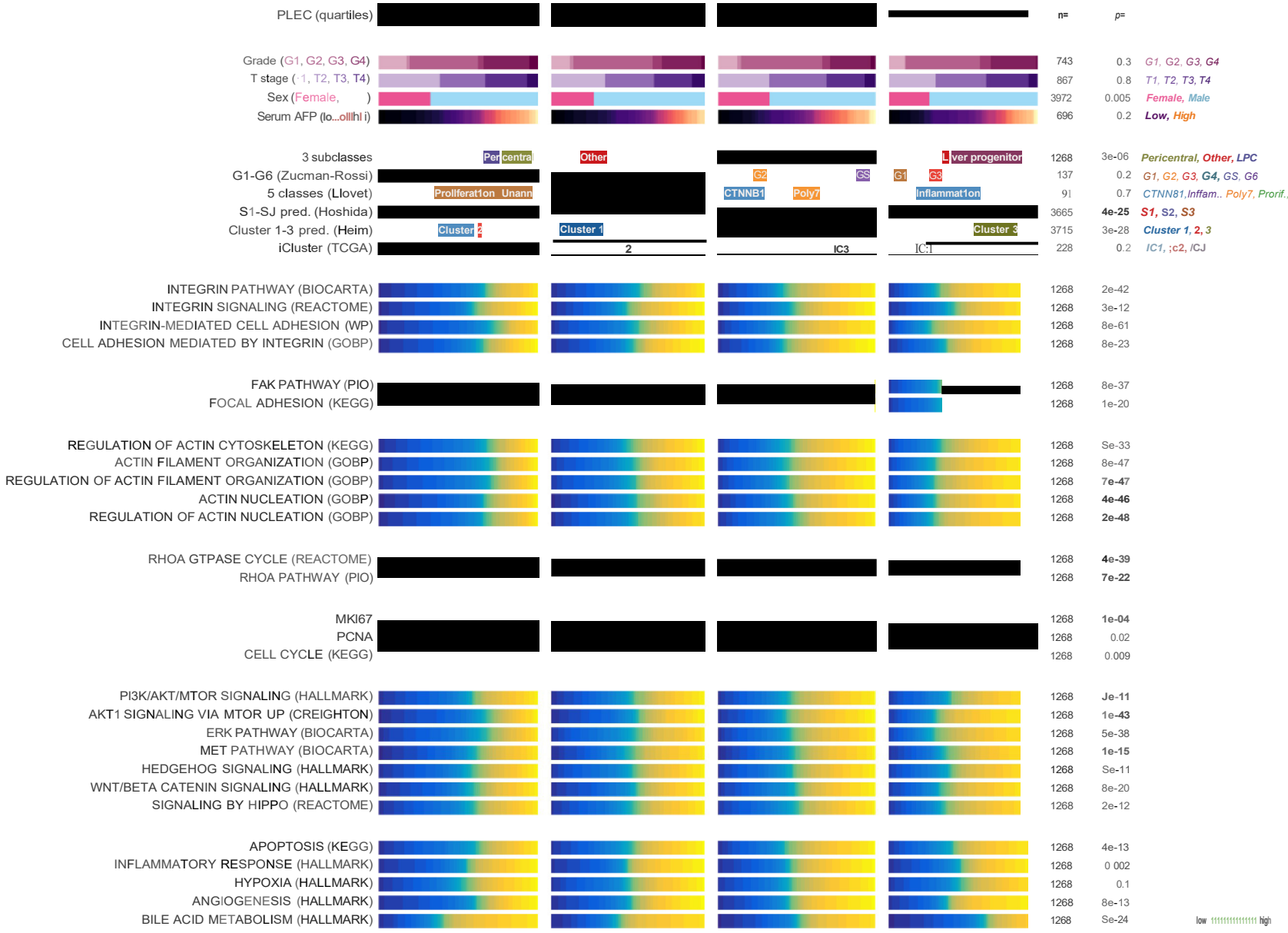
PLEC (quartiles)
n=
p=
Grade (G1, G2, G3, G4)
T stage (T1, T2, T3, T4)
Sex (Female,)
Serum AFP (low, high)
3 subclasses
G1-G6 (Zucman-Rossi)
5 classes (Llovet)
S1-SJ pred. (Hoshida)
Cluster 1-3 pred. (Heim)
iCluster (TCGA)
Pericentral
Other
Liver progenitor
G2
GS
G1
G3
CTNNB1
Poly7
Inflammation
Proliferation
Unann
Cluster 1
Cluster 3
2
IC3
IC1
INTEGRIN PATHWAY (BIOCARTA)
INTEGRIN SIGNALING (REACTOME)
INTEGRIN-MEDIATED CELL ADHESION (WP)
CELL ADHESION MEDIATED BY INTEGRIN (GOBP)
FAK PATHWAY (PIO)
FOCAL ADHESION (KEGG)
REGULATION OF ACTIN CYTOSKELETON (KEGG)
ACTIN FILAMENT ORGANIZATION (GOBP)
REGULATION OF ACTIN FILAMENT ORGANIZATION (GOBP)
ACTIN NUCLEATION (GOBP)
REGULATION OF ACTIN NUCLEATION (GOBP)
RHOA GTPASE CYCLE (REACTOME)
RHOA PATHWAY (PIO)
MKI67
PCNA
CELL CYCLE (KEGG)
PI3K/AKT/MTOR SIGNALING (HALLMARK)
AKT1 SIGNALING VIA MTOR UP (CREIGHTON)
ERK PATHWAY (BIOCARTA)
MET PATHWAY (BIOCARTA)
HEDGEHOG SIGNALING (HALLMARK)
WNT/BETA CATENIN SIGNALING (HALLMARK)
SIGNALING BY HIPPO (REACTOME)
APOPTOSIS (KEGG)
INFLAMMATORY RESPONSE (HALLMARK)
HYPOXIA (HALLMARK)
ANGIOGENESIS (HALLMARK)
BILE ACID METABOLISM (HALLMARK)
low
high

Figure 7—figure supplement 3. Plectin signature in HCC patients. The graph shows the association of *plectin* (*PLEC*) mRNA expression with indicated clinicopathological parameters, molecular classifications, and signature pathways among patients grouped into quartiles of PLEC expression. The analysis is based on data from gene set variation analysis (GSVA) used to produce quantitative enrichment scores for all gene sets from msigdb in pooled and batch-adjusted data. *P* values represent the result of a *chi*-square test (for categorical data) or analysis of variance (for numerical data such as gene signature expression levels).

Supplemental Video Legends

Video 1. Representative video of WT and KO SNU-475 cells invading the matrigel. Time-lapse covers total 21 h with frame taken every 15 min (~15 min elapsed time per frame of the movie). Scale bar, 200 μm. The fixed and immunolabeled cells from the endpoint of this experiment are shown in Fig. 6E.

Supplementary file 1. Table of patients clinical data.

Sample ID	**Etiology** 0 = unknown 1 = ALD/ASH 2 = NAFLD/NASH 3 = HBV 4 = HCV 5 = Other	**Age** [years]	**Sex** 0 = male 1 = female
MAP_1_HCC	4	78.5	1
MAP_10_HCC	4	51.4	0
MAP_11_HCC	2	79.0	0
MAP_12_HCC	1	86.2	0
MAP_13_HCC	1	69.2	0
MAP_14_HCC	3 + 4	49.5	0
MAP_15_HCC	1	83.9	0
MAP_16_HCC	4	59.2	1
MAP_17_HCC	4	54.8	0
MAP_18_HCC	1 + 4	68.4	0
MAP_19_HCC	1 + 4	56.5	1
MAP_2_HCC	2 + 5	61.8	1
MAP_20_HCC	1 + 4	48.2	0
MAP_21_HCC	2 + 5	63.5	1
MAP_3_HCC	1	67.5	0
MAP_4_HCC	1	71.9	0
MAP_5_HCC	0	66.1	0
MAP_6_HCC	1	83.0	0
MAP_7_HCC	0	63.3	1
MAP_8_HCC	2	68.6	0
MAP_9_HCC	3	57.9	0

Supplementary file 2. List of antibodies used in this study.

Primary antibodies					
Antigen	**Clone**	**Manufacturer**	**Cat. number**	**Application**	**Dilution**
rabbit anti-Akt	polyclonal	Cell Signaling	9272	WB	1:1000
rabbit anti-pAkt (Ser473)	D9E	Cell Signaling	4060	WB	1:2000
mouse anti-E-cadherin	36/E	BD Bioscience	610181	WB	1:4000
mouse anti-Erk2	D-2	Santa Cruz	sc-1674	WB	1:200
rabbit anti-pErk1/2 (Thr202/Tyr204)	D13.14.4E	Cell Signaling	4370	WB	1:1000
mouse anti-FAK	77/FAK Ruo	BD Bioscience	610088	WB	1:500
rabbit anti p-FAK (Tyr397)	polyclonal	Thermo-Fisher	44-624G	WB	1:1000
rabbit anti-GAPDH	FF26A	Sigma	G9545	WB	1:20.000
rabbit anti-GFP	polyclonal	Invitrogen	A-11122	immunofluorescence	1:100
rabbit anti-ILK	4G9	Cell Signaling	3856	WB	1:1000
rabbit anti- αV integrin	EPR16800	Abcam	ab179475	WB	1:5000
mouse anti-β1 integrin	A-4	Santa Cruz	sc-374429	WB	1:500
rabbit anti-Ki67	SP6	GeneTex	GTX16667	immunofluorescence	1:100
rabbit anti-N-cadherin	polyclonal	Abcam	ab18203	WB	1:1000
mouse anti-paxillin	349	BD Bioscience	612405	WB	1:1000
rabbit anti-PI3K p85	19H8	Cell Signaling	4257	WB	1:1000
rabbit anti-pPI3K p85/p55 (Tyr458/Tyr199)	polyclonal	Cell Signaling	4228	WB	1:1000
guinea pig anti-plectin	polyclonal	Progen	GP21	WB	1:1000
				immunofluorescence	1:250
mouse anti-talin	8d4	Sigma	T3287	WB	1:1000
mouse anti-vimentin	RV202	Santa Cruz	sc-32322	WB	1:500
rabbit anti-vimentin	polyclonal	GeneTex	GTX100619	immunofluorescence	1:200
mouse anti-vinculin	VIN-11-5	Sigma	V4505	WB	1:500
				immunofluorescence	1:250
Secondary antibodies					
Name	**Manufacturer**		**Cat. number**	**Application**	**Dilution**
anti-mouse AF-488	Jackson ImmunoResearch		715-545-150	immunofluorescence	1:500
anti-rabbit AF-488	Jackson ImmunoResearch		711-545-152	immunofluorescence	1:500
anti-rabbit AF-594	Life Tech		A11037	immunofluorescence	1:1000
anti-rabbit AF-647	Jackson ImmunoResearch			immunofluorescence	1:500
anti-guinea pig AF-488	Jackson ImmunoResearch		706-545-148	immunofluorescence	1:500
anti-mouse IgG IRDye® 680RD	Licor		926-68072	WB	1:20,000
anti-mouse IRDye® 800CW	Licor		926-32212	WB	1:20,000
anti-rabbit IRDye® 680RD	Licor		926-68073	WB	1:20,000
anti-rabbit IgG IRDye® 800CW	Licor		926-32213	WB	1:20,000
anti-guinea pig IRDye® 680RD	Licor		926-68077	WB	1:20,000
anti-mouse-IgG-HRP	Jackson ImmunoResearch		115-035-146	WB	1:5000
anti-rabbit-IgG-HRP	Jackson ImmunoResearch		111-035-044	WB	1:5000
anti-GuineaPig-IgG-HRP	Sigma		A7289	WB	1:5000

Supplemental references

1 Ackerl, R. *et al.* Conditional targeting of plectin in prenatal and adult mouse stratified epithelia causes keratinocyte fragility and lesional epidermal barrier defects. *J Cell Sci* **120**, 2435-2443, doi:10.1242/jcs.004481 (2007).

2 Jirouskova, M. *et al.* Plectin controls biliary tree architecture and stability in cholestasis. *J Hepatol* **68**, 1006-1017, doi:10.1016/j.jhep.2017.12.011 (2018).

3 Meier, S. M. *et al.* An Organoruthenium Anticancer Agent Shows Unexpected Target Selectivity For Plectin. *Angew Chem Int Ed Engl* **56**, 8267-8271, doi:10.1002/anie.201702242 (2017).

4 Stubb, A. *et al.* Fluctuation-Based Super-Resolution Traction Force Microscopy. *Nano Lett* **20**, 2230-2245, doi:10.1021/acs.nanolett.9b04083 (2020).

5 Bauer, A. *et al.* pyTFM: A tool for traction force and monolayer stress microscopy. *PLoS Comput Biol* **17**, e1008364, doi:10.1371/journal.pcbi.1008364 (2021).

6 Schindelin, J. *et al.* Fiji: an open-source platform for biological-image analysis. *Nat Methods* **9**, 676-682, doi:10.1038/nmeth.2019 (2012).

7 Piccolo, S. R. *et al.* A single-sample microarray normalization method to facilitate personalized-medicine workflows. *Genomics* **100**, 337-344, doi:10.1016/j.ygeno.2012.08.003 (2012).

8 McCall, M. N., Murakami, P. N., Lukk, M., Huber, W. & Irizarry, R. A. Assessing affymetrix GeneChip microarray quality. *BMC Bioinformatics* **12**, 137, doi:10.1186/1471-2105-12-137 (2011).

9 Dinh, T. A. *et al.* Comprehensive analysis of The Cancer Genome Atlas reveals a unique gene and non-coding RNA signature of fibrolamellar carcinoma. *Sci Rep* **7**, 44653, doi:10.1038/srep44653 (2017).

10 Viechtbauer, W. Conducting Meta-Analyses in R with the metafor Package. *Journal of Statistical Software* **36**, doi:10.18637/jss.v036.i03 (2010).

11 Iizuka, N. *et al.* Oligonucleotide microarray for prediction of early intrahepatic recurrence of hepatocellular carcinoma after curative resection. *Lancet* **361**, 923-929, doi:10.1016/S0140-6736(03)12775-4 (2003).

12 McHugh, J. T. Principles in regard to withholding or withdrawing artificially assisted nutrition/hydration. *Issues Law Med* **6**, 89-93 (1990).

13 Liberzon, A. *et al.* The Molecular Signatures Database (MSigDB) hallmark gene set collection. *Cell Syst* **1**, 417-425, doi:10.1016/j.cels.2015.12.004 (2015).

14 Yevshin, I., Sharipov, R., Kolmykov, S., Kondrakhin, Y. & Kolpakov, F. GTRD: a database on gene transcription regulation-2019 update. *Nucleic Acids Res* **47**, D100-D105, doi:10.1093/nar/gky1128 (2019).

15 Hanzelmann, S., Castelo, R. & Guinney, J. GSVA: gene set variation analysis for microarray and RNA-seq data. *BMC Bioinformatics* **14**, 7, doi:10.1186/1471-2105-14-7 (2013).

16 Cancer Genome Atlas Research Network. Electronic address, w. b. e. & Cancer Genome Atlas Research, N. Comprehensive and Integrative Genomic Characterization of Hepatocellular Carcinoma. *Cell* **169**, 1327-1341 e1323, doi:10.1016/j.cell.2017.05.046 (2017).

17 Chiang, D. Y. *et al.* Focal gains of VEGFA and molecular classification of hepatocellular carcinoma. *Cancer Res* **68**, 6779-6788, doi:10.1158/0008-5472.CAN-08-0742 (2008).

18 Shimokawa, K. *et al.* iCOD: an integrated clinical omics database based on the systems-pathology view of disease. *BMC Genomics* **11 Suppl 4**, S19, doi:10.1186/1471-2164-11-S4-S19 (2010).

19 Makowska, Z. *et al.* Gene expression analysis of biopsy samples reveals critical limitations of transcriptome-based molecular classifications of hepatocellular carcinoma. *J Pathol Clin Res* **2**, 80-92, doi:10.1002/cjp2.37 (2016).

20 Johnson, W. E., Li, C. & Rabinovic, A. Adjusting batch effects in microarray expression data using empirical Bayes methods. *Biostatistics* **8**, 118-127, doi:10.1093/biostatistics/kxj037 (2007).

21 Hoshida, Y. Nearest template prediction: a single-sample-based flexible class prediction with confidence assessment. *PLoS One* **5**, e15543, doi:10.1371/journal.pone.0015543 (2010).

22 Boyault, S. *et al.* Transcriptome classification of HCC is related to gene alterations and to new therapeutic targets. *Hepatology* **45**, 42-52, doi:10.1002/hep.21467 (2007).

23 Hoshida, Y. *et al.* Integrative transcriptome analysis reveals common molecular subclasses of human hepatocellular carcinoma. *Cancer Res* **69**, 7385-7392, doi:10.1158/0008-5472.CAN-09-1089 (2009).

24 Weiss, T. *et al.* Schwann cell plasticity regulates neuroblastic tumor cell differentiation via epidermal growth factor-like protein 8. *Nat Commun* **12**, 1624, doi:10.1038/s41467-021-21859-0 (2021).

25 Tyanova, S. *et al.* The Perseus computational platform for comprehensive analysis of (prote)omics data. *Nat Methods* **13**, 731-740, doi:10.1038/nmeth.3901 (2016).

26 Prechova, M. *et al.* Plectin-mediated cytoskeletal crosstalk controls cell tension and cohesion in epithelial sheets. *J Cell Biol* **221**, doi:10.1083/jcb.202105146 (2022).

Dynamics of compartment-specific proteomic landscapes of hepatotoxic and cholestatic models of liver fibrosis

Marketa Jirouskova[1], Karel Harant[2], Pavel Cejnar[3], Srikant Ojha[1,4], Katerina Korelova[1], Lenka Sarnova[1], Eva Sticova[5,6], Christoph Mayr[7], Herbert Schiller[7,8], Martin Gregor[1]

[1]Laboratory of Integrative Biology, Institute of Molecular Genetics of the Czech Academy of Sciences, Prague, Czech Republic

[2]Laboratory of Mass Spectrometry, BIOCEV, Faculty of Science Charles University in Prague

[3]Department of Mathematics, Informatics and Cybernetics, University of Chemistry and Technology, Prague, Czech Republic

[4]Department of Animal Physiology, Faculty of Science, Charles University, Prague, Czech Republic

[5]Clinical and Transplant Pathology Centre, Institute for Clinical and Experimental Medicine, Prague, Czech Republic

[6]Department of Pathology, The Third Faculty of Medicine, Charles University and University Hospital Kralovske Vinohrady, Prague, Czech Republic

[7]Comprehensive Pneumology Center (CPC)/Institute of Lung Health and Immunity (LHI), Helmholtz Munich; Member of the German Center for Lung Research (DZL), Munich, Germany

[8]Institute of Experimental Pneumology, LMU University Hospital, Ludwig-Maximilians University, Munich, Germany

Author Contributions

Conceptualization: M.G. and M.J. Acquisition of data: M.J., K.H., S.O., K.K., and L.S. Analysis and interpretation of data: M.J., K.H., P.C., S.O., and M.G. Drafting of the manuscript: M.J. and M.G. Critical revision of the manuscript for important intellectual content: all authors. Funding: M. G. and M.J. Technical and material support: H.S., E.S., and C.M.

Corresponding authors:

Marketa Jirouskova marketa.jirouskova@img.cas.cz

Martin Gregor martin.gregor@img.cas.cz

Laboratory of Integrative Biology

Institute of Molecular Genetics of the Czech Academy of Sciences

Vídeňská 1083, 142 20 Prague 4, Czech Republic

Conflict of interest: Nothing to declare.

Keywords:

mass spectrometry, matrisome, collagen deposits, atomic force microscopy, clusterin

List of Abbreviations: AFM, atomic force microscopy; BECs, biliary epithelial cells; B.H. FDR, Benjamini-Hochberg false discovery rate; CCl_4, carbon tetrachloride; DDC, 3,5-diethoxycarbonyl-1,4-dihydrocollidine; ECM, extracellular matrix; ECM1, extracellular matrix protein-1; GO term, gene ontology; HSC, hepatic stellate cell; IPA, Ingenuity Pathway Analysis; MRTF, myocardin-related transcription factor; MS, mass spectrometry; PCA, principal component analysis; PF, portal fibroblasts.

ABSTRACT

Accumulation of extracellular matrix (ECM) in liver fibrosis is associated with changes in protein abundance and composition depending upon etiology of the underlying liver disease. Current efforts to unravel etiology-specific mechanisms and pharmacological targets rely on several models of experimental fibrosis. Here, we characterize and compare dynamics of hepatic proteome remodeling during fibrosis development and spontaneous healing in experimental models of hepatotoxic (CCl_4 intoxication) and cholestatic (3,5-diethoxycarbonyl-1,4-dihydrocollidine (DDC) feeding) injury. Using detergent-based tissue extraction and mass spectrometry, we identified compartment-specific changes in the liver proteome with detailed attention to ECM composition and changes in protein solubility. Our analysis yielded unique time-resolved CCl_4 and DDC signatures underscoring restricted healing with higher carcinogenic potential upon cholestasis. Correlation of protein abundance profiles with fibrous deposits revealed extracellular chaperone clusterin with implicated role in fibrosis resolution. Dynamics of clusterin expression was validated in the context of human liver fibrosis. Atomic force microscopy of fibrotic livers complemented proteomics with profiles of disease-associated changes in local liver tissue mechanics. This study determined compartment-specific proteomic landscapes of liver fibrosis and delineated etiology-specific ECM components, providing thus a foundation for future antifibrotic therapies.

INTRODUCTION

Liver fibrosis and subsequent cirrhosis, two leading causes of liver disease-related deaths worldwide,[1] develop as a result of chronic liver injury of multiple etiologies.[2] Fibrosis is characterized by excessive accumulation of extracellular matrix (ECM) proteins forming fibrous scar tissue. In the liver, such pathological matrix is deposited by activated hepatic stellate cells (HSCs) and/or portal fibroblasts (PFs) in response to the inflammatory reaction.[2, 3] Recent multi-omics studies have framed fibrosis as a dynamic multicellular process associated with the remodeling of gene expression landscapes[4] and profound changes in liver protein abundance as well as composition.[5-7]

Hepatocellular injury alters parenchymal mechanical properties,[8] thus further facilitating activation of resident HSCs and PFs and their differentiation into myofibroblasts depositing collagen-rich ECM.[9] Accumulation of abnormal ECM further promotes ECM-depositing myofibroblasts and fosters progressive whole-organ stiffening as a result of ongoing fibrogenesis.[10] Thus, ECM-associated changes are increasingly perceived as causative, rather than consequential, and multiple efforts have focused on the identification of extracellular niche components that drive the pathogenesis of fibrosis.[11]

The ECM is a complex network of hundreds of proteins acting as a three-dimensional scaffold, supporting cells mechanically and functioning as a reservoir for secreted factors (e.g., growth factors and cytokines)[12] This so-called "matrisome" consists of "core matrisome" (the structural components of the ECM; i.e., collagens, glycoproteins, and proteoglycans) and "matrix-associated matrisome" (the ECM-interacting proteins).[13] Transitions of extracellular factors between the insoluble matrisome and the soluble pools modulate their signaling capabilities and bioavailability.[11] As fibrous ECM assemblies determine also tissue mechanics, matrisome constituents provide matrix-embedded cells with spatially distinct biochemical and biomechanical context.

In terms of etiology, chronic liver injury is inflicted either by hepatotoxic or cholestatic insult.[2] In recent decades, several corresponding animal models of liver fibrosis have been established.[14] Despite several translational limitations,[15] these experimental models mimic fundamental aspects of human liver fibrosis.[14] For instance, iterative carbon tetrachloride (CCl_4) intoxication causes hepatocellular damage, HSC activation, and development of pericentral liver fibrosis that evolves into severe bridging fibrosis.[14] In contrast, 3,5-diethoxycarbonyl-1,4-dihydrocollidine (DDC) feeding induces obstructive cholestasis, characterized by expansion of PFs and consecutive periportal fibrosis with typical portal–portal septa.[16] As both human and animal studies have shown that liver fibrosis can be ameliorated by either targeting progression or promoting resolution,[15] experimental models have become instrumental for identifying factors and mechanisms central to blocking fibrosis progression and promoting the reversal of advanced fibrosis.

In this comparative study, we employed CCl_4- and DDC-based mouse models to describe proteomic changes during liver injury, fibrosis development, and repair while focusing on matrisome remodeling and

associated alterations in tissue biomechanics. Our in-depth analysis of MS data obtained from total liver lysates and ECM-enriched insoluble fractions defines compartment- and time-resolved proteomic signatures in toxin- versus cholestasis-induced fibrosis and healing and delineates disease-specific matrisome.

MATERIALS AND METHODS

Animals and liver injury models

C57BL/6J male mice 8–10 weeks old were used for the analysis. All experiments were performed in accordance with an animal protocol approved by the Animal Care Committee of The Institute of Molecular Genetics and according to the EU Directive 2010/63/EU for animal experiments. To induce cholestatic liver injury, mice were either injected with 1 □l/g CCl_4 [14] or fed a diet supplemented with 0.1% DDC.[16]

Mass spectrometry sample preparation

A sample of ca 1 mm^3 excised from the middle section of left lateral liver lobe was cryo-homogenized using TissueLyser II (QIAGEN, Germantown, MD, USA), resuspended, and sonicated. An aliquot of the sample was precipitated and labeled "Total". The remaining solution was centrifuged at 16,000 × g for 20 minutes to separate the supernatant containing soluble (S)-fraction from the pellet, which itself contained insoluble ECM-enriched (E)-fraction.

Nano-liquid chromatography mass spectrometry analysis

Nano reversed-phase columns were used for liquid chromatography MS analysis. Eluting peptide cations were analyzed on a Thermo Orbitrap Fusion collision cell, linear ion trap mass analyzer (Q-OT-qIT, Thermo Scientific). Tandem MS was performed by isolation at 1.5 Th with the quadrupole, higher-energy collisional dissociation fragmentation, and rapid scan MS analysis in the ion trap. Peptides were identified and quantified by MaxQuant label-free quantification software (1.6.7 version) using *Mus musculus* UniProt protein database (UniProtKB version July 2020).

Human samples

The use of completely anonymized archived liver tissue samples for research purposes has been approved by the Ethical Committee of the Institute of Experimental and Clinical Medicine and Thomayer University Hospital, Prague, Czech Republic. Written informed consent was obtained from all patients enrolled in the study. All research was conducted in accordance with both the Declarations of Helsinki and Istanbul. Processing of human liver sections for immunofluorescence is detailed in the Supporting Information.

Atomic force microscopy

Atomic force microscopy (AFM) was performed on liver sections 30 □m thick as previously described.[17] Using the force mapping method, we measured 30 × 100 □m^2 (10 × 36 pixels) defined regions precisely located by polarized microscopy. Seven areas (two sections per mouse) were chosen from three different mice for each time point (control, T1, T2, and T4).

Statistics

All graphs and statistical tests indicated in graphs were performed using GraphPad Prism (GraphPad Software). All results are presented as mean ± SEM unless indicated otherwise. In the boxplots, the box represents 25th and 75th percentiles with the median indicated; whiskers reach to the last data point. Statistical tests used are specified in the figure legends. Statistical significance was determined at levels *, $p < 0.05$, **, $p < 0.01$, and ***, $p < 0.001$.

For further details regarding the materials and methods, please refer to the Supporting Information.

RESULTS

Proteomic analysis outlines the gradual fibrosis development and partial healing in both CCl_4- and DDC-induced liver injury

To compare time-resolved, compartment-specific proteomes of CCl_4- and DDC-induced models of liver fibrosis, total liver lysates (Total) together with two protein fractions obtained by one-step detergent extraction (ECM-enriched insoluble fraction (E-fraction) and soluble fraction (S-fraction)) were prepared for MS analysis (Figure 1A). The gradual fibrogenesis was assessed at two time points (T1 and T2) corresponding to mild fibrosis with partially bridging septa (T1, 3 weeks for CCl_4 and 2 weeks for DDC treatment) and advanced fibrosis (T2, 6 weeks for CCl_4 and 4 weeks for DDC). To characterize the dynamics of spontaneous fibrosis resolution, we allowed the mice 5 (T3) or 10 days (T4) to recover. Both models developed typical progressive liver damage with fibrotic scarring followed by partial healing upon insult withdrawal as demonstrated by plasma levels of liver injury markers and the extent of collagen-rich deposits in liver sections (Figure S1).

Using the two models, we quantified 4,737 proteins approximately evenly distributed across all time points and fractions (Figure 1B,C, Supporting Results). Principal component analysis (PCA) revealed clear temporal separation of CCl_4- and DDC-derived samples in both Total and E-fraction (Figure 1E). Unsupervised hierarchical cluster analysis of total lysate proteins together with annotation enrichment of the observed clusters further demonstrated substantial differences in the dynamic regulation of protein expression between the two models (Figure S2). This was evidenced by differential Total MS protein intensity temporal profiles of matrisome-enriched cluster constituents, such as vitronectin, galectin 8, fibrillin 1, or a putative portal myofibroblast marker collagen □-1(XV) chain (Figure 1F). Moreover, distinct galectin 8 and vitronectin expression profiles obtained for CCl_4 and DDC E-fractions revealed complex changes in protein association with the insoluble proteome. Taken together, our MS data allow for time-resolved identification of proteins differentially expressed during fibrosis progression and resolution in etiologically distinct models of liver fibrosis. Moreover, this approach enables analysis of complex changes in the solubility of the identified proteins and their transition between liver compartments.

Time-resolved analysis of Total proteomes shows limited healing and tumorigenic potential of the DDC model

To capture the proteome differences between toxin- vs. cholestasis-induced fibrogenesis, we determined proteins significantly regulated during fibrogenesis separately in CCl_4 and DDC Total samples (Benjamini-Hochberg false discovery rate (B.H. FDR) < 5%; see Supporting Materials and Methods). In total,

702 proteins were found to be shared by the two models, while 514 (CCl_4) and 1,074 (DDC) proteins were identified as unique for the respective model (Figure 2A).

Using Ingenuity Pathway Analysis (IPA), we predicted upstream transcriptional regulators and growth factors together with corresponding downstream biological signaling pathways differentially associated with identified protein groups (Figures 2B and S3A). Abundance changes in known targets indicated the activity of key regulators involved in fibrogenesis (TGF□1 and angiotensinogen), hypoxia response (HIF1A), and inhibition of factors mediating hepatocyte function (HNF4□ and HNF1□) or involved in HSC inactivation (PPARGC1A) in both fibrotic models (Figure S3A). Interestingly, the pro-proliferative mTOR pathway showed signaling attenuation in the course of CCl_4 treatment but upregulation in the case of DDC treatment, suggesting hyperplastic potential of the DDC model (Figure S3A). Consistently, analysis of the DDC signature revealed inhibition of tumor suppressor gene *Rb1* with simultaneous activation of potential oncogenic regulators KDM5A, MRTFA, MYC, and YAP, thus underscoring increased carcinogenic risk (Figures 2B and S3B). By contrast, the CCl_4 signature indicated activation of EGF and VEGF□ with simultaneous downregulation of the HNF4□ (Figure 2B). This supports previous reports on the importance of these factors during hepatotoxic injury.[18-20] While dynamic changes of regulatory networks and signaling pathways correlated well with fibrosis progression in both models, ineffective downregulation of profibrotic signaling in the DDC-induced model suggested a limited capacity of the liver to heal from cholestatic injury (Figures 2B and S3B).

Next, we analyzed CCl_4 and DDC Total proteomes using unsupervised hierarchical clustering and functional annotation term enrichment (Figure 2C,D). This allowed the separation of proteins with similar temporal abundance profiles while simultaneously revealing clusters comprising matrisome-annotated proteins (see Materials and Methods). In the CCl_4 proteome, three matrisome-annotated clusters (Figure 2C; clusters I, II, and III) containing 755 proteins showed a variable degree of time-dependent abundance decline over the course of healing. By contrast, two large matrisome-annotated clusters (Figure 2D; clusters I and II) with 799 constituents showed almost no decline in abundance over the recovery period in the DDC model. Our data reflect the reversibility of CCl_4-induced fibrogenesis and restricted healing with higher carcinogenic risk in the DDC model.

Matrisome linked with cholestasis is enriched in basement membrane (BM) proteins whereas deposits upon hepatotoxic injury contain matrisome-associated proteins

To further dissect disease-specific processes associated with matrisome-enriched clusters (Figure 2C,D), we followed the functional annotation of proteins using a comprehensive annotation matrix compiled from GO terms, UniProtKB keywords, and the MatrisomeDB matrisome database.[13, 21] This revealed that 303 proteins shared by CCl_4 and DDC Total proteomes were annotated not only with matrisome-related keywords but also as “Cell adhesion”, “Fibrinogen complex”, “Platelet aggregation”, and “Intermediate filaments”, thus

indicating engagement in cellular interaction with ECM (Figure 2E). Consistently, top canonical IPA pathways included “Signaling by Rho family GTPases”, “Integrin signaling” and “Actin cytoskeleton signaling” (Figure S3C). As anticipated, 452 proteins uniquely identified in CCl_4 matrisome-enriched clusters were also associated with inflammatory response, a well-described feature of this model.[22] A group of 496 proteins exclusive for DDC was found to associate with “Basement membrane” and “Cell substrate junction” reflecting an increased abundance of BM components synthesized during the development of periductal fibrosis (e.g., laminins, □-chains of collagens IV, VI, and XVIII; Figure 2E).

In a group of 60 matrisome proteins significantly changing in both Total CCl_4 and DDC proteomes (Figure 3A) there were mainly core matrisome proteins, such as collagens (e.g., □-chains of collagens I and V) and ECM glycoproteins (e.g., fibronectin, EMILIN1, and vitronectin). In contrast to previous reports,[7] we found collagen VI, a protein regulating ECM contractility,[23] upregulated during fibrogenesis in both models (Figure S4). In addition, we identified several matrisome-associated proteins (e.g., NGLY1, PLOD3, S100A4, MUG2, SERPINA7, SERPINF1, and P4HA1) not previously reported in liver fibrosis as uniquely induced in the CCl_4 model.[21] Among these, ECM glycoprotein lactadherin (MFGE8), has been shown to reduce liver fibrosis in mice.[24] In contrast, BM matrisome proteins, such as laminins, collagens IV and XVIII, and perlecan (HSPG2) were exclusively upregulated in the DDC proteome (Figures 3A and S4).

To validate our findings demonstrating distinct features of the fibrotic models used, we performed immunofluorescence (IF) analysis of major core matrisome proteins abundantly upregulated in both CCl_4 and DDC proteomes (Figure 3B–D). Collagen I accumulated at the sites of primary injury and, consistent with proteomics, was only partially reduced upon recovery in the DDC model (Figure 3B). Collagen I-rich areas were delineated by fibronectin, a protein serving as a scaffold for collagen fibril assembly.[25] Although fibronectin abundance in Total CCl_4 and DDC proteomes decreased with healing, IF analysis revealed persisting deposits within capillarized hepatic sinusoids even after a recovery period of 10 days (Figure 3C). Consistent with a report on human cirrhotic livers,[26] BM-associated collagen IV accumulated around fibrotic septa in both models and its persistent presence indicated incomplete liver healing after DDC withdrawal (Figure 3D).

Integrin αv is specifically induced on the membranes of injured hepatocytes within fibrotic scar tissue in the hepatotoxic CCl_4 model

The dynamic nature of fibrosis stems from interplay between injured hepatocytes, immune cells, and hepatic myofibroblasts.[3] Using previously published cell type-specific signatures (see Materials and Methods), we identified 10 different cell populations in CCl_4 and DDC samples and compared their abundances over the course of liver fibrosis (Figures 4A–D and S5A). A set of 18 proteins quantified from the signature of hepatocytes exhibited faster decline in the hepatotoxic CCl_4 than DDC model (Figure 4A), corresponding well to the extensive parenchymal injury evidenced by high alanine and aspartate transaminase levels (Figure S1A).

Rapid increase in HSC and activated PF signatures paralleled the activation and proliferation of ECM-depositing myofibroblasts in both fibrotic models (Figure 4B). However, faster upregulation of activated PFs in DDC confirms their predominant role in cholestatic fibrosis. Temporal abundance profiles of Kupffer cell, macrophage, monocyte, and B-cell signature proteins illustrate faster recovery from inflammation with healing in the CCl_4 than in DDC model (Figures 4C,D and S5A). These findings, together with matrisome-enriched protein cluster analysis (Figure 2E), emphasized the role of the inflammation component in the context of fibrosis and underscored the model-specific involvement of PFs in cholestatic fibrosis.

Cellular interactions with the changing microenvironment are mediated by integrins, a heterogeneous family of cell adhesion receptors. Thus, temporal changes in cell type-specific integrin subsets reflect the alterations in fibrotic injury-induced cell populations with the potential to predict the fibrogenicity of the ongoing disease. Our profiling revealed increased expression of integrin □1 (Figure S5B), the most abundant collagen receptor, which has been reported (together with integrins □1 and □5) to correlate with the stages of human liver fibrosis.[27] Given its cell type-specific expression prevalence, this finding likely corresponds to the expansion of HSCs, simultaneously with induced integrin □1 expression on LSECs and injured hepatocytes.[27] A rapid immune response is documented by extensive upregulation of main leukocyte integrin subunits □2 and □M (Figures 4E and S5B). Their differential expression kinetics between the models correlate well with cell type-specific signatures (Figures 4C,D and S5A). Unexpectedly, fibronectin receptor integrin □5 (typically expressed on HSCs, PFs, and LSECs[28, 29] was detected in Total DDC proteome only (Figure 4E). Inasmuch as a boosted expression of integrin □5 has been reported in liver tumors,[30] this finding further supports the tumorigenic potential of biliary fibrosis.

Strong induction of TGF□-activating integrin □v in both CCl_4 and DDC Total proteomes (Figure 4E) reflected its central role in fibrogenesis.[31] Strikingly, in E-fraction, integrin □v was found to increase only in the CCl_4 model (Figure 4E), suggesting its close association with ECM specifically during hepatotoxic injury. Subsequent IF analysis showed localization of antibodies to □v mostly to periportal hepatocytes and with little signal found in central hepatocytes of control livers (Figure 4F). During CCl_4-induced injury, □v staining was enhanced at the periphery of pericentral hepatocytes adjacent to the collagen-rich scars, reflecting ongoing liver periportalization with the injury.[22] The zonal distribution of □v was partially restored with fibrosis regression. In DDC-driven cholestasis, antibodies to □v stained strongly reactive biliary epithelial cells (BECs), the main drivers of fibrogenesis in biliary fibrosis (Figure 4F). Thus, our analysis reveals stage-specific induction of integrin □v on the surface of pericentral hepatocytes that has been unrecognized to date and suggests its potential as a marker of reactive cholangiocytes in cholestasis.

Analysis of solubility profile dynamics of liver proteome reveals extracellular matrix protein-1 among matrisome proteins induced by fibrogenesis

As ECM remodeling during fibrogenesis entails also changes in the solubility of its constituents and associated proteins,[11] we next set out to identify proteins that become increasingly insoluble with fibrosis progression. We found 1,273 (CCl_4) and 762 (DDC) differentially expressed proteins, defined by at least 3-fold higher expression in E- than in S-fraction (see Materials and Methods). Hierarchical clustering of their MS intensity ratios clearly reflected changes in protein solubility profiles in the course of disease progression (Figure S6A,B). Proteins grouped into three (CCl_4, 406 proteins) and two (DDC, 63 proteins) ECM-enriched clusters exhibited increasing insolubility during fibrogenesis. Matrisome proteins found in both fibrotic models were mainly collagens and ECM glycoproteins (Figure 5A). Interestingly, we identified 93 (CCl_4) and 16 (DDC) proteins not present in control samples but induced by treatment (Figure S6C, Supporting Results). Abundance of most of these proteins in E-fraction decreased with healing in the CCl_4 but not in the DDC model (Figure 5B), suggesting model-specific incorporation of matrisome-associated proteins into insoluble ECM.

Among proteins upregulated with disease onset in E-fractions of both fibrotic models was extracellular matrix protein-1 (ECM1; Figures 5C and S6C). Subsequent IF analysis confirmed weak ECM1 staining (corresponding to low expression levels) in control livers, which was confined mostly to Kupffer cells and the apical membrane of BECs (Figures 5E and S6B). Increased ECM1 abundance during fibrogenesis was paralleled by its increasing localization within the infiltrating inflammatory cells and activated Kupffer cells. In addition, ECM1 heavily decorated apical membranes of BECs forming reactive ductuli in DDC-treated livers, corresponding thus to higher MS intensity of ECM1 during the development of biliary fibrosis. Induction of ECM1 expression in the inflammatory cells at the sites of primary injury in the CCl_4 model and in reactive ductuli in the DDC model strongly indicates its involvement in fibrogenesis and healing. Although a previous study had identified ECM1 expression to be hepatocyte-specific,[32] our data suggest that its role might be more complex than anticipated.

Correlation of dynamic changes of hepatotoxic proteome and fibrotic deposits identifies clusterin as a novel protein associated with fibrosis resolution

The CCl_4 model gradually developed typical bridging liver fibrosis[14] followed by fibrosis resolution as documented by liver injury markers (Figure S1A) and collagen deposits (Figure S1B), as well as by results of our MS profiling (Figure 2). These dynamic changes allowed us to correlate protein abundance profiles (from both Total and E-fraction proteomes) with disease dynamics (captured as fibrotic area) in individual mice (Figure 6). For example, leukocyte-specific integrin □2-interacting protein coronin 1a displayed a significant positive correlation with fibrogenesis reflecting the time-course of the immune response while negatively

correlating methionine cycle enzyme adenosylhomocysteinase corresponded to hepatocellular death induced by fibrogenesis (Figure 6B,C).

In the Total CCl_4 proteome, proteins positively correlating with fibrogenesis included matrisome proteins (e.g., angiotensinogen, fibrinogen □,□, □-chain, fibrinogen-like protein 1, and fibronectin). The IPA analysis linked these to the inflammation and pathways associated with ECM-cell interactions, such as "Actin cytoskeleton signaling" and "Integrin signaling" (Figure S7A). Proteins with negative correlation were mostly enzymes involved in hepatocyte metabolism, such as alpha-enolase (ENO1), an enzyme shown to participate as plasminogen receptor in ECM degradation.[33] Analogously to Total proteome, proteins of CCl_4 E-fraction positively correlating with fibrosis area were linked to fibrogenesis (Figure S7B). Displaying negative correlation was a group of 41 proteins consisting mainly of enzymes associated with amino acid metabolism, necrosis, and apoptosis (Figure S7A,B). In addition, three core matrisome proteins – decorin, MFAP2, and collagen □-1 (I) – also were identified. As shown for collagen □-1 (I), their MS intensity temporal profiles indicated their upregulation in E-fraction while their overall abundance decreased with healing (Figure 6D), likely corresponding to the increased association of these matrisome proteins with degraded insoluble ECM.

Among proteins positively correlating with fibrotic scar development and resolution in both Total and insoluble proteomes was clusterin, a glycoprotein implicated in several diseases (Figure 6D).[34] As clusterin imparts extracellular chaperone function not previously linked to fibrosis, we next investigated clusterin's localization by IF microscopy (Figure 6E). In untreated livers, clusterin was detected in BECs and partially in hepatocytes. Upon CCl_4 intoxication, IF staining revealed its prominent expression by damaged hepatocytes. Strikingly, clusterin increasingly re-localized along the collagen deposits over the healing period. In DDC-treated livers, clusterin was found mostly in BECs forming reactive ductuli and hepatocytes, with minimal changes upon healing (Figure 6E). Moreover, extracellular clusterin deposition in close proximity of collagen fibers was further demonstrated in fibrotic and cirrhotic human livers of various etiologies at different stages of fibrosis (Figures 6F and S8). The gradual increase in clusterin expression with the progression of fibrosis against the background of chronic hepatitis C (METAVIR score F1-F4) further emphasized its role in the development of liver fibrotic diseases.

Interface hepatocyte elasticity responds dynamically to the pericentral injury in the course of fibrosis development

Identification of "Rho-A", "Rho family GTPases", "Actin cytoskeleton", and "Integrin/ILK signaling" among top canonical pathways elicited by proteins of Total CCl_4 proteome as well as proteins of matrisome-enriched clusters (Figure S3A,C) suggested that the hepatotoxic injury leads to increased cytoskeletal tension in injured hepatocytes. This was further supported by significant enrichment in intermediate filament proteins

(Figure 2E) and in myocardin-related transcription factor (MRTF) targets (e.g., ITGA1, THBS1, ACTR2, and MSN; Figure 7A), key regulators involved in cell and tissue mechanics, cytoskeletal dynamics, and mechanosensing.[35]

As variations in ECM composition and content also substantially affect the biomechanics of liver tissue, we decided to examine correlation between our proteomic results and mapping of dynamic changes in the biomechanical properties of CCl_4-treated livers. We used atomic force microscopy (AFM) combined with polarized microscopy[17] to precisely locate and probe the following compartments: 1) regions of collagen-rich scar tissue in close vicinity of the central vein, 2) injured hepatocyte regions next to the collagen scar, and 3) regions of hepatocytes on the interface between injured and not visibly damaged hepatocytes (so-called interface hepatocytes[36]) (Figure 7B). In parallel, we also measured stiffness of corresponding regions in nontreated control liver sections (Figure 7C).

Our AFM analysis revealed no substantial topological variations across defined compartments in control livers, with median Young's moduli ranging between 1.2 and 1.6 kPa (Figure 7C, Table S1). Fibrogenic response triggered progressive tissue stiffening apparent in all analyzed compartments (Figure 7D–F, Table S1), with collagen-rich regions the stiffest at maximal fibrosis (~4.4 kPa at T2; Figure 7D). Unexpectedly, interface regions exhibited initial softening (T1; median ~0.8 kPa vs. 1.2 kPa in control livers), which was followed by increase in stiffness up to ~2.0 kPa (T2). With healing (T4), all compartments demonstrated clear decrease in stiffness (Figure 7D–F), although this was only marginal in the regions corresponding to injured hepatocytes. Significant softening of collagen-rich scar tissue during healing indicated partial resolution of scar-associated ECM while it associated with the incorporation of several core matrisome proteins (e.g., COL1A1 and FBN1) into the scar tissue (Figures 1F and 6D). Although the heterogeneity of AFM-based measurements constituted a limitation on our correlation analysis relative to proteomic data (Figure S9), this analysis provides a coherent framework for better understanding the dynamics of proteomic landscapes in the context of fibrosis-associated changes in the local mechanics of liver tissue.

DISCUSSION

In this study, we comprehensively characterized and compared dynamic proteomic landscapes of liver fibrosis development and repair in two mouse models based either on repetitive CCl_4 intoxication[14] or DDC feeding.[16] These models are widely used to reliably mimic either hepatotoxic (CCl_4) or cholestatic (DDC) liver injuries leading to fibrosis in humans.[14] Previous attempts to grasp the complexity of etiology-specific fibrotic proteomes with a focus on diseased ECM[6, 7] were limited due to origins of the analyzed material (mostly decellularized samples) and yielded only fragmented insight into the time course of the disease. To fill this research gap, we employed detergent-based tissue extraction and analyzed both Total and insoluble fraction proteomes at multiple time points of disease progression and spontaneous healing. This approach allowed us to 1) compare time-resolved, compartment-specific proteomes of CCl_4 and DDC models, 2) define etiology-specific elements of fibrogenesis, and 3) detect even low-abundance matrisome and matrisome-interacting proteins in the ECM-enriched insoluble fraction samples. Further, our detailed AFM-based profiling of CCl_4-treated livers enabled us to relate our proteomic data to disease-associated changes in the local mechanics of liver tissue.

We and others have demonstrated that the nature of liver injury determines the set of components assembled in diseased ECM,[7] which thus reflects unique features of the injury. For instance, the initial decline in abundance of hepatocyte- and activated BEC-expressed COL18A1[37] and its consecutive increase thereafter in the hepatotoxic CCl_4 model corresponds to hepatocyte death followed by expansion of both COL18A1-expressing cell types.[38] By contrast, extensive COL18A1 expression in DDC-induced cholestasis was already apparent in the early fibrotic deposits due to a massive ductular reaction. A prominent group of BM-associated proteins uniquely identified in the cholestatic model can be attributed to activated BECs in proliferating bile ducts. Some of them (e.g., COL18A1, COL4A2, COL6A2, and HSPG2) are among the 14-gene signature potently predicting human patient cirrhosis progression and survival.[39] Other DDC matrisome constituents (e.g., COL3A1, elastin, and LAMC1) have been recently linked to the deterioration of hepatocyte functions in connection with ECM stiffening.[40] Notably, elastin is present in liver biopsies from patients with advanced fibrosis and adverse clinical outcome[41] and is associated with the irreversibility of liver fibrosis. Further, the increased incorporation of crosslinking protein LOXL1 and TGF□1-related protein LTBP4 into DDC-specific ECM underscores its resemblance to human cirrhotic liver ECM.[42] Hence, our findings indicate that cholestasis-driven ECM deposits contain numerous proteins detected in more advanced stages of liver disease favoring hepatocarcinogenesis with a compromised ability to heal. Moreover, identified cholestasis-induced unique signaling pathways were analogous to those recently identified in a subtype of mouse cancer models mimicking human cholangiocarcinoma-like hepatocellular cancer.[43]

Our observations are concordant with recently published studies (reviewed in[2]) revealing that in the fibrotic liver resident and nonresident cell types wire into dynamic intercellular hubs with shifting cell populations, reflecting and shaping the disease course in an etiology-specific manner. Many of the feedback

mechanisms between the cells and ECM regulating fibrosis are mediated by members of the integrin family. In agreement with previous studies,[27] we observed in both models significant upregulation of all detected integrin subunits during fibrosis progression. Strong induction of integrin □M expression in cholestatic but not hepatotoxic injury documents the role of leukocyte-specific integrin □M□2 in the modulation of biliary fibrosis,[44] suggesting that the integrin □M might thus serve as a possible selective target for treatment of cholestatic liver disease. Further, a prominent transition of TGF□1-activating integrin □v toward insoluble ECM exclusively upon hepatotoxic injury was accompanied by its localization to injured pericentral hepatocytes near collagen-rich scars and □SMA-positive HSCs. This finding, together with a measured increase in the stiffness of injured hepatocytes, implies an active role of integrin □v in the targeted activation of TGF□1 in the local microenvironment during centrilobular fibrosis. Indeed, integrin □v located on hepatocytes in the vicinity of biliary fibrotic septa has been suggested to indicate hepatocyte biliary transformation.[45] Here, we propose that compartment-specific induction of □v expression on the surface of scar-associated hepatocytes could be a general mechanism to promote fibrosis progression.

In contrast to the cholestatic DDC model, hepatotoxic injury in the CCl_4 model showed a substantial ability to heal 10 days after challenge withdrawal. Such healing capacity allowed us to correlate the dynamics in CCl_4 proteomes with the changes in fibrotic deposits not only during fibrosis progression but also in resolution. Among proteins correlating with scar tissue formation in both Total and insoluble proteomes, we identified a small molecular chaperone clusterin. Clusterin is believed to be associated with elastin fibers in cholestasis,[46] and recently it was linked to the attenuation of mouse hepatic fibrosis.[47] Here, we localized clusterin exclusively to injured, pathologically stiffer hepatocytes. Interestingly, the clusterin promoter comprises binding motifs for mechanosensitive transcription factors such as Fos and AP-1/Jun.[48, 49] This suggests that local clusterin induction can reflect the dynamic changes of microenvironmental mechanical cues. Most intriguingly, we also found clusterin to associate with collagen-rich ECM deposits in the course of mouse fibrosis regression and with pathological human matrix of various etiologies. As clusterin overexpression associates with increased activity of ECM-degrading matrix metalloproteinases,[50] we hypothesize that clusterin accumulation facilitates the remodeling and resolution of scar tissue. Although the specific molecular function of clusterin in fibrotic tissue repair processes remains to be determined, our results strongly suggest clusterin to be an attractive antifibrotic target.

Liver cell and tissue mechanics play a pivotal role in the processes that initiate and resolve fibrotic injury.[3] Initial disruption of mechanical homeostasis prompts cytoskeletal remodeling that alters cell-generated forces and cellular biomechanics. Here, such a shift to a higher stiffness regime is illustrated by prominent changes in cytoskeleton-related signatures (actin and intermediate filaments) and signatures of mechanosensitive transcription regulators (e.g., MRTF) accompanied by a significant stiffening of parenchymal compartments devoid of apparent collagen deposits. This indicates substantial cell-driven changes in the biomechanical properties of tissue microenvironment. An unexpected decrease in the stiffness of interface

hepatocytes with the initial fibrotic changes revealed by our AFM analysis suggests that the initial softening of interface hepatocytes upon injury counterbalances the stiffening of the injured hepatocytes and/or fibrous scar tissue regions. As the interface hepatocytes have been shown to undergo a phenotypic shift in response to the injury,[36] it will now be interesting to determine whether altered mechanical properties serve as the cue leading to the genetic fetal reprogramming or if this initial softening is due to the expression of fetal markers. Together, our AFM and proteomic data underscore the role of local tissue stiffening in fibrotic response and postulate involvement of tissue softening during resolution not only in the collagen scar tissue but also in regenerating parenchyma.

ACKNOWLEDGEMENTS

We would like to thank S.M. Meier-Menches (University of Vienna, Austria) and J. Masek (Charles University, Prague, Czech Republic) for critical reading of the manuscript; and D. Hadraba (Institute of Physiology, Prague, Czech Republic) for sharing his expertise. We also acknowledge the Light Microscopy Core Facility, IMG CAS, Prague, Czech Republic for support with the microscopy imaging presented herein.

This work was supported by the Grant Agency of the Czech Republic (18-02699S and 21-21736S); the Grant Agency of the Ministry of Health of the Czech Republic (NU21-04-00100); the Institutional Research Project of the Czech Academy of Sciences (RVO 68378050); the National Institute for Cancer Research (Programme EXCELES, LX22NPO5102) - Funded by the European Union - Next Generation EU; the Grant Agency of Charles University (273723), and MEYS CR projects (LM2023050, LM2018126, LQ1604 NPU II, LO1419, and LM2015040). CIISB, Instruct-CZ Centre of Instruct-ERIC EU consortium, funded by MEYS CR infrastructure project LM2018127 and European Regional Development Fund-Project "UP CIISB" (No. CZ.02.1.01/0.0/0.0/18_046/0015974) financially supported the measurements at the CF Nanobiotechnology, CEITEC MU (AFM measurements). The funding sources were not involved in the study design, data collection and analysis, decision to publish, or preparation of the article.

Presentation: none.

DATA AVAILABILITY STATEMENT

The data that support the findings of this study are available from the corresponding author upon reasonable request.

REFERENCES

1. Karlsen TH, Sheron N, Zelber-Sagi S, et al. The EASL-Lancet Liver Commission: protecting the next generation of Europeans against liver disease complications and premature mortality. Lancet 2022;399:61-116.
2. Kisseleva T, Brenner D. Molecular and cellular mechanisms of liver fibrosis and its regression. Nat Rev Gastroenterol Hepatol 2021;18:151-166.
3. Henderson NC, Rieder F, Wynn TA. Fibrosis: from mechanisms to medicines. Nature 2020;587:555-566.
4. Ramachandran P, Dobie R, Wilson-Kanamori JR, et al. Resolving the fibrotic niche of human liver cirrhosis at single-cell level. Nature 2019;575:512-518.
5. Niu L, Geyer PE, Gupta R, et al. Dynamic human liver proteome atlas reveals functional insights into disease pathways. Mol Syst Biol 2022;18:e10947.
6. Massey VL, Dolin CE, Poole LG, et al. The hepatic "matrisome" responds dynamically to injury: Characterization of transitional changes to the extracellular matrix in mice. Hepatology 2017;65:969-982.
7. Klaas M, Kangur T, Viil J, et al. The alterations in the extracellular matrix composition guide the repair of damaged liver tissue. Sci Rep 2016;6:27398.
8. Georges PC, Hui JJ, Gombos Z, et al. Increased stiffness of the rat liver precedes matrix deposition: implications for fibrosis. Am J Physiol Gastrointest Liver Physiol 2007;293:G1147-54.
9. Olsen AL, Bloomer SA, Chan EP, et al. Hepatic stellate cells require a stiff environment for myofibroblastic differentiation. Am J Physiol Gastrointest Liver Physiol 2011;301:G110-8.
10. Saneyasu T, Akhtar R, Sakai T. Molecular Cues Guiding Matrix Stiffness in Liver Fibrosis. Biomed Res Int 2016;2016:2646212.
11. Schiller HB, Fernandez IE, Burgstaller G, et al. Time- and compartment-resolved proteome profiling of the extracellular niche in lung injury and repair. Mol Syst Biol 2015;11:819.
12. Hynes RO. The extracellular matrix: not just pretty fibrils. Science 2009;326:1216-9.
13. Naba A, Clauser KR, Hoersch S, et al. The matrisome: in silico definition and in vivo characterization by proteomics of normal and tumor extracellular matrices. Mol Cell Proteomics 2012;11:M111 014647.
14. Liu Y, Meyer C, Xu C, et al. Animal models of chronic liver diseases. Am J Physiol Gastrointest Liver Physiol 2013;304:G449-68.
15. Trautwein C, Friedman SL, Schuppan D, et al. Hepatic fibrosis: Concept to treatment. J Hepatol 2015;62:S15-24.
16. Fickert P, Stoger U, Fuchsbichler A, et al. A new xenobiotic-induced mouse model of sclerosing cholangitis and biliary fibrosis. Am J Pathol 2007;171:525-36.
17. Ojha S, Pribyl J, Klimovic S, et al. Measurement of Liver Stiffness using Atomic Force Microscopy Coupled with Polarization Microscopy. J Vis Exp 2022.
18. Komuves LG, Feren A, Jones AL, et al. Expression of epidermal growth factor and its receptor in cirrhotic liver disease. J Histochem Cytochem 2000;48:821-30.
19. Yang L, Kwon J, Popov Y, et al. Vascular endothelial growth factor promotes fibrosis resolution and repair in mice. Gastroenterology 2014;146:1339-50 e1.
20. Yue HY, Yin C, Hou JL, et al. Hepatocyte nuclear factor 4alpha attenuates hepatic fibrosis in rats. Gut 2010;59:236-46.
21. Shao X, Taha IN, Clauser KR, et al. MatrisomeDB: the ECM-protein knowledge database. Nucleic Acids Res 2020;48:D1136-D1144.
22. Ghallab A, Myllys M, Holland CH, et al. Influence of Liver Fibrosis on Lobular Zonation. Cells 2019;8.
23. Williams LM, McCann FE, Cabrita MA, et al. Identifying collagen VI as a target of fibrotic diseases regulated by CREBBP/EP300. Proc Natl Acad Sci U S A 2020;117:20753-20763.
24. An SY, Jang YJ, Lim HJ, et al. Milk Fat Globule-EGF Factor 8, Secreted by Mesenchymal Stem Cells, Protects Against Liver Fibrosis in Mice. Gastroenterology 2017;152:1174-1186.
25. Sottile J, Shi F, Rublyevska I, et al. Fibronectin-dependent collagen I deposition modulates the cell response to fibronectin. Am J Physiol Cell Physiol 2007;293:C1934-46.

26. Mak KM, Chen LL, Lee TF. Codistribution of collagen type IV and laminin in liver fibrosis of elderly cadavers: immunohistochemical marker of perisinusoidal basement membrane formation. Anat Rec (Hoboken) 2013;296:953-64.
27. Nejjari M, Couvelard A, Mosnier JF, et al. Integrin up-regulation in chronic liver disease: relationship with inflammation and fibrosis in chronic hepatitis C. J Pathol 2001;195:473-81.
28. Olsen AL, Sackey BK, Marcinkiewicz C, et al. Fibronectin extra domain-A promotes hepatic stellate cell motility but not differentiation into myofibroblasts. Gastroenterology 2012;142:928-937 e3.
29. Couvelard A, Scoazec JY, Feldmann G. Expression of cell-cell and cell-matrix adhesion proteins by sinusoidal endothelial cells in the normal and cirrhotic human liver. Am J Pathol 1993;143:738-52.
30. Lai KK, Shang S, Lohia N, et al. Extracellular matrix dynamics in hepatocarcinogenesis: a comparative proteomics study of PDGFC transgenic and Pten null mouse models. PLoS Genet 2011;7:e1002147.
31. Reed NI, Jo H, Chen C, et al. The alphavbeta1 integrin plays a critical in vivo role in tissue fibrosis. Sci Transl Med 2015;7:288ra79.
32. Fan W, Liu T, Chen W, et al. ECM1 Prevents Activation of Transforming Growth Factor beta, Hepatic Stellate Cells, and Fibrogenesis in Mice. Gastroenterology 2019;157:1352-1367 e13.
33. Didiasova M, Schaefer L, Wygrecka M. When Place Matters: Shuttling of Enolase-1 Across Cellular Compartments. Front Cell Dev Biol 2019;7:61.
34. Wilson MR, Zoubeidi A. Clusterin as a therapeutic target. Expert Opin Ther Targets 2017;21:201-213.
35. Esnault C, Stewart A, Gualdrini F, et al. Rho-actin signaling to the MRTF coactivators dominates the immediate transcriptional response to serum in fibroblasts. Genes Dev 2014;28:943-58.
36. Ben-Moshe S, Veg T, Manco R, et al. The spatiotemporal program of zonal liver regeneration following acute injury. Cell Stem Cell 2022;29:973-989 e10.
37. Schuppan D, Cramer T, Bauer M, et al. Hepatocytes as a source of collagen type XVIII endostatin. Lancet 1998;352:879-80.
38. Manco R, Clerbaux LA, Verhulst S, et al. Reactive cholangiocytes differentiate into proliferative hepatocytes with efficient DNA repair in mice with chronic liver injury. J Hepatol 2019;70:1180-1191.
39. Wu Y, Cao Y, Xu K, et al. Dynamically remodeled hepatic extracellular matrix predicts prognosis of early-stage cirrhosis. Cell Death Dis 2021;12:163.
40. Acun A, Oganesyan R, Uygun K, et al. Liver donor age affects hepatocyte function through age-dependent changes in decellularized liver matrix. Biomaterials 2021;270:120689.
41. Kendall TJ, Dolman GE, Duff CM, et al. Hepatic elastin content is predictive of adverse outcome in advanced fibrotic liver disease. Histopathology 2018;73:90-100.
42. Mazza G, Telese A, Al-Akkad W, et al. Cirrhotic Human Liver Extracellular Matrix 3D Scaffolds Promote Smad-Dependent TGF-beta1 Epithelial Mesenchymal Transition. Cells 2019;9.
43. Tang M, Zhao Y, Zhao J, et al. Liver cancer heterogeneity modeled by in situ genome editing of hepatocytes. Sci Adv 2022;8:eabn5683.
44. Joshi N, Kopec AK, Ray JL, et al. Fibrin deposition following bile duct injury limits fibrosis through an alphaMbeta2-dependent mechanism. Blood 2016;127:2751-62.
45. Popov Y, Patsenker E, Stickel F, et al. Integrin alphavbeta6 is a marker of the progression of biliary and portal liver fibrosis and a novel target for antifibrotic therapies. J Hepatol 2008;48:453-64.
46. Aigelsreiter A, Janig E, Sostaric J, et al. Clusterin expression in cholestasis, hepatocellular carcinoma and liver fibrosis. Histopathology 2009;54:561-70.
47. Seo HY, Lee SH, Lee JH, et al. Clusterin Attenuates Hepatic Fibrosis by Inhibiting Hepatic Stellate Cell Activation and Downregulating the Smad3 Signaling Pathway. Cells 2019;8.
48. Jin G, Howe PH. Transforming growth factor beta regulates clusterin gene expression via modulation of transcription factor c-Fos. Eur J Biochem 1999;263:534-42.
49. Miyamoto-Sato E, Fujimori S, Ishizaka M, et al. A comprehensive resource of interacting protein regions for refining human transcription factor networks. PLoS One 2010;5:e9289.
50. Shim YJ, Kang BH, Jeon HS, et al. Clusterin induces matrix metalloproteinase-9 expression via ERK1/2 and PI3K/Akt/NF-kappaB pathways in monocytes/macrophages. J Leukoc Biol 2011;90:761-9.

FIGURES & FIGURE LEGENDS

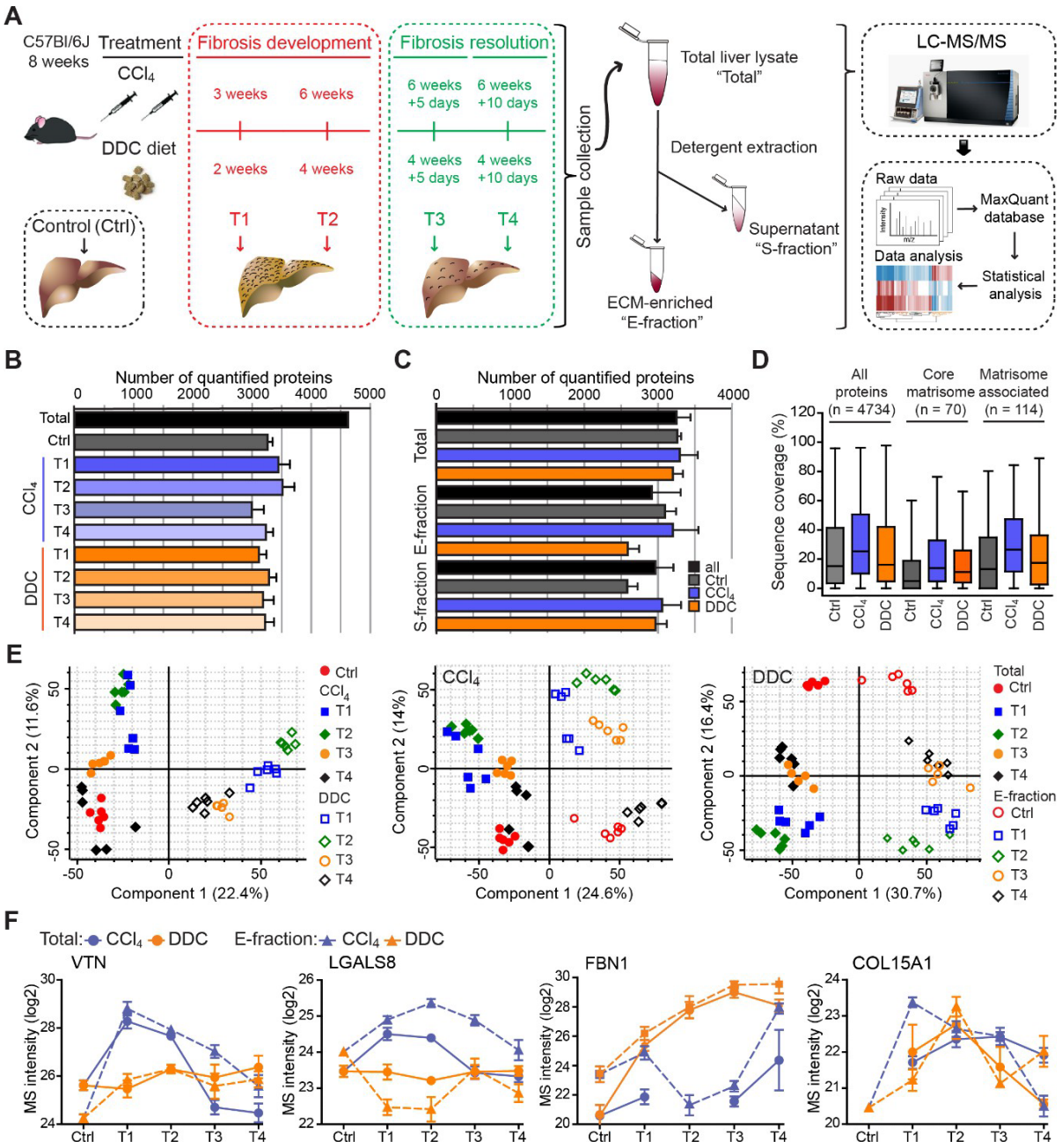

FIGURE 1 Hepatotoxic and cholestatic injury generate distinct time-resolved and compartment-specific protein signatures. (**A**) Schematic overview of the experimental setup. Six animals were used in each model at each time point. (**B**) Numbers of quantified proteins at the indicated time points and experimental conditions; n = 6. (**C**) Box plots show the distribution of protein sequence coverage (coverage of possible tryptic peptides per protein in %) for the indicated matrisome categories (as defined by Naba et al.[13]) and all detected proteins in experimental conditions indicated. (**D**) Principal component analysis (PCA) of Total proteome separates time-dependent fibrogenesis and healing in CCl_4- (closed symbols) and DDC- (open symbols) induced fibrosis. The first two components of data variability of 3,624 proteins identified in Total liver fractions in CCl_4 and 3,521 proteins in DDC are shown; n = 6. (**E**) PCA shows the separation of Total (closed symbols) and E-fraction (open symbols) proteomes in time; the first two components of data variability are shown; n = 6. (**F**) Line plots show time-dependent changes in mass spectrometry intensities in Total (solid line) and E-fraction (broken line) proteomes for indicated selected proteins in CCl_4 and DDC models; n = 4–6.

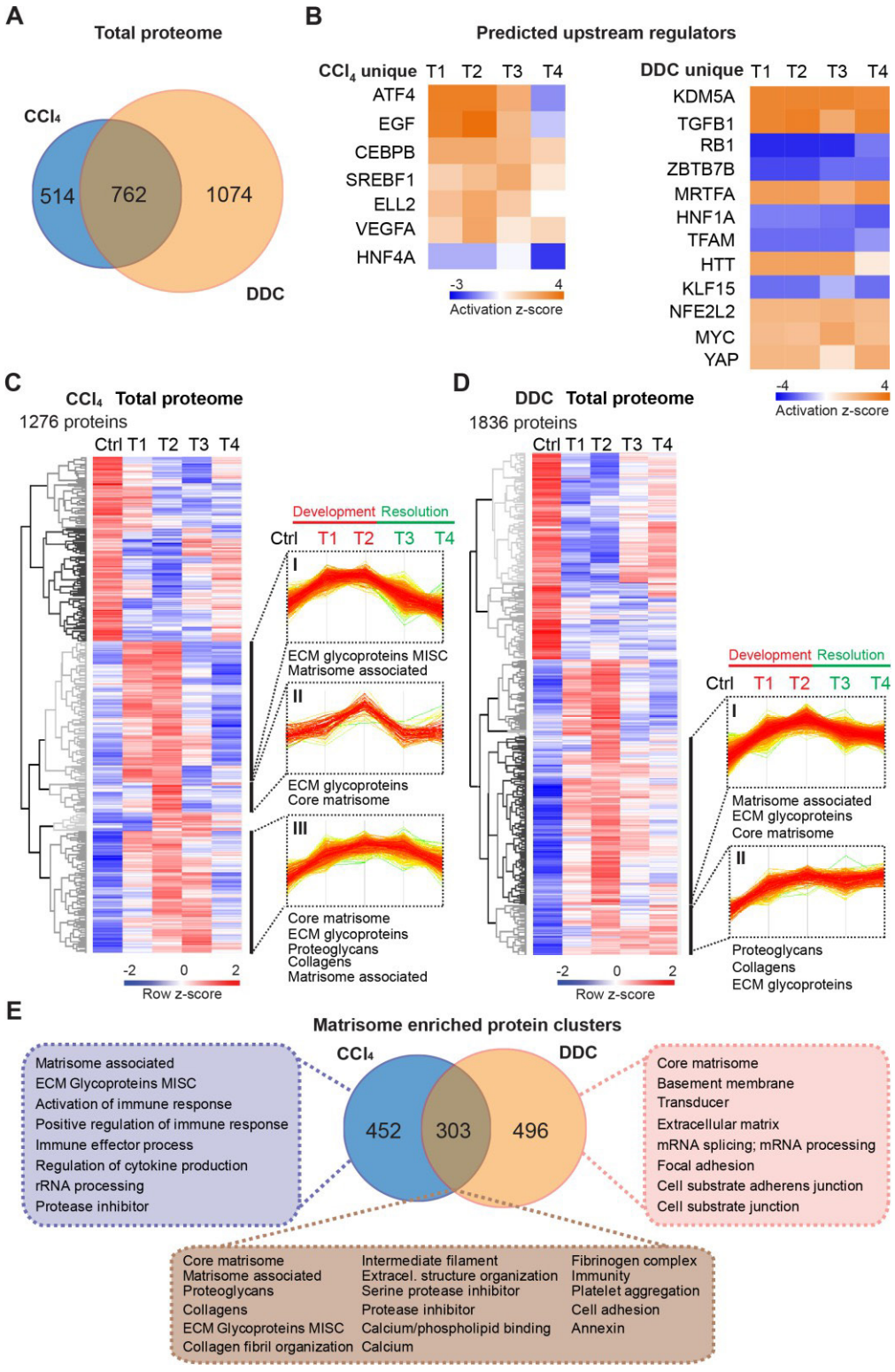

FIGURE 2 Time-resolved analysis of Total proteomes shows limited healing in matrisome-enriched protein clusters in the cholestatic model. (**A**) Venn diagram shows relative proportion of 1,276 and 1,836 proteins differentially expressed (*t*-test; Benjamini-Hochberg FDR < 5%) in Total CCl_4 and DDC proteomes. (**B**) Hierarchical cluster analysis of the activity score of the upstream regulators at the indicated time points predicted by Ingenuity Pathway Analysis (IPA) from unique CCl_4 and DDC protein signatures shown in A. (**C,D**) Hierarchical clustering of mean *z*-scored mass spectrometry (MS) intensities of proteins of Total CCl_4 (C) or DDC (D) proteomes; n = 6. Profiles of *z*-scored MS intensities of proteins from matrisome-annotated clusters for CCl_4 (I–III) and DDC (I and II) models are shown. (**E**) Venn diagram compares proteins from matrisome-annotated clusters shown in C and D. UniProt keyword enrichment annotation for each group within the diagram is indicated (Fisher's test, Benjamini-Hochberg FDR < 4%).

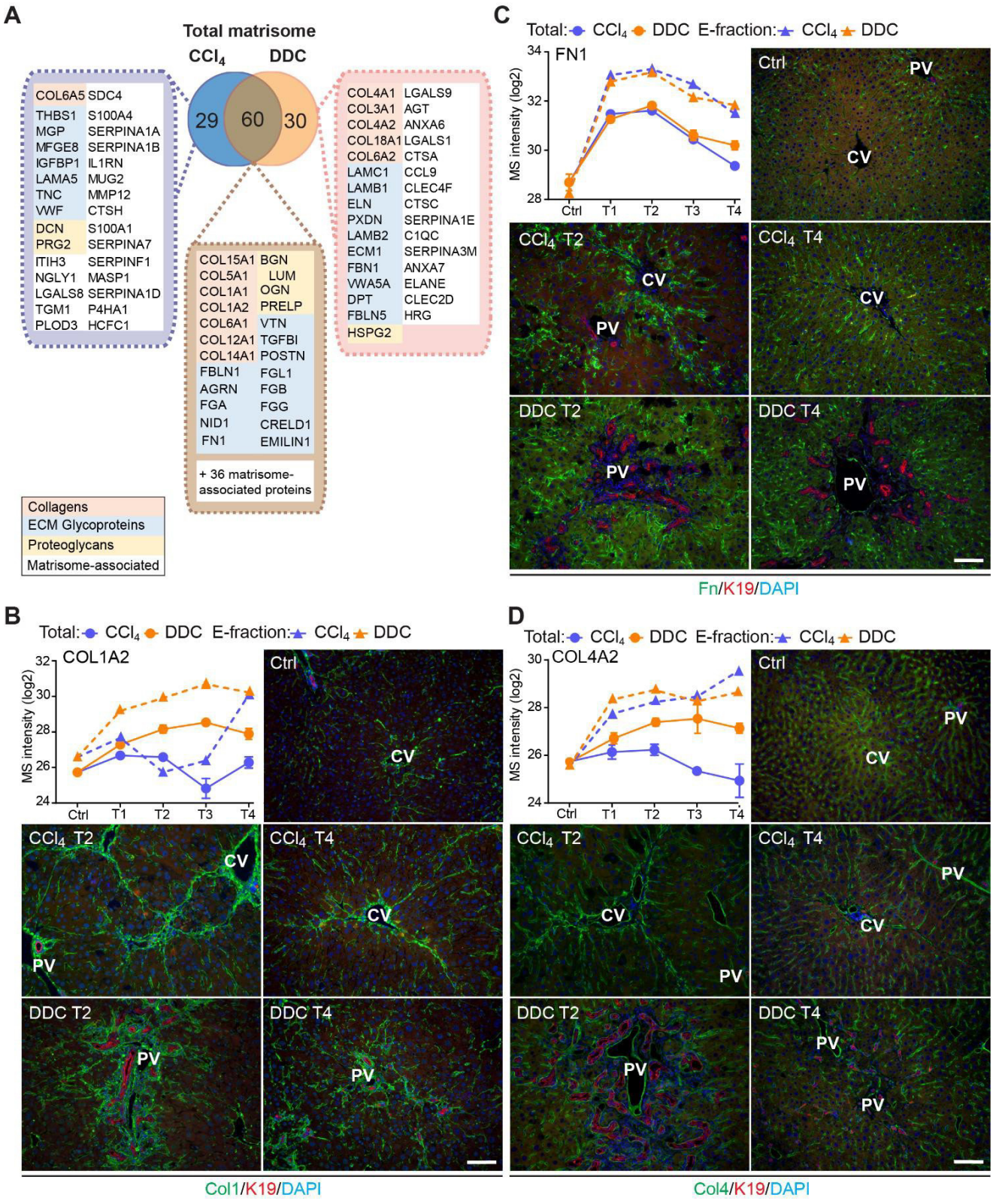

FIGURE 3 Comparison of matrisome proteins differentially expressed between the CCl_4- and DDC-derived Total proteomes with immunofluorescence (IF) localization of the main core matrisome proteins within the injured livers. (**A**) Venn diagram shows a comparison of matrisome proteins differentially enriched in Total CCl_4 and DDC proteomes. Color coding indicates identified matrisome categories. (**B–D**) Representative IF images of fibronectin (B), collagen I (C), and collagen IV (D), all in green in liver sections from untreated controls (Ctrl), CCl_4-, and DDC-treated mice at time points of fibrosis development (T2) and resolution (T4). Bile ducts were visualized with antibodies to keratin 19 (K19; red); nuclei were stained with DAPI (blue). CV, central vein; PV, portal vein. Scale bar = 100 □m. Line plots show time-dependent change in respective mass spectrometry intensities in Total (solid line) and E-fraction (broken line) proteomes in CCl_4 and DDC models; n = 4–6.

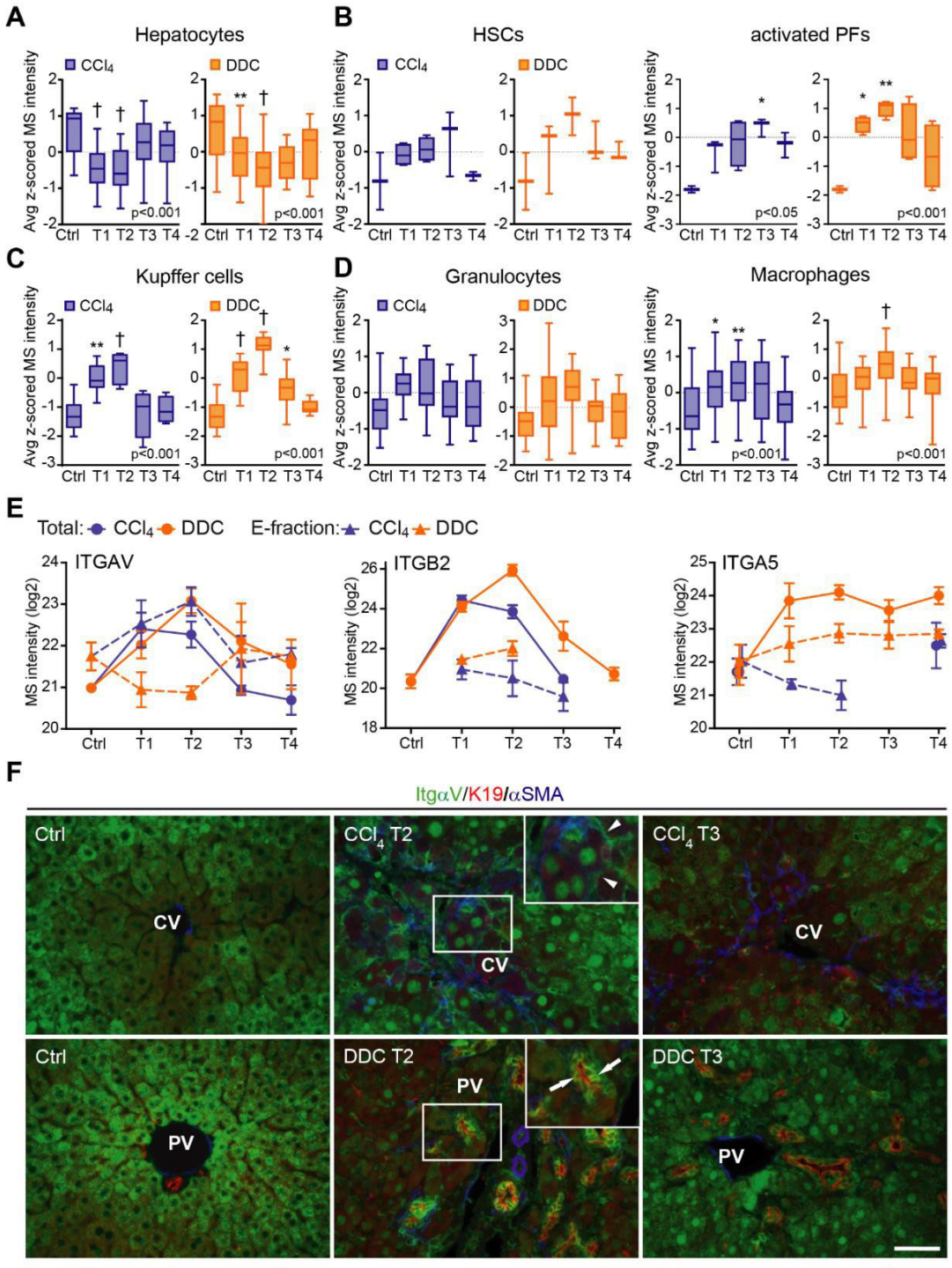

FIGURE 4 Liver cell type dynamics and cell type-specific integrin expression during fibrogenesis and healing. (**A–D**) Box plots show mean *z*-scored mass spectrometry (MS) intensities of the indicated cell type-specific protein signatures in time. Hepatocytes (A; n = 18), HSCs, and activated portal fibroblasts (PFs) (B; n = 3 and 4), Kupffer cells (C; n = 6), granulocytes, and macrophages (D; n = 16 and 33). One-way ANOVA with Bonferroni's post-test; $*p < 0.05$; $**p < 0.01$; †$p < 0.001$. (**E**) The line plots show the time-dependent change in MS intensities of indicated selected integrins in Total (solid line) and E-fraction (broken line) proteomes in CCl_4 and DDC models; n = 4–6. (**F**) Representative immunofluorescence images of liver sections from untreated controls (Ctrl), CCl_4-, and DDC-treated mice at time points of fibrosis development (T2) and resolution (T4) immunolabeled for integrin □v (green), K19 (red), and □SMA (blue). Arrowheads, integrin □v-positive injured hepatocytes; arrows, integrin □v-positive biliary epithelial cells of reactive ductuli. CV, central vein; PV, portal vein. Boxed areas, ×2 images. Scale bar = 50 □m.

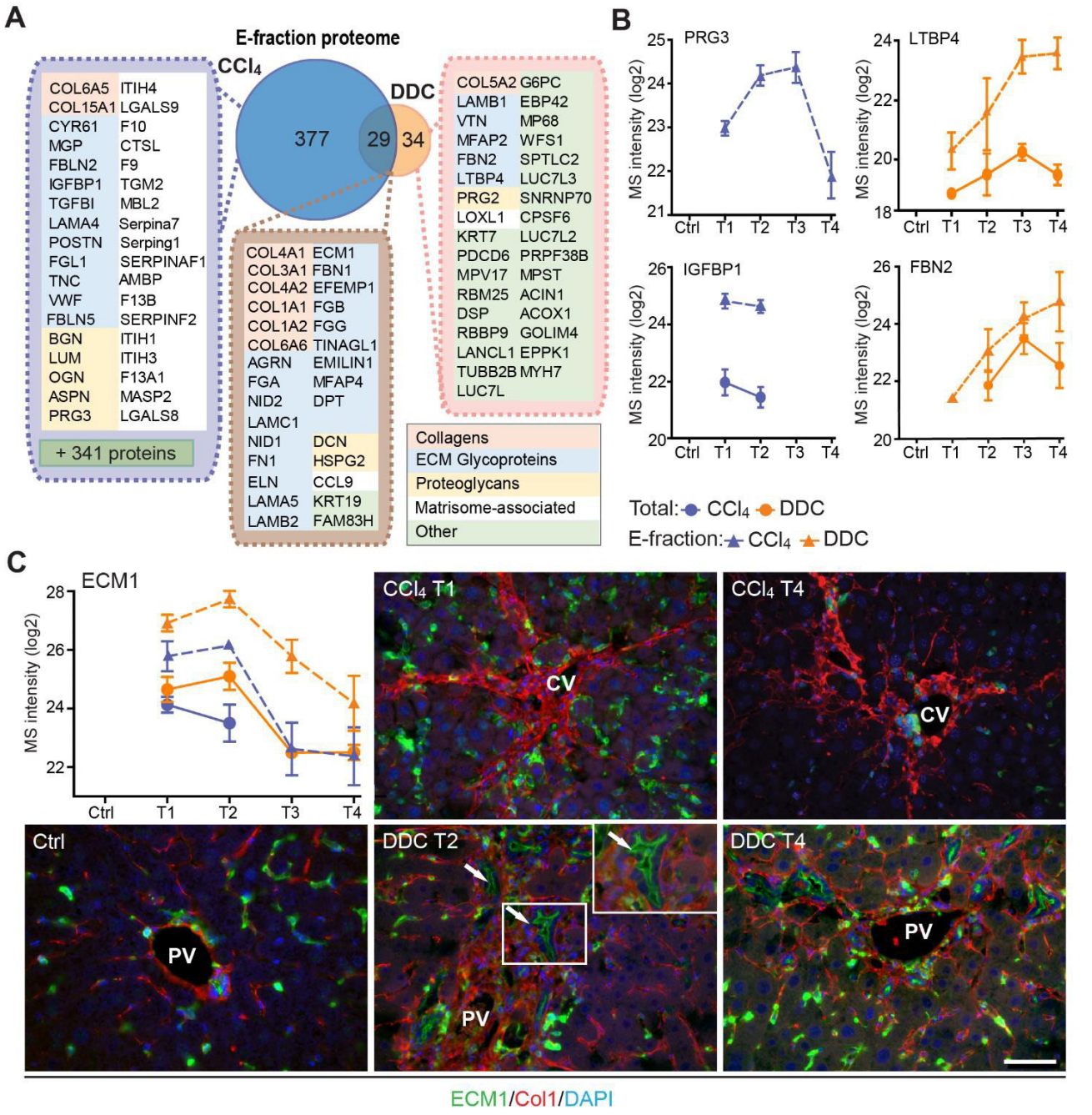

FIGURE 5 Solubility profiling provides in-depth analysis of model-specific matrisome composition. (**A**) Venn diagram shows relative proportion of proteins from E-fraction proteome identified as proteins with increasing insolubility over the course of fibrosis in each model (see Figure S6 and Supporting Materials and Methods). Matrisome proteins are highlighted with color coding to indicate identified matrisome categories. (**B**) Line plots show time-dependent change in mass spectrometry (MS) intensities of indicated selected matrisome proteins uniquely identified in E-fraction (broken line) proteomes in CCl_4 and DDC models; n = 4–6. (Solid line shows MS intensity profile in Total proteome.) (**C**) Representative immunofluorescence images of liver sections from untreated controls (Ctrl), CCl_4-, and DDC-treated mice at indicated time points of fibrosis development (T1 and T2) and resolution (T4) immunolabeled for ECM1 (green) and collagen 1 (red). Nuclei were stained with DAPI (blue). Arrows, ECM1-positive reactive biliary epithelial cells. CV, central vein; PV, portal vein. Boxed areas, ×2 images. Scale bar = 50 □m.

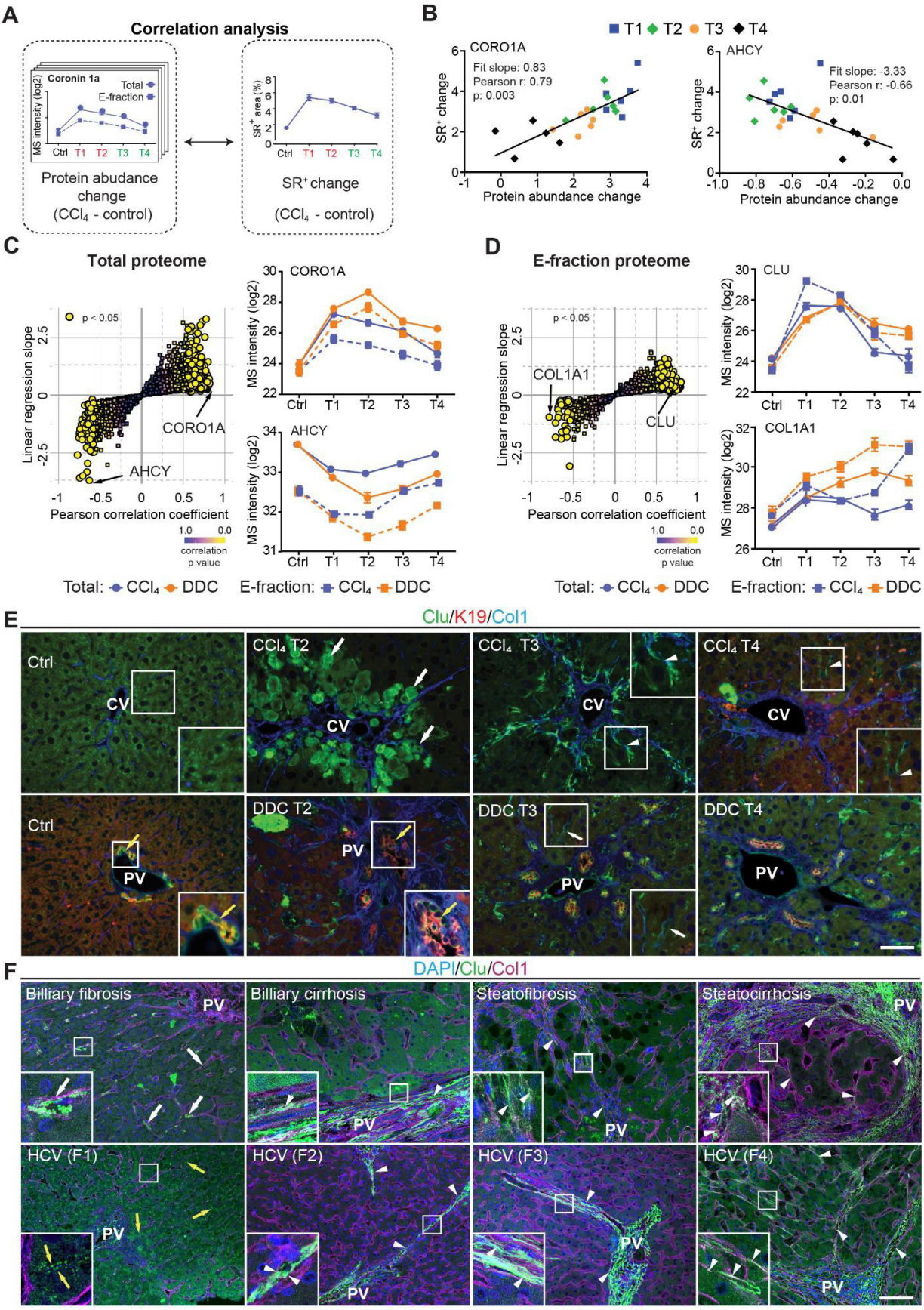

FIGURE 6 Correlation analysis of protein abundance and changes in fibrotic deposits in the hepatotoxic model associates clusterin with fibrosis resolution. (**A**) Schematic illustrates the correlation of protein abundance changes with changes in sirius red-positive (SR^+) areas of fibrous ECM deposits in CCl_4-treated animals at the

indicated time points. (**B**) The regulator of the actin cytoskeleton, coronin 1a (CORO1A), serves as an example of a protein with a positive slope of the correlation fit. The methionine cycle enzyme, adenosylhomocysteinase (AHCY), serves as an example of a protein with a negative slope of the correlation fit. (**C,D**) The scatter plots show the linear regression slope and the Pearson correlation coefficient for proteins of CCl_4 Total (C), and E-fraction (D) proteomes. Statistical significance of the correlation is color-coded as indicated. The line plots show time-dependent change in mass spectrometry intensities of indicated representative proteins with significant correlation in Total (solid line) and E-fraction (broken line) proteomes in CCl_4 and DDC models; n = 4–6. (**E**) Representative immunofluorescence (IF) images of liver sections from untreated controls (Ctrl), CCl_4-, and DDC-treated mice at indicated time points of fibrosis development (T2) and resolution (T3 and T4) immunolabeled for clusterin (green), keratin 19 (K19, red), and collagen 1 (Col1, blue). Nuclei were stained with DAPI (blue). Arrowheads, clusterin staining signal delineating collagen deposits; arrows, clusterin-positive injured hepatocytes; yellow arrows, clusterin-positive biliary epithelial cells. CV, central vein; PV, portal vein. Boxed areas, ×2 images. Scale bar = 50 □m. (**F**) Representative IF images of human liver sections from different stages of chronic liver diseases of various etiologies (biliary-type, steatotic liver disease, and chronic HCV infection) immunolabeled for clusterin (Clu, green) and collagen 1 (Col1, magenta). Nuclei were stained with DAPI (blue). Top row shows increase in clusterin expression along collagen fibrils in biliary-type and metabolic syndrome-related cirrhosis compared to the stage of mild fibrosis. Bottom row documents change in clusterin staining pattern with chronic hepatitis C progression from fibrosis stage F1 to stage F4 (METAVIR grading system: F1, portal fibrosis; F2, periportal fibrosis; F3, bridging septal fibrosis; F4, cirrhosis). Arrowheads, clusterin staining delineating collagen deposits; arrows, clusterin-positive capillarized sinusoids; yellow arrows, clusterin-positive bile canaliculi (stage F1 only). PV, portal vein. Boxed areas, ×4 images. Scale bar = 50 □m.

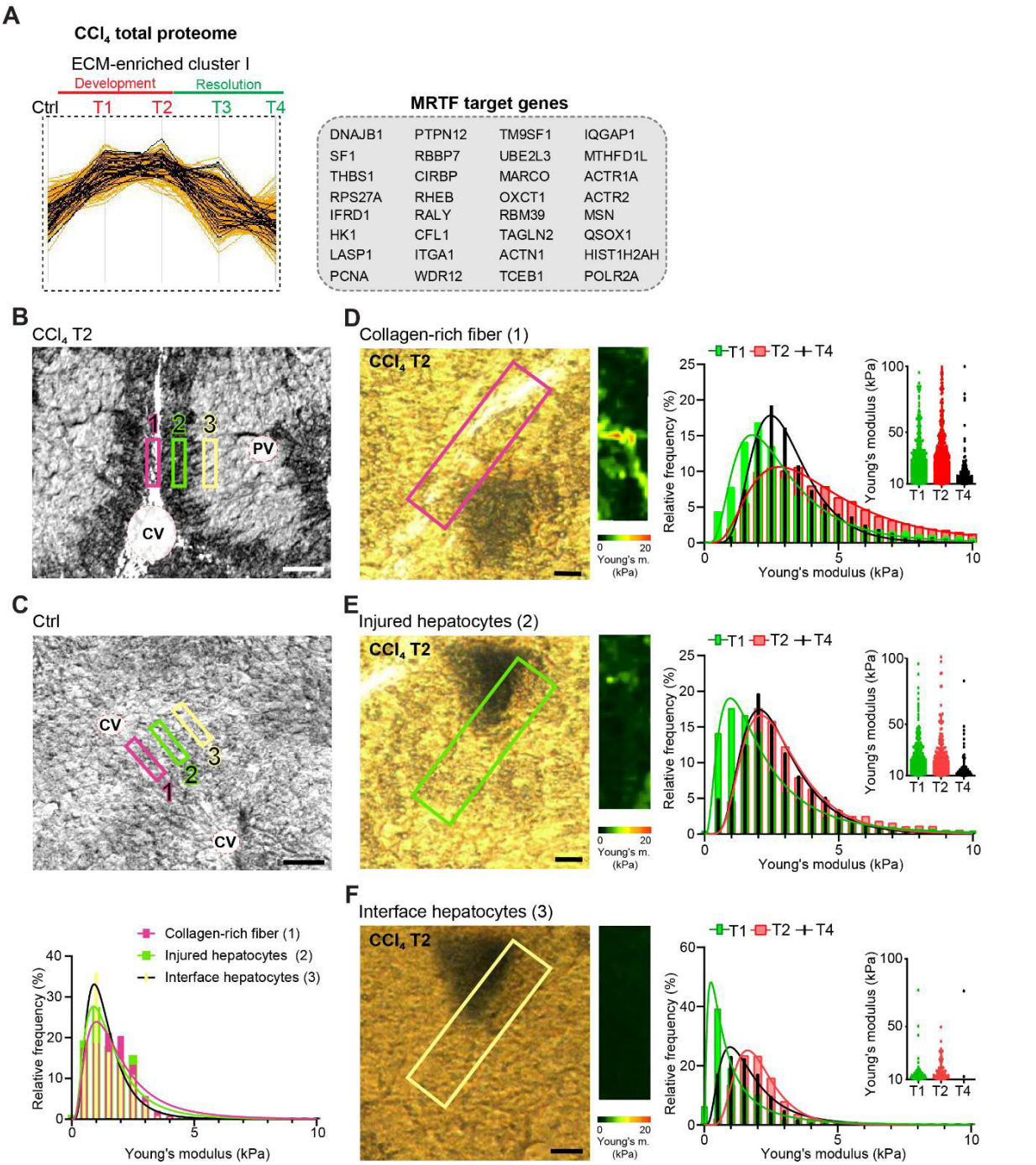

FIGURE 7 Atomic force microscopy (AFM) stiffness mapping reveals changes in the local mechanics of liver tissue upon hepatotoxic injury. (**A**) The line plot shows the dynamics of 32 myocardin-related transcription factor (MRTF) targets (highlighted in black) significantly enriched in ECM-enriched cluster I of CCl_4 Total proteome (Figure 2C) identified by Fisher's exact test (p = 0.01; Benjamini-Hochberg FDR = 0.03). (**B,C**) Representative polarized microscopy images of CCl_4-treated (T2, B) and untreated control (Ctrl, C) liver sections with indicated regions (1–3) selected for AFM measurements. Note white areas corresponding to collagen fibers visualized by polarized light. Pink rectangle, region 1 (collagen-rich fiber); green rectangle, region 2 (injured hepatocytes); yellow rectangle, region 3 (interface hepatocytes). CV, central vein; PV, portal vein. Scale bar = 100 □m. Histogram shows Young's moduli for the measured regions; n = 7 regions in three mice. (**D–F**) Representative polarized microscopy images of CCl_4-treated (T2) liver sections with rectangle indicating the regions of AFM measurements (30 × 100 □m^2) and corresponding pseudocolor Young's modulus maps determined by AFM. Scale bar = 25 □m. Histograms show Young's moduli for indicated regions of collagen-rich fibers (D), injured hepatocytes (E), and interface hepatocytes (F) at indicated time points of fibrosis development (T1 and T2) and spontaneous resolution (T4). Inset scatter plots show Young's modulus values above 10 kPa for each time point.